PREPARATION AND CHARACTERIZATION OF SUITABLE INSULATING AND TRANSPARENT CONDUCTING THIN FILMS FOR THIN FILM ELECTROLUMINESCENT DEVICES BY SOL-GEL PROCESS

A Thesis
Submitted to
Dublin City University

For the degree of
Doctor of Philosophy (PhD)

By

Mohammad Jahangir Alam, ***B.Sc. Eng., M.Sc. Eng.***

School of Electronic Engineering
Dublin City University

Research Supervisor
Professor David Cameron, ***BSc, PhD, CEng, MIEE***

November 2001

DECLARATION

I hereby certify that this material, which I now submit for assessment on the programme of study leading to the award of Ph.D. is entirely my own work and has not been taken from the work of others save and to the extent that such work has been cited and acknowledged within the text of my work.

Signed: Mohammad Jahangir Alam

Mohammad Jahangir Alam

ID No.: 96971479

Date: 23rd November 2001

ACKNOWLEDGEMENTS

I would like to thank my academic supervisor Professor David Cameron for his guidance, valuable suggestions and constructive criticism for this work. His expertise, availability to discuss ideas and willingness to give of his knowledge were instrumental in the completion of this thesis.

I would like to thank Professor M. S. J. Hashmi for his all kind of support and encouragement during the period of my studies in Ireland and also for affording me the opportunity to pursue this work.

I am grateful to Professor Charles McCorkell for his support and encouragement during my research.

I am grateful to Dr. David Doff, Department of Geology, Trinity College, Dublin, for his help in X-ray diffraction measurements. Grateful acknowledgement is also made to Savcor Coatings Oy, Mikkeli, Finland, for the use of their XRD instrument.

I like to thank Dr. Greg Hughes, School of Physical Science, Dublin City University, for his assistance in carrying out the X-ray Photoelectron Spectroscopic (XPS) analysis. I also like to thank Dr. Brian Lawless, School of Physical Science, Dublin City University, for his assistance in using the ellipsometer.

I am grateful to Physics and Chemistry department of Dublin City University for allowing me to use their UV/VIS and FTIR instrument.

I would like to thank John Whelan, Robert Clare, Conor Maguire, Paul Wogan, Liam Meany and Theresa Collins of School of Electronic Engineering, for their help and cooperation during the period of my research.

I have to thank my loving wife, Shayla Haque, for her sacrifice, constant inspiration, patience and understanding during the period of my studies.

Finally, I would like to thank all Bangladeshi friends in Ireland for their encouragement and inspiration during the period of my research.

DEDICATION

To

My beloved Parents,

Wife and Son

CONTENTS

DECLARATION i

ACKNOWLEDGEMENTS ii

DEDICATION iii

ABSTRACT x

Chapter 1

INTRODUCTION

1.1 Introduction 1
1.2 Objectives of the work described in this thesis 3
1.3 Organization of this thesis 3

Chapter 2

THE STRUCTURE, DEVICE PHYSICS AND MATERIAL PROPERTIES OF THIN FILM ELECTROLUMINESCENT DEVICES

2.1 Introduction 5
2.2 History of electroluminescence 5
2.3 Device structure 7
2.4 Electrical properties of thin film EL devices 8
2.5 Device physics 10
    2.5.1 Tunnel emission 11
    2.5.2 Electron acceleration 13
    2.5.3 Impact excitation 13
    2.5.4 De-excitation 13
2.6 Material properties 14

  2.6.1 Glass Substrates 15
  2.6.2 Transparent Electrodes 15
  2.6.3 Metal Electrodes 16
  2.6.4 Insulating Layers 17
  2.6.5 Phosphor Layers 20
    2.6.5.1 Host materials 21
    2.6.5.2 Luminescent centers 21
2.7 Reliability of Thin Film EL Devices 22
2.8 Advantages of Thin Film EL Displays Compare to Other Displays 22
2.9 Conclusions 23

Chapter 3

DEPOSITION TECHNOLOGY OF THIN FILMS

3.1 Introduction 25
3.2 Classification of deposition technologies 25
  3.2.1 Liquid Phase 26
    3.2.1.1 Sol-gel Process 26
    3.2.1.2 Spray Pyrolysis 26
  3.2.2 Vapour Phase 27
    3.2.2.1 Chemical Vapour Deposition 27
    3.2.2.2 Physical Vapour Deposition 30
      3.2.2.2.1 Sputtering 30
        3.2.2.2.1.1 DC Diode Sputtering 31
        3.2.2.2.1.2 Bias Sputtering 31
        3.2.2.2.1.3 RF Diode Sputtering 32
        3.2.2.2.1.4 Magnetron Sputtering 34
        3.2.2.2.1.5 Ion-Beam Sputtering 35
      3.2.2.2.2 Resistance Evaporation 37
      3.2.2.2.3 Electron Beam Evaporation 38
      3.2.2.2.4 Ion Vapour Deposition 39
      3.2.2.2.5 Cathodic Arc Deposition 40
      3.2.2.2.6 Laser Ablation 42
3.3 Criteria for the selection of a deposition technology for specific applications 43
3.4 Material Characteristics 44
3.5 Conclusions 45

Chapter 4

SOL-GEL TECHNOLOGY

4.1 Introduction 47
    4.1.1 Sol-gel processing 47
    4.1.2 History of sol-gel technology 48
4.2 Theory of Sol-gel Technology 49
    4.2.1 Hydrolysis and Condensation 49
    4.2.2 Gelation 50
    4.2.3 Aging of Gels 51
    4.2.4 Drying of Gels 52
    4.2.5 Avoiding Fracture 53
    4.2.6 porosity 54
    4.2.7 Sintering of Gels 54
4.3 Physics of Film Formation 55
    4.3.1 Dip Coating 55
    4.3.2 Spin Coating 57
    4.3.3 Other Coating Methods 59
        4.3.3.1 Electrophoresis 59
        4.3.3.2 Thermophoresis 60
        4.3.3.3 Settling 60

4.4 Applications 61

Chapter 5

MEASUREMENT TECHNIQUES

5.1 Introduction 63
5.2 Measurement of Film Thickness 63
    5.2.1 Interferometry 63
    5.2.2 Ellipsometry 65
5.3 Electrical measurement 67
    5.3.1 Measurement of Film Resistivity 67
    5.3.2 Measurement of Hall Mobility and Carrier Concentration 71
5.4 Measurement of Surface Roughness 74
5.5 Bonding structure measurement 76
    5.5.1 Fourier Transform Infrared Spectroscopy 77

5.5.2 Raman Spectroscopy 78
5.6 Measurement of X-ray diffraction (XRD) 80
5.6.1 Principles 81
5.7 Measurement of X-ray photoelectron spectroscopy (XPS) 83
5.7.1 The basic XPS experiment 83
4.7.2 X-ray interaction with matter, the photoelectron effect and photoemission from solids 85
5.8 Measurement of Transmittance 86

Chapter 6

INSULATING MATERIALS

6.1 Introduction 88
6.2 Titanium Dioxide (TiO_2) Thin Films Deposited by Sol-gel Process 89
6.2.1 Introduction 89
6.2.2 Experimental procedure 90
6.2.3 Results and discussion 92
6.2.3.1 Electrical Properties 92
6.2.3.2 Roughness 97
6.2.3.3 Structural Properties 98
6.2.3.3.1 Fourier Transform Infrared (FTIR) Spectroscopy 98
6.2.3.3.2 Raman Spectroscopy 101
6.2.3.3.3 X-ray Diffraction Spectroscopy 104
6.2.3.3.4 X-ray Photoelectron Spectroscopy 106
6.2.3.4 Optical Properties 108

6.2.4 Conclusions 110
6.3 Tantalum oxide (Ta_2O_5) Thin Films Deposited by Sol-gel Process 112
6.3.1 Introduction 112
6.3.2 Experimental procedure 113
6.3.3 Results and Discussion 113
6.3.3.1 Electrical Properties 113
6.3.3.2 Roughness 120
6.3.3.3 Structural Properties 121
6.3.3.3.1 Fourier Transform Infrared (FTIR) Spectroscopy 121
6.3.3.3.2 X-ray Diffraction Spectroscopy 123
6.3.3.4 Optical Properties 125
6.3.4 Conclusions 128

Chapter 7

TRANSPARENT CONDUCTING MATERIALS

7.1 Introduction 130

7.2 Preparation and properties of transparent conductive aluminum-doped zinc oxide thin films deposited by sol-gel process 132

- 7.2.1 Introduction 132
- 7.2.2 Experimental Procedure 134
- 7.2.3 Results and discussion 135
  - 7.2.3.1 Electrical Properties 135
  - 7.2.3.2 Roughness 143
  - 7.2.3.3 Structural Properties 143
    - 7.2.3.3.1 X-ray Diffraction Spectroscopy 143
    - 7.2.3.3.2 Raman Spectroscopy 146
  - 7.2.3.4 Optical Properties 148
- 7.2.4 Conclusions 150

7.3 Preparation and properties of transparent conductive ITO thin films deposited by sol-gel process 151

- 7.3.1 Introduction 151
- 7.3.2 Experimental procedure 152
- 7.3.3 Results and discussion 152
  - 7.3.3.1 Electrical Properties 152
  - 7.3.3.2 Roughness 160
  - 7.3.3.3 Structural Properties 160
    - 7.3.3.3.1 X-ray Diffraction Spectroscopy 160
    - 7.3.3.3.2 X-ray Photoelectron Spectroscopy 163
  - 7.3.3.4 Optical Properties 165
- 7.3.4 Conclusions 168

Chapter 8

COMBINED EFFECT OF INSULATING AND TRANSPARENT CONDUCTING LAYERS USED IN THIN FILM ELECTROLUMINESCENT DEVICES

8.1 Introduction 170

8.2 Characterization of Transparent Conductive ZnO:Al Thin Films Deposited on Titanium Dioxide Film and Tantalum Oxide Film by Sol-gel Process 172
8.2.1 Introduction 172
8.2.2 Results and Discussion 173
8.3 Characterization of Transparent Conductive ITO Thin Films Deposited on Titanium Dioxide Film and Tantalum Oxide Film by Sol-gel Process 177
8.3.1 Introduction 177
8.3.2 Results and Discussion 178
8.4 Conclusions 182

Chapter 9

CONCLUSIONS AND RECOMMENDATIONS

9.1 Conclusions of the Work 184
9.2 Future Work 187

REFERENCES 190

APPENDIX A X-Ray Diffraction Data Table A-1

APPENDIX B Publications on This Work B-1

PREPARATION AND CHARACTERIZATION OF SUITABLE INSULATING AND TRANSPARENT CONDUCTING THIN FILMS FOR THIN FILM ELECTROLUMINESCENT DEVICES BY SOL-GEL PROCESS

Mohammad Jahangir Alam, *B.Sc. Eng., M.Sc. Eng.*

ABSTRACT

Thin film electroluminescent (TFEL) displays are attractive because they are light, have low power consumption, wide viewing angle and long lifetime, are extremely rugged and can be used in hostile environments. Recently, there has been a renewed interest in thin film electroluminescent devices because of their promising application to head mounted displays for use in automobiles, aircraft, microsurgery and virtual reality applications. Both conventional and inverted thin film electroluminescent device structures consist of insulating film, transparent conducting film and luminescent layer. In a thin film electroluminescent device, the luminescent layer is sandwiched between two insulating layers. Electrodes outside both insulating layers are used to apply an electric field, with one electrode being transparent.

These thin films are found to be sensitive to preparation conditions and can be prepared by a variety of methods, such as, magnetron sputtering, chemical vapour deposition, reactive electron beam evaporation, reactive thermal deposition, spray pyrolysis, laser ablation and more recently by sol-gel process. Nowadays, the sol-gel process is a well-accepted technology for the preparation of thin films, monoliths, fibers and monosized powders. Compared to conventional thin film forming processes such as CVD, evaporation or sputtering, sol-gel film formation requires considerably less equipment and is potentially less expensive; however the most important advantage of sol-gel processing over conventional coating methods is the ability to control precisely the microstructure of the deposited film, i.e., the pore volume, pore size and surface area.

The sol-gel process is a method where the substrate to be coated is dipped into a liquid solution containing the active material. When the substrate is removed from the solution a thin layer remains. On exposure to the atmosphere a hydrolysis reaction takes place which solidifies the liquid film.

In this work, all the thin films have been prepared by using sol-gel process. Insulating films of titanium dioxide and tantalum oxide were prepared from titanium and tantalum alkoxides respectively and their characteristics have been investigated. The most important requirements for the insulating layers are high dielectric constant and high electric field strength. The dielectric constants of the films were calculated from the maximum capacitance of the Al/film/Si structure. The maximum dielectric constants for TiO_2 and Ta_2O_5 films were approximately 50 and 82 respectively annealed at 700^0C in

oxygen. These results suggest that the TiO_2 and Ta_2O_5 thin film can be used as a high dielectric constant insulating layer in thin film electroluminescent devices.

Highly conductive and transparent aluminum-doped zinc oxide thin films have been prepared from the solution of zinc acetate and aluminum nitrate in ethanol by the sol-gel process. The effect of changing the aluminum-to-zinc ratio from 0 to 5 at. % and annealing temperature from 0 to 700^0C in air, oxygen and nitrogen has been investigated. The resistivities of thin films were measured as a function of annealing temperature and also as a function of aluminum dopant concentration in the solution. As-deposited films have high resistivity and high optical transmission. Annealing of the as-deposited films in atmosphere leads to a substantial reduction in resistivity. The films have a minimum value of resistivity of 1.3×10^{-4} Ω-cm for 0.8 at. % aluminum-doped zinc oxide annealed at 500^0C in nitrogen and a maximum transmission of about 88% when deposited on glass substrates. X-ray diffraction measurements employing CuKα radiation were performed to determine the crystallinity of the ZnO:Al films which showed that the films were polycrystalline with a hexagonal structure when annealed at higher temperatures in air, oxygen and nitrogen.

Transparent conductive indium tin oxide (ITO) thin films have been prepared by a sol-gel process. The starting solution was prepared by mixing indium chloride dissolved in acetylacetone and tin chloride dissolved in ethanol. 0-20 % by weight Sn-doped indium oxide (ITO) films were prepared by heat-treatment at above 400^0C. The electrical, optical and structural properties of ITO thin films were investigated. The electrical resistivity was measured by using four-point probe method. The ITO thin films containing 10 wt.% Sn showed the minimum resistivity of $\rho = 8.0 \times 10^{-4}$ Ω-cm annealed at 500^0C in nitrogen. The films have an optical transparency up to 89% at 900 nm. X-ray diffraction measurements employing CuKα radiation were performed to determine the crystallinity of the ITO films which showed that the ITO films were polycrystalline with a cubic bixbyite structure annealed in air, oxygen and nitrogen.

Aluminum doped zinc oxide thin films have been deposited on titanium dioxide and tantalum oxide films on glass by sol-gel process. The resistivity of ZnO:Al thin films deposited on titanium dioxide and tantalum oxide films on glass have a minimum value of 2.5×10^{-3} Ω-cm and 9.6×10^{-4} Ω-cm respectively annealed at 500^0C in nitrogen. ZnO:Al thin films deposited on titanium dioxide film on glass have a higher resistivity than that deposited on glass. This increase in resistivity on titanium dioxide film is due to the diffusion of titanium into the zinc oxide layer.

Indium tin oxide thin films have been deposited on titanium dioxide and tantalum oxide films on glass for thin film electroluminescent devices. The resistivity of ITO films deposited on titanium dioxide and tantalum oxide films has a minimum value of 9.5×10^{-4} Ω-cm and 9.0×10^{-4} Ω-cm respectively annealed at 500^0C in nitrogen which are as low as the resistivity of ITO films deposited on glass. This combination of transparent

conductive ITO thin films and titanium dioxide or tantalum oxide insulating layer can be used for thin film electroluminescent devices.

Chapter 1

INTRODUCTION

1.1 Introduction

Electroluminescence (EL) is a non-thermal generation of light resulting from the application of an electric field to a substance. There are two types of EL devices. In the familiar light-emitting diodes (LED) devices, light is generated by electron-hole pair recombination near a pn junction. In the second type of EL device, light is generated by impact excitation of a light-emitting center, called an activator or a luminescent centre, by high-energy electrons. The electrons gain their high energy from a high electric field on the order of 10^8 V/m and thus this type of EL is often called high-field electroluminescence. In these devices, the behaviour of the majority carriers (the electrons) predominantly determines the device physics. Based on this high-field electroluminescent phenomenon, four types of EL devices have been developed. They are categorized according to the phosphor (discussed in section 2.6.5) configuration and the drive voltage waveforms: ac thin film EL, ac powder EL, dc thin film EL and dc powder EL. Among these, the first two types are now commercially available: ac thin film EL devices are used as flat screens of laptop personal computers and word processors and ac powder EL devices are used as back lights for liquid crystal displays.

Thin film electroluminescent devices consist of insulating films, transparent conducting film and electroluminescent phosphor layer. There are two types of thin film electroluminescent device structures: (a) conventional device structure and (b) inverted device structure. Fig. 1.1 and 1.2 show the fundamental device structures of conventional and inverted thin film electroluminescent devices respectively.

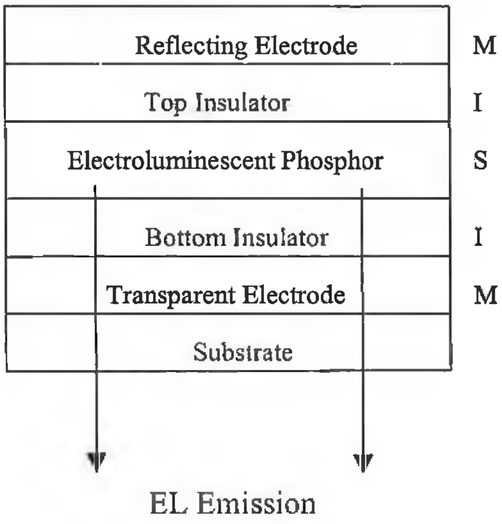

Figure 1.1 Conventional MISIM (metal-insulator-semiconductor-insulator-metal) device structure of a thin film EL display.

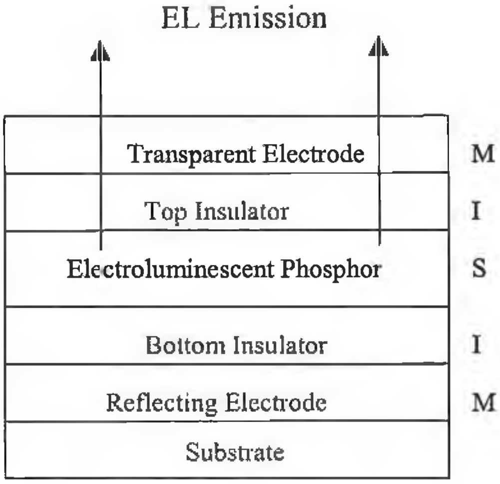

Figure 1.2 Inverted thin film EL device structure.

1.2 Objectives of the Work Described in This Thesis

- To prepare the insulating and transparent conducting films by sol-gel process.

- To measure the electrical properties, e.g. dielectric constant, breakdown voltage and resistivity for the insulating films and resistivity, hall mobility and carrier concentration for the transparent conducting films annealed at different temperatures in the presence of air, oxygen and nitrogen.

- To characterize the bonding structure of the films annealed at different temperatures in the presence of air, oxygen and nitrogen.

- To investigate the crystallinity of the films annealed at different temperatures in the presence of air, oxygen and nitrogen.

- To measure the optical properties, e.g. optical transmission of the films annealed at different temperatures in the presence of air, oxygen and nitrogen.

- To deposit transparent conducting films on top of insulating films by sol-gel process as this combination is used to prepare the inverted thin film electroluminescent devices.

- To characterize the combined structures of transparent conducting and insulating films and to find the best possible combination for thin film electroluminescent devices.

1.3 Organization of This Thesis

This thesis is organized into nine chapters and two appendices.

- Chapter 1 presents the introductory chapter, which includes the summary and objectives of this thesis.

- Chapter 2 presents the review of the structure, device physics and material properties of thin film electroluminescent devices.

- Chapter 3 describes the various deposition technologies of thin films.
- Chapter 4 describes the sol-gel technology.
- Chapter 5 deals with measurement techniques used in this work.
- Chapter 6 describes the preparation and characterization of insulating films by sol-gel process.
- Chapter 7 describes the preparation and characterization of transparent conducting films by sol-gel process.
- Chapter 8 investigates the combined characteristics of transparent conducting films deposited on insulating films by sol-gel process.
- Chapter 9 presents the conclusions of this work and offers suggestions for further studies.
- Appendix A presents the X-ray diffraction data for titanium dioxide, tantalum oxide, zinc oxide and indium tin oxide.
- Appendix B presents the list of publications from this work.

Chapter 2

THE STRUCTURE, DEVICE PHYSICS AND MATERIAL PROPERTIES OF THIN FILM ELECTROLUMINESCENT DEVICES

2.1 Introduction

Fundamental to an EL device is its solid state construction which can be fully integrated onto the substrate of the drive electronics. This has the advantage that a fully integrated optoelectronic flat panel display can be produced on a single substrate. Additionally, since EL displays are emissive, the viewing angle is greater than 160^0 which has been an inherent problem with the liquid crystal displays (LCD). EL panels offer a temperature range of -25^0 C to 60^0 C which is limited by the drive electronics, and the solid state construction makes them inherently more shock and vibration resistant. The ruggedness and temperature range of flat panels are very critical for certain military and industrial applications. Currently, thin film EL is the longest lasting, most reliable flat panel display technology on the market. Display panels have demonstrated device lifetimes of over 50,000 h with less than 10% luminance change [1,2].

To understand the fundamentals of a thin film electroluminescent device, one must consider the device structure, the electrical and optical properties, the device physics and the unique materials requirements.

2.2 History of electroluminescence

Electroluminescence (EL) is the phenomenon in which electrical energy is converted to luminous energy without thermal energy generation. The first observations of the electroluminescence phenomenon were reported in 1929 [3]. Important, but often overlooked, experiments by Gudden and Pohl first demonstrated the effect that an electric field has on the photoluminescent decay of a copper-doped zinc sulphide (ZnS:Cu) phosphor. In 1936, Georges Destriau [4] observed light emission from a suspension consisting of ZnS:Cu and oil; this work is often cited as the first published report on the phenomenon of electroluminescence. Very few people published work on electroluminescence after Destriau's discovery, until the early 1950s when GTE Sylvania received a patent for an EL powder lamp [5]. Subsequent to this patent, research efforts concentrated on powder EL phosphors in order to achieve a brighter, long lifetime light source with minimal power requirements. This effort, however, soon ended when it was determined that the phosphors being investigated were unable to provide adequate sustained brightness over the minimum commercially acceptable lifetimes (500h).

In the 1960s there was a resurgence in EL research which was focused on display technologies. One of the first a.c. thin film dot matrix displays was unveiled in 1965 by Sigmatron Corp., which was followed by the demonstration of a sunlight readable numeric display in 1968 [6]. No commercial products were ever produced from this effort and eventually this company folded. Later, in 1968, Vecht [7] demonstrated the first d.c. driven EL panel, but again a commercial product was not generated. In the 1960s great strides were made in thin film technology, which helped Soxman and Ketchpel [8] fabricate thin film devices. These devices had acceptable lifetimes and multiplexing capabilities, but failed to achieve acceptable reliability. A breakthrough in EL technology was made by Inoguchi et al. (Sharp Corporation) [9] which introduced a new a.c. thin film approach in 1974. The key to this approach was the concept put forward by Russ and Kennedy (1967) [10] which described a three-layer sandwich design. The team of researchers at Sharp fabricated a device modelled on a capacitor structure which consisted of a manganese-doped zinc sulphide (ZnS:Mn) central phosphor layer and two yttrium oxide (Y_2O_3) insulators that sandwiched the phosphor layer. This was the first high brightness, long lifetime device. This paper is credited with transforming the research and development of electroluminescence into a viable display technology. While both a.c. and d.c. driven devices have been explored for display applications, the interest in a.c. driven thin film electroluminescent devices has dominated. Sharp succeeded in developing this technology and introduced a monochrome television display in 1978 [11]. In order to compete with other display technologies, multicoloured displays were introduced by

Coovert et al. (Planar Systems) [12], and by 1994 Planar Systems had introduced a prototype full colour thin film EL display [13]. While thin film EL research has dominated much of the EL research and development efforts, parallel work has been performed in powder EL technology. In the early 1990s, a.c. powder EL light sources began to re-establish themselves based on improved control of moisture which was necessary to ensure adequate lifetimes. Using a glass microencapsulation technique to avoid moisture-induced degradation of ZnS powders, Durel Corp. demonstrated a flexible thin EL lamp which was incorporated as a back light into LCD flat panel displays (i.e. in wrist watches). Thus, today both thin film and powder EL displays are active in the market place.

2.3 Device structure

A typical thin film EL device structure is shown in Fig. 1.1. The MISIM (metal-insulator-semiconductor-insulator-metal) structure is usually deposited on a transparent glass substrate which varies in composition depending on the phosphor processing temperature. Typically, Corning 7059 glass is used as a substrate because of its low cost and high availability. In addition, it does not contain alkali metals which have been found to diffuse into the semiconducting phosphor layer and cause the devices to degrade over time [14]. Some EL phosphors, however, require a high temperature-annealing step which is above the 598^0C softening temperature of the Corning 7059 glass. When processing temperatures exceed 598^0C, high temperature glass ceramics are used. These glass ceramics typically cost 10 times more than standard 7059 glass.

Another structure that has been developed is the so-called ‘inverted’ structure which is shown in Fig. 1.2. This structure has been used in active matrix electroluminescent (AMEL) [15] displays as well as thick film dielectric hybrid electroluminescent (TDEL) displays [16]. The inverted thin film electroluminescent device structure uses the transparent electrode on the top of the top insulator.

Regardless of whether the conventional or inverted structure is used, the basic function of each layer is the same. Before discussing the thin film EL equivalent circuit diagram it is appropriate to first summarise the basic function of each layer. First of all, the middle semiconducting layer (commonly called the phosphor layer) is the light emitting material. This material consists of two constituents: (1) the host material which dominates the electrical properties of the phosphor layer, and (2) the luminescent center which dominates the optical properties of the phosphor layer. When a large electric field is induced across the phosphor layer, electrons are injected from the phosphor/insulator interface and accelerate through the phosphor layer. These electrons then excite the luminescent centers which subsequently generate light. The phosphor layer is sandwiched between two insulators which limit the current transported across the device. These insulating layers have been found to effectively prolong the lifetime of the thin film electroluminescent device. Finally, the top and bottom electrodes simply complete the device structure and make electrical contact to the drive electronics.

2.4 Electrical properties of thin film EL devices

The basic thin film EL device structure can be modelled as a simple circuit where the insulators are represented by perfect capacitors and the phosphor layer is represented by a capacitor below threshold and a pair of back-to-back diodes above threshold [17]. The threshold is the voltage or electric field at which the phosphor layer experiences a Zener breakdown. Schematically, the equivalent circuit is shown in Fig. 2.1.

Below threshold, the thin film EL device is simply a three series capacitor circuit where the voltage drop across each layer is proportional to the dielectric constant and the layer thickness. At threshold, the phosphor layer experiences a Zener breakdown as electrons are injected by tunnelling into the phosphor layer. This produces a real current which is transported across the phosphor layer and is represented by the back- to-back Zener diodes in the diagram. Thin film EL devices are driven at high voltages (200-250 V) which induce large electric fields (1-2 MeV cm^{-1}) across the insulators and the phosphor layer. While this simple model accurately describes most of the device characteristics, more sophisticated models have been suggested which account for the time dependence [18] and waveform dependence [19], respectively.

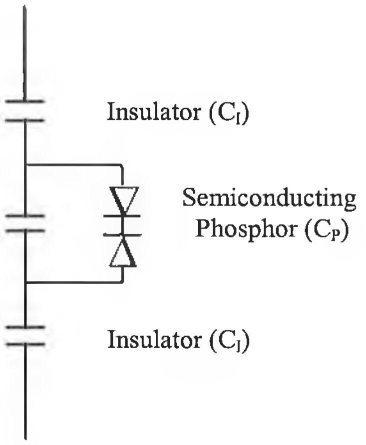

Figure 2.1 Equivalent circuit diagram for a thin film EL device.

One very useful measurement that illustrates the electrical characteristics in a thin film EL device is the charge-voltage (Q-V) diagram, which is illustrated in Fig.2.2 [2]. Initially, in a virgin device, there is no stored polarization charge so at zero voltage there is a corresponding zero charge. As the voltage is ramped below threshold, the slope of the Q-V curve (dQ/dV) is equal to the total capacitance of the insulators and the phosphor layer. When threshold (V_{th}) is reached, the phosphor layer breaks down and charge is transported which causes the slope of the Q-V diagram to increase sharply. The new slope is equal to the series capacitance of the two insulators only. The charge that is transported across the phosphor layer accumulates at the anodic phosphor/insulator interface and creates an opposing polarisation field. When the voltage is reduced below threshold, the slope decreases and the capacitance again becomes equal to the combined capacitance of the insulators and the phosphor. Because of the trapped charge at the interface, at 0 V the charge is now non-zero and only when the external field equals the internal polarisation field does the charge reduce to zero. When the voltage is cycled through an entire a.c. pulse, a hysteresis loop is formed whose area is proportional to the power dissipated in the device. The power density (P) is given by:

$$P=2fC_iV_{mod}V_{dth} \qquad (2.1)$$

Where f is the frequency, C_i is the insulator capacitance, V_{mod} is the modulation voltage, and V_{dth} is the internal diode threshold voltage. Ci and V_{dth} are both functions of the dielectric properties of the phosphor and insulator layers and minimising the phosphor dielectric constant and maximising the insulator dielectric constant is critical to lowering the power consumed in thin film EL displays.

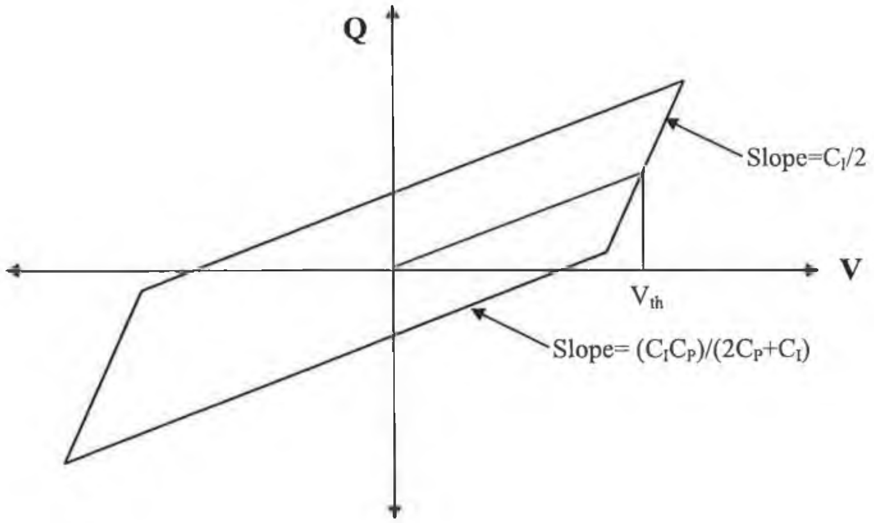

Figure 2.2 Schematic diagram of charge-voltage (Q-V) plot.

2.5 Device physics

The device physics of an EL device can be divided into four main topics, namely (1) tunnel emission of electrons from interface states, (2) acceleration of electrons to high energies, (3) impact excitation or impact ionisation of the luminescent center, and (4) de-excitation of the excited electron by radiative (photon generation) or non-radiative recombination [1]. These four processes are illustrated in fig. 2.3.

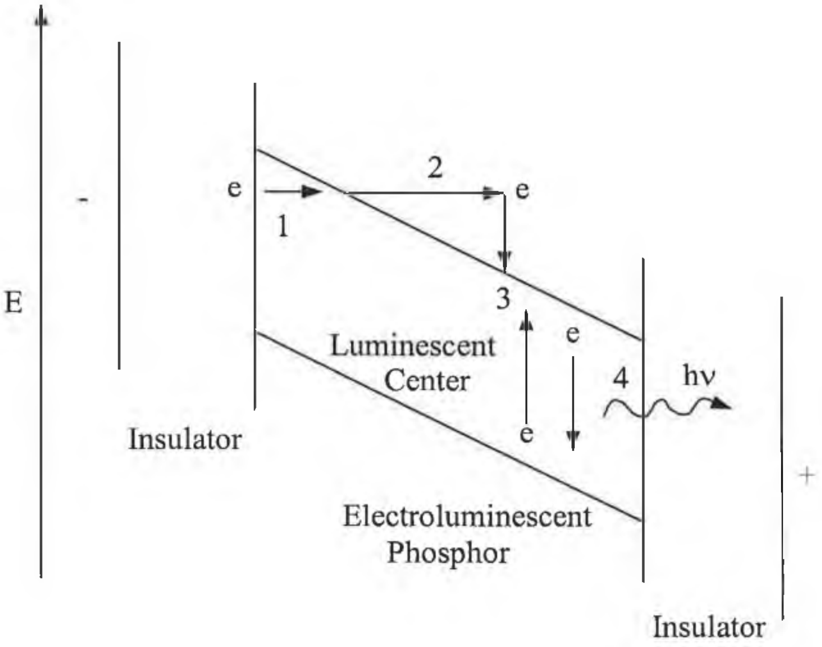

Figure 2.3 Four mechanisms that occur in a thin film electroluminescent device: (1) tunnel emission of electrons from interface states, (2) acceleration of electrons to high energies, (3) impact excitation of the luminescent center, and (4) radiative de-excitation of the excited state electron (photon generation).

2.5.1 Tunnel emission

The mechanism of electron injection in thin film EL devices is critical to understanding the device operation. In general there are two mechanisms responsible for carrier injection, namely (1) thermionic emission, and (2) field emission or tunnelling (fig. 2.4). In thin film EL devices, one must also consider the origin of these carriers, which either come from the bulk or from the phosphor/insulator interface. The accepted theory for carrier injection in most EL phosphors is tunnelling from interface states. While the pure tunnelling mechanism has been shown to be temperature independent, there is a slight temperature dependence on the thin film EL device current. Consequently, this tunnelling mechanism has been suggested to be thermally assisted [20].

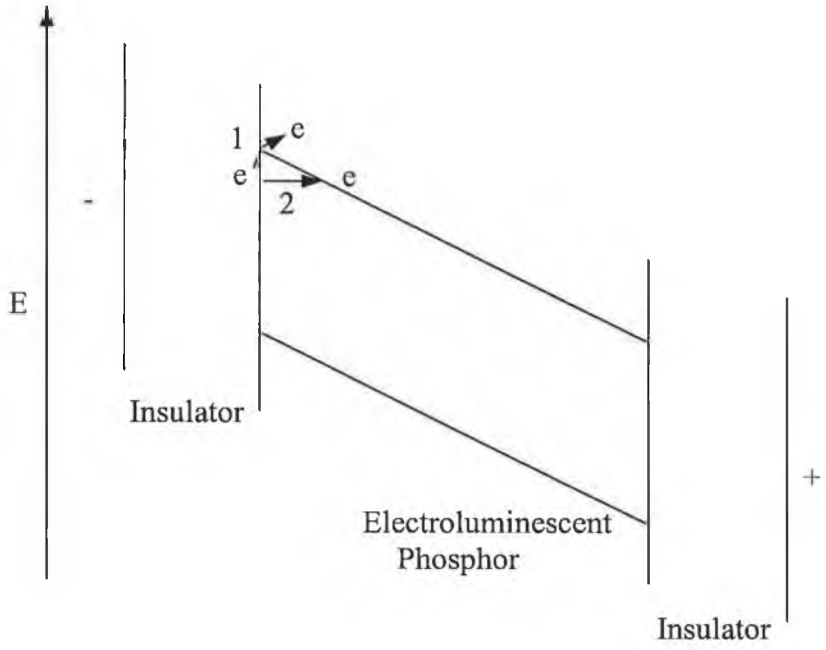

Figure 2.4 Energy band diagram illustrating the two electron injection mechanisms: (1) thermionic and (2) field emission or tunnelling.

There are several experimental observations that support the idea that the electrons trapped at the phosphor/insulator interface are the carrier source, and that the thermally assisted tunnelling mechanism is responsible for their injection. First of all, it has been shown that the threshold voltage (field) varies for opposite polarities of the same device when different top and bottom insulators are used, which suggests that the interface is the source of carriers. Specifically, devices with different top and bottom insulators have demonstrated asymmetric device currents and threshold fields as a function of the polarity of the applied voltage. Second, the observation that the device current is such a strong function of the phosphor field suggests that the tunnelling mechanism dominates. Finally, the fact that the electrical properties are only a weak function of temperature rules out a strict thermionic emission process and suggests that tunnelling dominates [21].

2.5.2 Electron acceleration

Once the electrons are tunnel injected into the phosphor layer conduction band, they are accelerated under the influence of the electric field. The electric field in the phosphor layer can be calculated by rearranging Maxwell's equations for series capacitors. The resultant equation for the phosphor electric field (E_P) is [22]:

$$E_p = \frac{\varepsilon_i}{\varepsilon_i d_p + \varepsilon_p (2) d_i} V_{tot} \qquad (2.2)$$

where ε is the dielectric constant, d is the layer thickness, and the subscripts i and p represent the insulator and the phosphor, respectively (assuming the top and bottom insulators are the same). This phosphor electric field is extremely high. At these high electric fields, the injected electrons accelerate to high energies extremely quickly.

2.5.3 Impact excitation

After the electrons accelerate to high enough energies, they can interact with a luminescent center and promote one of the luminescent center's ground state electrons. The electron can either be promoted into a higher atomic state of the luminescent center, or into the conduction band of the host material which is called impact excitation [23] or impact ionisation [24], respectively. When the electron is excited into a higher atomic state (impact excitation), it can relax back into its ground state either radiatively or non-radiatively.

2.5.4 De-excitation

De-excitation can occur either radiatively (which produces a photon) or non-radiatively. Typically, non-radiative relaxation occurs by phonon generation which produces heat from lattice vibrations. Fig. 2.5 schematically demonstrates these two de-excitation pathways. Local lattice imperfections such as point defects (interstitials, vacancies...), line defects (dislocations), and volume defects (grain boundaries) also act as non-radiative recombination centers which are deleterious to the radiative efficiency. The non-radiative recombination rate increases with temperature while the radiative recombination rate is temperature insensitive.

Subsequently, the radiative efficiency decreases as the temperature increases due to an increase in the non-radiative recombination rate.

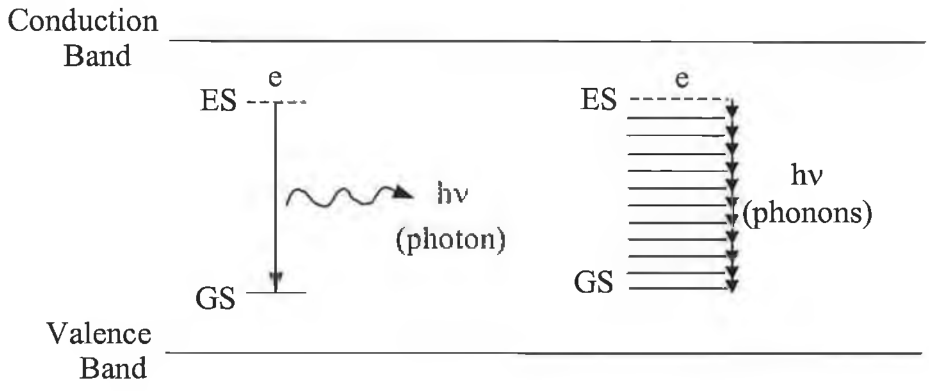

Figure 2.5 Energy band diagram showing the radiative de-excitation pathway which produces a photon and a non-radiative pathway which generates phonons.

The radiative decay time of a luminescent center is an important property for thin film EL phosphors, a fast decay time does not necessarily mean that it will be a good thin film EL material. Similarly, a slow decay time does not mean that a luminescent center will necessarily be a poor thin film EL material. It is often difficult to know, a priori, whether a material will be efficient or not, because one must consider both the electrical and optical characteristics of the material.

2.6 Material properties

Both conventional and inverted thin film EL device structures consist of the following materials:

(i) glass substrate,
(ii) transparent electrode,
(iii) metal electrode,
(iv) insulating layer, and
(v) phosphor layer.

The requirements of these materials in terms of electrical, optical and physical characteristics are discussed in this section.

2.6.1 Glass Substrates

The characteristics and surface conditions of the glass substrates control the properties and reliability of EL devices. During EL fabrication, severe processing conditions are used, such as high temperature (~550^{0}C) annealing and immersion in acid or alkaline fluids, and so the glass substrates must be heat resistant and acid and alkali resistant. Furthermore, diffusion of alkali-metal ions from the glass into the phosphor layer must be prevented, because they deteriorate the EL characteristics. A final requirement is that the glass surface should be as smooth as necessary for photomasking.

Physical properties required for the glass substrates are as follows:

(i) high transmission coefficient in the visible-light region,
(ii) thermal expansion coefficient that matches that of the deposited films,
(iii) high softening temperature, i.e., above 650^{0}C,
(iv) low or no alkali-metal content, and
(v) high electrical resistivity.

2.6.2 Transparent Electrodes

Large conductivity values and high transmittance in the visible light region are necessary for transparent conducting films for EL devices. The most common transparent electrode used is indium tin oxide (ITO) which has a sheet resistance of about 5-10 Ω/square for thicknesses that range from 300-500 nm. Though optically transparent, ITO has a high conductivity because of a high concentration of shallow donors that lie only a few meV below the conduction band. At room temperature, these donors are thermally activated into the conduction band and lead to high conductivity. There are basically two sources believed to contribute to the shallow donor level in ITO, namely (1) Sn^{+4} sitting substitutionally on an In^{+3} site, and (2) oxygen vacancies. While ITO is the predominant transparent electrode material, ZnO and ZnO: (Al, In, Ga) have also been used for thin film electroluminescent devices. A similar conduction mechanism that is responsible for ITO conduction occurs in ZnO films as well. For un-doped ZnO, a high oxygen vacancy concentration is believed to induce a shallow donor level, and for the doped ZnO, Al, In, and Ga all have a +3 valence state which act as shallow donors when substituting for the Zn^{+2} site [25].

2.6.3 Metal Electrodes

The requirements for the rear electrode materials in the conventional thin film EL structure are as follows:

(i) good adhesion to the insulating layer,
(ii) no metal-ion migration at high electric field,
(iii) an ability to prevent breakdown spread when dielectric breakdown of the phosphor layer or insulating layers occurs, and
(iv) low resistivity.

Among the materials satisfying these conditions, aluminum (Al) is considered to be the best and frequently used as top electrode in conventional EL devices. One drawback of aluminum, however, is its extremely high reflectivity of light. External light that penetrates into the EL device is reflected back by the aluminum which has a negative effect on the contrast of the display. This reflection can be suppressed by a smoke filter of 50-70% or by circularly polarising filters.

On the other hand, in the inverted thin film EL structure, in which the metal electrode is deposited first on the glass substrate, additional requirements for the lower metal electrode are as follows:

(v) high temperature resistance to deformation above 550^0C during annealing, i.e., high melting point,
(vi) thermal expansion coefficient that matches that of the glass substrate, and
(vii) small reflection coefficient in the visible light region to obtain good contrast.

Molybdenum (Mo) and tungsten (W) are suitable for the metal electrodes in the inverted EL device structure due to their high melting point.

2.6.4 Insulating Layers

The most important role of the insulating layers is to protect the phosphor layer from electrical breakdown in the electric field of more than 2×10^8 V/m. They must satisfy critical mechanical requirements in terms of adhesion and stress over process temperatures that range up to 550^0C. Furthermore, they must prevent metal-ion diffusion into the phosphor layer and provide interface states at the boundary of the phosphor layer and the insulating layer.

Insulating layers should have the following properties to produce reliable and efficient thin film EL devices [26-28]:

(i) high dielectric constant $\varepsilon_0\varepsilon_r$,
(ii) high dielectric breakdown electric field E_{BD},
(iii) small number of pinholes and defects,
(iv) uniform thickness,
(v) good adhesiveness, and
(vi) small $\tan\delta$.

Here ε_0 and ε_r are the dielectric constant of a vacuum and relative dielectric constant, respectively; $\tan\delta$ is a measure of dissipative characteristics defined by $1/(2\pi fCR)$, where f is the drive frequency, C is the capacitance, and R is the resistance of the insulating layer.

The high dielectric constant requirement for insulators can be justified by applying Maxwell's equations to an EL device below the threshold voltage. The threshold is defined to be the voltage or field that marks the onset of the Zener breakdown of the semiconducting phosphor. To optimise device performance, careful consideration must be given to maximise the electric field across the phosphor layer, and minimise the field across the insulators. As described previously, below the threshold voltage the device can be approximated as three series capacitors with the electric field across each layer given by:

$$\varepsilon_i^t E_i^t = \varepsilon_p E_p = \varepsilon_i^b E_i^b \qquad (2.3)$$

where E is the electric field, ε is the dielectric constant at the frequency of operation, subscript i and p represent the insulators (t = top, and b = bottom) and the phosphor layers, respectively. Furthermore, the voltage drop across each layer is simply the product of the electric field in each layer and the thickness (d) of each layer. The total applied voltage (V_{tot}) is divided between each layer according to the following equation:

$$V_{tot} = E_i^t d_i^t + E_p d_p + E_i^b d_i^b \qquad (2.4)$$

Eqs. (2.3) and (2.4) demonstrate that the threshold, or turn-on, characteristics of a thin film EL device is a function of the dielectric constant and the thickness of each layer in this three series capacitor structure. To maximize the phosphor electric field, the insulators should have a high dielectric constant and sufficient electric field strength to avoid breakdown. In addition, the insulators should be processed to be as thin as possible without compromising device reliability. Generally, as the insulator film thickness decreases, device reliability gets worse because pinholes in the films cause localized high field regions which result in premature dielectric breakdown. There are two groups of dielectric materials used in thin film electroluminescent devices: (a) amorphous oxides and nitrides, such as Al_2O_3, SiO_2, Y_2O_3, TiO_2, Si_3N_4 and Ta_2O_5; (b) ferroelectric materials, such as $BaTiO_3$ and $PbTiO_3$. Group-(a) dielectric materials have a small dielectric constant and high breakdown electric field. On the other hand, group (b) dielectric materials have a large dielectric constant and low breakdown electric field. A survey of the insulators that have been tested for thin film EL devices reveals that, as the dielectric constant increases, the electric field strength decreases. Because these properties are usually inversely proportional to one another, Howard introduced a figure of merit for insulator materials [29]. The figure of merit is simply the product of the dielectric constant and the electric field strength of the insulator. Figures of merit for several insulators have been tabulated and a range of 2-25 $\mu C\ cm^{-2}$ has been reported [30,31]. Table 2.1 lists several insulating materials used in thin film EL devices including the dielectric constant, the electric field breakdown strength, the figure of merit, and the breakdown mode of the material. Unfortunately, the high dielectric constant insulators ($SrTiO_3$, $BaTiO_3$ and $PbTiO_3$) that have yielded the highest figures of merit (19-25 C cm^{-1}), exhibit 'propagating breakdown.' In these materials, when breakdown initiates it catastrophically spreads and destroys the device. Lower dielectric constant insulators (Al_2O_3, Si_3N_4, $BaTa_2O_6$,...) that have lower figures of merit (3-7 C cm^{-1}) have proven to be more practical for EL devices. These materials have so-called 'self-healing' breakdown which inherently isolates the localized breakdown and prevents catastrophic breakdown. Generally, dielectric thin films with large dielectric constants tend to have a propagating breakdown mode. Coupled with other dielectric thin films, insulating layers with the propagating breakdown mode can be converted into the self-healing type.

Table 2.1: Insulators and properties

Material	Relative dielectric constant (ε_r)	Dielectric breakdown strength (MV cm^{-1})	Figure of merit (μC cm^{-2})	Breakdown mode
TiO_2	60	0.2	1	Propagating
SiO_2	4-6	6-7	2-4	Self Healing
Sm_2O_3	15	2-4	3-5	Self Healing
Y_2O_3	12	3-5	3-5	Self Healing
Al_2O_3	8	5-8	3.5-6	Self Healing
Ta_2O_5	23-25	1.5-3	3-7	Self Healing
$BaTiO_3$	14	3.3	4	Self Healing
Si_3N_4	8	6-8	4-6	Self Healing
$BaTa_2O_6$	22	3.5	7	Self Healing
$PbTiO_3$	150	0.5	7	Propagating
Ta_2O_5-TiO_2	20	7	12	Self Healing
$SrTiO_3$	140	1.5-2	19-25	Propagating
$Sr(Zr, Ti)O_3$	100	3	26	Propagating

2.6.5 Phosphor Layers

All phosphors consist of a host material and a light-emitting dopant called an activator or a luminescent center. The classical thin film EL phosphor uses ZnS for the host material and the Mn atom for the light emitting dopant. Table 2.2 summarises some of the thin film EL phosphor materials and their colours.

Table 2.2: Thin film EL phosphor materials

Phosphor material	Colour
ZnS:Mn	Yellow
$ZnS:DyF_3$	Yellow
ZnS:Tb	Green
ZnS:TbOF	Green
ZnS:TbF	Green
$ZnS:HoF_3$	Green
$ZnS:EeF_3$	Green
$Zn_2SiO_4:Mn$	Green
ZnS:Sm,F	Red
ZnS:Sm,P	Red
ZnS:Sm,Cl	Red
CaS:Eu	Red
CaS:Eu,F,Cu,Br	Red
ZnS:Tm	Blue
SrS:Ce,F	Blue
$CaGa_2S_4:Ce$	Blue
SrS:Ce,Mn,Cl	Blue-green
SrS:Ce	Blue-green
ZnS:Pr,F	White
ZnS:Pr,K	White
SrS:Ce,K,Eu	White
CaS:Ce,K,Eu	White

The requirements for phosphor host materials and luminescent centers (activators) are discussed below:

2.6.5.1 Host materials

In order to be an efficient thin film EL phosphor, the host material should have the best possible crystalline order to allow electron acceleration to a kinetic energy sufficient for impact excitation. The requirements for the phosphor host materials are as follows:

(i) they should have a large enough band gap to emit visible light from the doped luminescent centers without significant absorption,

(ii) they must hold a high electric field of the order of 10^8 V/m without electric breakdown,

(iii) they must withstand a post annealing temperature of 550^0C.

Phosphor host materials satisfying the above requirements are limited to II-VI compounds, such as IIb-VIb compounds, such as ZnS and ZnSe, and IIa-VIb compounds, such as CaS, SrS, and SrSe.

2.6.5.2 Luminescent centers

In order for the luminescent center (activator) atoms to emit light efficiently, they should be incorporated into a substitutional lattice site, otherwise the excited center will lose its energy non-radiatively to a nearby lattice defect. Luminescent centers must satisfy the following requirements:

(i) they must be properly incorporated into host materials and emit visible light,

(ii) they must have a large cross section for the impact excitation,

(iii) they must be stable in the high electric field of the order of 10^8 V/m.

Luminescent centers found to be suitable, satisfying the above requirements are the transition metals such as Mn and rare earth elements such as Tb, Sm, Tm, Eu and Ce.

2.7 Reliability of Thin Film EL Devices

In considering the reliability of thin film EL devices, three important factors must be taken into account:

(i) electrical reliability with respect to electric breakdown,
(ii) long-time reliability , and
(iii) shifts in luminance-voltage (L-V) characteristic curve with operation.

Electrical breakdown properties depend strongly on the electrical properties of the insulating layer materials and the thin film fabrication processes. For long-time reliability, the hygroscopic, adhesive and photolithographic resistant properties of phosphor layer and dielectric layer materials must be taken into account, and proper choices of passivation and sealing materials are essential. Shifts in luminance-voltage (L-V) characteristics curve with operation time are not suitable because they result in luminance deterioration. It has become possible to obtain EL devices [32] with no shifts in L-V characteristics curve with proper choices of the insulating layer structure and crystallinity control of the phosphor layer films. In addition, effects of various stresses on the performance of EL panels and display units should be considered [33].

2.8 Advantages of Thin Film EL Displays Compared to Other Displays

With advance of display technology, the following types of flat-panel displays can be listed:

(i) Electroluminescent displays,
(ii) Cathodoluminescent displays,
(iii) Cathode Ray Tube displays,
(iv) Vacuum Fluorescent displays,
(v) Plasma displays,
(vi) Light Emitting Diode displays,
(vii) Liquid Crystal displays,
(viii) Electrochromic displays, and
(ix) Electrophoretic displays.

In comparison with other flat-panel display technologies, thin film electroluminescence possesses many important features, such as, excellent visual characteristics, a rugged and compact device with a simple multicolour display structure. Thin film EL displays have the following advantages:

(i) an emissive display with large viewing angle and good contrast,
(ii) good resolution, higher than 8 lines/mm [34],
(iii) temperature independent emission and suitable for automotive equipment used under very severe temperature requirements,
(iv) rugged and vibration resistant due to all solid devices and suitable for personal computers used under very severe vibrational conditions, such as, in military equipment or spacecraft,
(v) fast with good luminous efficiency,
(vi) inherently easy to produce,
(vii) has long life,
(viii) a relatively simple structure, thickness of less than 30 mm and weight of less than 700 gm [34], and
(ix) lowest power consumption compared to other emissive flat-panel displays.

2.9 Conclusions

In this chapter, the device structure, the device physics and the material properties of thin film electroluminescent displays are reviewed. The conventional and inverted structures that are commonly used each employ the metal-insulator-semiconductor-insulator-metal (MISIM) multilayer structure. Each thin film layer has unique electrical and optical properties that must be satisfied for optimum device performance. The metal layers are the electrodes which simply make contact to the drive electronics, therefore the electrical requirements of both electrodes are not unique. One of the electrodes must be transparent to visible light so the display can be viewed and the other must satisfy reflectivity issues so the contrast is not compromised. The dielectric properties of the insulating layer are important because it is necessary to maximise the electric field experienced by the phosphor layer, and the breakdown mode is crucial for the device reliability and lifetime. The final layer considered was the semiconducting (phosphor) layer. The electron injection and the electron acceleration phenomena are both dependent on the band structure of the phosphor layer. In addition, the excitation and de-excitation mechanisms are dependent on the phosphor luminescent center.

Chapter 3

DEPOSITION TECHNOLOGY OF THIN FILMS

3.1 Introduction

From the typical device structures of the conventional and inverted thin film electroluminescent devices as shown in fig. 1.1 and 1.2, we can see that both the devices consist of the following layers of thin film deposited on top of each other:

(a) insulating layer,
(b) transparent conducting layer, and
(c) phosphor layer.

Thin films of insulating layer, transparent conducting layer and phosphor layers can be deposited by various deposition techniques. Each of the deposition technology has its own advantages and disadvantages over each other. In most of the cases, especially for thin film electroluminescent displays, the desired material characteristics of the deposited films are the decisive factor for the selection of a preferred deposition technology.

3.2 Classification of deposition technologies

There are many types of deposition technologies for thin film formation [35-38] in practical application. Since the concern here is with thin film deposition methods for forming layers in the thickness range of a few nanometers to about ten micrometers, the task of classifying the technologies is made simpler by limiting the number of technologies to be considered.

Basically, thin film deposition technologies can be classified into liquid phase and vapour phase. Liquid phase of deposition technology consists of sol-gel deposition and spray pyrolysis. Vapour phase may be either purely physical, such as evaporative methods or purely chemical, such as chemical vapour deposition process. A considerable number of processes that are based on glow discharges and reactive sputtering combine both physical and chemical reactions; these overlapping process can be categorized as physical-chemical methods.

A brief description of the principles, salient features and applications of some important technologies for thin film deposition are given below:

3.2.1 Liquid Phase

3.2.1.1 Sol-gel Process

In the sol-gel process, film formation takes place by evaporation of the solvent from a polymer solution. The substrate is dipped into the polymer solution, taken out at a constant speed and dried by allowing the solvent to evaporate, leaving behind a solid polymer film on the substrate. The thickness of the coating depends on the viscosity of the solution, the rate of the solvent evaporation and the speed and angle at which the substrate is taken out. Films of thickness as small as 50-100 $\overset{0}{A}$ may be deposited by using very dilute and low-viscosity solutions. Films may also be formed by spinning the solution on a rotating substrate. This gives rise to more uniform films. Sol-gel process has the advantages of coating on the desired shape and area, easy control of the doping level, solution concentration and homogeneity without using expensive and complicated equipment. This technique has been commercially used for the deposition of films on the substrate of large area (about 10-12 m^2) for a multitude of applications [39].

3.2.1.2 Spray Pyrolysis

Spray pyrolysis involves spraying of solution, usually aqueous, containing soluble salts of the constituent atoms of the desired compounds onto the heated substrates. A large number of metallic salt solutions when sprayed onto a hot substrate decompose to yield oxide films. Similarly films of sulfides and selenides can be prepared by pyrolytic decomposition of a solid complex compound formed on the surface of a substrate by spraying a mixed solution of the corresponding metallic salt and a sulphur/selenium-bearing compound. For example, $CdCl_2$ and $(NH_4)_2CS$ (thiourea) solutions when mixed at room temperature do not react to form CdS (provided the solution is not deliberately made alkaline). But when sprayed onto a substrate held at

~400^0C, a solid complex of composition $CdCl_2$ thiourea is formed, which decomposes on the substrate to yield CdS films [40].

The atomization of the chemical solution into a spray of fine droplets is effected by the spray nozzle with the help of a filtered carrier gas which may or may not be involved in the pyrolytic reaction. The carrier gas and the solution are fed into the spray nozzle at predetermined and constant pressure and flow rates. The substrate temperature is maintained with the help of a feedback circuit which controls a primary and an auxiliary heater power supply. Large-area uniform coverage of the substrate is effected by scanning either or both the spray head and the substrate, employing mechanical or electromechanical arrangements.

The geometry of the gas and the liquid nozzle strongly determines the spray pattern, size distribution of droplets and spray rate, which in turn determine the growth kinetics and hence the quality of the films obtained.

Doped and mixed films can be prepared very easily, simply by adding to the spray solution a soluble salt of the desired dopant or impurity. Two very important examples of the materials deposited by this technique for device fabrications are (1) CdS for solar cells and (2) InF-or Sb-doped SnO_2 for conducting glass.
By spray pyrolysis, films can be deposited on large substrate easily, but the films are not very uniform, unlike the sol-gel process.

3.2.2 Vapour Phase

3.2.2.1 Chemical Vapour Deposition

The growth of thin films by chemical vapour deposition (CVD) has become one of the most important methods of film formation and now constitutes a corner stone for modern technologies such as solid-state electronics. The reasons for the rapidly growing importance of CVD in the past decade lie primarily in its versatility for depositing a very large variety of elements and compounds at relatively low temperatures, in the form of both vitreous and crystalline layers having a high degree of perfection and purity.

Chemical vapour deposition techniques are vapour deposition techniques based on homogeneous and/or heterogeneous chemical reactions. These processes employ various gaseous, liquid and solid chemicals as sources of the elements of which the film is to be made. The following chemical vapour deposition processes are used in practice [41]:

i) Thermally activated CVD: Thermally activated CVD processes are initiated only with thermal energy (resistance heating, RF heating or by infrared radiation). They are usually performed at normal or low pressure down to ultralow pressure. The sources are inorganic.

ii) Metalorganic CVD (MOCVD): MOCVD is also a thermal CVD process but sources are metalorganic gases or liquids. With the availability of pure metalorganic precursors, their use offers significant advantages in the practical aspects of delivering the reactants to the substrate surface. MOCVD is usually applied for epitaxial growth of II-VI and III-V semiconducting and for high-T_c superconducting films. In addition, dielectric and metallic films can be prepared using MOCVD.

iii) Plasma-enhanced CVD (PECVD): PECVD uses a plasma to ionize and dissociate gases. This can enhance the growth rate, allowing deposition processes at much lower temperatures than in thermal CVD. PECVD has several features in common with low-pressure CVD, such as the pressure range, sources and films to be deposited.

iv) Photo-assisted CVD: Photo-assisted CVD uses light to enhance the reaction rate. The effect of the radiation is either a local heating of the wafer or a photochemical reaction. In the last case the reactant gases undergo photolytic reactions.

vi) Atomic layer epitaxy (ALE): Atomic layer epitaxy is a relatively new approach to thin film fabrication techniques. In ALE the reactants are supplied onto the growing surface sequentially, one at a time. At each sequence the surface is saturated, resulting in the formation of one monolayer. The desired thickness of a thin film can be realized by counting the number of reaction sequences in the process. It is used to deposit thin films of II-VI and III-V materials, but also of elemental semiconductors, oxides, nitrides and sulphides. The sources are the same as in CVD and MOCVD.

The chemical processes used in CVD of thin films can be classified into the following types of reactions [41]:
i) thermal decomposition (pyrolysis),
ii) reduction,
iii) oxidation,
iv) hydrolysis,
v) nitridation,
vi) chemical transport
vii) disproportionation
viii) catalysis,
ix) synthesis,
x) photolysis, and
xi) combined reactions.

The major advantages of the CVD techniques are as follows:
i) in general, only low-vacuum facilities are required and, thus, a relatively simple set up and fast recycling are possible;
ii) high (~1μm/min) deposition rates are possible;
iii) it is possible to deposit compounds with easily controlled stoichiometry;
iv) it is relatively easy to dope the deposits with controlled amounts of impurities;
v) it is possible to deposit multicomponent alloys;
vi) refractory materials can be deposited at relatively lower temperatures as compared to vacuum evaporation;
vii) epitaxial layers of high perfection and low impurity content can be easily grown;
viii) objects of complex shapes and geometries can be coated; and
ix) in situ chemical vapour etching of the substrates prior to deposition is possible.

Disadvantages of the CVD techniques are as follows:

i) the generally complex thermodynamics and kinetics are poorly understood;

ii) higher substrate temperatures are required than those in the corresponding PVD techniques;

iii) the reactive gases used for deposition and the volatile reaction products formed are, in most cases, highly toxic, explosive, inflammable or corrosive;

iv) the corrosive vapours may attack the substrate, the deposited film and the materials of the deposition set up;

v) the chemical reactions generally produce intermediate products;

vi) the volatile products generated during the deposition process may lead to incorporation of impurities in the film;

vii) the high substrate temperature may lead to diffusion, alloying or chemical reaction on the substrate surface, thus restricting the choice of the substrate;

viii) high substrate temperature may also give rise to segregation effects when metastable multicomponent materials are being deposited;

ix) it is difficult to control the uniformity of the deposit; and

x) masking of the substrate is generally difficult.

Transparent conductors and dielectric films can be deposited by chemical vapour deposition method. In CVD, a large vacuum system is required for coating on large substrates, which is really expensive. By the sol-gel process, large substrates can be coated without using expensive and complicated equipment.

3.2.2.2 Physical Vapour Deposition

3.2.2.2.1 Sputtering

When a solid surface is bombarded with energetic particles such as accelerated ions surface atoms of the solid are scattered backward due to collisions between the surface atoms and the energetic particles. This phenomena is called “back-sputtering” or simply “sputtering”. Different types of sputtering systems are as follows:

3.2.2.2.1.1 DC Diode Sputtering

The dc diode sputtering system is composed of a pair of planar electrodes. One of the electrodes is a cold cathode and the other is an anode. The top plasma-facing surface of the cathode is covered with a target material and the reverse side is water-cooled. The substrates are placed on the anode. When the sputtering chamber is kept in Ar gas at 0.1 Torr and several kilovolts of dc voltage with series resistance of 1 to 10 kΩ are applied between the electrodes, the glow discharge is initiated. The Ar ions in the glow discharge are accelerated at the cathode fall and sputter the target resulting in the deposition of thin film on the substrates.

In the dc diode system, sputtered particles collide with gas molecules and then eventually diffuse to the substrate since the gas pressure is so high and the mean free path of the sputtered particles is less than the electrode spacing. The amount of sputtered material deposited on a unit substrate area W is then given by [42],

$$W \approx kU/pd \qquad (3.1)$$

and the deposition rate R is given by

$$R = W/t \qquad (3.2)$$

where k is a constant, U is the amount of sputtered particles from the unit cathode area, p is the discharge gas pressure, d is the electrode spacing, W is the density of the sputtered films and t is the sputter time.

The amount of sputtered particles from the unit cathode area U is given by [40],

$$U = (j_+/e)st(A/N) \qquad (3.3)$$

where j_+ is the ion current density at the cathode, e is the electron charge, s is the sputter yield, A is atomic weight of sputtered materials and N is Avogadro's number.

3.2.2.2.1.2 Bias Sputtering

In bias sputtering, electric fields near the substrate are modified in order to vary the flux and energy of incident charged species. This is achieved by applying either a negative dc or RF bias to the substrate. With target voltages of –1000 to –3000 V, bias voltages of –50 to –300 V are typically used. Due to charge exchange process in the anode dark space, very few discharge ions strike the substrate with full bias voltage. Rather a broad low energy distribution of ions and neutrals bombard the growing film. The technique has been utilised in all sputtering configurations (dc, RF, magnetron and reactive) [42].

Biasing adds enormous flexibility to the sputter deposition technique; almost any film property can be influenced by the biasing sputtering technique, such as resistivity, hardness, residual stress, dielectric properties, etch rate, optical reflectivity, step coverage, film morphology, density and adhesion. The control of the gas content of films is also an important role of bias. There is no doubt that by changing the flux and energy of ions and electrons bombarding the substrate, many other effects on parameters affecting the nature of the films take place, such as thermal effects and influences on the nucleation and growth stages of the films.

In addition, energetic particle bombardment prior to and during film formation and growth promotes numerous changes and processes at a microscopic level, including removal of contaminants, alteration of surface chemistry, enhancement of nucleation and renucleation, higher surface mobility of adatoms and elevated film temperatures with attendant acceleration of atomic reaction and interdiffusion rates. Film properties are then modified through roughening of the surface, elimination of interfacial voids and subsurface porosity, creation of a finer, more isotropic grain morphology and elimination of columnar grains-in a way that strongly dramatises structure-property relationships in practice.

3.2.2.2.1.3 RF Diode Sputtering

By simple substitution of an insulator target for the metal target in a dc diode sputtering system, the sputtering glow discharge can not be sustained because of the immediate build-up of a surface charge of positive ions on the front side of the insulator. To sustain the glow discharge with an insulator target, the dc voltage power supply is replaced by an rf power supply. This system is called an rf sputtering system.

Sputtering in the rf discharge was observed by Robertson and Clapp in 1933 [43]. They found that the glass surface of the discharge tube was sputtered during the rf discharge. In the 1960's, sputtering in the rf discharge has been used for the deposition of dielectric thin films and a practical rf sputtering system was developed [44,45]. At present, the rf sputtering system holds an important position in the deposition of thin films.

The rf diode sputtering system requires an impedance-matching network between the power supply and discharge chamber. The impedance of the rf power supply is almost always 50Ω. The impedance of the glow discharge is of the order of 1 to 10 kΩ.

In rf diode sputtering, the target current density i_s is given by

$$i_s \approx C\, dV/dt \qquad (3.4)$$

where C is capacitance between discharge plasma and the target, dV/dt denotes the time variations of the target surface potential. This indicates that the increase of the frequency increases the target ion currents. In practical systems, the frequency used is 13.56 Mhz.

In the rf discharge system the operating pressure is lowered to as low as 1 mTorr, since the rf electrical field in the discharge chamber increases the collision probability between secondary electrons and gas molecules. In the rf sputtering system, a blocking capacitor is connected between the matching network and the target. The target area is much smaller than the grounded anode and the chamber wall. This asymmetric electrode configuration induces negative dc bias on the target and this causes sputtering in the rf system. The dc bias is on the order of one half of the peak-to-peak voltage of the rf power supply.

In the rf sputtering systems the target and inductance in the matching network are usually cooled by water. The electrical resistivity of the cooling water should be high enough as to serve as electrical insulation.

3.2.2.2.1.4 Magnetron Sputtering

Low pressure sputtering is one of the most promising techniques for the production of thin film devices. A wide variety of thin films can be made with little film contamination and at a high deposition rate by this technique.

In 1935 Penning first studied low pressure sputtering in which a transverse magnetic field was superposed on a dc glow discharge tube [46]. The experimental system was composed of coaxial cylindrical electrodes with an axial magnetic field, similar to a cold cathode magnetron. He found that superimposition of the magnetic field of 300G lowered the sputtering gas pressure by a factor of ten and increased the deposition rate of sputtered films. However this kind of system was not used in practice.

In the early 1960's, magnetron sputtering was reconsidered as an attractive process for thin film deposition by a few workers. Kay studied the glow discharge in the presence of a magnetic field in relation to thin film deposition [47,48]. Gill and Kay proposed an inverted magnetron sputtering system and demonstrated that the sputtering gas pressure was as low as 10^{-5} Torr, which was two orders lower than conventional sputtering systems. The strength of the magnetic field was several hundred gauss and the PSC (positive space charge) mode was dominant in the sputtering discharge.

Hayakawa and Wasa also studied this type of discharge in relation to glow discharge mode [49], plasma instability [50] and cathode sputtering [51-53]. They invented an original planar magnetron sputtering system with a solenoid coil [54]. It was also found that the presence of a strong magnetic field changed the glow discharge mode; i.e. the NSC (negative space charge) mode appeared and enhanced the cathode sputtering. However in those days, this type of magnetron sputtering system was not widely used in practice.

In the 1970's, magnetron sputtering become more widely used for its potential applications for Si integrated circuits, as well as for various other thin film coating processes [55,56]. Today, it is in broad scale practical use [57] in industries ranging from microelectronics, to automobiles, to architectural glass to hard coatings. Two types of magnetron sputtering systems are widely used for thin film deposition. One is a cylindrical type, the other is a planar type.

Actually in magnetron sputtering processes, sputtering sources uses magnetic fields transverse to the electric fields at sputtering-target surfaces. Sputtering with a transverse magnetic field produces several important modifications of the basic processes. Target-generated secondary electrons do not bombard substrates because they are trapped in cycloidal trajectories near the target and thus do not contribute to increased substrate temperature and radiation damage [42]. This allows the use of substrates that are temperature-sensitive (for example, plastic materials) and surface-sensitive (for example, metal-oxide-semiconductor devices) with minimal adverse effects. In addition, this class of sputtering sources produces higher deposition rates than conventional sources and lends itself to economic, large area industrial application. There are cylindrical, conical and planar magnetron sources, all with particular advantages and disadvantages for specific applications. As with other forms of sputtering, magnetron sources can be used in a reactive sputtering mode. Alternatively, one can forego the low-temperature and low radiation damage features and utilize magnetron sources as high-rate sources by operating them in a bias-sputtering mode.

3.2.2.2.1.5 Ion-Beam Sputtering

The low-pressure gas plasma method is relatively frequently used for the growth of films by means of sputtering target materials. Plasma sputtering is specially advantageous when growth on a large area and high productivity are required. However, since this method is performed in a low-pressure gas environment, problems such as scattering of sputtered particles (atoms, molecules or ions) from the target before their arrival at the substrate and incorporation of discharged gas molecules into the growing film have been pointed out [41].

In order to solve these problems, a new method was developed [41] wherein ions used for sputtering the target are independently produced using an ion source. An ion beam is created by converging and accelerating these ions and then a target placed in a high-vacuum chamber is irradiated. This method is called the ion-beam sputtering deposition (IBSD).

With IBSD, film growth can be performed in a high-vacuum environment, in contrast to plasma sputtering deposition and the following advantages can be listed:

(i) The ion beam current and energy are determined by the structure of the ion source and operating conditions; they can be considered independent of the potential of the target and the substrate. Therefore, exact control of sputtering conditions is possible.

(ii) By selecting the target potential arbitrarily, bombardment of the substrate by secondary electrons and secondary ions can be avoided. Thus, unnecessary temperature increase of the substrate and damage of the deposited film can be avoided.

(iii) The deposition rate of the film fabricated by the IBSD is low compared with that for plasma sputtering deposition. However, through periodic sputtering of different kinds of targets, formation of multilayered films can easily be accomplished. In such a case, by computer control, multilayered films with a complex structure can be reproduced with high accuracy.

(iv) Deposition of oxide, nitride and compound semiconductor films has been attempted experimentally by introducing a reactive gas or ion beam and creating a chemical reaction in the IBSD.

The ion beam current ranges from 10 mA to several amperes, depending on the dimensions of the sources. The ion energy can be varied from 0.5 to 2.5 kV. The gas pressure of the sputtering chamber is typically in the high 10^{-5} to low 10^{-4} Torr. This kind of system is widely used for sputter etching of semiconducting devices. Increasing interest has been recently paid to ion beam sputtering not only for semiconducting process but also for developing exotic materials.

Sputtering also requires large vacuum systems for the deposition of films on large substrate.

3.2.2.2.2 Resistance Evaporation

Deposition of thin films from resistance heated evaporation sources was the first practical thin film deposition technique [58]. Since then, despite being technologically eclipsed by electron beam heated evaporation sources and sputtering, resistance evaporation finds wide use, offering a unique combination of reliability and economy.

During the 1930s the art of lens blooming became the science of optical coating [59,60]. By the late 1930s multilayer optical coatings, all deposited with resistance heated sources, were invented [61]. The multilayer resistance source deposited films used in most production dichroic lighting reflectors [62] are an example of cost efficient, modern production technology.

The resistance heated refractory metal source is the heart of the evaporation system. Selection of a suitable source is the critical decision in designing a resistance evaporation process. The source is the evaporant heater and container and the most probable cause of failure. The catalogues of source manufacturers contain a plethora of designs and little specific performance or application data. A source is selected to meet the following process requirements: evaporant compatibility, capacity and power availability. The most difficult of these to meet is evaporant compatibility because many important evaporants (Al, Au, Fe and Pt) dissolve all refractory metals to some extent.

In general, sources are made of refractory metal (Mo, Ta, W) of three design classes: coils, boats and special purpose designs.

Resistance evaporation system requires large vacuum system for the deposition of films on large substrates.

3.2.2.2.3 Electron Beam Evaporation

The electron beam heated evaporation source is a thermal evaporator as is a resistance heated source. Electron beam heated sources differ from resistance heated sources in two ways: the heating energy is supplied to the top of the evaporant by the kinetic energy of a high current electron beam and the evaporant is contained in a water cooled cavity or hearth. Heating by electron beam allows attainment of temperatures limited only by radiation and conduction to the hearth. Evaporants contained in a water-cooled hearth do not significantly react with the hearth, which provides a nearly universal evaporant container.

The bent beam evaporation source as is now used in thin film fabrication for electronics, optics and research was first envisioned by L Holland [63] and the modern 270^0 gun was developed in the early 1960s by Hugh Smith and Charles Hanks of Temescal Corporation [64]. In the late 1960s and 1970s electron beam guns were principally used for the deposition of aluminum metallization on semiconductor devices. Today these sources have been largely supplanted for semiconductors because of the switch to alloy metallization coupled with the development of high rate, easily automated planar magnetron sputtering sources. Magnetron sources are much better suited for alloy deposition and more stable in automated production applications. The use of lift-off metallization technology for gallium arsenide and other high performance devices is causing a resurgence of electron beam deposited semiconductor metallization. The development of the new generation of hard multilayer optical coatings has made electron beam evaporation the technology of choice in optics.

The electron beam heated evaporation source, as used for high technology thin film fabrication has three basic sections: the electron gun, the beam deflection magnetic lens and the evaporant containing hearth. The beam is formed in the gun, passes through the magnetic lens and is focused upon the evaporant.

Application of an electron beam heated source is governed by the following three complex relationships:

(i) The energy balance of the evaporant charge and the requirement for stable dissipation of the beam energy.

(ii) The complex distribution of the evaporant vapour flux from the evaporant surface caused by the pressure within this vapour and the resultant evaporant surface geometry.

(iii) The ionizing effects of the electron beam, as it passes through the evaporant vapour cloud, impacts the melt surface and is partially reflected from that surface.

Electron Beam Evaporation system also requires a large vacuum system for the deposition of films on large substrate.

3.2.2.2.4 Ion Vapour Deposition

Ion vapour deposition or ion plating are the names given to a class of ion assisted physical vapour deposition process. These processes apply a negative voltage on or near the substrate, creating a plasma that ionises a working gas and coating material then accelerates both in the direction of the substrate while simultaneously sputtering the substrate. The ionised gas, usually argon, collides with non-ionised coating material, increasing its energy thereby imparting energy to the growing film, increasing its adhesion and density. It also imparts compressive stress in the coating, reducing cracking.

Conventional high vacuum evaporation imparts an arrival energy to the evaporant at the substrate on the order of 0.1-1 eV. In the early 1970s D M Mattox experimented with evaporating onto substrates at high voltage, developing the ion plating process [65]. He recognised that when a voltage of 500-2500 V is applied to a conducting substrate, any evaporant that ionises will be accelerated through this voltage and arrive with up to 2500 eV of energy. Because evaporation sources ionise only about 0.1-1 % of the evaporant, the effect of a high voltage substrate bias was small. When an argon working gas at 10-50 mTorr was introduced into the coating system a sputtering discharge was generated at the substrate. This creates a unique and powerful deposition technology. The cathode in ion plating, the substrate, acts as the target in a sputtering system. As a result, there are two deposition processes occurring simultaneously. The substrate is sputtered and the evaporant is deposited. The film is grown to the extent the deposition rate exceeds the sputtering rate. The neutral atoms of evaporant are now ‘hammered’ into the substrate by the working gas ions. Their average energy of arrival is on the order of 250 eV when 2500 V is applied to the substrate. An additional capability of ion plating is sputter cleaning substrates before commencing deposition. As the sputtering target, the substrate can be etched to any extent desired.

Limitations

The intense energy of ion vapour deposition is the cause of its limitations. The energetic deposition imparts substantial energy to the substrates beyond that of evaporation or sputtering. This can easily melt plastic or anneal aluminium substrates.

The energy of the ion deposition sharply heats the deposition chamber and tooling, driving off the absorbed gas and contaminates. These gases contaminate the plasma, reacting with the films. Ion vapour deposition requires the same cleanliness and operating care as sputtering. The heat deposited on the chamber and tooling also requires water-cooling, care to avoid burns and long cooling cycles, slowing production.

3.2.2.2.5 Cathodic Arc Deposition

The technique of thin film deposition by cathodic arc evaporation has been used almost exclusively for the deposition of wear-resistant coatings onto cutting and forming tools. The technology was developed principally in the Soviet Union and much of the research and development has concentrated on the synthesis of titanium nitride. The method is fast, efficient and relatively cost effective, providing an attractive method for the deposition of functional thin film with good mechanical properties. The quality of the deposited films is determined by the properties of the products emitted during the evaporation and these products offer both advantages and disadvantages for specific applications.

The cathodic arc evaporation process is based upon the vacuum arc, the physics of which is still under investigation. The vacuum arc is an arc sustained by material originating from a cathode in an environment that would otherwise be a vacuum. Before the arc is established there is no matter in the interelectrode gap to sustain the discharge but once triggered matter is transported and a feedback mechanism established in which a very small area of the cathode surface is heated by electron emission and further matter is ejected. The area of the cathode emitting material is characterized by an ensemble of luminous cathode spots that move in a rapid and chaotic manner across the surface. The spots move to a new sites rather than remain on the original hot sites and in the presence of a magnetic field, will move in the opposite direction to the JxB force (retrograde motion). Plasma expands in all directions from the cathode spots towards the anode and vacuum chamber walls. Measurements of the plasma [66] show that:

(i) The plasma contains few neutral species.
(ii) The kinetic energy of the ions is relatively high (20-100 eV) and greater than eU_0, where U_0 is the arc voltage.
(iii) The electrons have near thermal energies.
(iv) The electric current carried by the ions is ~ 8 %.
(v) The electric field in the plasma is weak.

The cathodic spot is small (10^{-8} to 10^{-4} m in diameter) and an intense source of plasma with a current density of 10^{6}-10^{12} $A.m^{-2}$. The spot velocity is determined by factors that include the nature of the cathode, the residual vacuum and the presence of external magnetic fields. The cathode erosion rate is dependent upon the state of the surface and the cathode spot characteristics change as the surface is cleaned of contamination and oxides during arcing.

The high energy of the ions is advantageous in thin film formation processes because arc evaporation is intrinsically an ion-assisted deposition process. Ion bombardment of a growing film leads to better adhesion to the substrate, the removal of loosely bonded surface atoms through sputtering and the densification of the film through forward recoil sputtering and the disruption of possible columnar growth [67]. The average energy of the ions is about 40 eV per particle compared to 0.1 eV for evaporation-based technologies [68] and 5-10 eV for sputtering processes [69]. The high ion fraction removes the requirement for any additional ion bombardment, as in ion-assisted electron beam evaporation, which greatly simplifies the process. The ion fractions for most materials are also extremely high compared to those in other processes such as ion plating (~0.2) and sputtering (~0.1). High ionisation also enhances the reactivity of metal and gaseous species in the formation of compounds such as nitrides, oxides and carbides [70].

Both ion vapour and cathodic arc deposition require large vacuum systems for the deposition of films on large substrates.

3.2.2.2.6 Laser Ablation

Film deposition by laser ablation is carried out by irradiation of the target by a focused laser beam. The laser beam ablates target materials from the target and materials are transferred to the substrates. As a result, a film is grown on the substrate. During laser ablation a luminous cloud can be seen along the normal to the target. This cloud is called a ‘plume’. Various kinds of pulsed laser are often employed for thin film deposition by laser ablation. Compared with other conventional film deposition techniques, e.g. thermal evaporation, molecular beam epitaxy (MBE), sputtering, organometallic chemical vapour deposition (OMCVD), etc., laser ablation has the following characteristics.

(i) Materials with high melting points can also be deposited if the materials absorb laser light.

(ii) Almost no contamination is present, unlike the situation often observed in films prepared using an evaporation heater or filament.

(iii) It is possible to prepare films in an oxidation environment with relatively high pressure because of the absence of a heater or filament in the deposition chamber.

(iv) The target composition is transferred to the film, leading to stoichiometric deposition.

(v) A large number of droplets of submicron size are often seen on the surface of the deposited film.

Film deposition by laser ablation is undoubtedly an attractive technique for the preparation of a variety of materials. Disadvantages are droplet formation on the deposited film, the limitation on large area deposition, the high cost of the excimer laser, etc. Considering the current technique and the cost of the laser, the use of laser ablation in mass production is, however, not so suitable. For the moment, the laser ablation technique is of great importance in sophisticated material and device research in laboratories and the small-scale production of high cost-performance devices. In the near future an improved pulsed laser with a low cost will be available, leading to mass production.

Compared to the sol-gel process, laser ablation is expensive and has the limitation on large area deposition.

3.3 Criteria for the selection of a deposition technology for specific applications

The selection of a specific technology for the deposition of thin films can be based on a variety of considerations. A multitude of thin films of different materials can be deposited for a large variety of applications; hence, no general guidelines can be given of what the most suitable deposition technology should be. In selecting an appropriate deposition technology for a specific application, several criteria have to be considered.

Most thin films are deposited by evaporation (vacuum deposition), sputtering or chemical vapour deposition. A suitable selection of deposition process is required when thin films are used for the preparation of active electronic devices such as semiconducting devices, since the surface of the semiconducting substrates is often damaged during deposition. The nature of deposited films is governed by the deposition parameters including deposition rate, substrate temperature, substrate materials and deposition atmosphere [71].

The chemical composition of deposited films is governed by the substrate temperature and/or the deposition atmosphere. Under low substrate temperatures the chemical composition of deposited films coincides to that of the source materials. Under high substrate temperatures the chemical composition of the deposited films differs from the source materials due to the reevaporation of high vapor pressure materials from the films during the deposition.

The gas molecules of the deposition atmosphere are frequently included in the deposited films. The chemically active gas molecules react with the thin films during film growth and the resultant films become the compounds between the evaporated source and the active gas in the deposition atmosphere. Thin films of metal oxides, for instance, are prepared by the reactive sputtering from metal target in oxygen atmosphere.

The crystalline properties of the deposited films are controlled by the selection of the substrate materials and the substrate temperature. Amorphous thin films are prepared on a glass and/or ceramic substrate at substrate temperatures below the crystallization temperature of the thin films. Polycrystalline films are prepared on a glass and/or ceramic substrates at substrate temperatures above the crystallization temperature.

3.4 Material Characteristics

The fabrication of thin film electroluminescent devices requires conductive films, transparent and conductive films, luminescent or fluorescent films as well as dielectric and insulating films. The electrical, optical, structural and chemical properties of these thin films can be quite different from those of the bulk materials. The surface and/or interface properties of the substrate to be coated can influence thin film characteristics due to surface contamination, surface mobility, chemical surface reactions, surface topography and crystallographic orientation. As we are concerned with the suitable transparent conducting and insulating film in this work, the electrical, optical, structural and chemical properties of these thin films to be considered for the fabrication of thin film electroluminescent devices, are listed as follows:

Electrical:	Conductivity for conductive films
	Dielectric constant
	Dielectric strength
	Dielectric loss
	Permittivity
Optical:	Refractive index
	Absorption
Structural:	Crystalline or amorphous
	Structural defect density
	Crystallite orientation
Chemical:	Composition
	Impurities
	Reactivity with substrate and ambient
	Stability

3.5 Conclusions

As discussed above, a wide variety of process technologies are available for the deposition of thin films. The technologies differ from each other to a large degree in their physical and chemical principles of operation and in the commercially available types of equipment. Each process technology has been pursued or developed because it has unique advantages over others. However, each process technology has its limitations. In order to optimise the desired film characteristics, a good understanding of the advantages and restrictions applicable to each technology is necessary.

Considerable attention has to be given to the source materials and their delivery into the deposition reactor. They can not only be a source of impurity contamination but can also influence the uniformity of the deposited films. The source materials used for the thin film deposition can be either solid, liquid or gaseous. The purity of the deposited film not only depends on the purity of the source materials delivered to the reactor and the leak tightness of the system but also to a large degree on the substrate cleaning procedure used.

Of considerable importance is the stability and repeatability of the processes used, especially in the large-scale manufacturing. Many different factors can influence the deposition process and it is extremely important to understand and control these parameters. To make a film deposition process acceptable for device fabrication, an extensive and careful study of the processes and equipment is often required. Any process instabilities or uncontrolled deposition parameters should be discovered and rectified during this procedure.

The uniformity of the deposited films, both in thickness and composition, is of great concern for most deposition processes. These requirements impose severe restrictions on the selection of the deposition process, the type of the source materials and also the control of the process parameters. The deposition processes for thin film electroluminescent device fabrication require many steps in the fabrication process sequence. It is important that compatible deposition processes are selected that do not interfere with the structures already built into the device. The process integration, which has to consider thermal effects, chemical and metallurgical compatibility as well as functional requirements and limitations, is a major consideration in successful process selection. Frequently, the deposition processes have to offer a high degree of flexibility in meeting the demands for specific device requirements.

Chapter 4

SOL-GEL TECHNOLOGY

4.1 Introduction

4.1.1 Sol-gel processing

A colloid is a suspension in which the dispersed phase is so small (~1-1000 nm) that gravitational forces are negligible and interactions are dominated by short-range forces, such as van der Waals attraction and surface charges. A sol may be defined as a colloidal suspension of solid particles in a liquid. The sol may be produced from inorganic or organic precursors and may consist of dense oxide particles or polymeric clusters. In the sol-gel process, the precursors (starting compounds) for preparation of a colloid consist of a metal or metalloid elements surrounded by various ligands. The precursor most widely used in sol-gel research [72] is termed as an alkoxide.

Metal alkoxides are members of the family of metalorganic compounds, which have an organic ligand attached to a metal or metalloid atom. The most thoroughly studied example is silicon tetraethoxide (or tetraethoxy-silane, or tetraethyl orthosilicate, TEOS), $Si(OC_2H_5)_4$. Metal alkoxides are popular precursors because they react readily with water. The reaction is called hydrolysis, because a hydroxyl ion becomes attached to the metal atom. Key steps in sol-gel processing are the hydrolysis of the alkoxides and the condensation of the hydrolysis products, both of which are stimulated by catalysts such as acids. The hydrolysis step is described by

$$M(OR)_4+H_2O \rightarrow HO\text{-}M(OR)_3+ROH \qquad (4.1)$$

R represents a proton or other ligand and ROH is an alcohol. In reaction (4.1) the metal alkoxide $M(OR)_4$ is partially hydrolyzed forming a suitable species for polymerization as shown in the reaction

$$(OR)_3M\text{-}OR+HO\text{-}M(OR)_3 \rightarrow (OR)_3M\text{-}O\text{-}M(OR)_3+ROH \qquad (4.2)$$

By definition, condensation liberates small molecules, such as water or alcohol. This type of reaction can continue to build up larger and larger molecules by the process of polymerization. Dilute solutions containing these polymerized species can then be used to coat substrates by spinning or dip coating.

4.1.2 History of sol-gel technology

The first metal alkoxide was prepared from $SiCl_4$ and alcohol by Ebelmen [73], who found that the compound gelled on exposure to the atmosphere. However, these materials remained of interest only to chemists for almost a century. It was finally recognized by Geffeken [74] in the 1930s that alkoxides could be used in the preparation of oxide films. This process was developed by the Schott glass company in Germany and was quite well understood, as explained in the excellent review by Schroeder [75].

Inorganic gels from aqueous salts have been studied for a long time. Graham [76] showed that the water in silica gel could be exchanged for organic solvents, which argued in favor of the theory that the gel consisted of a solid network with continuous porosity. Competing theories of gel structure regarded the gel as a coagulated sol with each of the particles surrounded by a layer of bound water, or as an emulsion. The network structure of silica gels was widely accepted in the 1930s, largely through the work of Hurd [77], who showed that they must consist of a polymeric skeleton of silicic acid enclosing a continuous liquid phase. The process of supercritical drying to produce aerogels was invented by Kistler [78] in 1932, who was interested in demonstrating the existence of the solid skeleton of the gel, and in studying its structure.

Around the same time, mineralogists became interested in the use of sols and gels for the preparation of homogeneous powders for use in studies of phase equilibria [79,80]. This method was later popularized in the ceramics community by Roy [81,82] for the preparation of homogeneous powders. That work, however, was not directed toward an understanding of the mechanisms of reaction or gelation, nor the preparation of shapes (monoliths). Much more sophisticated work, both scientifically and technologically, was going on in the nuclear-fuel industry, but it was not published until later [83,84]. The goal of this work was to prepare small spheres (tens of μm in diameter) of radioactive oxides that would be packed into fuel cells for nuclear reactors. The advantage of sol-gel processing was that it avoided generation of dangerous dust, as would be produced in conventional ceramics processing, and facilitated the formation of spheres. The latter was accomplished by dispersing the aqueous sol in a hydrophobic organic liquid, so that the sol would form into small droplets, each of which would subsequently gel.

The ceramics industry began to show interest in gels in the late sixties and early seventies. Controlled hydrolysis and condensation of alkoxides for preparation of multicomponent glasses was independently developed by Levene and Thomas [85] and Dislich [86]. Ceramic fibers were made from metalorganic precursors on a commercial basis by several companies [87-89]. However, the explosion of activity that continues today can be dated from the demonstration by Yoldas [90,91] and Yamane *et al.* [92] that monoliths could be produced by careful drying of gels. This is a bit ironic in retrospect, as it is evident that monoliths are the least technologically important of the potential applications of gels.

As is usually the case, the technology preceded the science of sol-gel processing, but great strides have been made in the past few years in understanding the fundamental aspects of preparing homogeneous multicomponent ceramics (crystalline and amorphous) from alkoxide-derived gels. The sol-gel process is now an well-accepted technology for preparing thin films.

4.2 Theory of Sol-gel Technology

3.2.1 Hydrolysis and Condensation

If one molecule reaches macroscopic dimensions so that it extends throughout the solution, the substance is said to be a gel. The gel point is the time (or degree of reaction) at which the last bond is formed that completes this giant molecule. Thus a gel is a substance that contains a continuous solid skeleton enclosing a continuous liquid phase. Gels can also be formed from particulate sols, when attractive dispersion forces cause them to stick together in such a way as to form a network. The sol-gel process uses inorganic or metal organic compounds as raw materials. In aqueous or organic solvents these compounds are hydrolyzed and condensed to form inorganic polymers. For inorganic compounds hydrolysis proceeds by removal of a proton from an aqueous reaction to form a hydroxy (M-OH) or (M=O) ligand. Condensation reactions involving the hydroxy ligands result in inorganic polymers in which the metal centres are bridged by oxygens or hydroxyls. The most commonly used metal organic compounds are metal alkoxides $M(OR)_x$, where R is an alkyl group C_nH_{2n+1}.

A macromolecular oxide network is obtained through hydrolysis and condensation. The reactions are usually expressed as follows, Hydrolysis:

$$M(OR)_x + H_2O \rightarrow M(OH)(OR)_{x-1} + HOR \tag{4.3}$$

Condensation:

$$M(OH)(OR)_{x-1} + M(OR)_x \rightarrow (OR)_{x-1}M\text{-}O\text{-}M(OR)_{x-1} + HOR \tag{4.4}$$

The overall reaction being:

$$M(OR)_x + \frac{x}{2}H_2O \rightarrow MO_{\frac{x}{2}} + xROH \tag{4.5}$$

Chemical additives are always used in order to improve the process and obtain better materials. Acid or base catalysts can influence both the hydrolysis and condensation rates and the structure of the condensed product. Acids serve to protonate negatively charged alkoxide groups, enhancing the reaction kinetics. Hydrolysis goes to completion when sufficient water is added. Usually base additions promote the hydrolysis.

4.2.2 Gelation

The hydrolysis and condensation reactions shown above lead to the growth of clusters that eventually collide and link together into a gel. Gels are sometimes defined as "strong" or "weak" according to whether the bonds connecting the solid phase are permanent or reversible. The chemical reactions that bring about gelation continue long after the gel point, permitting flow and producing gradual changes in the structure and properties of the gel.

The simplest picture of gelation is that clusters grow by condensation of polymers or aggregation of particles until the clusters collide; then links form between the clusters to produce a single giant cluster that is called a gel. The giant spanning cluster reaches across the vessel that contains it, so the sol does not pour when the vessel is tipped. At the moment that the gel forms, many clusters will be present in the sol phase, entangled in but not attached to the spanning cluster; with time, they progressively become connected to the network and the stiffness of the gel will increase. According to this picture, the gel appears when the last link is formed between two large clusters to create the spanning cluster. This bond is no different from innumerable others that form before and after the gel point, except that it is responsible for the onset of elasticity by creating a continuous solid network.

The sudden change in rheological behavior is generally used to identify the gel point in a crude way. For example, the time of gelation, t_{gel}, is sometimes defined as corresponding to a certain value of viscosity, η; alternatively, it may be defined as the point where the gel shows so much elasticity that a probe (e.g., rotating spindle) tears the gel.

4.2.3 Aging of Gels

The chemical reactions that cause gelation continue long after the gel point, producing strengthening, stiffening and shrinkage of the network. The process of dissolution and reprecipitation may coarsen the pore structure, while separation may occur into mixtures of solid/liquid, liquid/liquid or solid/solid phases. These changes can have a major influence on the subsequent processes of drying and sintering. The processes of change during aging after gelation include polymerization and phase transformation.

Polymerization is the increase in connectivity of the network produced by condensation reactions, such as

$$\equiv Si\text{-}OH + HO\text{-}Si \equiv \rightarrow \equiv Si\text{-}O\text{-}Si \equiv + H_2O \qquad (4.6)$$

Studies based on nuclear magnetic resonance (NMR) [93] and Raman spectroscopy [94,95] indicate that condensation in silica gels continues long after gelation, because of large concentration of labile hydroxyl groups. In addition to condensation, aging can result in further hydrolysis,

$$\equiv Si\text{-}OR + H_2O \rightarrow \equiv Si\text{-}OH + ROH \qquad (4.7)$$

or in the reverse reaction, re-esterification,

$$\equiv Si\text{-}OH + ROH \rightarrow \equiv Si\text{-}OR + H_2O \qquad (4.8)$$

The latter reaction is suppressed by using excess water.

Several types of phase transformation can occur during aging, such as microsyneresis, in which solid phase separates from the liquid on a local scale. There may also be segregation of the liquid into two or more phases.

The structural changes that occur during aging have an important effect on the drying process. The structure of the gel also influences the sintering behaviour, since the process of densification is driven by the interfacial energy. Crystalline gels sinter much more slowly than amorphous gels with the same composition, so phase transformation during aging can be profoundly important.

4.2.4 Drying of Gels

The process of drying of a porous material can be divided into several stages. At first, the body shrinks by an amount equal to the volume of liquid that evaporates, and the liquid-vapour interface remains at the exterior surface of the body. The second stage begins when the body becomes too stiff to shrink and the liquid recedes into the interior, leaving air-filled pores near the surface. Even as air invades the pores, a continuous liquid film supports flow to the exterior, so evaporation continues to occur from the surface of the body. Eventually, the liquid becomes isolated into pockets and drying can proceed only by evaporation of the liquid within the body and diffusion of the vapour to the outside.

The driving forces and transport mechanisms are important during drying of gels. The driving forces for shrinkage include chemical effects, such as condensation reactions, and physical effects, such as capillary pressure. Fluid transport can occur by flow down a pressure gradient or diffusion down a chemical potential gradient, and deformation of the network may involve elastic, plastic, or viscoelastic strains. As liquid is removed by evaporation, tension that develops in the pores produces contraction of the network; when the pressure is not uniform, warping and cracking of the gel can result.

4.2.5 Avoiding Fracture

Drying produces a pressure gradient in the liquid phase of a gel, which leads to differential shrinkage of the network. When the exterior of the gel tries to shrink faster than the interior, tensile stresses arise that tend to fracture the network at the exterior. The material on either side of the crack can contract more freely, so it is favorable for the crack to grow into the drying surface. It may seem odd that compression of the network by the liquid causes fracture. In fact, if the pressure in the liquid were uniform, the whole network would be isotropically compressed and the gel would shrink without risk of cracking. However, the higher tension in the liquid at the exterior causes greater contraction of the network in that region. Since that contraction is inhibited by the slower-contracting interior (where the tension in the liquid is less), the network at the exterior is effectively stretched and this promotes cracking. Thus, it is the differential contraction that produces macroscopic tension in the network and this leads to cracking. Cracking occurs when the stress in the network exceeds its strength. Cracking is sometimes attributed to the existence of a pore size distribution in gel.

A variety of strategies have been employed to avoid fracture from drying stresses, including developing gels with larger pores, aging to increase the strength of the gel, as well as increasing the pore size, using chemical additives to lower interfacial energies or encourage diffusion within the pores, supercritical drying to eliminate entirely the liquid-vapor interfacial energy, thereby preventing fracture and reducing shrinkage.

4.2.6 Porosity

Surface tension forces created in a gel during solvent removal cause the network to fold or crumple as the coordination of the particles is increased. Porosity develops when, due to additional cross linking or neck formation, the gel network becomes sufficiently strengthened to resist the compressive forces of surface tension. Thus the dried xerogel (xerogel is a gel which is dried by evaporation) structure will be a contracted distorted version of the structure originally formed in solution.

4.2.7 Sintering of Gels

Sintering is a process of densification driven by interfacial energy. Material moves by viscous flow or diffusion in such a way as to eliminate porosity and thereby reduce the solid-vapor interfacial area. In gels, that area is enormous, so the driving force is great enough to produce sintering at exceptionally low temperatures, where the transport process are relatively slow. Amorphous materials sinter by viscous flow and crystalline materials sinter by diffusion, so the paths along which material moves, and the relationship between the rate of transport and the driving force, are quite different [96].

Viscous sintering is driven by the energy gained by reduction in surface area of the porous body. Given a microstructural model, it is possible to relate the change in surface area to the overall change in dimensions (i.e., the strain). The energy gained when this strain occurs is the product of the specific surface energy and the change in surface area [74]. When a viscous body flows, energy is expended, and the rate of this dissipation of energy is proportional to the square of the strain rate. Frenkel [97] suggested that the rate of strain (or densification) could be found by equating the rate of change in the surface energy to the rate of energy dissipation.

The kinetics of densification of crystalline materials are slower and much more dependent on microstructure. The difficulty of reaching theoretical density is exacerbated in gels by the fact that the dried gel is rarely the equilibrium crystal phase. One important respect in which crystalline and amorphous materials differ is that the plane of contact between crystals, called the grain boundary, has a specific interfacial energy. This energy reflects the fact that the crystal planes in the respective particles do not match perfectly at the boundary. The existence of the grain boundary energy means that the energy gained by eliminating porosity is partially offset by the energy invested in creating necks between the grains. It is advantageous to sinter the gel while it is amorphous and then to crystallize after complete densification.

Sintering of composites is most difficult, even for glass matrices, because the inclusions prevent shrinkage. These encourage cracking during drying and prevent contraction during sintering.

4.3 Physics of Film Formation

4.3.1 Dip Coating

In dip coating processes, film formation takes place by evaporation of the solvent from a polymer solution. The substrate is dipped into the polymer solution, taken out at a constant speed and dried by allowing the solvent to evaporate, leaving behind a solid polymer film on the substrate. Scriven [98] divided the dip coating process into five stages: (1) immersion, (2) start-up, (3) deposition, (4) drainage, and (5) evaporation, shown in fig. 4.1. The thickness of the deposited film is related to the position of the streamline dividing the upward and downward moving layers. There are five forces in the film deposition region governing the thickness of the film and the position of the streamline: (1) viscous drag upward on the liquid by the moving substrate, (2) force of gravity, (3) resultant force of surface tension in the concavely curved meniscus, (4) inertial force of the boundary layer liquid arriving at the deposition region, and (5) surface tension gradient [98].

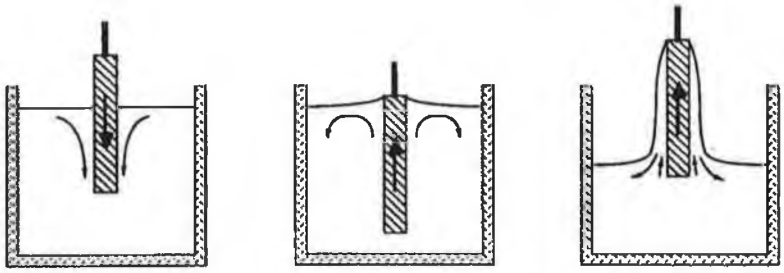

Immersion
(a)

Start-up
(b)

Deposition & Drainage
(c)

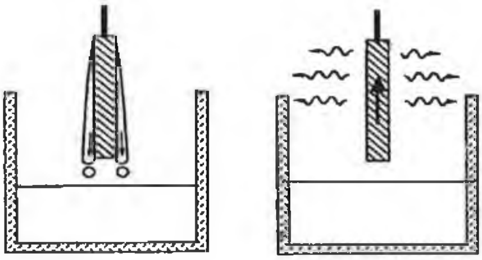

Drainage
(d)

Evaporation
(e)

Fig. 4.1 Stages of dip coating process.

The thickness of the coating layer depends on the following factors:

1) the speed at which the substrate is taken out,
2) the concentration of the solution,
3) the viscosity of the solution,
4) the rate of solvent evaporation,
5) the angle at which the substrate is taken out,
6) the surface tension of the solution,
7) the vapour pressure, temperature and relative humidity above the coating bath,
8) the precise control of air velocity, and
9) the temperature of substrate and solution.

When the liquid viscosity (η) and the substrate speed (U) are high enough to lower the curvature of the meniscus, then the deposited film thickness (t) is the thickness that balances the viscous drag ($\eta U/t$) and the gravity force (ρgt) [98,99]:

$$t = C\left(\frac{\eta U}{\rho g}\right)^{1/2} \qquad (4.9)$$

where the proportionality constant, C, is about 0.8 for Newtonian liquids [99], ρ is the density of the liquid and g is the gravitational acceleration.

When the substrate speed and the liquid viscosity are not high enough, as is often the case in sol-gel processing, this balance is modulated by the ratio of viscous drag to liquid-vapour surface tension (γ_{LV}) according to the following relationship derived by Landau and Levich [100]:

$$t = 0.94\frac{(\eta U)^{2/3}}{\gamma_{LV}^{1/6}(\rho g)^{1/2}} \qquad (4.10)$$

4.3.2 Spin Coating

Films may also be formed by spinning the solution on a rotating substrate. Bornside et al. [101] divided spin coating into four stages: (1) deposition, (2) spin-up, (3) spin-off, and (4) evaporation, shown in fig. 4.2. An excess of liquid is dispensed on the surface during the deposition stage. In the spin-up stage, the liquid flows radially outward, driven by centrifugal force. In the spin-off stage, excess liquid flows to the perimeter and leaves as droplets. As the film thins, the rate of removal of excess liquid by spin-off slows down, because the thinner the film, the greater the resistance to flow, and also because the concentration of the nonvolatile components increases raising the viscosity. In the fourth stage, evaporation takes over as the primary mechanism of thinning.

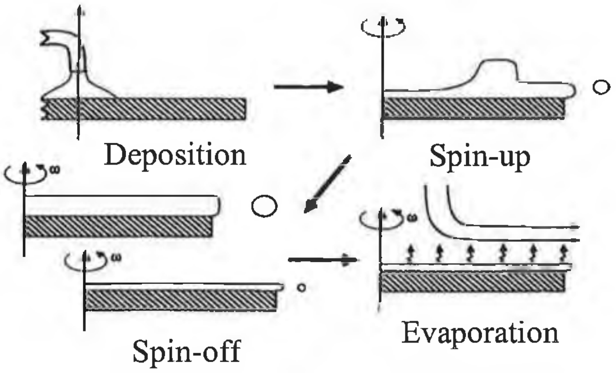

Fig. 4.2 Stages of spin coating process.

An advantage of spin coating is that a film of liquid tends to become uniform in thickness during spin-off and once uniform, tends to remain so provided that the viscosity is not shear dependent and does not vary over the substrate. This tendency arises due to the balance between the two main forces: centrifugal force, which drives flow radially outward, and viscous force (friction), which acts radially inward [102]. During spin-up, the centrifugal force overwhelms the force of gravity, and the rapid thinning quickly squelches all inertial forces other than centrifugal force.

The final thickness of film depends on the following factors:

1) initial thickness,
2) time between spin-up and spin-off,
3) angular velocity,
4) the evaporation rate in spin coating, and
5) the viscosity of the liquid.

The thickness of an initially uniform film during spin-off is described by [98,103]:

$$h(t) = \frac{h_0}{\left(1 + 4\rho\omega^2 h_0^2 t / 3\eta\right)^{1/2}} \qquad (4.1.1)$$

where h_0 is the initial thickness, t is the time, ω is the angular velocity, η is the viscosity, and ρ is the density of the liquid.

4.3.3 Other Coating Methods

Although dipping and spinning are the most extensively investigated sol-gel coating methods, they suffer from the general requirements of axially or radially symmetric substrates and the difficulty in achieving thick layers with a single coating. For these reasons, other coating methods such as electrophoresis, thermophoresis and sedimentation (also called settling) have been explored.

4.3.3.1 Electrophoresis

The phenomenon of electrophoresis (EP) is the movement of charged particles through a liquid under the influence of an external electric field applied across the suspension [104]. The particles or polymers move in a direction opposite or parallel to the external current, depending on their charge, and deposit on either the cathode or anode. EP is therefore limited to conductive substrates that can serve as an electrode, but complicated shapes are easily accommodated.

Unlike dip coating, in EP the particles move in linear trajectories and impact the stationary substrate with a maximum velocity, v, that depends on the applied electric field, E, and the particle charge, q. Foss derived the following expression for v [105]:

$$v = \left(\frac{qE}{6\pi\eta r} \right) X\, 10^{9} \qquad (4.12)$$

where q is in Coulombs, E in volts/cm, the viscosity (η) in centipoise (m Pa.s), the hydrodynamic radius (r) in cm, and v in cm/see. However, unlike settling, where the largest particles settle first, causing a deposit whose particle size decreases from bottom to top, in EP the compensating effects of the particle charge and hydrodynamic radius cause all the particles to have approximately the same velocity [106]. Therefore, the particle size distribution is the same at all levels of the deposit in electrophoresis.

4.3.3.2 Thermophoresis

Thermophoresis is the movement of suspended particles through a fluid under the influence of an applied thermal gradient [107]. The thermal gradient causes the particles to experience a net force in the direction of decreasing temperature (positive thermophoresis), because molecules impacting the particle on opposite sides through thermal motion have different average velocities due to their differences in temperature. The thermophoretic velocity acquired by a particle suspended in a liquid in the direction of decreasing temperature gradient, ∇T, has the general form [108]:

$$v_t = -K_t(\eta / T)\nabla T \qquad (4.13)$$

where K_t is a constant that depends on the molecular flow regime of the sol.

Particles suspended in a temperature gradient should move in more or less ballistic trajectories and impact the coating surface with a velocity normal to the surface proportional to the temperature gradient. It is expected therefore that, like EP coatings, thermophoretic coatings may be denser than dip coatings. Unlike EP coatings, thermophoretic coatings have the advantage that electrically conductive substrates are not a requirement.

4.3.3.3 Settling

Settling is also a coating method that is amenable to particulates adapted by Garino [109-111] for deposition of particulate sols. The sol is spread onto a horizontal substrate with a moving rod. The particles deposit on the substrate surface under the influence of gravity accompanied by the convective motion resulting from solvent evaporation. For large particles that settle within the time constraints established by evaporation, this method is similar to EP since the particles impact the surface with a finite velocity component normal to the surface. According to Stoke's law [112] the steady-state velocity of a spherical particle settling in a viscous medium is:

$$v = g(\rho_p - \rho_0)D_S^2 / 18\eta_0 \qquad (4.14)$$

where ρ_p is the particle density, ρ_0 is the density of the fluid, D_S is the diameter, and η_0 is the viscosity. Unlike EP the largest particles arrive first, potentially causing a gradation in particle size, and the deposition and evaporation stages may overlap, depending on the relative rates of settling and evaporation. For smaller particles that do not settle quickly, this method differs from dip or spin coating in that the depositing film is not thinned by draining and no shear field is established. Unlike any of the previously discussed methods, all the particles in the sol are deposited on the substrate surface.

4.4 Applications

There are many potential applications of sol-gel derived materials in the form of films, fibers, monoliths, powders, composites and porous media. Certainly one of the most technologically important aspects of sol-gel processing is that, prior to gelation, the fluid sol or solution is ideal for preparing thin films by such common processes as dipping, spinning or spraying. Compared to conventional thin film forming processes, such as CVD, evaporation or sputtering, sol-gel film formation requires considerably less equipment and is potentially less expensive; however, the most important advantages of sol-gel processing over conventional coating methods is the ability to control precisely the microstructure of the deposited film, i.e., the pore volume, pore size and surface area.

In comparison with other thin film deposition technologies the sol-gel process has the following advantages:

(i) it gives wide possibility to vary the film properties by changing the composition of the solution (change in film microstructure, introduction of dopants, etc.);

(ii) low process cost, specially for large-scale substrates;

(iii) it is possible to coat on the desired shape and area without using expensive and complicated equipment;

(iv) better purity and homogeneity from raw materials;

(v) low temperature of preparation which can

  a) save energy;

  b) minimize evaporation losses;

   c) minimize air pollution;
   d) minimize reactions with containers, thus producing purity;
   e) bypass phase separation;
   f) bypass crystallization.

(vi) while for thin films applied by vacuum techniques it is difficult to provide a stoichiometric ratio of the elements [113] and appropriate quality of the dielectric-semiconductor interface (as a result of bombardment of the substrate by high energy particles), the sol-gel method allows one to overcome these problems.

Some disadvantages [114] of the sol-gel process are:

(i) high cost of raw materials;
(ii) large shrinkage during processing that accompanies drying and sintering;
(iii) residual fine pores;
(iv) residual hydroxyl;
(v) residual carbon;
(vi) health hazards of organic solutions;
(vii) long processing times.

Chapter 5

MEASUREMENT TECHNIQUES

5.1 Introduction

Electrical, optical and structural properties of thin films are very important for their use in thin film electroluminescent devices. The following measurements were done for the investigation of the properties of thin films:

a. Thickness measurement:
  1. Interferometry
  2. Ellipsometry

b. Electrical measurement:
  1. Resistivity
  2. Hall mobility and Carrier concentration

c. Surface roughness measurement

d. Bonding structure measurement
  1. Fourier Transform Infrared spectroscopy
  2. Raman spectroscopy

e. Crystal structure measurement
  1. X-ray diffraction

f. Chemical composition
  1. X-ray photoelectron spectroscopy

g. Optical measurement
  1. Transmittance

5.2 Measurement of Film Thickness

5.2.1 Interferometry

An interferometer was used to measure the thickness of the deposited film. Interference occurs when radiation from the same source follows more than one path to the point of detection. When a path difference is present, a set of fringes can be seen as light and dark bands called interference fringes. This phenomenon of interference is a striking illustration of the wave nature of light [115]. A sample is masked and coated, allowing a portion of the substrate to remain uncoated. An interferometric microscope is used to observe the fringe pattern obtained from the monochromatic light reflected from the uncoated and coated side of the sample. If there is a difference in height between the two sides of the specimen, the fringe pattern will appear to be shifted as it crosses the edge between them, shown in figure 5.1. Two adjacent fringes are separated by half of the wavelength of light ($\lambda/2$). The step on the specimen surface displaces the fringe pattern and this is a measure of the difference in height between the coated and uncoated specimen sides. The coating thickness is measured as the displacement or shift of the fringe pattern at the step area. If L is the fringe spacing and ΔL the displacement of the fringes, then the film thickness, t is given by

$$t = \frac{\Delta L}{L}\frac{\lambda}{2} \tag{5.1}$$

Where λ is the wavelength of the monochromatic light. This is a convenient method of evaluating film thickness, although it is only really applicable where both the substrate and coating are reflective and film thickness is large (>0.2μm), enabling the interference patterns to be clearly distinguished.

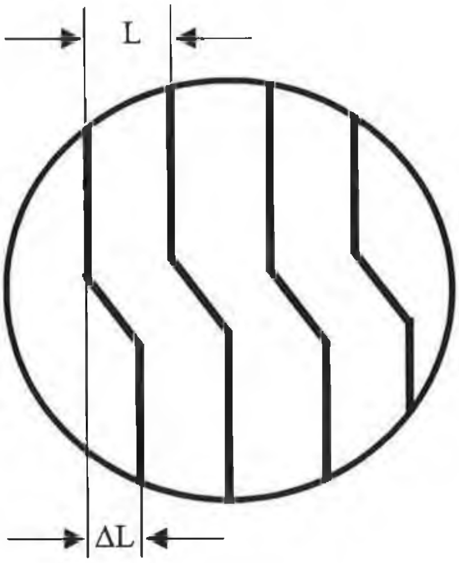

Figure 5.1 Interference patterns for thickness measurements.

5.2.2 Ellipsometry

Ellipsometry is a non-destructive and contact-less technique for the optical characterization of the surface, especially measurement of thickness and refractive index of thin films. This technique has also been called polarimetry and polarization spectroscopy. It is very useful for extremely thin films but may also be used for very accurate measurements of thicker films. The widespread use of ellipsometry was demonstrated by the symposium sponsored in 1963 by the National Bureau of Standards [116].

When linearly polarized light impinges on a surface, generally it will be reflected elliptically polarized. This occurs because the parallel and perpendicular components (relative to the surface) of the linear polarization are reflected with different efficiencies and a phase shift occurs.

Ellipsometry has the following advantages over other conventional methods of measuring thickness:

a) It can measure the film thickness at least an order of magnitude smaller than can be measured by other methods such as interferometry.
b) It can determine the refractive index of thin films of unknown thickness.
c) It can make measurements in optically transparent environments such as air or liquids.
d) It does not require special conditions (such as vacuum, heat or electron bombardment) that may change the optical properties of the surface being measured but does permit measurements under such conditions, if desired.
e) Nulling ellipsometers have the additional special advantages that the measured quantities are usually azimuth angles (of rotation of the polarizing components), which can be measured with high resolution and accuracy. This almost completely eliminates the effects caused by variations of intensity of the incident light beam, variations in total reflectance of the samples being measured and variations in sensitivity of the detector-amplifier system used to measure the intensity of the reflected beam.

Measurements on thin films are made under the assumption that there is an abrupt interface between the substrate and the film. When two linearly polarized light waves with the same wavelength are combined in phase, the resultant wave is also linearly polarized. However, when they are combined out of phase, they are elliptically polarized.

Ellipsometry is based on the fact that a monochromatic and linearly polarized electromagnetic wave changes its state of polarization if it strikes an interface between two media in a non-perpendicular fashion. When light passes from one medium to another, some of the incident light is reflected, while some enters the second medium. The phase difference between the parallel component (E_s) and the perpendicular component (E_p) of the incident wave is denoted δ_1 and for the outgoing wave δ_2 (see figure 5.2).

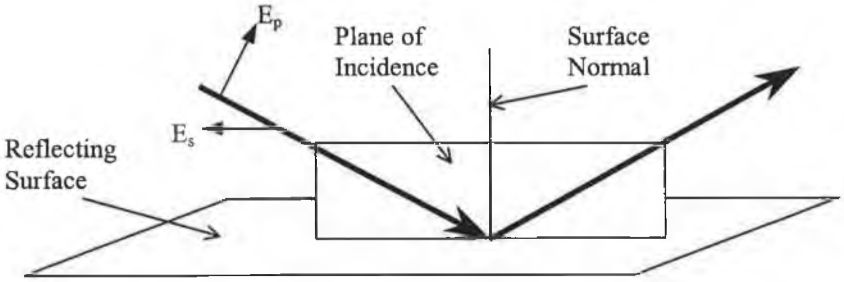

Figure 5.2 Reflection of a light beam from a surface.

Then, the change in phase difference that occurs upon reflection is given as delta $\Delta = \delta_1 - \delta_2$ [117]. Ellipsometry, based on the reflection of light from the surface of a sample, measures the change in phase difference Δ between the incident and reflected waves, and the ratio of the magnitudes of the total reflection coefficients (ψ) such that [117].

$$\tan \psi e^{j\Delta} = \frac{R^p}{R^s} \tag{5.2}$$

where R^p = reflectance in plane of incidence

R^s = reflectance normal to plane of incidence

$e^{j\Delta}$ = exponential complex notation of Δ

Δ = phase difference between incident and reflected waves

Calculations based on Δ and ψ and the refractive index (n) for the substrate and the angle of incidence of the light beam (ϕ) will yield values for the refractive index (n) and the extinction coefficient (k) for a film on a substrate. Based on plots of Δ vs. ψ, with different beam wavelengths (λ) and incident angle (ϕ), different values of n can be plotted. The curve on which the measured point, given by co-ordinates (ψ,Δ), falls, indicates the refractive index of the film. The position on which it falls indicates the thickness of the film [117,118].

An ellipsometer often uses a helium neon laser, polarizer, quarter-wave compensator and a detector. The polarizer produces a linearly polarized wave which is then converted to elliptical polarization by the quarter-wave compensator. The elliptically polarized radiation is incident on the sample and the reflected wave is passed through an analyzer. When the analyzer is nulled to the detector, the ellipticity generated is the opposite of that made by the reflection. From this, $\tan\Psi$ and Δ can be found and hence the thickness and refractive index of the film can be calculated.

Instrumentation

The thickness and refractive index were measured on films deposited onto Silicon substrates using an Auto EL-III Rudolph Research null ellipsometer with a wavelength of 632.8 nm.

5.3 Electrical measurement

5.3.1 Measurement of Film Resistivity

The properties of the thin films used for the fabrication of transistors and other semiconductor devices are essential in determining the characteristics of the completed devices. Resistivity and lifetime [119] (of minority carriers) measurements are generally made on thin films to determine their suitability. The resistivity, in particular, must be measured accurately since its value is critical in many devices.

Several techniques are employed to measure the electrical resistivity of thin films. The four-point probe technique is one of the most common methods for measuring the semiconductor resistivity, because the two-point probe method is more difficult to interpret. The total resistance between the two probes is given by

$$R_T = \frac{V}{I} = 2R_c + 2R_{sp} + R_s \tag{5.3}$$

where R_c is the contact resistance at each metal probe/semiconductor contact, R_{sp} is the spreading resistance under each probe and R_s is the semiconductor resistance. Neither R_c nor R_{sp} can be accurately calculated so that R_s can not be accurately extracted from the measured resistance.

This problem can be solved using four-point probe method. Two probes carry the current and other two are used for voltage sensing. The four-point probe method was originally proposed by Wenner in 1916 [120]. This measurement technique is referred to in Geophysics as Wenner's method. It was adopted for semiconductor wafer resistivity measurements by Valdes in 1954 [121].

The basic model for four-point probe measurements is shown in fig. 5.3. Four sharp probes are placed on a flat surface of the film to be measured, current is passed through the two outer electrodes and the floating potential is measured across the inner pair. In order to use this four-point probe method to measure the resistivity of the thin film, it is necessary to assume that:

i) The resistivity of the film is uniform in the area of measurement.

ii) The measurements should be made on surfaces which have a high recombination rate, such as mechanically lapped surfaces.

iii) The surface on which the probes rest is flat with no surface leakage.

iv) The four probes used for resistivity measurements contact the surface at points that lie in a straight line.

v) The diameter of the contact between the metallic probes and the semiconductor should be small compared to the distance between probes.

vi) The probes are far from any of the other surfaces of the sample and the sample can thus be considered a semi-infinite volume of uniform resistivity material.

Figure 5.3 shows the geometry being considered. Four probes are spaced s_1, s_2, and s_3, apart. Current I is passed through the outer probes (1 and 4) and the floating potential V_f is measured across the inner pair of probes 2 and 3.

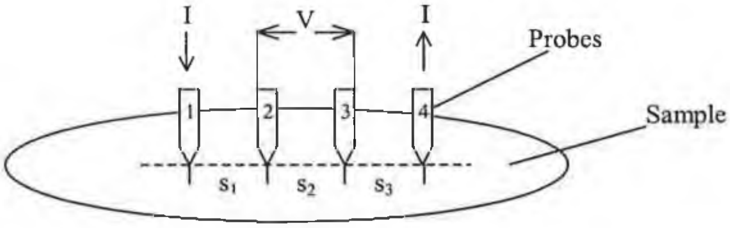

Figure 5.3 Model for the four probe resistivity measurements.

The floating potential V_f at a distance r from an electrode carrying a current I in a material of resistivity ρ is given by [122].

$$V_f = \frac{\rho I}{2\pi r} \tag{5.4}$$

In figure 5.3 there are two current-carrying electrodes (1 and 4), therefore the floating potential V_f, at any point in the film is the difference between the potential induced by each of the electrodes, since they carry currents of equal magnitude but in opposite directions. Thus:

$$V_f = \frac{\rho I}{2\pi}\left(\frac{1}{r_1} - \frac{1}{r_4}\right) \tag{5.5}$$

where r_1 is the distance from probe 1 and r_4 is the distance from probe 4.

The floating potential at probe 2 (V_{f2}) and 3 (V_{f3}) can be calculated from (5.5) by substituting the proper distances as follows:

$$V_{f2} = \frac{\rho I}{2\pi}\left(\frac{1}{s_1} - \frac{1}{s_2 + s_3}\right) \qquad (5.6)$$

$$V_{f3} = \frac{\rho I}{2\pi}\left(\frac{1}{s_1 + s_2} - \frac{1}{s_3}\right) \qquad (5.7)$$

The potential difference V between the probes is then

$$V = V_{f2} - V_{f3} = \frac{\rho I}{2\pi}\left(\frac{1}{s_1} + \frac{1}{s_3} - \frac{1}{s_2 + s_3} - \frac{1}{s_1 + s_2}\right) \qquad (5.8)$$

and now, the resistivity can be calculated from equation (5.8) as

$$\rho = \frac{V}{I}\frac{2\pi}{\left(\frac{1}{s_1} + \frac{1}{s_3} - \frac{1}{s_1 + s_2} - \frac{1}{s_2 + s_3}\right)} \qquad (5.9)$$

When the point probe spacing is equal ($s_1 = s_2 = s_3 = s$), the equation (5.9) simplifies to

$$\rho = \frac{V}{I} 2\pi s \qquad (5.10)$$

If the sample to be measured has a thickness $t << s$, and is resting on an insulating support, it may be considered as essentially two-dimensional like an infinite sheet having an infinitesimal thickness. In such a case, and if the film is large in extent compared with the probe assembly, equation (5.10) becomes, [121]

$$\rho = \frac{V}{I} \times \frac{\pi}{\ln 2} \times t = 4.5324 \times t \times \frac{V}{I} \qquad (5.11)$$

The electrical circuitry used for the measurements carried out in this project consists of an ammeter (electrometer), voltmeter and power supply, is as shown in figure 5.4.

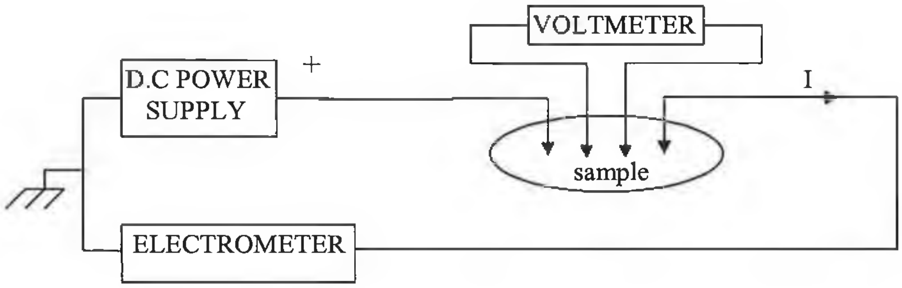

Figure 5.4 Experimental setup for measurements with d.c current.

5.3.2 Measurement of Hall Mobility and Carrier Concentration

Van der Pauw [123] developed a perfectly general method to determine the hall mobility and carrier concentration of a film using four probes located arbitrarily on the film surface. The van der Pauw arrangement for hall effect measurements is shown in fig.5.5, in which the current and voltage contacts are crossed, and a magnetic field B is applied perpendicular to the sample surface. The Hall effect is briefly described below. The Hall coefficient is obtained from [124]

$$R_H = \frac{t}{B} \times \left[\frac{R_{31,24} + R_{42,13}}{2} \right] \tag{5.12}$$

where $R_{ij,kl} = V_{kl} / I_{ij}$, t is the film thickness in meters, B is the magnetic field in Teslas (T) (1 T=1 Weber/m^2 = 1 V.s/m^2).

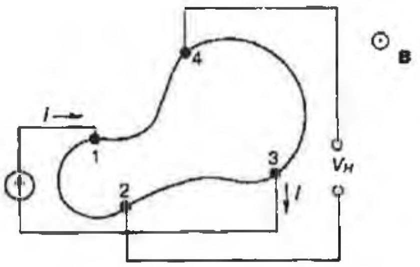

Figure 5.5 Van der Pauw arrangement for Hall effect measurements.

Although this technique is applicable to specimens of arbitrary shape, a symmetrical shape is nearly always used. There are several sample geometries, which are used for van der Pauw measurements, depending on the accuracy required and the feasibility of fabrication. For aluminum doped zinc oxide and indium tin oxide films investigated here, a square shape was chosen, since it is one of the most accurate van der Pauw structures for avoiding finite-contact size corrections [125]. Thin films of square shape were deposited onto glass substrates. The samples were then pasted onto a supporting board, with contacts soldered at the back of the board for connecting the measurement instruments.

For the contact onto the samples in the four corners, very thin flexible wire was used; crude contacts were made using a mixture of silver paint and epoxy hardener which was cured at room temperatures for 24 hours. The schematic diagram for the measurements is shown in fig. 5.6.

The Hall effect was discovered by E.H. Hall in 1879 [126] and is widely used in the semiconductor industry because of its simplicity and the importance of the parameters it measures, namely carrier concentration and mobility. The prototype structure for Hall-effect measurements is shown in figure 5.7.

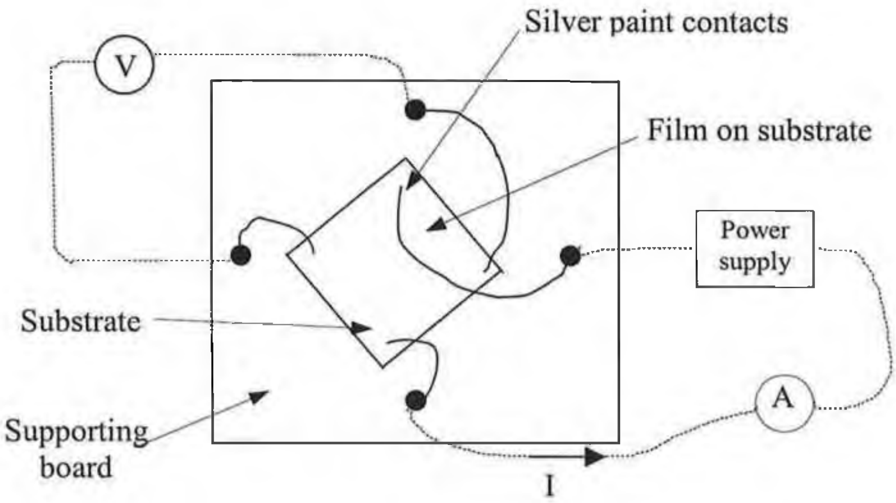

Figure 5.6 Schematic diagram for Hall effect measurements.

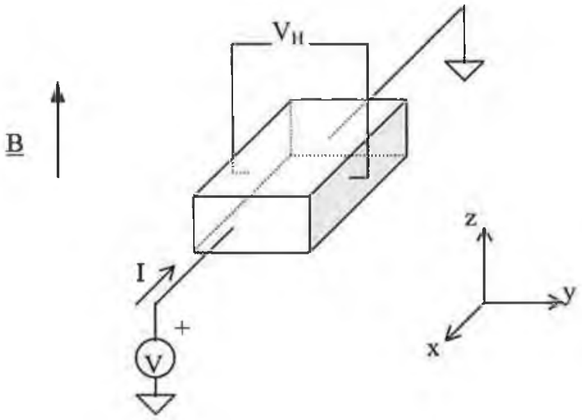

Figure 5.7 Hall-bar configuration for Hall-effect measurements.

In the simplest model of the Hall effect, the charge carriers are assumed to be electrons which are travelling with a velocity v in the x direction upon the application of an electric field. Upon application of a magnetic field $\underline{B}$ in the z direction, the electrons experience a force $-e\underline{v}\times\underline{B}$, which will have a y component $-e(\underline{v}\times\underline{B})_y=-e(v_zB_x-v_xB_z)=ev_xB_z$. The electronic charge will build up on the +y face of the sample until an opposing force $-eE_y$ just balances the ev_xB_z force. With this balance, the electrons again have no y component of velocity, just as was the case when B=0. The total current density is $j_x=-nev_x$, so that $eE_y=ev_xB_z=-eBj_x/ne$. The Hall coefficient R_H is defined as

$$R_H = \frac{E_y}{j_x B} = -\frac{1}{ne} \tag{5.13}$$

The general working equations to carry out a simple Hall effect experiment are:

$$\mu_H = \left|R_H \times \sigma\right| \tag{5.14}$$

$$n_H = \frac{1}{\left|e \times R_H\right|} \tag{5.15}$$

where μ_H is the Hall mobility, σ is the conductivity, R_H is the Hall coefficient, n_H is the Hall carrier concentration and e is the electron charge. When the electrons all have the same magnitude of x-axis velocity, then $\mu_H = \mu$ (conductivity mobility) and $n_H=n$ defined by the equation $\sigma = ne\mu$. The Hall-bar configuration [124] of figure 5.7 is the most simple geometry to analyze, but is not a feasible configuration to use for thin films, therefore, the van der Pauw method described earlier was employed using the configuration shown in figure 5.6. The current and voltage contacts were crossed, and a permanent magnet capable of providing a magnetic field of 0.2 Tesla was used. Equation (5.12) was used to evaluate the Hall coefficient.

5.4 Measurement of Surface Roughness

The surface is the boundary that separates an object from another object, substance or space. Surface roughness is the finer irregularities of the surface texture that usually result from the inherent action of the production process or material condition.

The two parameters in most common use for the measurement of surface roughness are: (1) the roughness average (R_a) value, defined as the mean vertical deviation of the profile from the center line, treating deviations both above and below the center line as positive; (2) the root mean square (RMS) value, defined as the square root of the mean of the square of these deviations. The R_a has traditionally been the most common parameter in use in the UK, while the RMS value has been the most common in the USA. The roughness average (R_a) value is normally expressed in terms of micro-inch or microns (μm).

Let us consider a profile height function, *Z(x)* which represents the point by point deviations between the measured profile and the reference mean line shown in fig. 5.8. For digital instruments, the profile *Z(x)* is approximated by a set of digitized values (Z_i) recorded using the sampling interval (d_0).

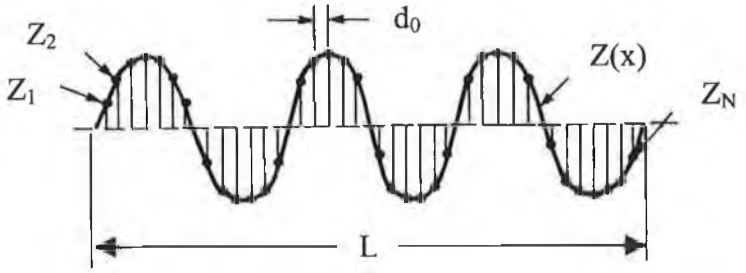

Figure 5.8 Illustration for the calculation of roughness average, R_a.

Roughness average is the arithmetic average of the absolute values of the profile height deviations recorded within the evaluation length and measured from the mean line. As shown in the fig. 5.8, R_a is equal to the sum of the shaded areas of the profile divided by the evaluation length, *L*. Analytically, R_a is given by [127],

$$R_a = \left(1/L\right)\int_0^L \left|Z(x)\right| dx \qquad (5.16)$$

For digital instruments, an approximation of the R_a value may be obtained by adding the individual Z_i values without regard to sign and dividing the sum by the number of data points, N.

$$R_a = (|Z_1| + |Z_2| + |Z_3| \,\ldots\ldots |Z_N|)/N \tag{5.17}$$

Root mean square (RMS), R_q is the root mean square average of the profile height deviations taken within the evaluation length and measured from the mean line. Analytically, it is given by:

$$R_q = \left[(1/L) \int_0^L Z(x)^2 \, dx \right]^{1/2} \tag{5.18}$$

The digital approximation is:

$$R_q = \left[\left(Z_1^2 + Z_2^2 + Z_3^2 + \ldots\ldots\ldots. + Z_N^2 \right) / N \right]^{1/2} \tag{5.19}$$

Instrumentation

The surface roughness average, R_a value is measured by using a Mitutoyo Surftest-402. Minimum resolution of the instrument is 0.01 μm.

5.5 Bonding structure measurement

Infrared (IR) and Raman spectroscopy are two of the widely used techniques for the determination of bonding structure and for the identification of compounds. Infrared and Raman spectroscopies provide information on molecular vibrations. These methods cause molecules to undergo changes in vibrational energy state by subjecting them to excitation radiation in selected spectral regions. IR and Raman spectroscopy differ in the means by which photon energy is transferred to the molecule and in the instrumentation used. Thus, the information extracted exhibits different characteristics. Infrared and Raman spectroscopy are complementary rather than competing techniques. The molecular vibrational frequencies observed by both techniques are nearly the same but the vibrational band intensities differ because of the different excitation mechanisms.

5.5.1 Fourier Transform Infrared Spectroscopy

With the advent of Fourier Transform Infrared (FTIR) spectrometers and the concomitant advantages of speed and sensitivity, infrared absorption spectroscopy has become one of the preeminent tools for molecular characterization and identification. The position of FTIR as a useful technique for characterization of industrial materials has been firmly established within the last decade. FTIR has brought additional merits such as high sensitivity, high precision, speed of measurement and extensive data processing capability besides the intrinsic advantages of infrared spectroscopy such as wide applicability, nondestructiveness, measurement under ambient atmosphere, capability of providing detailed structural information and a huge data base. The introduction of FTIR has changed infrared spectroscopy from a technique of identification of bulk materials to a comprehensive system of material characterization and has opened up a new field especially in surface studies and microanalyses of industrial materials.

Electromagnetic radiation is a good source to understand the bonding structure of compounds when it interacts with the atoms of that compound. Electromagnetic radiation, of which visible light forms an obvious but very small part, may be considered as a simple harmonic wave propagated from a source and travelling in straight lines except when refracted or reflected. The properties which undulate, corresponding to the physical displacement of a stretched string vibrating, or the alternate compression and rarefaction of the atmosphere during the passage of a light wave, are interconnected electric and magnetic fields. This is the basis of molecular spectroscopy.

In IR spectroscopy, the vibrational excitation is achieved by radiating the sample with a broad-band source of radiation in the infrared region, which is generally 4000-200 cm^{-1} (2.5-50 μm). For a vibration to be IR active, it is necessary to impart a change in the dipole moment. The dipole moment is defined as the magnitude of either charge in a dipole multiplied by the charge spacing. If an atom has the same number of protons and electrons, it is electrically neutral and does not contribute to the dipole moment. The chemical forces that exist in the molecule tend to redistribute the electrons so that a given atom may have a deficit or an excess of electrons, being considered as a particle with a small positive or negative charge. When applying IR excitation, this charge may change due to molecular vibration. If the negatively charged atom vibrates in one direction, and the positively charged one in the opposite direction, the vibration is IR active. However, if the molecule retains the center of symmetry so that the dipole moment remains unchanged, the vibration is IR inactive. If a molecule is excited to a higher vibrational state by directly absorbing the infrared radiation, the transmittance at a given wavenumber can be calculated according to equation 5.20 [128]. Similarly, the absorbance at a given wavenumber can be obtained by using the Beer-Lambert equation (Eq. 5.21) [128] as shown below:

$$T = \frac{I}{I_0} \tag{5.20}$$

$$\begin{aligned} A &= \log\left(\frac{I_0}{I}\right) \\ &= \alpha c t \end{aligned} \tag{5.21}$$

where T is transmittance, A is absorbance, I_0 is the light intensity without absorption, I is the intensity of light which has passed through the sample, t is the sample thickness, α is the molecular absorption coefficient and c is the concentration of material under test.

Instrumentation of FTIR

The FTIR spectra were measured using a Perkin Elmer FT-IR system. The scanning resolution was 2 cm^{-1}. A Deuterated Triglycine Sulphate (DTGS) detector was used for the reflected beam. All scans were performed at room temperature and normal atmospheric conditions.

5.5.2 Raman Spectroscopy

When a beam of light, of a wavelength not corresponding to an absorption in the sample, passes through it, a small fraction of the light is scattered by the molecules, and so, exits the sample at a different angle. This is called Rayleigh scattering if the wavelength of the scattered light is the same as the original wavelength; but, if the wavelength is different, it is called Raman scattering. Differences in wavelengths correspond to the wavelength of certain vibrational and rotational processes. The information obtained is of use in structural chemistry, because the rules allowing and forbidding transitions are different from those in absorption spectroscopy.

In Raman spectroscopy, the sample is irradiated with an intense source of monochromatic radiation. Generally this radiation frequency is much higher than the vibrational frequencies but lower than the electronic frequencies. The radiation scattered by the sample is analyzed in the spectrometer. Rayleigh scattering can be looked on as an elastic collision between the incident photon and the molecule. Since the rotational and vibrational energy of the molecule is unchanged in an elastic collision, the energy and therefore the frequency of the scattered photon is the same as that of the incident photon. This is by far the strongest component of the scattered radiation. The Raman effect can be looked on as an inelastic collision between the incident photon and the molecule where, as a result of the collision, the vibrational or rotational energy of the molecule is changed by an amount ΔE_m. In order that energy may be conserved, the energy of the scattered photon, $h\nu_{s,}$ must be different from the energy of the incident photon $h\nu_{i,}$ by an amount equal to ΔE_m [129]:

$$h\nu_i - h\nu_s = \Delta E_m \qquad (5.22)$$

In Raman scattering, the frequency of the incident photon is usually much greater than the molecular frequency ν_m. If a molecule gains energy, then ΔE_m is positive and $\nu_s < \nu_i$ which results in Stokes lines in the Raman spectrum. This terminology arose from Stokes rule of fluorescence which stated that fluorescent radiation always occurs at lower frequencies than that of the excitation radiation. If a molecule loses energy, then ΔE_m is negative and $\nu_s > \nu_i$ which results is anti-Stokes lines in the Raman spectrum. In order for a molecular vibration to be Raman active, the vibration must be accompanied by a change in the polarizability of the molecule [129].

Fig. 5.9 shows the mechanisms of Raman scattering [130]. In the case of Stokes lines, the molecules at $\nu = 0$ is excited to the $\nu = 1$ state by scattering light of frequency $\nu - \nu_1$. Anti-Stokes lines arise when the molecule initially in the $\nu = 1$ state scatters radiation of frequency $\nu + \nu_1$ and reverts to the $\nu = 0$ state. Since the population of molecules is larger at $\nu = 0$ than at $\nu = 1$ (Maxwell-Boltzmann distribution law), the Stokes lines are always stronger than the anti-Stokes lines.

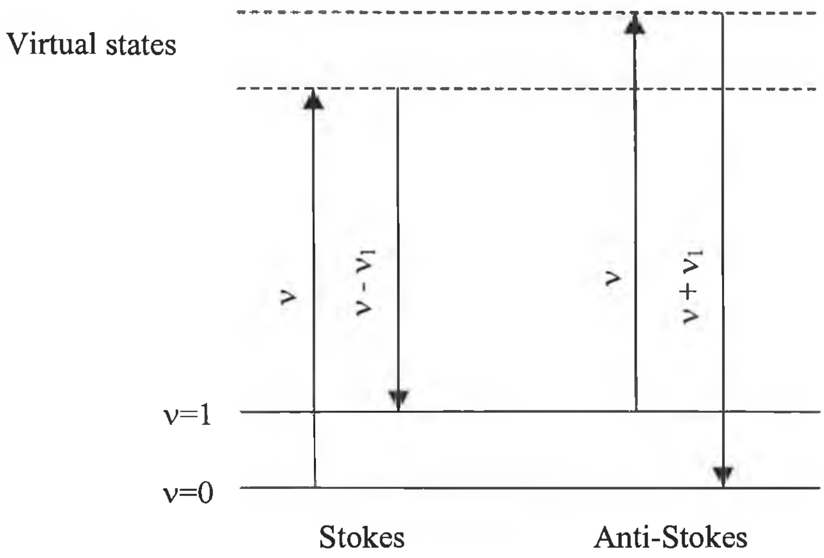

Figure 5.9 Mechanisms of Raman scattering.

Instrumentation

Raman data were recorded using a Jobin-Yvon Micro-Raman Spectroscopy System LabRam® HR-800 using a 325 nm He-Cd laser. Integration time was 5 sec and 10 spectra were averaged for each measurement.

5.6 Measurement of X-ray diffraction (XRD)

X-ray diffraction is a versatile, non-destructive analytical technique for identification and quantitative determination of the various crystalline forms, known as 'phases', of compounds present in powder and solid samples. Identification is achieved by comparing the x-ray diffraction pattern or 'diffractogram'-obtained from an unknown sample with an internationally recognized database containing reference patterns for more than 70,000 phases. Modern computer-controlled diffractometer systems use automatic routines to measure, record and interpret the unique diffractograms produced by individual constituents in even highly complex mixtures.

5.6.1 Principles

When an incident X-ray beam impinges upon the lattice planes in a crystal, general scattering occurs, such that the scattered waves interfere with and destroy one another. In certain specific directions, however, the scattered waves are in phase with one another and combine to form new wave-fronts. This constructive interference is known as diffraction. The direction in which diffraction occurs depend upon the size and shape of the unit cell of the crystal, whereas the intensity of the diffraction is determined by the actual atomic array or the nature of the crystal structure.

Von Laue, who, with Friedrich and Knipping, discovered the diffraction of X-rays by crystals in 1912, interpreted the observed diffraction patterns in terms of a theory analogous to that used to treat diffraction by gratings, extended to three dimensions. On the other hand, W. L. Bragg, who worked out the first crystal structures with his father in 1913 [131], showed that the angular distribution of scattered radiation could be understood by considering that the diffracted beams behaved as if they were reflected from planes passing through points of the crystal lattice. This "reflection" is analogous to that from a mirror, for which the angle of incidence of radiation is equal to the angle of reflection.

When a monochromatic x-ray beam with wavelength λ is incident on lattice planes in a crystal at an angle θ, diffraction occurs only when the distance travelled by the rays reflected from successive planes differs by an integral multiple of the wavelength, $n\lambda$.

From such considerations Bragg derived the famous equation that now bears his name [132]:

$$n\lambda = 2d \sin\theta \qquad (5.23)$$

where, n is an integer, λ is the wavelength of the X-rays, d is the perpendicular spacing between the lattice planes in the crystal and θ is the complement of the angle of incidence of the X-ray beam (and thus also the complement of the angle of scattering or "reflection"). Since it appears as if reflection has occurred from these lattice planes, with the direct beam deviated by the angle 2θ from its original direction, diffracted beams are commonly referred to as "reflections".

By varying the angle θ, the Bragg's Law conditions are satisfied by different d-spacings in polycrystalline materials. Plotting the angular positions and intensities of the resultant diffraction peaks produces a pattern which is characteristic of the sample. When a mixture of different phases is present, the diffractogram is formed by addition of the individual patterns.

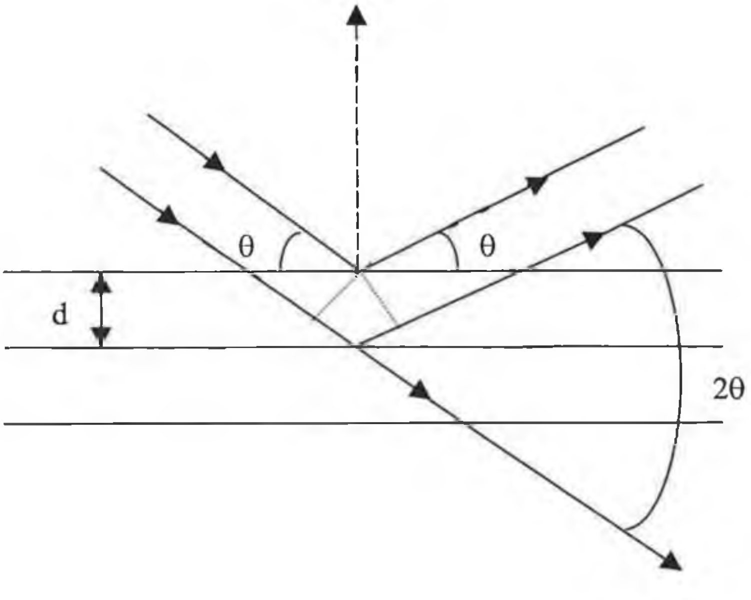

Figure 5.10 X-ray diffraction from atoms in a crystalline material.

The Bragg equation can be derived by considering that the path difference between waves scattered from adjacent parallel lattice planes must be an integral number of wavelengths. The equation is satisfied and thus diffraction maxima occur, only when the relation of wavelength, interplanar spacing and angle of incidence is appropriate. If a nearly monochromatic beam of X-rays is used with a single crystal specimen, diffraction maxima will be observed only for special values of the angle of incidence of the beam of x-rays and not for any arbitrary angle. If the crystal is rotated in the beam, additional diffracted beams will be formed at certain rotation angles. These "reflections" will only occur when the angle of incidence of the X-ray beam is such as to satisfy equation (5.23) for some set of lattice spacings present in the crystal, that is, λ, d and θ must all be such that the Bragg equation holds.

Instrumentation of XRD

X-ray diffraction analysis on the films was performed by using a Philips X'Pert XRD system. The scattering intensities were recorded as a function of diffraction angle. The scan step was 0.05 deg. and scan time per step was 0.5 sec. The incident beam was Cu Kα radiation (λ=1.54 $\overset{0}{A}$).

5.7 Measurement of X-ray photoelectron spectroscopy (XPS)

5.7.1 The basic XPS experiment

Of all the contemporary surface characterization methods, X-ray photoelectron spectroscopy (XPS) is the most widely used technique. The popularity of XPS as a surface analysis technique is attributed to its high information content, its flexibility in addressing a wide variety of samples and its sound theoretical basis. XPS has its origins in the investigations of the photoelectric effect (discovered by Hertz in 1887) in which X-rays were used as the exciting photon source. Before the First World War several groups analyzed the energies of the electrons emitted from metals bombarded by hard X-rays, the most prominent of which was Rutherford's group in Manchester. This group had extensive experience of the measurement of X-ray spectra from radioactive materials using magnetic analysis and was furthermore, at the forefront of X-ray spectroscopy. The early experiments were carried out by Moseley, Rawlinson and Robinson before the outbreak of First World War. Indeed, in 1914 Rutherford made a first stab [133] at stating the basic equation of XPS, which was subsequently modified to

$$E_K = h\nu - E_B \qquad (5.24)$$

where, E_K is the photoelectron kinetic energy, $h\nu$ the exciting photon energy and E_B the electron binding energy.

The basic XPS experiment is illustrated in fig. 5.11 [134]. The surface to be analyzed is first placed in a vacuum environment and then irradiated with photons. For XPS, the photon source is in the X-ray energy range. The atoms comprising the surface emit electrons (photoelectrons) after direct transfer of energy from the photon to the core-level electron. These emitted electrons are subsequently separated according to energy and counted. The energy of the photoelectrons is related to the atomic and molecular environment from which they originated. The number of electrons emitted is related to the concentration of the emitting atom in the sample.

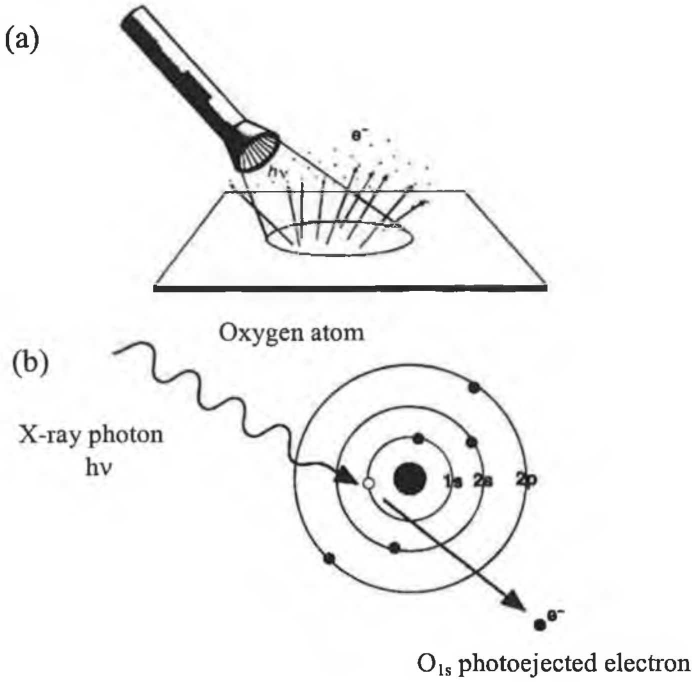

Figure 5.11 (a) A surface irradiated by a photon source of sufficiently high energy will emit electrons. If the light source is in the X-ray energy range, this is the XPS experiment, (b) The X-ray photon transfers its energy to a core-level electron imparting enough energy for the electron to leave the atom.

XPS is an information-rich method. The most basic XPS analysis of a surface provides qualitative and quantitative information on all the elements present (except H and He).

5.7.2 X-ray interaction with matter, the photoelectron effect and photoemission from solids

An understanding of the photoelectric effect and photoemission is essential in order to appreciate the surface analytical method, XPS. When a photon impinges upon an atom, one of three events may occur: (1) the photon can pass through with no interaction; (2) the photon can be scattered by an atomic orbital electron leading to partial energy loss; and (3) the photon may interact with an atomic orbital electron with total transfer of the photon energy to the electron, leading to electron emission from the atom. In the first case, no interaction occurs. The second possibility is referred to as 'Compton scattering' and can be important in high-energy process. The third process accurately describes the photoemission that is the basis of XPS. Total transfer of the photon energy to the electron is the essential element of photoemission.

Let us examine four observations associated with this photoelectric effect in more detail. First, no electrons will be ejected from an atom regardless of the illumination intensity unless the frequency of excitation is greater than or equal to a threshold level characteristic for each element. Thus, if the frequency (energy) of the excitation photon is too low, no photoemission will be observed. As the energy of this photon is gradually increased, at some value, we will begin to observe the photoemission of electrons from the atom. Second, once the threshold frequency is exceeded, the number of electrons emitted will be proportional to the intensity of the illumination. Third, the kinetic energy of the emitted electrons is linearly proportional to the frequency of the exciting photons-if we use photons of higher energy than our threshold value, the excess energy of the photons above the threshold value will be transmitted to the emitted electrons. Finally, the photoemission process from excitation to emission is extremely rapid (10^{-16} s).

Instrumentation of XPS

XPS analysis of the samples was carried with a VG-Scientific ESCA-LAB analyzer using a Al Kα (1486.6 eV) X-ray source operating at 240 W. Step size was 0.5 eV for wide scans, while 0.1 eV was used for narrow scans. The binding energies were calibrated with reference to C 1s peak at 284.8 eV.

5.8 Measurement of Transmittance

UV-VIS spectroscopy is one of the oldest methods in molecular spectroscopy. The definitive formulation of the Bouguer-Lambert-Beer law in 1852 [135] created the basis for the quantitative evaluation of absorption measurements at an early date. This led firstly to colorimetry, then to photometry and finally to spectrophotometry. This evolution ran parallel with the development of detectors for measuring light intensities, i.e. from the human eye via the photo-element and photocell, to the photomultiplier and from the photographic plate to the present silicon-diode detector both of which allow simultaneous measurement of the complete spectrum.

There are two classes of spectra, namely emission and absorption spectra. An emission spectrum is obtained by analysing the light emitted by a luminous source. An absorption spectrum is obtained by the spectroscopic analysis of the light transmitted by an absorbing medium which is placed between the light source and the spectroscope.

When a molecule absorbs radiation, its energy increases. This increase is equal to the energy of the photon as expressed by the relation

$$E = h\nu = hc/\lambda \qquad (5.25)$$

where h is Planck's constant, ν and λ are the frequency and the wavelength of the radiation respectively and c is the velocity of light. The change in energy may be in the electronic, vibrational or rotational energy of the molecule. Changes in electronic energy involve relatively large quanta. Changes in vibrational energy involve smaller quantities of energy and changes in rotational energy involve quanta even smaller than those of vibrational energy.

Optical transmission or absorption of transparent, insulating and emission films in EL display devices influences the characteristics of the EL devices directly. Impurities in films determine the spectra in the uv-visible range and properties of films. Optical transmission or absorption measurements are used to determine the properties of the films.

During transmission measurements light is incident on the film and the transmitted light is measured as a function of wavelength. The transmittance T of a film with identical front and back reflection coefficient and light incident normal to the film surface is given by [136]

$$T = \frac{(1-R)^2 e^{-\alpha d}}{1 + R^2 e^{-2\alpha d} - 2\mathrm{R}e^{-\alpha d}\cos(\phi)} \qquad (5.26)$$

where $\phi = 4\pi n_1 d/\lambda$, α is the absorption coefficient and the reflectance R is given by [136]

$$R = \frac{(n_0 - n_1)^2 + k_1^2}{(n_0 + n_1)^2 + k_1^2} \qquad (5.27)$$

where n_0 and n_1 are the refractive indices of the film corresponding to two successive peaks of the transmission curve. The absorption coefficient is related to the extinction coefficient k_1 by $\alpha = 4\pi k_1/\lambda$.

Instrumentation

Transmittance of the films was measured by using a monochromator-based Perkin Elmer Instrument UV/VIS Spectrometer.

Chapter 6

INSULATING MATERIALS

6.1 Introduction

Thin film electroluminescent (TFEL) devices provide an attractive alternative for solid state flat panel displays [137]. Dielectric materials play a decisive role in the performance of these Metal-Insulator-Semiconductor-Insulator-Metal (MISIM) structures [28,29,137,138]. Under actual operating conditions, very high electrical fields of the order of 100-200 MV/m are applied to the phosphor layer [139]. The role of the dielectric materials is to prevent the device breakdown under these high electric fields. Most important of all, a dielectric with a high permittivity lowers the operation threshold voltage as it increases the electric field in the emitting layer for a same applied voltage.

Generally, ac thin film electroluminescent devices consist of a triple layer structure, namely, an active layer sandwiched between two insulating layers. Because of this sandwich structure, undesirable leakage current flowing through the device is prevented. Consequently, the device can keep a sufficiently high electric field for EL operation across the active layer without breakdown.

AC thin film electroluminescent devices impose rather stringent requirements on the properties of the insulating layers, which have limited the number of insulating materials suitable for practical devices. The most important requirements for the insulating layers are (1) a high dielectric constant, (2) a high electric field and (3) a uniform thickness. Of these requirements, the dielectric constant and electric field strength are material dependent, while the thickness uniformity is process dependent. A number of studies have reported attempts at finding suitable insulators for TFEL device applications having the highest figure of merit, which is defined as the product of dielectric constant and breakdown electric field [140]. This figure of merit, which indicates the maximum-trapped charge density for an insulating material, is of the order of 4-6 $\mu C/cm^2$ in classical TFEL devices [30]. There are various types of insulating materials, such as TiO_2, SiO_2, Al_2O_3, Ta_2O_5, $BaTiO_3$, Y_2O_3, $PbTiO_3$ or Si_3N_4, which can be used as the insulating layer in thin film electroluminescent devices. Among these materials, the electrical, optical and structural properties of titanium dioxide (TiO_2) and tantalum oxide (Ta_2O_5) thin films have been studied in this work.

6.2 Titanium Dioxide (TiO_2) Thin Films Deposited by Sol-gel Process

6.2.1 Introduction

Because of their high dielectric constant, titanium dioxide (TiO_2) films have attracted much attention for use in thin film electroluminescent devices as insulators. Titanium dioxide (TiO_2) has many interesting physical properties which make it suitable for thin film applications. Because of their good transmittance in the visible region, high refractive index and chemical stability, TiO_2 films have found wide application for various optical coatings [141-144]. The high dielectric constant, ε, of TiO_2 opens up prospects for the use of TiO_2 thin films in microelectronic devices, e.g. in capacitors or as a gate dielectric in metal-dielectric-semiconductor devices [145,146]. During the last decade TiO_2 films have been suggested as photoanodes in the process of photoelectrolysis of water in solar energy conversion systems [147-149] and as electrochromic materials for display devices [149,150].

Because of their wide usefulness, a number of techniques have been used to prepare TiO_2 thin films, such as thermal [151] or anodic oxidation [152], sputtering [153-155], pyrolysis [156,157], chemical vapor deposition (CVD) [158,159], including plasma-enhanced chemical vapor deposition [160] and more recently by the sol-gel method [161-164].

In comparison with other oxide film technologies the sol-gel process has the following advantages:

(i) it gives a wide possibility to vary the film properties by changing the composition of the solution (change in film microstructure, introduction of dopants, etc.);

(ii) low process cost, specially for large-scale substrates (e.g. TiO_2 antireflective coatings of photovoltaic solar cells prepared by the sol-gel method cost 20-40 times less than those obtained by vacuum coating techniques [143];
(iii) while for thin films applied by vacuum techniques it is difficult to provide a stoichiometric ratio of the elements [113] and appropriate quality of the dielectric-semiconductor interface (as a result of bombardment of the substrate by high energy particles), the sol-gel method allows one to overcome these problems.

The following section describes the preparation of titanium dioxide thin films by the sol-gel process. Electrical, optical and structural properties of as-deposited thin films and films annealed at different temperatures in the presence of air, oxygen and nitrogen are also studied.

6.2.2 Experimental procedure

Three different solutions with 50 ml, 100 ml and 150 ml of ethanol were used to prepare the thin films of TiO_2. Among them, the following recipe was found best for the preparation of TiO_2 thin films. The quality of the TiO_2 films prepared from the solutions with 50 ml and 150 ml of ethanol was not good and they came off the substrate after multiple coating and also after high temperature annealing.

Titanium dioxide thin films have been formed on silicon and glass substrates by the sol-gel method as shown in fig.6.1. 100 ml of ethanol (C_2H_5OH) was added to 0.1 mol of titanium tetra-isopropoxide [$Ti(O\text{-}i\text{-}C_3H_7)_4$] which was cooled with ice and stirred. 100 ml of ethanol was mixed with 0.15 mol of water and 5 mmol of hydrochloric acid. The $C_2H_5OH/H_2O/HCl$ solution was added to the $Ti(O\text{-}i\text{-}C_3H_7)_4/C_2H_5OH$ solution under stirring and cooling with ice.

Titanium dioxide gel films were obtained by dipping the substrates into the titanium dioxide solution and pulling them up at 0.6 cm/sec. The titanium dioxide films were subjected to heat-treatment at 260^0C for 10 minutes. The thickness of the film was approximately 70 nm for each dipping. By repeating the above procedure, titanium dioxide films of different thickness were obtained.

For electrical measurements, a metal-insulator-semiconductor (MIS) structure with Al electrodes was fabricated. Al electrodes with 1.8 mm diameter were prepared by using a shadow mask in an Edwards Coating System E306A. Capacitance was measured by using a Boonton Electronics Capacitance meter at 1 Mhz frequency. The dielectric constant was calculated by using the measured capacitance and film thickness.

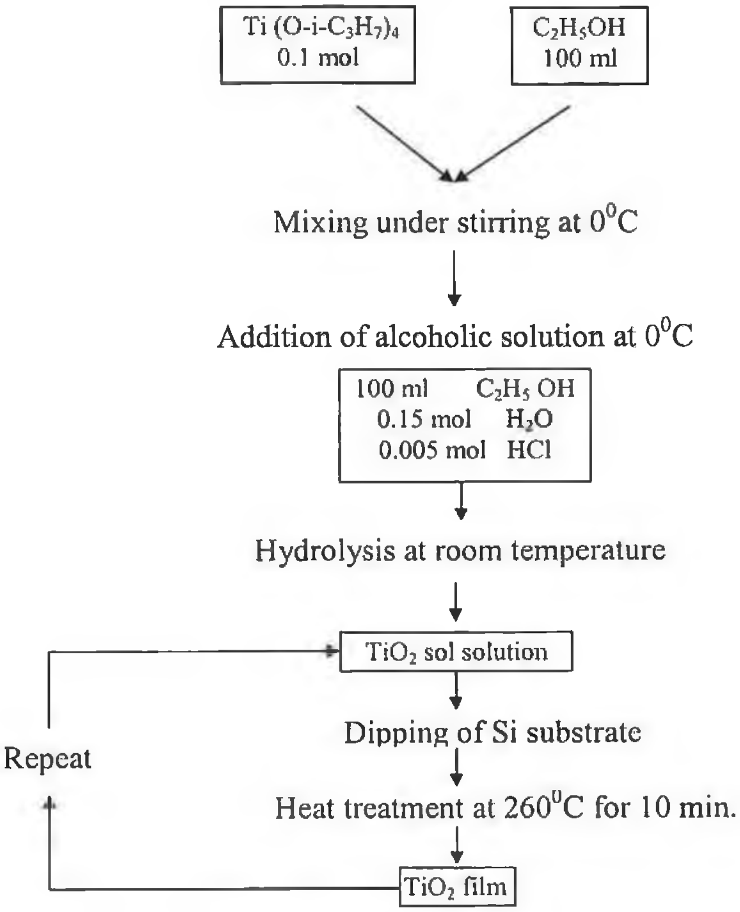

Figure 6.1 Preparation process of titanium dioxide film by sol-gel process.

6.2.3 Results and discussion

6.2.3.1 Electrical Properties

Capacitance-voltage measurements were performed using the Al/TiO_2/p-Si structure to determine the dielectric constant of the TiO_2 layer. The capacitance was measured at a frequency of 1 Mhz at room temperature, while the d.c. bias was swept between +5 and -5 V. A typical C-V curve for one of the as-deposited Al/TiO_2/p-Si samples is shown in fig. 6.2. The insulator capacitance was taken as the maximum capacitance when the metal-insulator-semiconductor (MIS) diode was in accumulation, i.e. at –5 V bias.

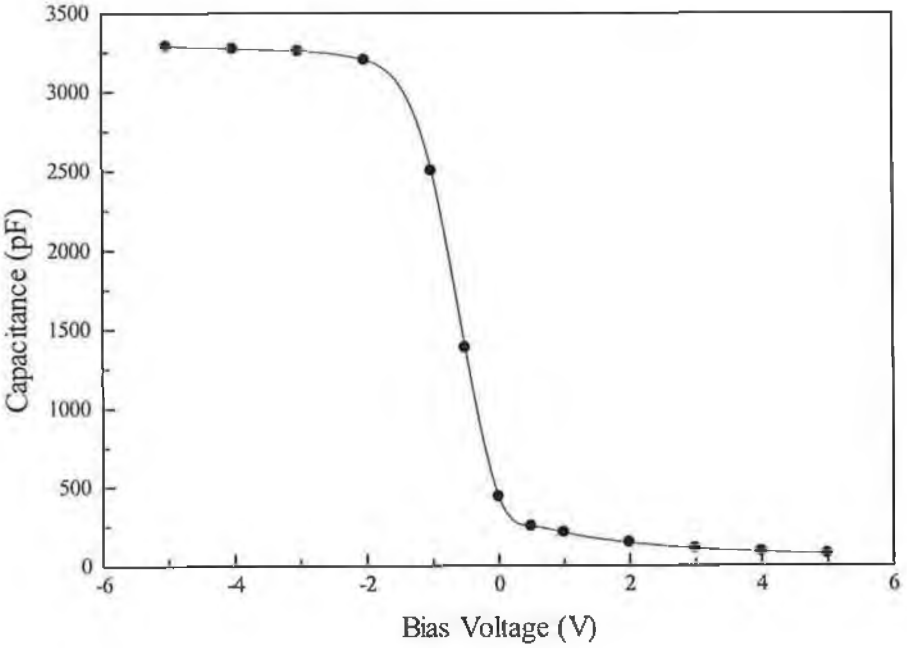

Figure 6.2 Typical capacitance-Voltage characteristics for the as-deposited Al/TiO_2/p-Si sample.

Fig. 6.3 shows the dielectric constant of the TiO_2 films as a function of annealing temperature in air, oxygen and nitrogen. The dielectric constant of the TiO_2 film was calculated from the maximum capacitance and it was found to be approximately 26 for the as-deposited film. From the figure, it is seen that dielectric constant of the films increased upon annealing at higher temperature in all cases and it varies from 75 to 82 annealed at 700^0C in different atmosphere. The reason for this increase in dielectric constant with annealing temperatue is assumed to result from some film densification and crystallisation of minor amorphous phase in the as-deposited films that occurred during the heat treatment [165].

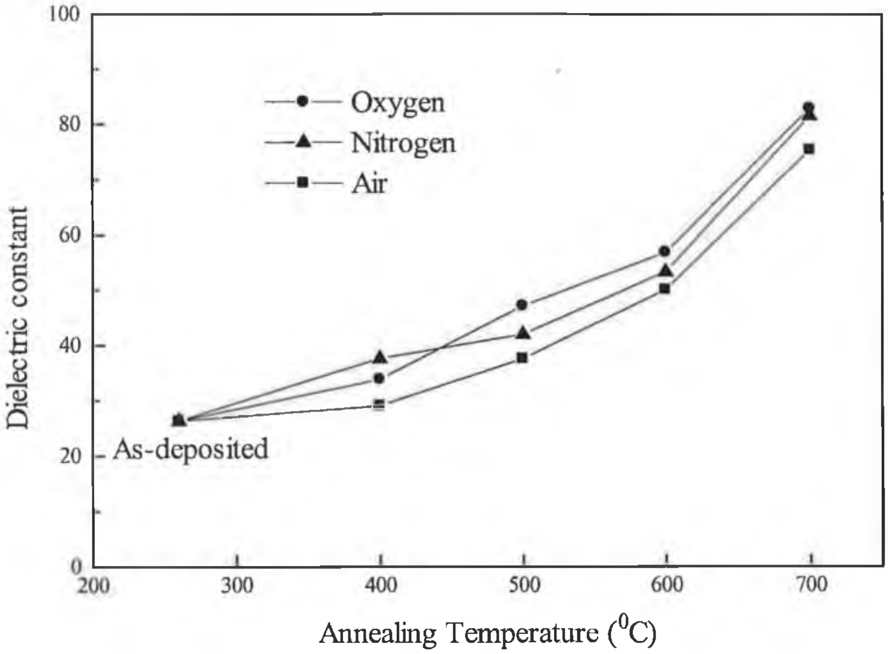

Figure 6.3 Variation of dielectric constants as a function of annealing temperature

Fig. 6.4, 6.5 and 6.6 show the leakage current variations with electric field for the as-deposited TiO_2 films and the films annealed at different temperatures in the presence of air, oxygen and nitrogen respectively. From the figures, it is seen that as the applied field increases, the leakage current increases parabolically up to a saturation point at each annealing temperature and the leakage current decreases upon annealing at higher temperatures in all the cases. The shape of the curves suggests that the conduction mechanism in these films corresponds to the Fowler-Nordheim (FN) tunneling process [166]. The leakage current for the as-deposited film is approximately $5.0\text{x}10^{-5}$ A/cm^2 at 1 MV/cm and it decreases to $6.0\text{x}10^{-6}$ A/cm^2 upon annealing at 700^{0}C in different atmosphere. The leakage current densities for the 700^{0}C annealed films are $6.6\text{x}10^{-6}$ A/cm^2, $6.0\text{x}10^{-6}$ A/cm^2 and $6.8\text{x}10^{-6}$ A/cm^2 annealed in presence of air, oxygen and nitrogen respectively. So the best leakage property of the films was achieved after annealing at 700^{0}C in presence of oxygen in accordance with the results of fig. 6.4, 6.5 and 6.6. Electric breakdown was observed at a field strength of 2.7 MV/cm. The as-deposited film exhibits high leakage current. This may be attributed to an inferior film structure containing a high density of oxygen vacancies and high defect density due to carbon contamination [167-170]. When the films are annealed at high temperature in atmosphere, oxygen molecules are broken by high temperature and produce excited atoms in single states which have one unoccupied electron orbital and therefore are thought to be strong electron trap levels. The excited oxygen atoms are adsorbed on the surface of the TiO_2 film and diffuse into it. Diffused excited atoms fill the oxygen vacancies in the TiO_2 which are source of free electrons in the conduction band, accept free electrons and occupy the lattice site. As the annealing temperature increases, the concentration of the excited oxygen atoms increases, the number of vacancies decreases and the leakage current lowers. Upon annealing at higher temperature, a new interfacial silicon dioxide layer is formed between the TiO_2 film and the Si substrate which can also reduce the leakage current.

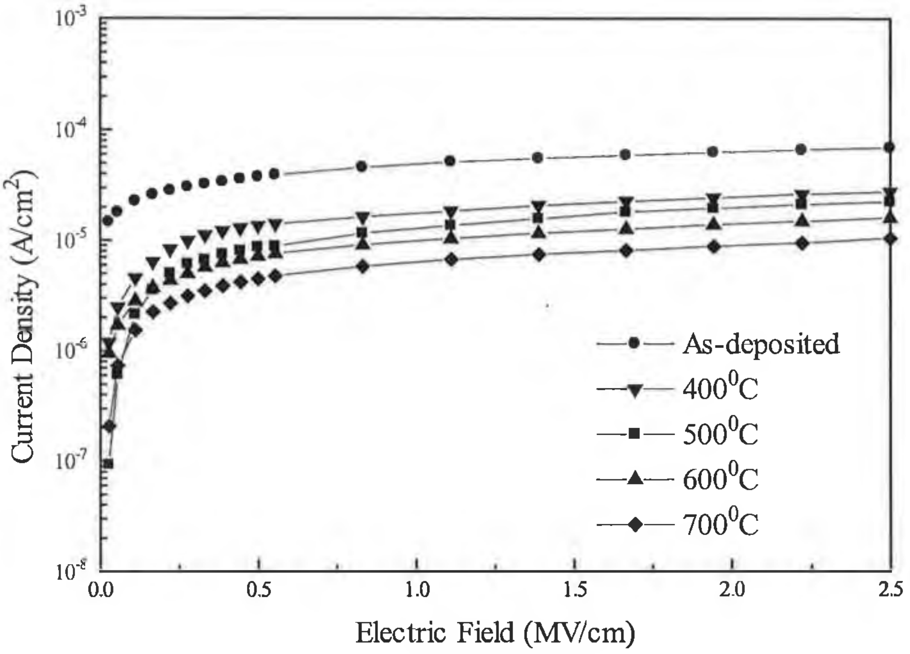

Figure 6.4 Current density vs. electric field characteristics for TiO_2 films annealed at different temperatures in air.

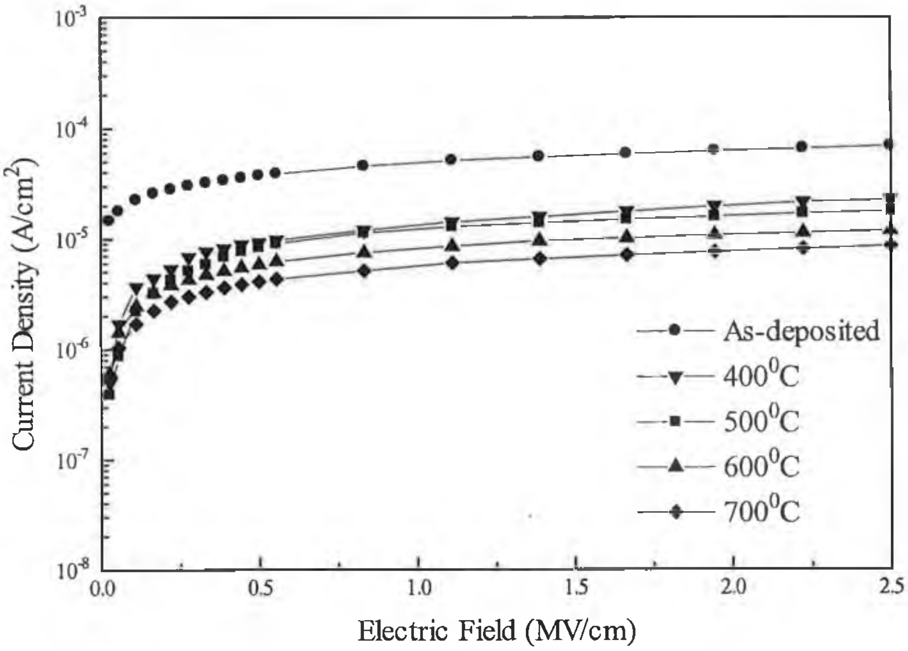

Figure 6.5 Current density vs. electric field characteristics for TiO_2 films annealed at different temperatures in oxygen.

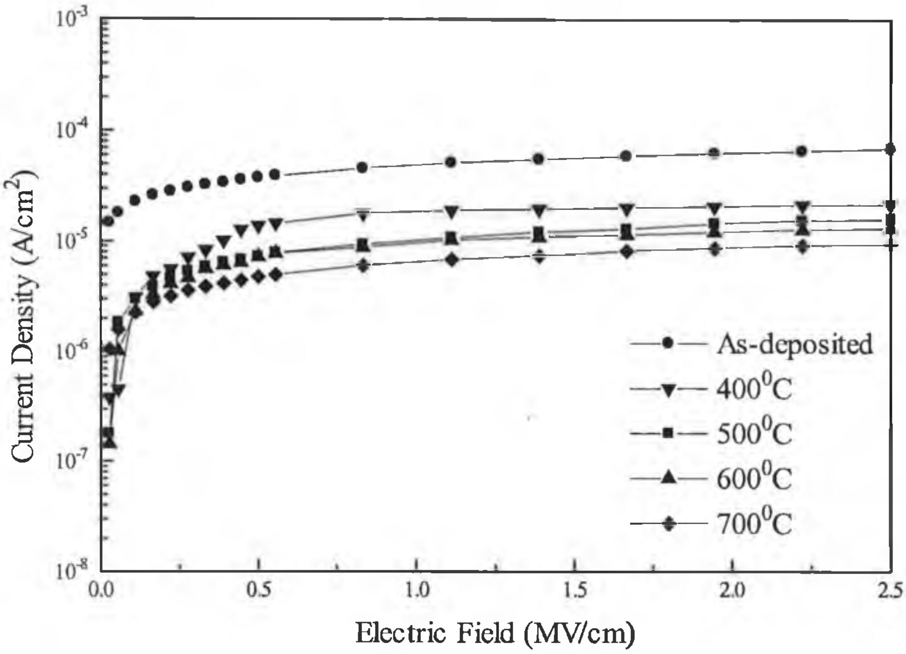

Figure 6.6 Current density vs. electric field characteristics for TiO_2 films annealed at different temperatures in nitrogen.

Fig. 6.7 shows the variation of resistivity of TiO_2 films as a function of annealing temperature in air, oxygen and nitrogen. The resistivities, ρ, of the films were calculated from the I-V data [I=V/R and ρ=(V.A)/(I.t), where A is the area of Al contact and t is the thickness of the film]. From the figure, it is seen that the resistivity increases with the annealing temperature. The resistivities are measured for an electric field of 1 MV/cm. The as-deposited films have a resistivity of $2.18x10^{10}$ Ω-cm while the resistivities for 700^0C annealed films are $1.66x10^{11}$ Ω-cm, $1.85x10^{11}$ Ω-cm and $1.62x10^{11}$ Ω-cm annealed in the presence of air, oxygen and nitrogen respectively. So the resistivity of the films annealed at 700^0C are almost the same for air and nitrogen atmosphere and higher in oxygen atmosphere. The increase in resistivity at higher temperatures may be because of high temperature annealing, the entire TiO_2 film undergoes rapid lattice vibration, with rearrangement of its stoichiometric structure (TiO_2), outdiffusion of impurities and improvement of the crystal defects.

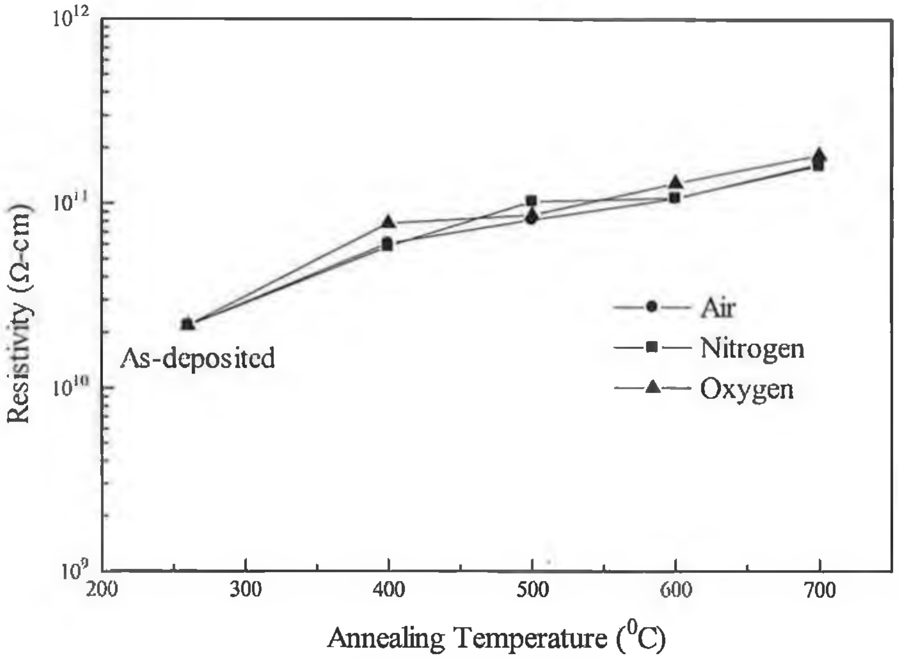

Figure 6.7 Resistivity of TiO_2 films as a function of annealing temperature in air, oxygen and nitrogen.

6.2.3.2 Roughness

Ellipsometric measurements showed that the thickness of the TiO_2 film deposited on silicon was approximately 70 nm for each dipping and the refractive index was 2.10. The average roughness (R_a) values were measured for TiO_2 thin films annealed at different temperature in presence of air, oxygen and nitrogen. Fig.6.8 shows the variation of R_a with annealing temperature. Roughness of the substrate was measured to be 0.01 μm and for the as-deposited film 0.03 μm. Roughness decreases with temperature and a small change in R_a was observed with varying the temperature due to the crystallisation effect. The instrument resolution was 0.01 μm, so we could not measure the roughness beyond this limit.

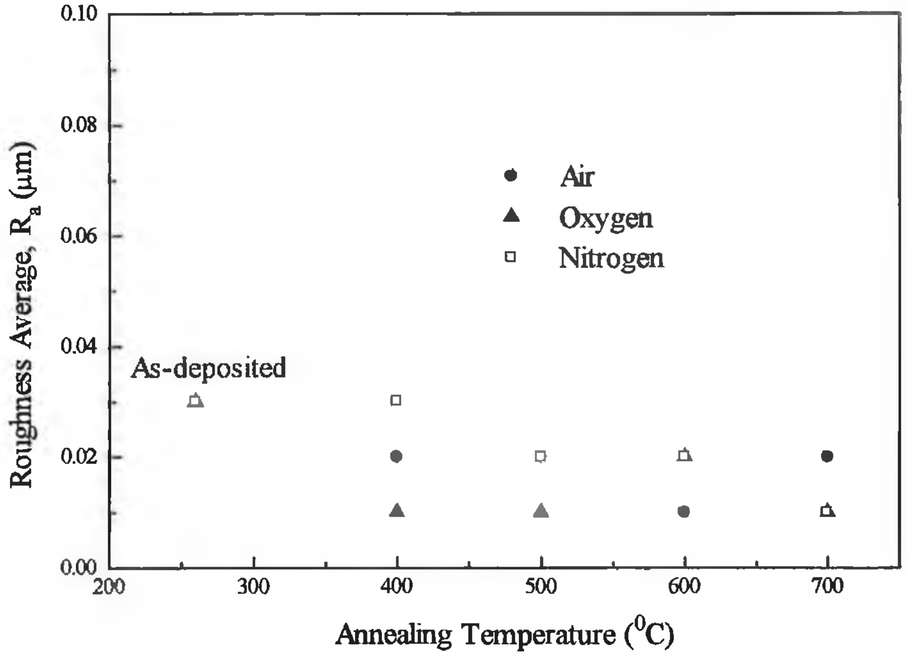

Figure 6.8 Variation of Roughness as a function of annealing temperature annealed in air, oxygen and nitrogen for TiO_2 film.

6.2.3.3 Structural Properties

6.2.3.3.1 Fourier Transform Infrared (FTIR) Spectroscopy

The bond configuration of TiO_2 thin films was analysed by using FTIR in the wavenumber range from 400 to 4000 cm^{-1} for as-deposited films and films annealed at different temperatures in the presence of air, oxygen and nitrogen as shown in the fig.6.9, 6.10 and 6.11 respectively. The features at 3000-3700 cm^{-1} and 1300-1800 cm^{-1} in the as-deposited films show that there are significant amounts of water and carbonaceous materials, whose presence was also reported by other authors [171,172]. The spectrum of as-deposited TiO_2 film exhibits a strong, broad absorption band in the region 400-800 cm^{-1}. The presence of a broad band in this region corresponds to the formation of Ti-O and Ti-O-Ti bonds in the solutions and to the development of the titanium dioxide network in the films [173,174].

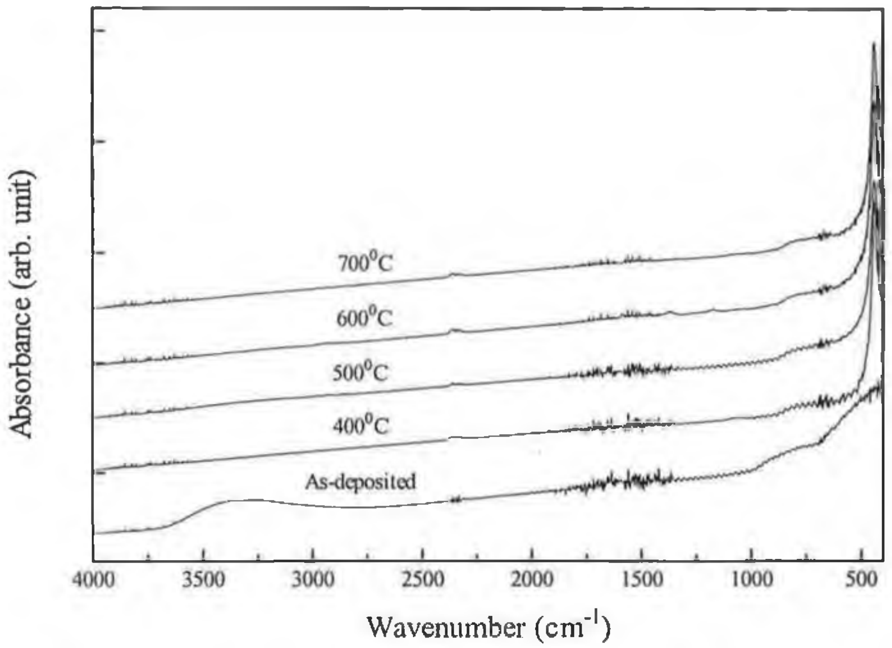

Figure 6.9 The FTIR spectra for TiO_2 films deposited on Si (100) annealed at different temperatures in air.

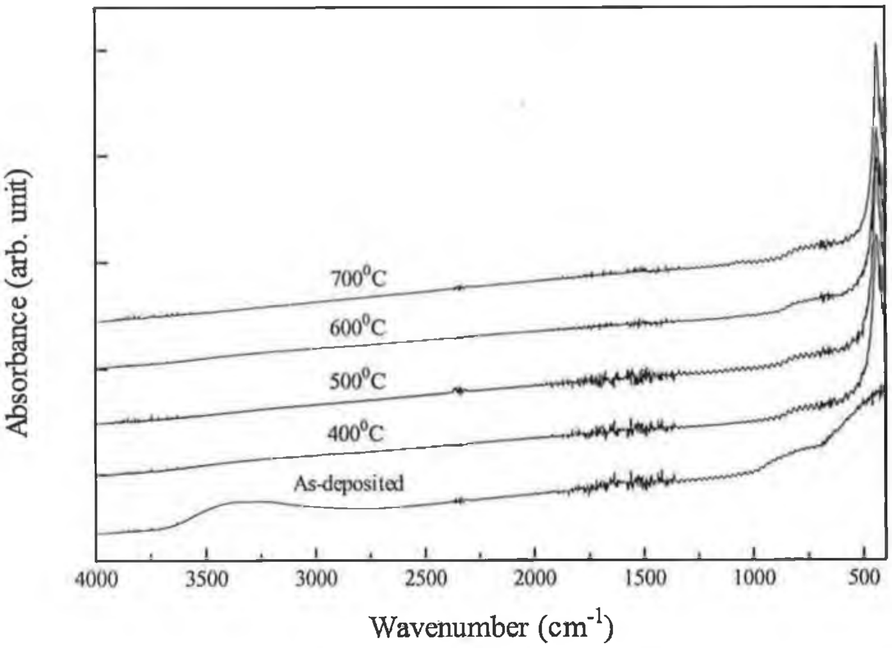

Figure 6.10 The FTIR spectra for TiO_2 films deposited on Si (100) annealed at different temperatures in oxygen.

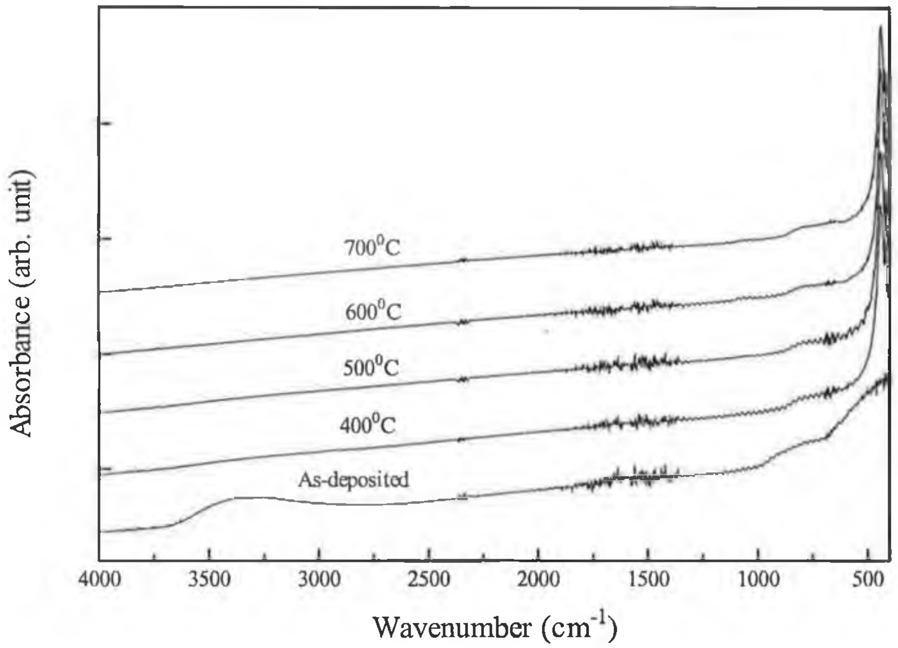

Figure 6.11 The FTIR spectra for TiO_2 films deposited on Si (100) annealed at different temperatures in nitrogen.

The cause of peak broadening related to the Ti-O bond might come from the amorphous nature of TiO_2 thin film due to the incorporation of carbon and/or hydroxyl groups into the Ti-O bond network. Carbon incorporation was detected by XPS analysis. Pronounced changes upon annealing were observed in the absorption bands related to Ti-O-Ti. The broad band between 400-800 cm^{-1} sharpened and increased in intensity with increasing the annealing temperature, corresponding to an increase in the degree of condensation. It was also found that water and its related materials in as-deposited TiO_2 films were diminished after high temperature annealing. The peak at around 2350 cm^{-1} in all FTIR spectra is due to atmospheric absorption. From the FTIR spectra of TiO_2 films in three different atmospheres, we can see that the peak intensity corresponding to the Ti-O bond increases with annealing temperatures in all the cases. So we can conclude that the bonding structure of the TiO_2 films are temperature dependent rather than atmosphere dependent.

Fig. 6.12 shows the variation of full width at half maximum (FWHM) as a function of annealing temperature for the Ti-O-Ti absorption peak from the FTIR spectra annealed in air, oxygen and nitrogen. From the figure, it is seen that the width of the peak for the as-deposited film is very large where there is a sharp decrease in peak width upon annealing at high temperature showing the crystallisation of the films at high temperature.

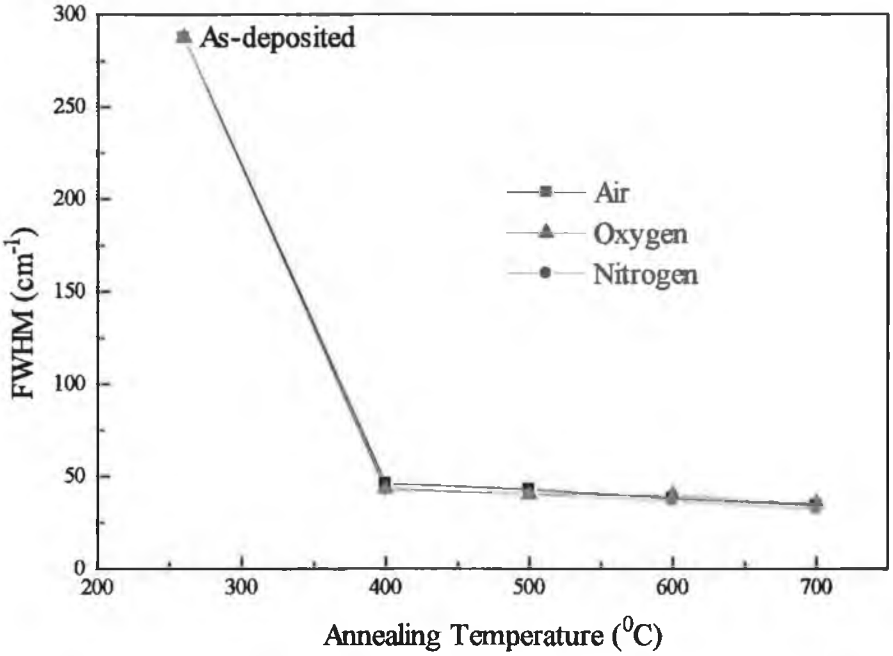

Figure 6.12 Variation of FWHM as a function of annealing temperature for the Ti-O-Ti absorption peak from the FTIR spectra annealed in air, oxygen and nitrogen.

6.2.3.3.2 Raman Spectroscopy

Fig. 6.13, 6.14 and 6.15 show the Raman spectra of a TiO_2/Si structure annealed at different temperatures in air, oxygen and nitrogen respectively. The Raman scattering measurements were made using a 325 nm He-Cd laser. The as-deposited TiO_2 film shows a broad spectrum with some indication of the anatase Raman modes. In the spectrum of the films annealed at 400^0C and higher temperatures, emission bands typical of the anatase form appear at 399, 516 and 640 cm^{-1}. The peak at 640 cm^{-1} is assigned to the anatase E_g mode and the peak at 399 cm^{-1} to the B_{1g} mode of the TiO_2 anatase phase [175]. The peak at 516 cm^{-1} is a doublet of A_{1g} and B_{1g} modes of TiO_2 anatase phase. The features in the spectrum are assigned to the characteristic Raman modes of anatase form [176]. All the spectra show that the intensity of these bands increased upon annealing at higher temperatures. From the Raman spectra of TiO_2 films, it can be concluded that the peak intensities are dependent on the annealing temperatures, not on the atmospheres.

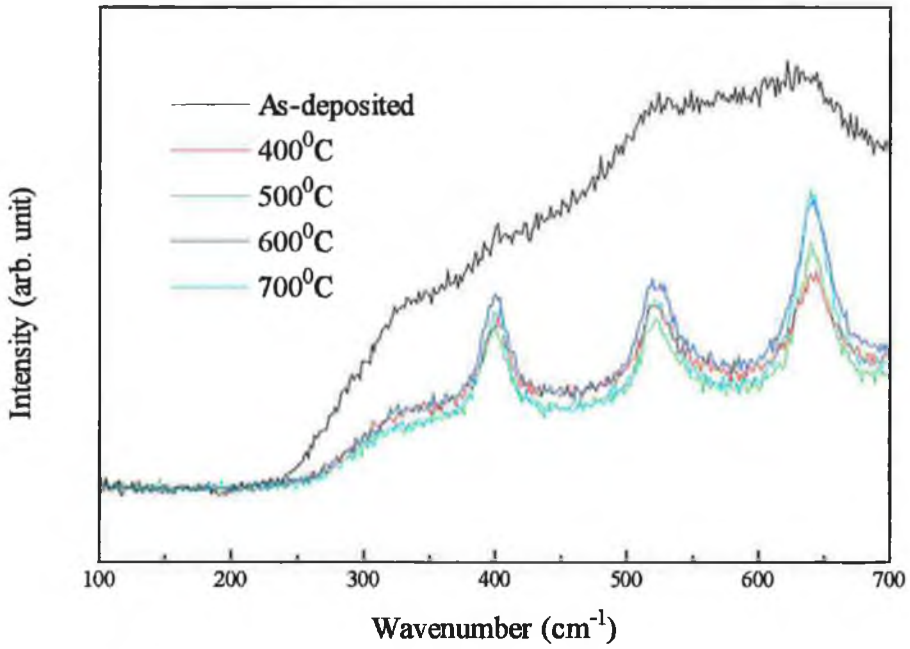

Figure 6.13 Raman spectra for TiO_2 films deposited on Si (100) annealed in air for different temperatures.

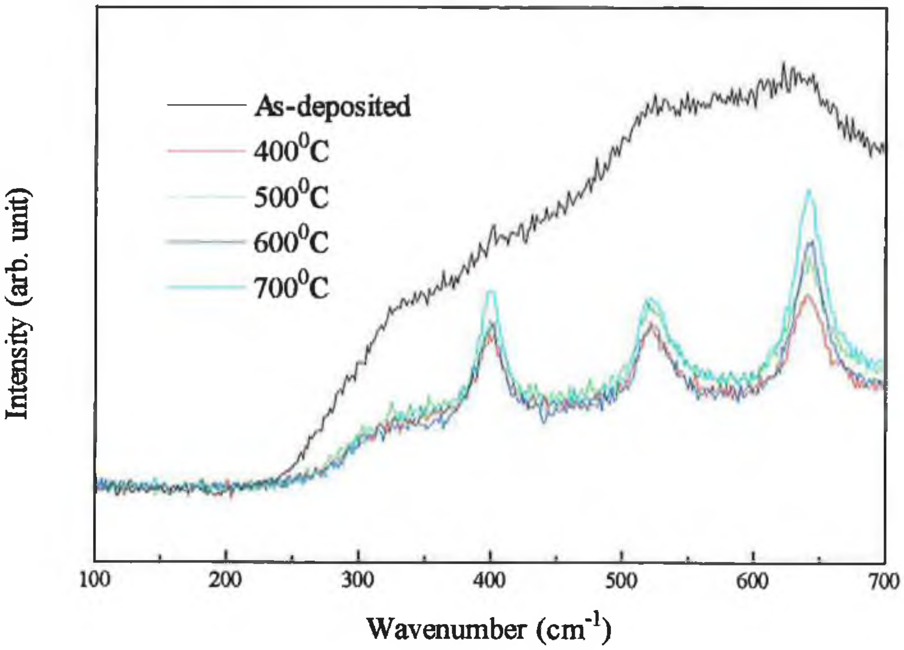

Figure 6.14 Raman spectra for TiO_2 films deposited on Si (100) annealed in oxygen for different temperatures.

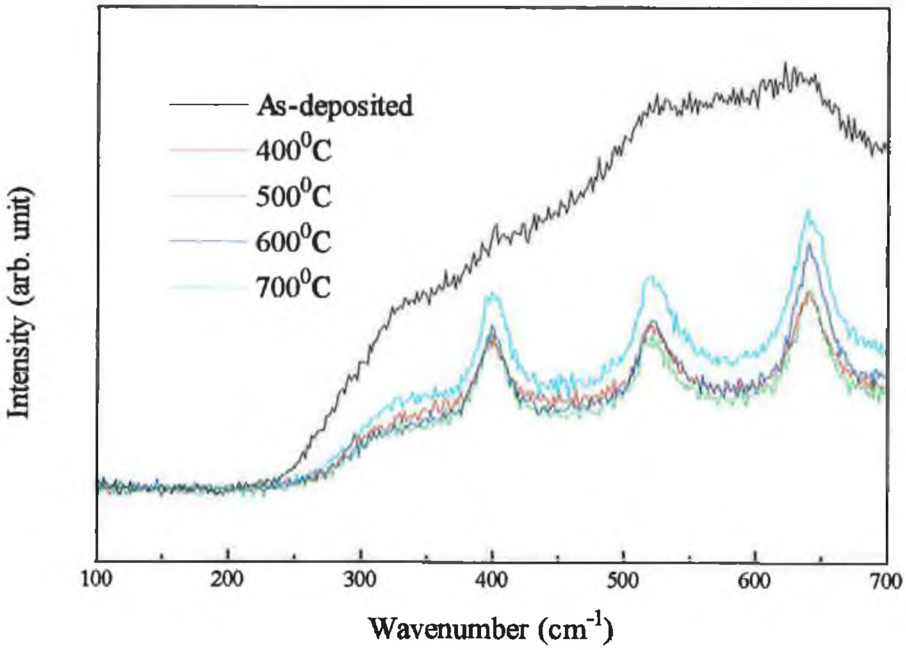

Figure 6.15 Raman spectra for TiO_2 films deposited on Si (100) annealed in nitrogen for different temperatures.

6.2.3.3.3 X-ray Diffraction Spectroscopy

Fig. 6.16, 6.17 and 6.18 show the results of x-ray diffraction employing CuKα radiation for the sample having a TiO_2 layer deposited on silicon substrate annealed at different temperatures. As-deposited TiO_2 films are basically amorphous. However, as the samples are annealed at 400^0C and higher temperature, the structure of as-deposited films is converted from a fully amorphous state to anatase crystalline state, which could be confirmed by the appearance of peaks of (101), (103), (004), (112), (200), (105) and (211) orientation. As is seen from the spectra, the positions of the peaks are in very good agreement with the Joint Committee on Powder Diffraction Standards (JCPDS) database (Card No. 21-1272).

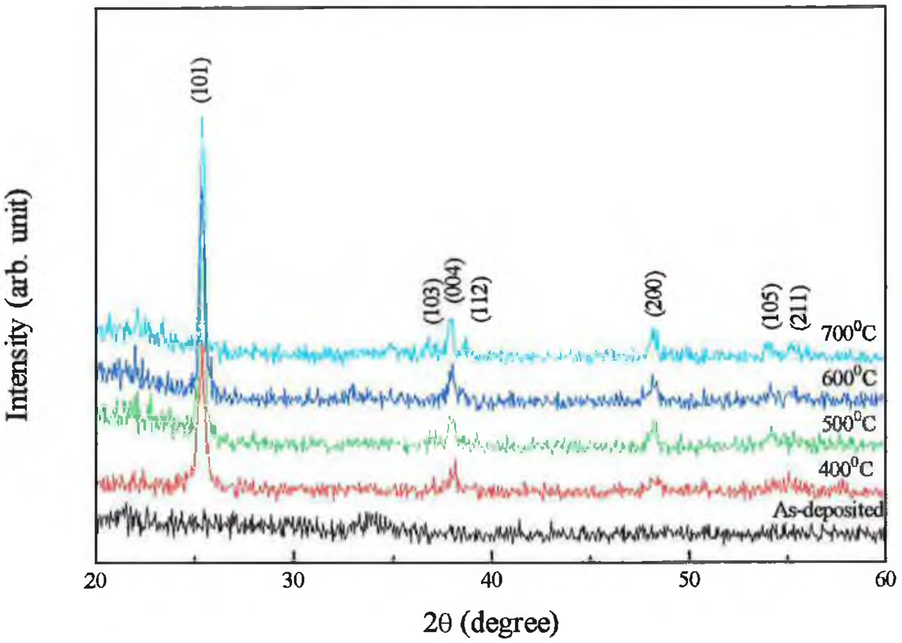

Figure 6.16 XRD spectra for TiO_2 films annealed at different temperatures in presence of air.

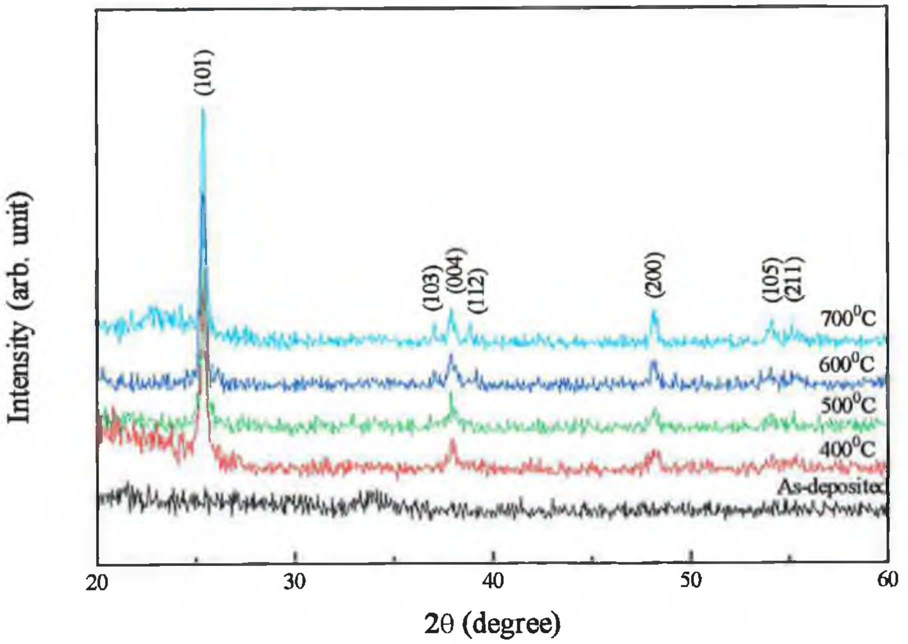

Figure 6.17 XRD spectra for TiO_2 films annealed at different temperatures in presence of oxygen.

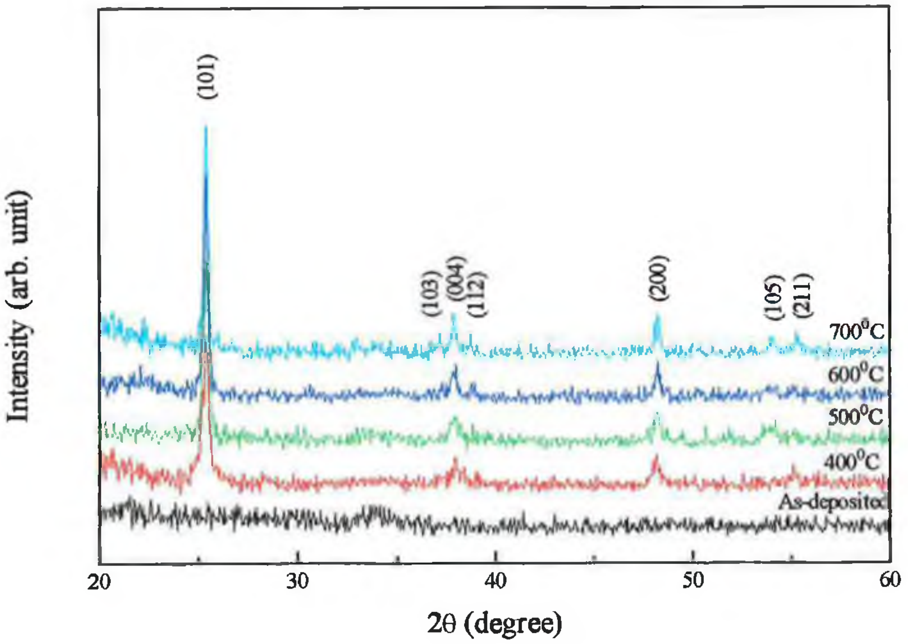

Figure 6.18 XRD spectra for TiO_2 films annealed at different temperatures in presence of nitrogen.

In random orientation the (101)/(004) peak ratio is 5 if we calculate the ratio of the peak intensities from the standard data (See Appendix A). In this work, for the samples annealed at 700^{0}C in all the atmospheres, the (101)/(004) peak ratio is also 5. So we can say that the films are randomly oriented. From the XRD spectra, it is seen that the peak intensities increased with the annealing temperature annealed in air, oxygen and nitrogen. So it can be concluded that the crystallinity of TiO_2 films is improved upon annealing at higher temperatures and the TiO_2 films show the same crystalline state in all the atmospheres indicating that the crystallinity of the films is temperature dependent and not on the atmosphere. X-ray diffraction scans were also carried out for the films deposited on glass substrates and this showed the similar behaviour.

6.2.3.3.4 X-ray Photoelectron Spectroscopy

The XPS spectrum of as-deposited titanium dioxide thin films deposited on a silicon wafer is shown in fig. 6.19. Photoelectron peaks for Ti, O and C were recorded for the TiO_2 film. The Ti $2p_{3/2}$ line is composed of a single peak at a binding energy of 460.66 eV. The separation between the Ti $2p_{3/2}$ and Ti $2p_{1/2}$ peaks is 5.7 eV. The binding energy of the O 1s photoelectron peak is 534 eV. A carbon C 1s peak at a binding energy of 284 eV is also observed on the surface of the film. The presence of this peak is related to surface pollution which corresponds to the fact that the samples were exposed to air before the XPS measurements.

Fig. 6.20 shows the electron spectroscopy for chemical analysis (ESCA) spectrum of the Ti 2p region obtained on the surface of the TiO_2 film. Two pronounced features are observed at binding energies of 460.66 and 466.36 eV, evoked by the Ti $2p_{3/2}$ and Ti $2p_{1/2}$ states respectively. The measured binding energy of the Ti $2p_{3/2}$ peak and the splitting of the doublet (ΔBE=5.7 eV) indicate a +4 titanium oxidation state [177,178]. These results suggest that the coatings have an almost stoichiometric composition ($TiO_{2.00}$).

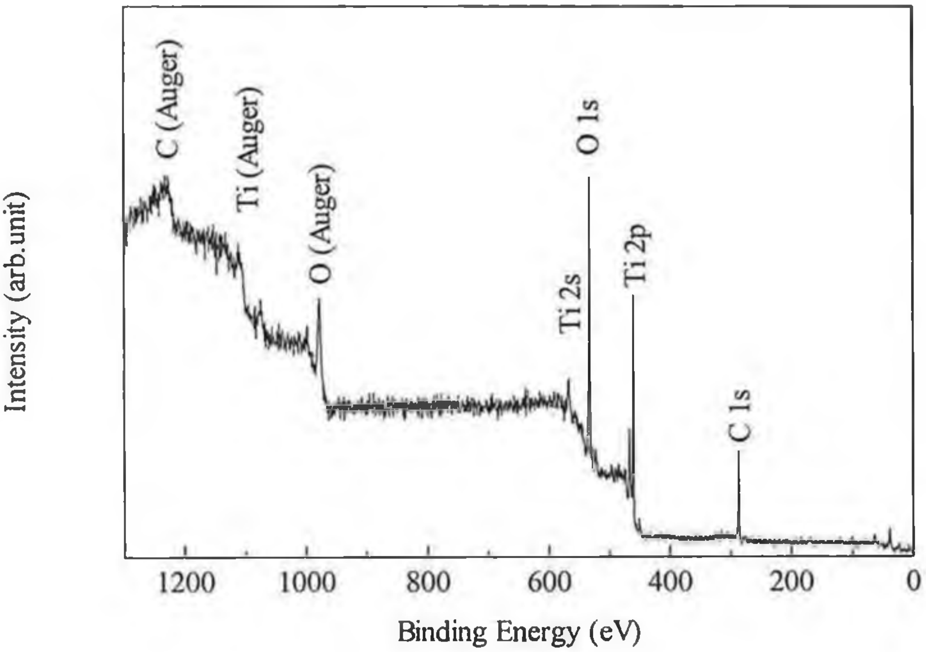

Figure 6.19 XPS spectrum of as-deposited TiO_2 film on silicon.

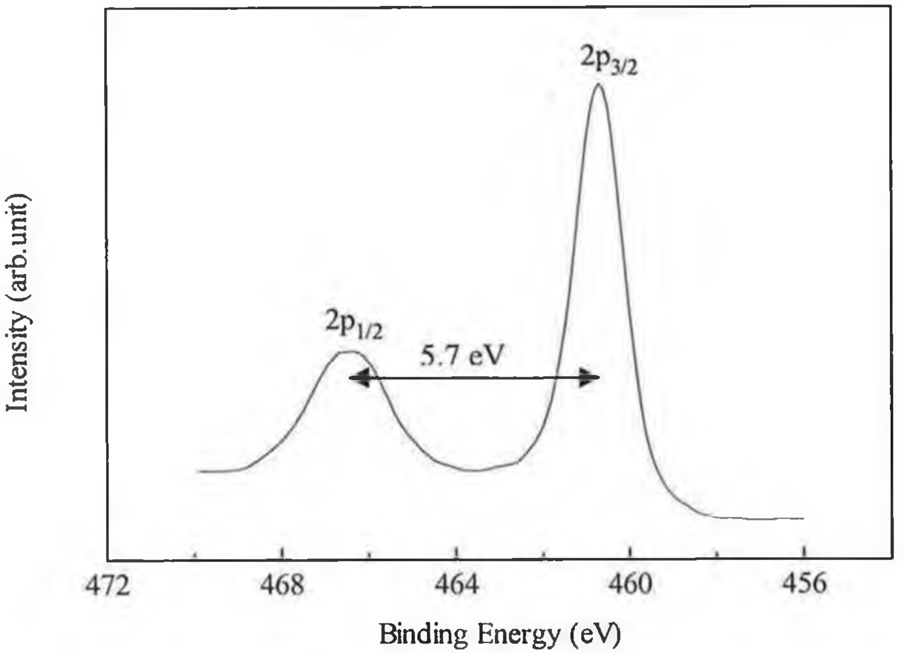

Figure 6.20 ESCA spectrum of the Ti 2p doublet for the as-deposited TiO_2 film.

6.2.3.4 Optical Properties

Fig. 6.21, 6.22 and 6.23 show the optical transmission spectra of TiO_2 thin film with a thickness of approximately 210 nm deposited on glass annealed at various temperatures in air, oxygen and nitrogen respectively. The spectral transmittance was measured in the wavelength range from 200 to 900 nm. The transmission for the as-deposited TiO_2 film is 83% and the maximum transmission rates are 90%, 90.11% and 90.5% annealed at 700^0C in air, oxygen and nitrogen respectively. From the transmission spectra of TiO_2 films, it is seen that the transmission increases with the annealing temperature in all the atmospheres and the atmosphere has no significant affect on the transmission. The oscillations in the spectrum are due to interferences in the TiO_2 film due to reflection at the air-TiO_2 and TiO_2 - glass interfaces.

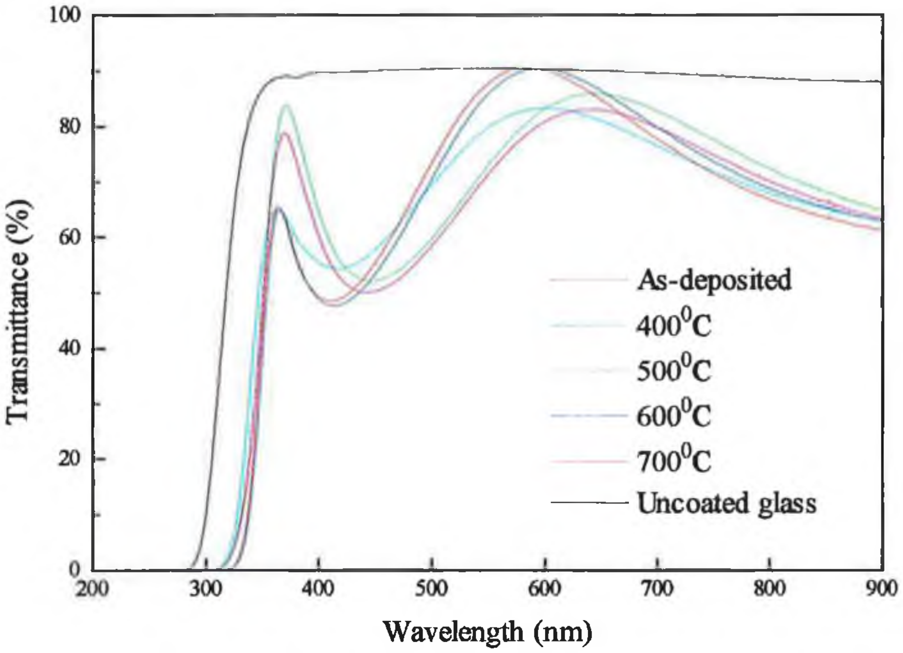

Figure 6.21 Optical transmission spectra for TiO_2 films with a thickness of 210 nm annealed at different temperatures in presence of air.

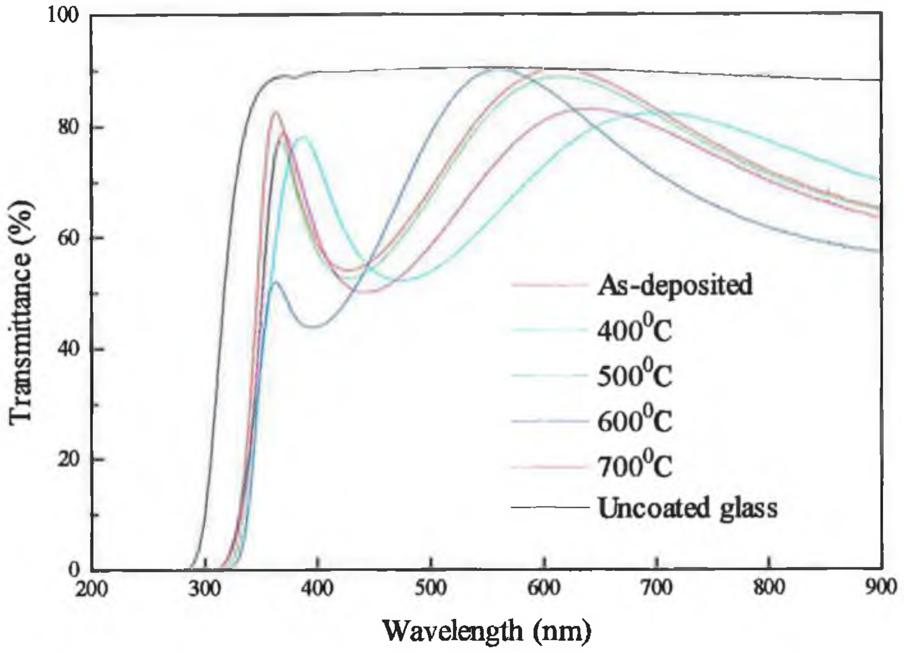

Figure 6.22 Optical transmission spectra for TiO_2 films with a thickness of 210 nm annealed at different temperatures in presence of oxygen.

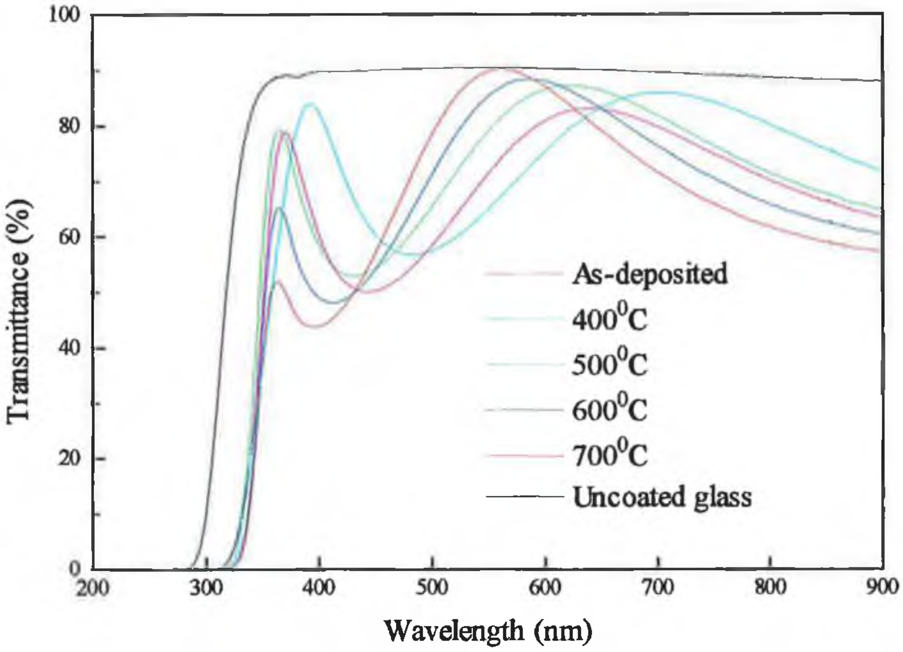

Figure 6.23 Optical transmission spectra for TiO_2 films with a thickness of 210 nm annealed at different temperatures in presence of nitrogen.

The refractive index, n for the TiO_2 films has been calculated from the transmittance vs. wavelength spectra. The square of the refractive index (n^2) is proportional to the dielectric constant of the film. To compare these values with the dielectric constant calculated from the maximum value of capacitance, n^2 is plotted against the annealing temperature for the TiO_2 films annealed in the presence of air, oxygen and nitrogen, shown in fig. 6.24. If we compare this figure with fig. 6.3, we can see that both the figures show the same trend of behaviour.

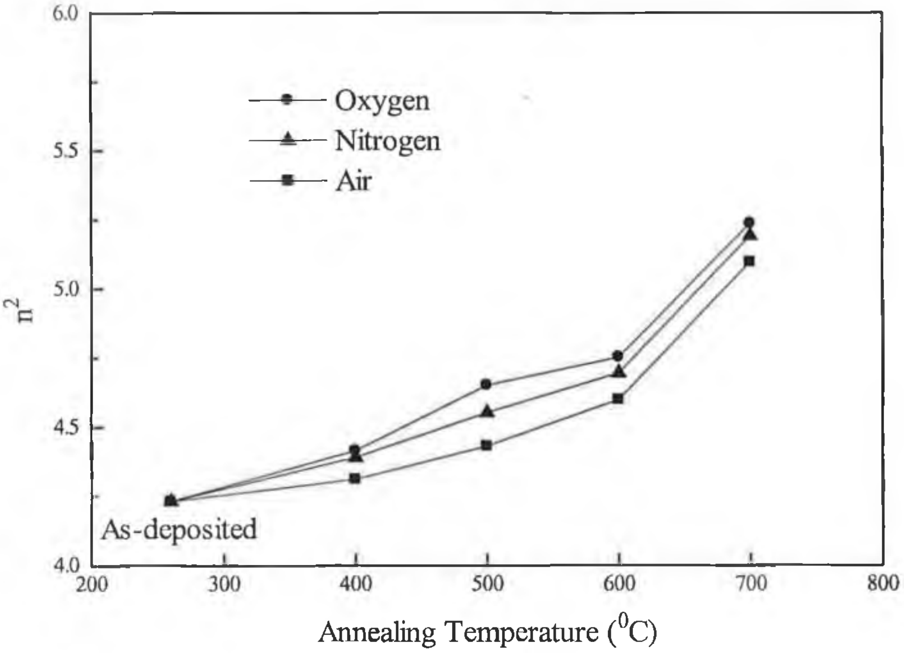

Figure 6.24 Variation of n^2 vs. Temperature for TiO_2 films annealed in air, oxygen and nitrogen.

6.2.4 Conclusions

Titanium dioxide thin films have been successfully deposited by sol-gel process and annealed at different temperatures in the presence of air, oxygen and nitrogen. UV-visible spectroscopy shows that the as-deposited TiO_2 films and the films annealed at high temperatures are transparent. X-ray diffraction spectra show that the as-deposited TiO_2 films are basically amorphous. However, if the films are annealed at high temperature, the structure of as-deposited films is converted from the amorphous state to the anatase crystalline state. From the optical transmission spectra, Fourier transmission infrared spectra, Raman spectra and X-ray diffraction spectra of the TiO_2 films annealed at different temperatures in different atmospheres, it is seen that the optical transmission, bonding structure and the crystallinity of the films depend on the annealing temperature and not on the atmosphere.

XPS analysis has shown that TiO_2 films deposited by sol-gel process are stoichiometric with carbon as the dominant impurity on the surface of the films.

The electrical properties of the as-deposited and annealed TiO_2 thin films were characterised by C-V and I-V measurements. The I-V measurement shows that the leakage current density of the films decreases upon annealing at higher temperatures where this reduction in leakage current density is due to the reduction of the concentration of impurities such as carbon and the reduction of oxygen vacancies in TiO_2 films. The leakage current density for the as-deposited film was 5.0×10^{-5} A/cm^2, where a leakage current density as low as 6.0×10^{-6} A/cm^2 at an electric field of 1 MV/cm can be achieved annealing at 700^0C in presence of oxygen. The leakage currents are 6.6×10^{-6} A/cm^2 and 6.8×10^{-6} A/cm^2 annealed at 700^0C in air and nitrogen respectively, which are higher than that in oxygen.

The dielectric constant obtained from the maximum capacitance of the $Al/TiO_2/Si$ structure under the accumulation condition varies from 75 to 82 for the annealed films deposited by this sol-gel process which is higher than any other conventionally produced TiO_2 films. These results suggest that the deposited TiO_2 thin film can be used as a high permittivity insulator in thin film electroluminescent devices.

6.3 Tantalum oxide (Ta_2O_5) Thin Films Deposited by Sol-gel Process

6.3.1 Introduction

Because of its wide field of applications in semiconductor sciences, tantalum oxide (Ta_2O_5) has been extensively studied both experimentally and theoretically over the past three decades. Tantalum oxide (Ta_2O_5) films show high dielectric constant, low leakage current and high transmittance in the UV visible range, which are interesting characteristics for electrical and optical applications. Some of these applications include antireflecting coatings for silicon solar cells [179], wave guides for light [180], insulating layers in electroluminescent display devices requiring high permittivity [181,182], in electrochromic devices for solid electrolytes [183,184] and also as storage capacitor material for dynamic random access memories (DRAM) [185]. Ta_2O_5 coatings are also used as interference coatings [186] and as protective coatings against corrosion [187,188].

Ta_2O_5 films can be deposited by various techniques, such as chemical vapor deposition (CVD) [189,190], plasma enhanced chemical vapor deposition (PECVD) [191,192], electron beam evaporation [186], ion beam and dual-ion beam sputtering [193,194], reactive r.f. sputtering [180,195], d.c. sputtering [196], pulsed-laser assisted deposition [197], ion-assisted deposition [198], anode oxidation [182] and sol-gel methods [199-201].

Synthesis of dielectric films by sol-gel methods has recently received attention due to many advantages compared to conventional preparation techniques. By this technique, high purity and good homogeneity materials can be prepared utilizing lower processing temperatures and shorter annealing times. Thin films can be deposited by simple and compact equipment through dip or spin coating, enabling high control of the film thickness size and shape, as well as good reproducibility of the stoichiometry.

In this work, we report the preparation of Ta_2O_5 films by the sol-gel dip coating deposition technique and also an investigation of the electrical, optical and structural properties of Ta_2O_5 films annealed at different temperatures in different atmospheres.

6.3.2 Experimental procedure

Tantalum oxide thin films have been prepared on silicon and glass substrates by the sol-gel method as shown in fig. 6.25. The coating solutions were prepared by reacting tantalum ethoxide [$Ta(OC_2H_5)_5$] (Aldrich) with ethanol. The starting solution was prepared by mixing $Ta(OC_2H_5)_5$ with ethanol and acetic acid while stirring for 30 minutes. Ethanol was mixed with acetic acid and stirred for 10 minutes. This solution was mixed with the previous solution and stirred for 18 hours to get a transparent solution.

Tantalum oxide gel films were obtained by dipping the substrates into the solution and pulling them up at 1.2 cm/sec. The tantalum oxide films were subjected to heat-treatment at 260^0C for 10 minutes. The thickness of the film was approximately 60 nm for each dipping. By repeating the above procedure, tantalum oxide films of different thickness were obtained. The above conditions were used for the preparation of Ta_2O_5 films because with these conditions the quality of the films was found to be good. The pulling rates of 1.0 cm/sec. and 1.5 cm/sec. were also used to prepare the thin films of Ta_2O_5. But the films prepared with these speeds were not uniform and they also came off the substrate after high temperature annealing.

6.3.3 Results and Discussion

6.3.3.1 Electrical Properties

Capacitance-voltage (C-V) measurements were performed using the Al/Ta_2O_5/p-Si MIS diode structure to determine the dielectric constant of the Ta_2O_5 layer. The capacitance was measured at a frequency of 1 Mhz at room temperature, while the d.c. bias was swept between +5 and -5 V. A typical C-V curve for one of the as-deposited Al/Ta_2O_5/p-Si samples is shown in fig. 6.26. The insulator capacitance was taken as the maximum capacitance when the MIS diode was in accumulation, i.e. at –5 V bias.

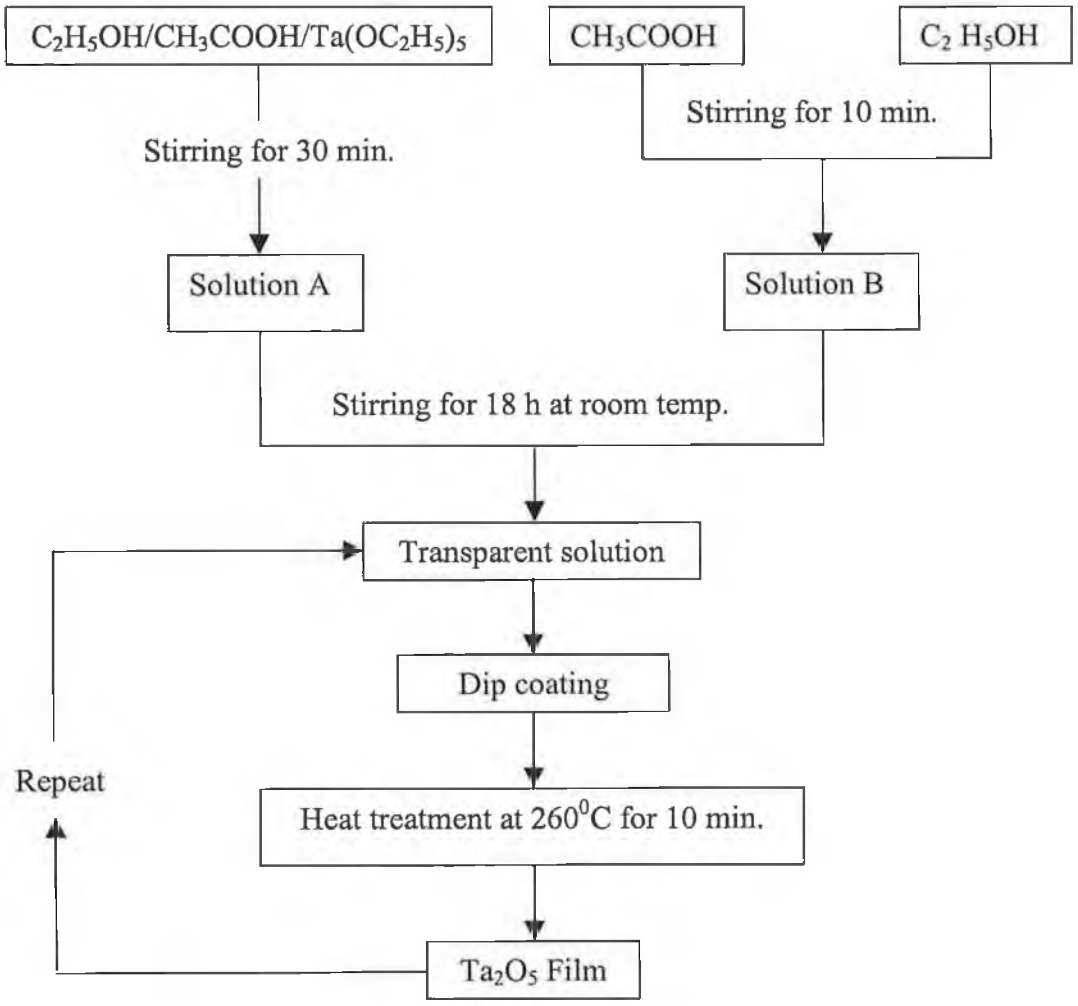

Figure 6.25 Preparation process of tantalum oxide film by sol-gel process.

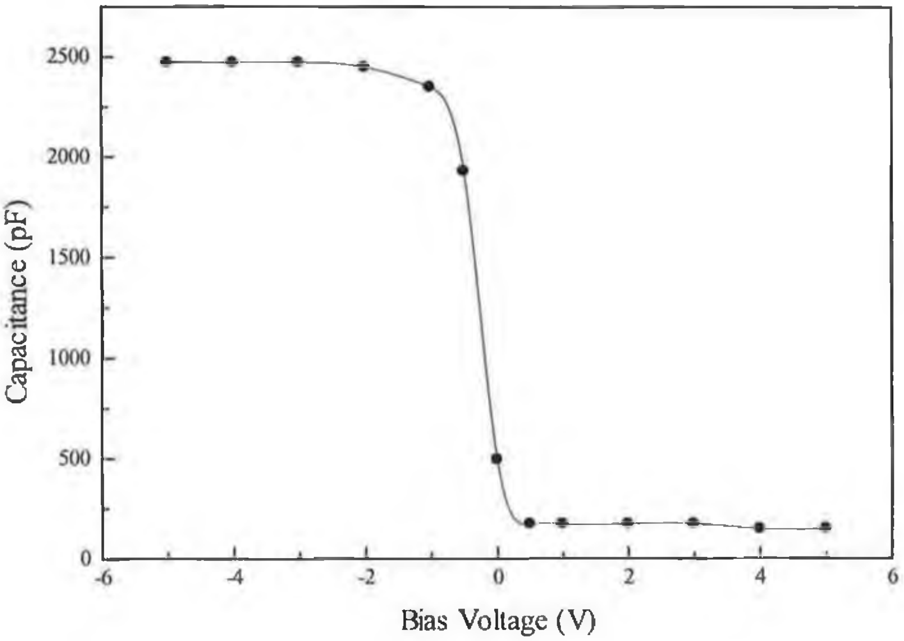

Figure 6.26 Typical capacitance-Voltage characteristics for the as-deposited Al/Ta_2O_5/p-Si sample.

Fig. 6.27 shows the dielectric constant of the Ta_2O_5 films as a function of annealing temperature in air, oxygen and nitrogen. The dielectric constant of the Ta_2O_5 film was calculated from the maximum capacitance and it was found to be approximately 20 for the as-deposited film. From the figure, it is seen that dielectric constant of the films increased upon annealing at higher temperature in all cases and it varies from 37 to 50 annealed at 700^0C in different atmosphere. The reasons for this variation in dielectric constant with annealing temperatue in different atmosphere are thought to be a reduction of defects or oxygen vacancies and better crystallization of Ta_2O_5 films.

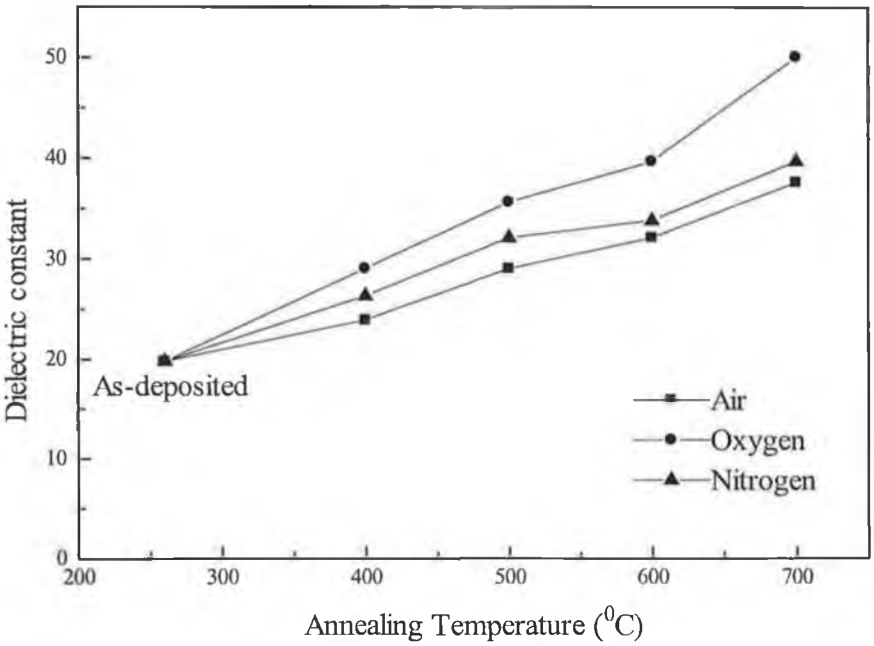

Figure 6.27 Variation of dielectric constants as a function of annealing temperature annealed in air, oxygen and nitrogen for Ta_2O_5 film.

Fig. 6.28, 6.29 and 6.30 show the dependence of the leakage current density on the applied electric field for as-deposited film and annealed films, annealed in air, oxygen and nitrogen respectively. As the applied field increases, the leakage current increases parabolically up to a saturation point at each annealing temperature and the leakage current decreases upon annealing at higher temperatures in all cases. The shape of the curves suggests that the conduction mechanism in these films was via the Fowler-Nordheim (FN) tunneling process [166]. It can be seen that the leakage current for the as-deposited tantalum oxide film for an applied field of 1 MV/cm is $1.0x10^{-5}$ A/cm^2, where the leakage currents are $1.5x10^{-6}$ A/cm^2, $8.0x10^{-7}$ A/cm^2 and $1.2x10^{-6}$ A/cm^2 for the films annealed at 700^{0}C in air, oxygen and nitrogen respectively. The electric breakdown voltage was observed at 3.5 MV/cm.

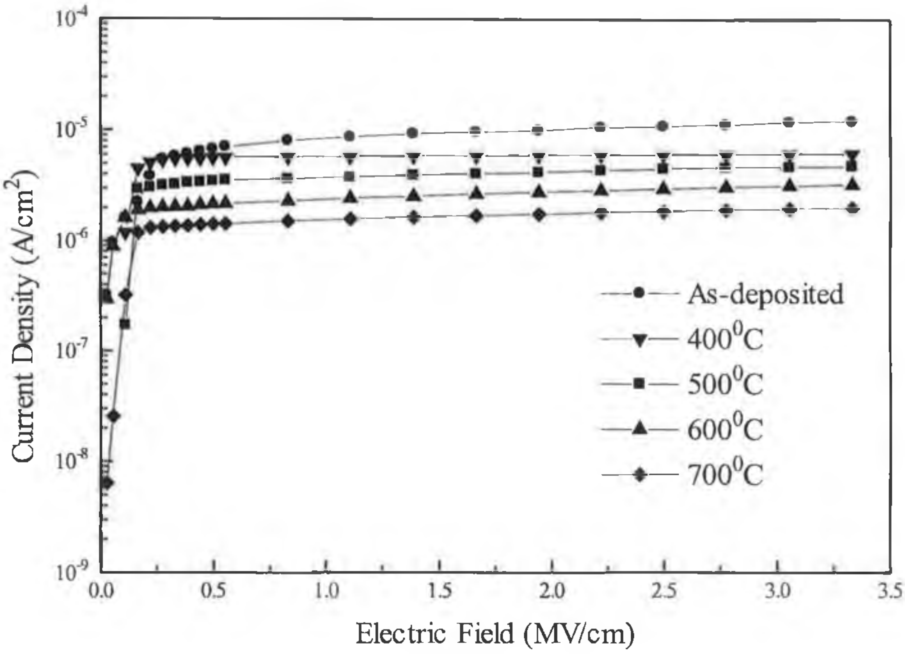

Figure 6.28 Current density vs. electric field characteristics for Ta_2O_5 films annealed at different temperatures in air.

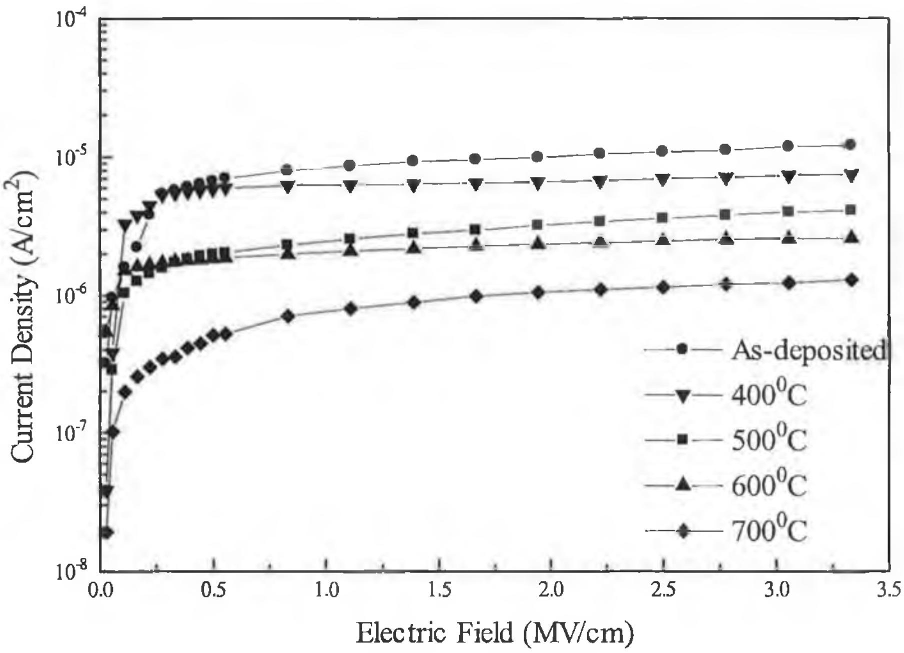

Figure 6.29 Current density vs. electric field characteristics for Ta_2O_5 films annealed at different temperatures in oxygen.

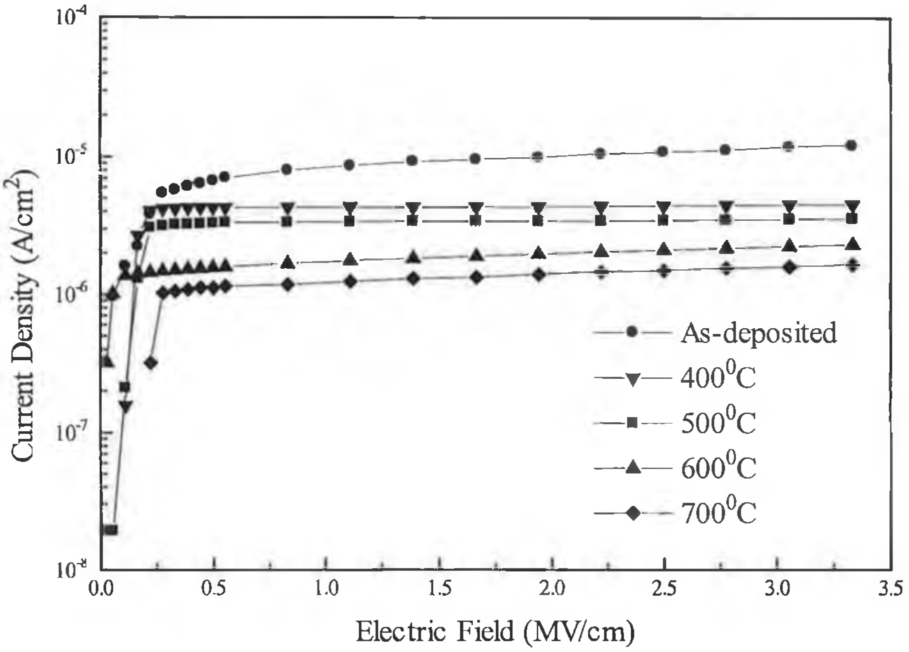

Figure 6.30 Current density vs. electric field characteristics for Ta_2O_5 films annealed at different temperatures in nitrogen.

The high leakage current of as-deposited film might originate from the defects in the as-deposited Al/Ta_2O_5/Si structure. According to the results of XRD and FTIR spectroscopies of as-deposited and annealed films shown later, the decrease of the leakage current after high temperature annealing could be attributed to the crystallization and densification of the as-deposited Ta_2O_5 film. During annealing, oxygen atoms are diffused into the Ta_2O_5 film. The diffused oxygen inside tantalum oxide reduces the possible oxygen deficiency and causes the carbon and hydrogen impurities to oxidize [202]. These impurities are unintentionally introduced into the oxide film during processing and annealing. This causes the trap concentration to be reduced. Upon annealing at higher temperatures, decreasing the concentration of oxygen atom vacancies as well as the growth of an interfacial silicon dioxide layer between Ta_2O_5 and the silicon substrate cause the decrease of the leakage current.

Fig. 6.31 shows the variation of resistivity of Ta_2O_5 films as a function of annealing temperature in air, oxygen and nitrogen. The resistivities, ρ, of the films were calculated from the I-V data [I=V/R and ρ=(V.A)/(I.t), where A is the area of Al contact and t is the thickness of the film]. From the figure, it is seen that the resistivity increases with the annealing temperature. The resistivities are measured for an electric field of 1 MV/cm. The as-deposited films have a resistivity of 1.30×10^{11} Ω-cm and the resistivities for 700^0C annealed films are 7.09×10^{11} Ω-cm, 1.39×10^{12} Ω-cm and 8.95×10^{11} Ω-cm annealed in presence of air, oxygen and nitrogen respectively. Annealing results suggests that native defects such as Ta and O_2 vacancies and impurities such as carbon present in Ta_2O_5 out diffuses as an effect of annealing, resulting in improved film quality.

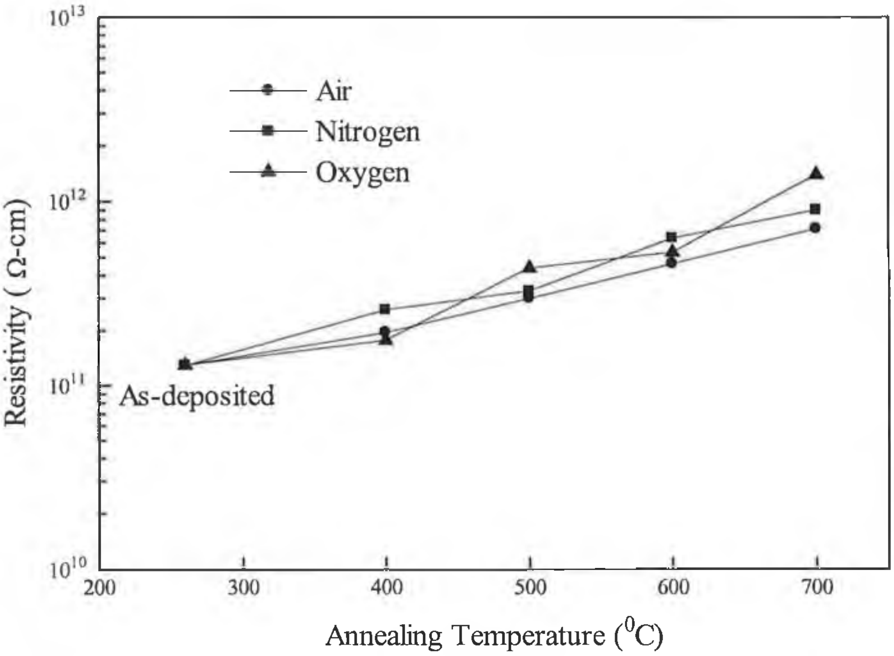

Figure 6.31 Resistivity of Ta_2O_5 films as a function of annealing temperature in air, oxygen and nitrogen.

6.3.3.2 Roughness

The average roughness (R_a) values were measured for Ta_2O_5 thin films annealed at different temperatures in the presence of air, oxygen and nitrogen. Fig. 6.32 shows the variation of R_a with annealing temperature. Roughness of the substrate was measured to be 0.01 μm and for the as-deposited film 0.02 μm. A small change in R_a was observed with varying the temperature due to the crystallization effect. Variations in roughness are of the same order as the measurement resolution. No real conclusions can be drawn except that the roughness is not more than 0.02 μm.

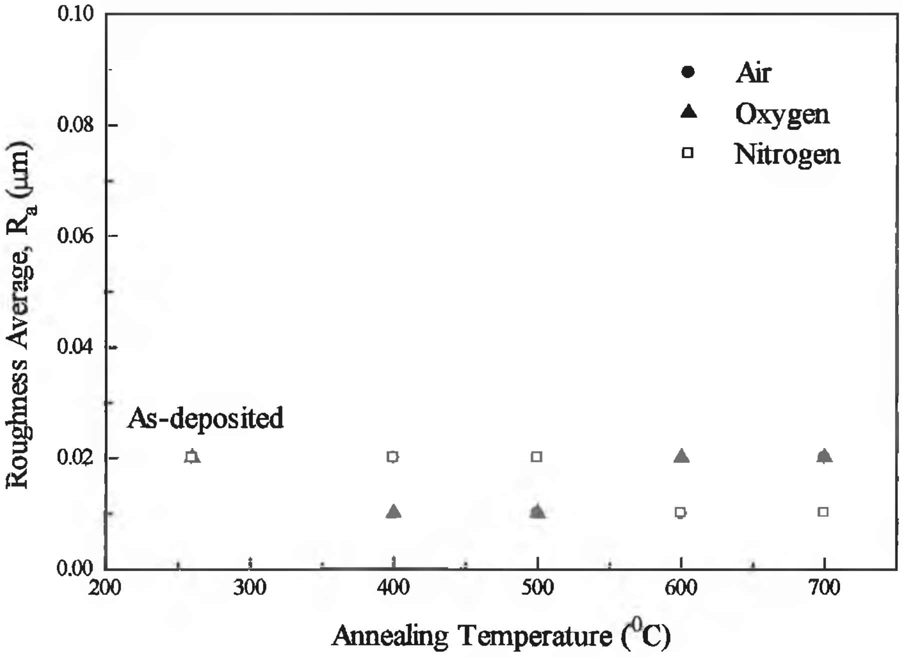

Figure 6.32 Variation of Roughness as a function of annealing temperature annealed in air, oxygen and nitrogen for Ta_2O_5 film.

6.3.3.3 Structural Properties

6.3.3.3.1 Fourier Transform Infrared (FTIR) Spectroscopy

Fig. 6.33, 6.34 and 6.35 show the FTIR spectra in the wavenumber range from 400 to 4000 cm^{-1} for as-deposited films and films annealed at different temperatures in presence of air, oxygen and nitrogen respectively. The broad absorption peak in the wavenumber range between 400 to 800 cm^{-1} corresponding to Ta-O-Ta and Ta-O stretching vibrational modes are observed annealed at all temperatures indicating the formation of Ta_2O_5. The cause of peak broadening related to the Ta-O-Ta and Ta-O bonds might come from the amorphous nature of Ta_2O_5 films. The Ta_2O_5 films annealed at 700^{0}C in air, oxygen and nitrogen show a narrow absorbance peak around at 530 cm^{-1} indicating the formation of crystallized structure. There is a slight absorption around 1300-1800 cm^{-1} due to the C-H vibration in the unannealed alkoxy group. The broad band at 3000-3700 cm^{-1} in the as-deposited films corresponds to the stretching vibration of O-H, indicating the presence of H_2O and O-H group in the films. The O-H and water groups were completely removed from the films after high temperature annealing. The peak at around 2350 cm^{-1} in all FTIR spectra is due to atmospheric absorption.

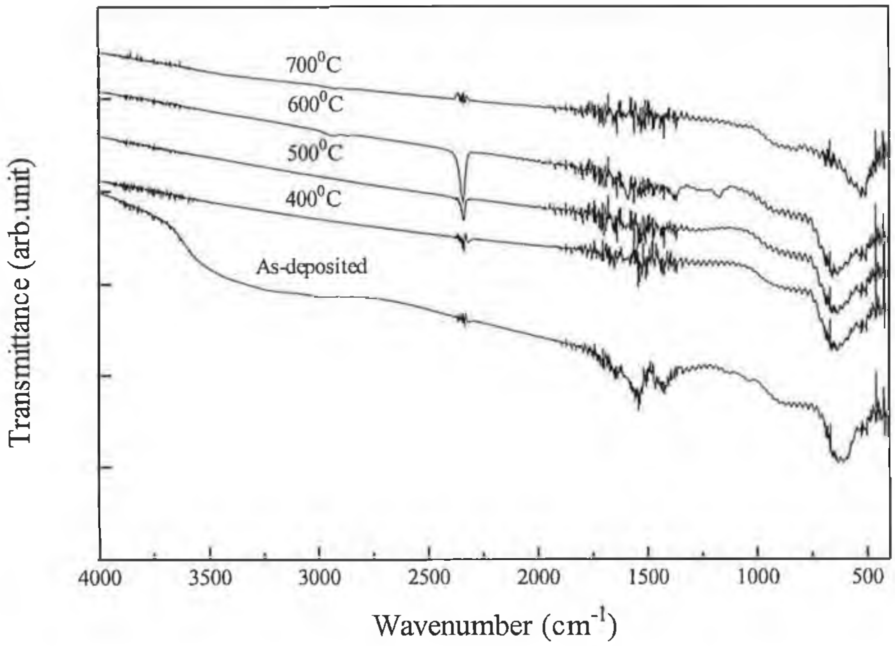

Figure 6.33 The FTIR spectra for Ta_2O_5 films deposited on Si (100) annealed at different temperatures in air.

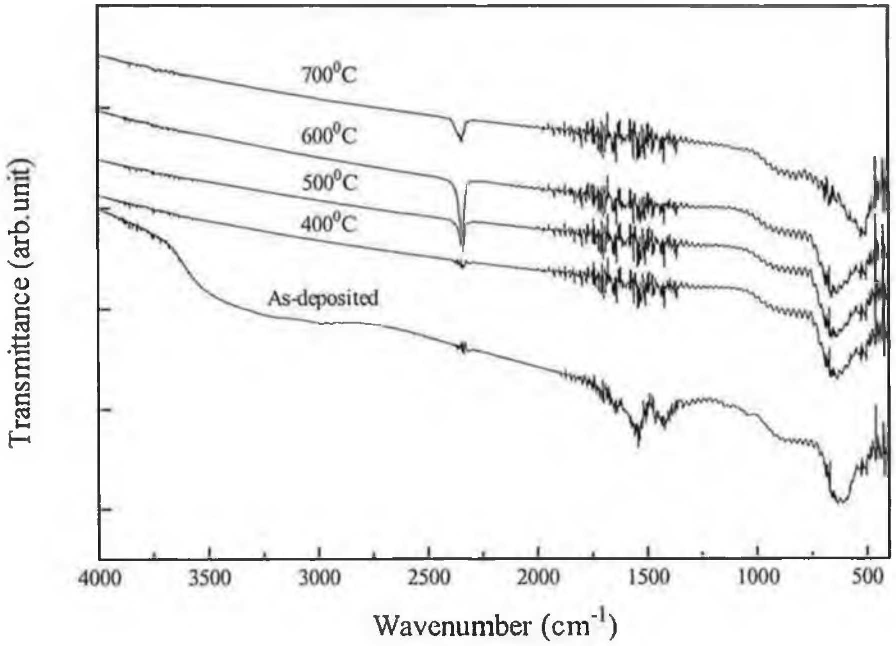

Figure 6.34 The FTIR spectra for Ta_2O_5 films deposited on Si (100) annealed at different temperatures in oxygen.

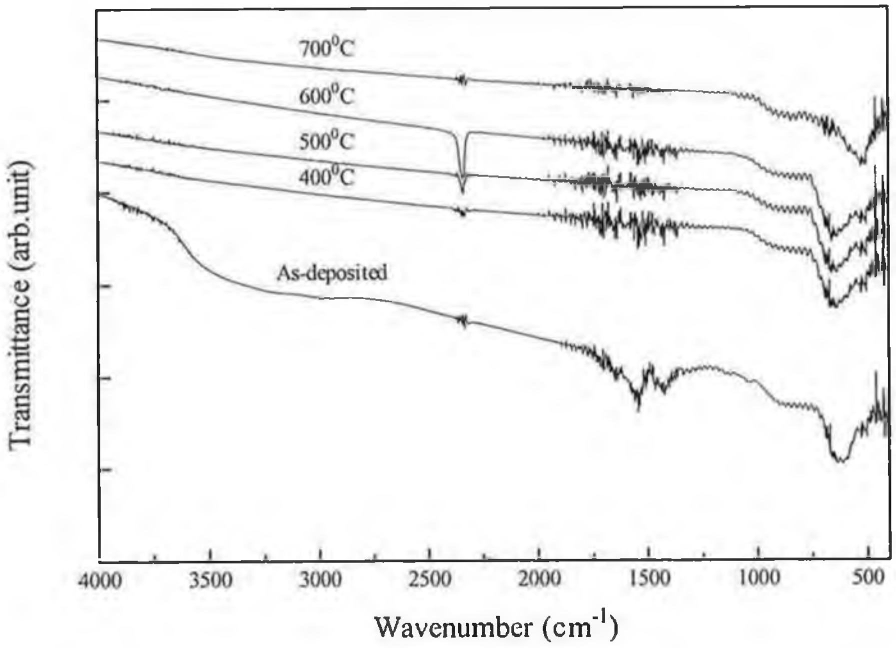

Figure 6.35 The FTIR spectra for Ta_2O_5 films deposited on Si (100) annealed at different temperatures in nitrogen.

6.3.3.3.2 X-ray Diffraction Spectroscopy

Fig. 6.36, 6.37 and 6.38 show the X-ray diffraction patterns for the Ta_2O_5 films annealed at different temperatures in air, oxygen and nitrogen respectively. All the XRD spectra show that as-deposited films and films annealed at 400, 500 and 600^0C are amorphous while annealing at 700^0C crystallization process take place, indicating sharp and intensive peaks. As is seen from the XRD spectra for the three cases, all the diffraction peaks agree well with the orthorombic crystal structure confirming the formation of Ta_2O_5 films according to the database (Card No. 25-0922) of the Joint Committee on Powder Diffraction Standards (JCPDS).

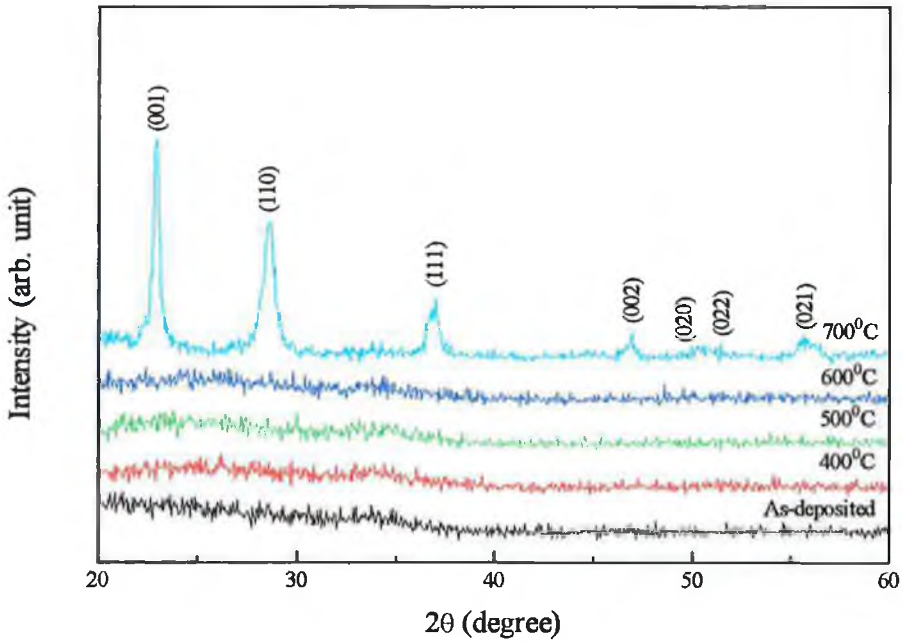

Figure 6.36 XRD spectra for Ta_2O_5 films annealed at different temperatures in presence of air.

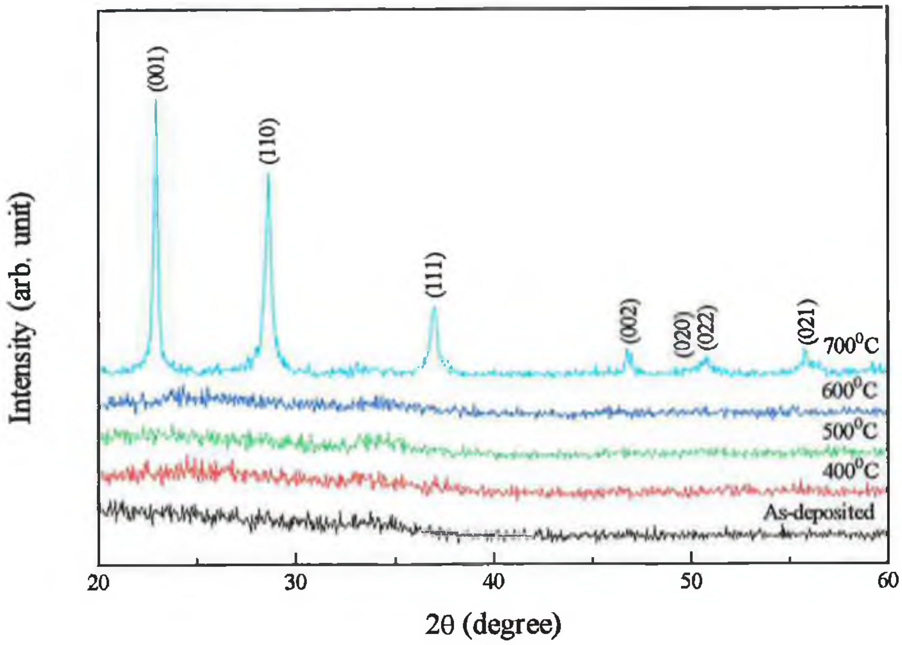

Figure 6.37 XRD spectra for Ta_2O_5 films annealed at different temperatures in presence of oxygen.

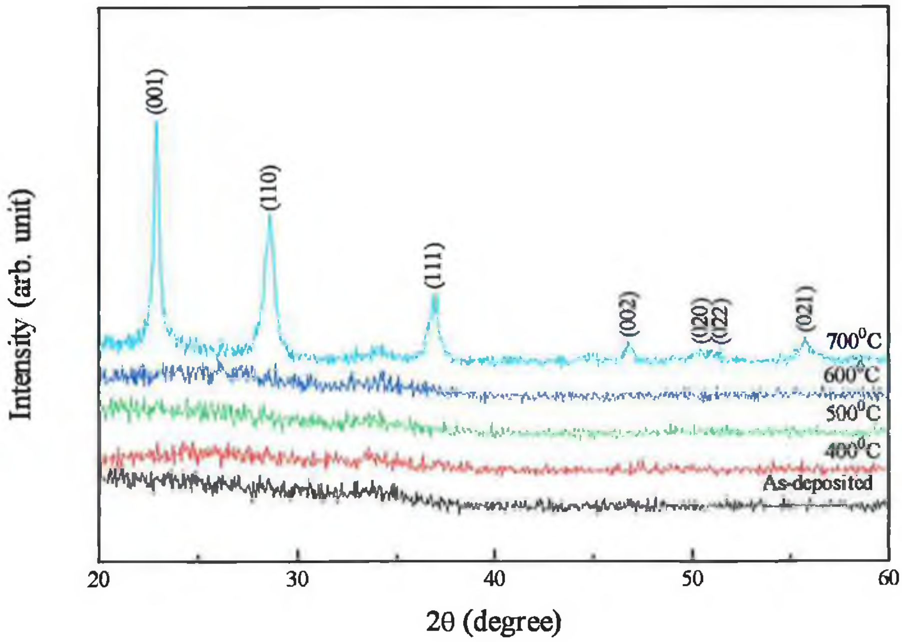

Figure 6.38 XRD spectra for Ta_2O_5 films annealed at different temperatures in presence of nitrogen.

In random orientation the (001)/(110) peak ratio is 0.85 if we calculate the ratio of the peak intensities from the standard data (See Appendix A). In this work, for the samples annealed at 700^0C in all the atmospheres, the (001)/(110) peak ratio is 1.35. So we can say that the films annealed at 700^0C in all the atmospheres have the preferential orientation of [001] parallel to the substrate. From the X-ray diffraction spectra of Ta_2O_5 films annealed in different atmospheres, it is seen that the as-deposited films and the films annealed up to 600^0C in all the atmospheres are amorphous and the films are crystallized at 700^0C showing the same peaks in all the atmospheres. So it can be concluded that the crystallinity of Ta_2O_5 films is dependent as temperature not atmosphere. X-ray diffraction scan was also carried out for the films deposited on glass substrates, which showed the similar crystal structure.

6.3.3.4 Optical Properties

Fig. 6.39, 6.40 and 6.41 show the optical transmission spectra of the Ta_2O_5 films with a thickness of 300 nm annealed at different temperatures in air, oxygen and nitrogen respectively. The films have an average optical transparency up to 90%. The oscillations on the spectrum are due to the film thickness and the consequent interference in the layer. The optical transmission of Ta_2O_5 films in the visible region improves with annealing at higher temperature showing maximum transmittance of 80% for as-deposited films and 88.30%, 89.97% and 90.50% when annealed at 700^0C in air, oxygen and nitrogen respectively. From the optical transmission spectra of the Ta_2O_5 films, it is seen that the optical transmission of the films increases with the annealing temperatures but it does not vary significantly with the atmosphere.

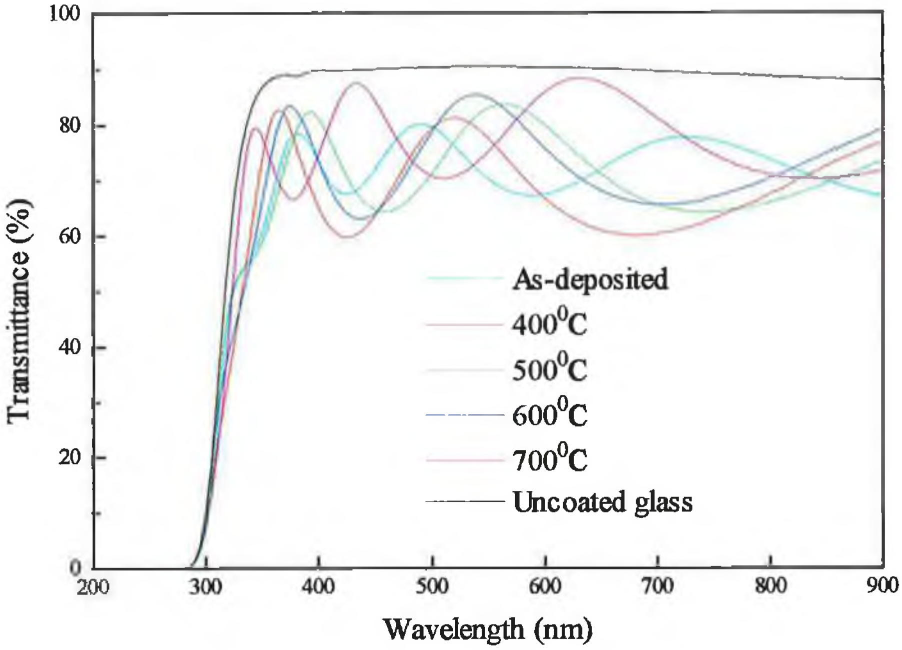

Figure 6.39 Optical transmission spectra for Ta_2O_5 films with a thickness of 300 nm annealed at different temperatures in presence of air.

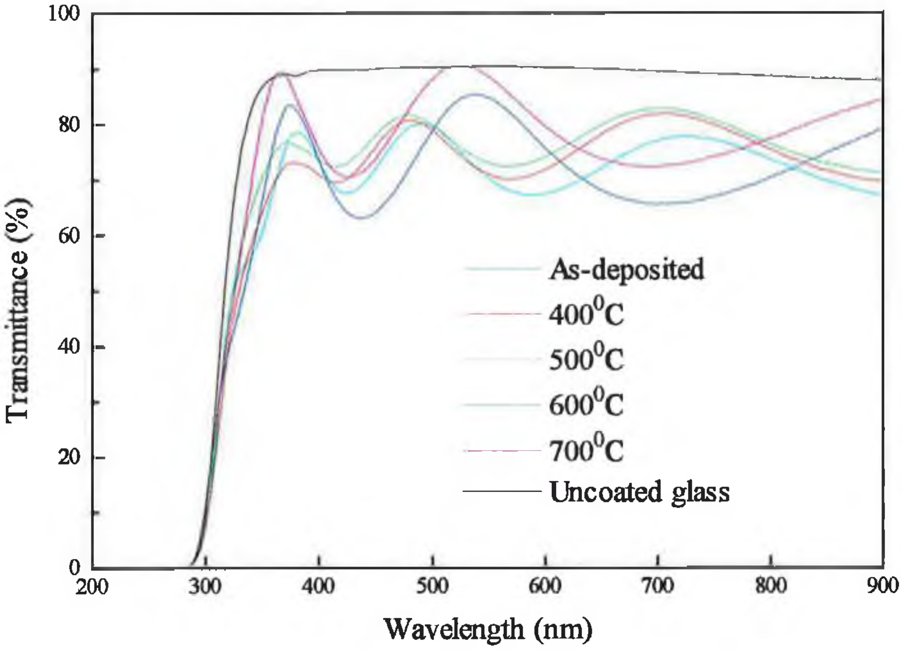

Figure 6.40 Optical transmission spectra for Ta_2O_5 films with a thickness of 300 nm annealed at different temperatures in presence of oxygen.

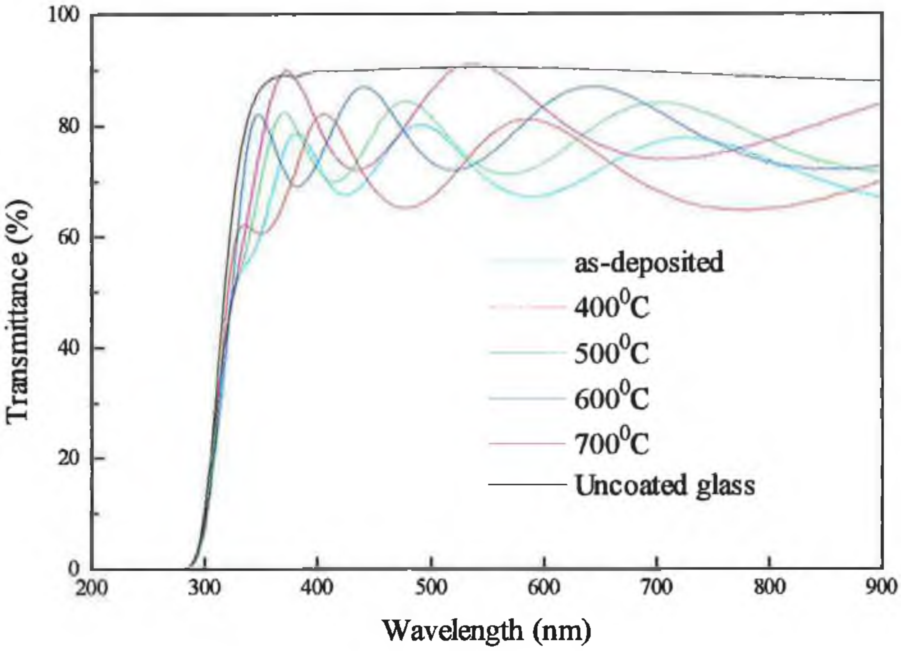

Figure 6.41 Optical transmission spectra for Ta_2O_5 films with a thickness of 300 nm annealed at different temperatures in presence of nitrogen.

The refractive index, n for the Ta_2O_5 films has been calculated from the transmittance vs. wavelength spectra. The square of the refractive index (n^2) is proportional to the dielectric constant of the film. To compare these values with the dielectric constant calculated from the maximum value of capacitance, n^2 is plotted against the annealing temperature for the Ta_2O_5 films annealed in the presence of air, oxygen and nitrogen, shown in fig. 6.42. If we compare this figure with fig. 6.27, we can see that both the figures show the same trend of behaviour.

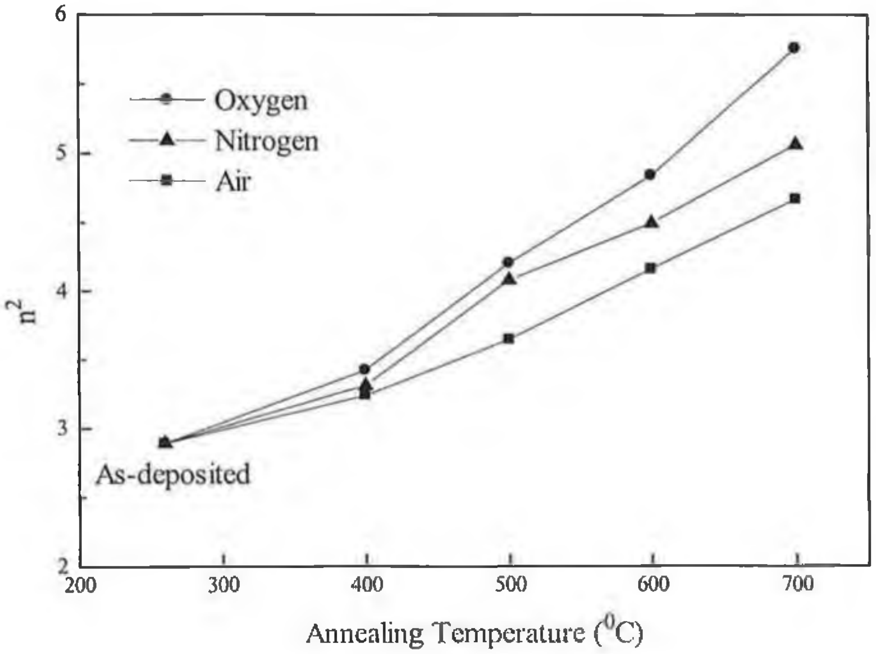

Figure 6.42 Variation of n^2 vs. Temperature for Ta_2O_5 films annealed in air, oxygen and nitrogen.

6.3.4 Conclusions

Tantalum oxide thin films have been prepared by sol-gel dip coating technique on bare Si (100) and glass substrates and annealed at different temperatures in the range 400-700^{0}C in the presence of air, oxygen and nitrogen.

An optical transmittance of around 90% in the visible region of the spectrum was obtained for the films annealed at different temperatures. Optical transmission spectra of the Ta_2O_5 films show that the optical transmission of the films increases with the annealing temperatures indicating that it depends on the temperature not on the atmosphere.

X-ray diffraction analysis shows that the as-deposited films and the films annealed up to 600^0C are amorphous, whereas the films are crystallized when annealed at 700^0C leading to the formation of orthorhombic β-Ta_2O_5 crystalline structures. X-ray diffraction spectra of the Ta_2O_5 films annealed at different temperatures in different atmospheres show that the crystallinity of the films depends on the temperature not on the atmosphere.

Current-voltage (I-V) and dielectric characteristics of Ta_2O_5 films exhibited a strong annealing temperature dependency. The leakage current density for the as-deposited film was $1.0\text{x}10^{-5}$ A/cm^2, whereas a leakage current density as low as $8.0\text{x}10^{-7}$ A/cm^2 at an electric field of 1 MV/cm can be achieved annealing at 700^0C in the presence of oxygen. The leakage currents are $1.5\text{x}10^{-6}$ A/cm^2 and $1.2\text{x}10^{-6}$ A/cm^2 annealed at 700^0C in air and nitrogen respectively, which are higher than that in oxygen.

The dielectric constant of the as-deposited Ta_2O_5 film is estimated to be about 20 and varies from 37 to 50 depending on annealing temperature in different atmosphere. Thus, the electrical, optical and structural properties of Ta_2O_5 thin films produced by this sol-gel technique are suitable for the use of this material as a high permittivity insulator in thin film electroluminescent display devices.

Chapter 7

TRANSPARENT CONDUCTING MATERIALS

7.1 Introduction

Studies of transparent and highly conducting oxide films have attracted the attention of many research workers due to their wide range of applications both in industry and in research. Transparent and conductive layers of some metallic oxides, such as cadmium oxide, tin oxide, indium oxide and zinc oxide, have been known for a long time. Thin films of cadmium oxide (CdO) were first reported by Badeker [203] in 1907, who prepared these films by thermal oxidation of sputtered films of cadmium. These films were reported to be transparent as well as conductive.

Wide-ranging applications of these coatings in electronic devices have generated interest in research related to the growth and characterization of these materials. Such films have demonstrated their utility as transparent electrical heaters for windscreens in the aircraft industry. The high transparency of these materials in the solar spectrum, together with their high reflectivity in their infrared, makes them very attractive for use as transparent heat reflecting materials. Such spectrally selective films have wide applications in window insulation and thermal insulation in lamps [204-206].

There has been considerable interest in recent years directed towards the development of conducting transparent oxide-based solar cells [207-210]. These oxides offer the possibility of fabrication of low-cost solar cells with performance characteristics suitable for large-scale terrestrial applications. Transparent conducting oxides are particularly effective in solar cell applications because of the following advantages: (a) the conducting transparent film permits the transmission of solar radiation directly to the active region with little or no attenuation; (b) ease of fabrication of the junction because of lower junction formation temperatures; and (c) these transparent conducting films can serve simultaneously as a low resistance contact to the junction and as an antireflection coating for the active region.

Transparent conducting oxide films can be used as gas sensors [211,212]. The use of these films as gas sensors is based on the fact that the conductance changes in semiconductor materials are large and are caused primarily by changes in carrier concentrations due to charge exchange with the species adsorbed from the gas phase. This variation in conductance with active gas pressure made conducting materials attractive for the fabrication of gas sensing electronic transducers.

Transparent conducting oxide films can also be used as protective coatings, such as, abrasion-resistant coatings and corrosion-resistant coatings. It has been reported [213-215] that the application of a metallic oxide coating on glass containers appreciably reduces the coefficient of friction of the glass surfaces, facilitating the movement of containers through high-speed fitting lines. Metallic films which are used in thin film magnetic recording do not have adequate mechanical durability and corrosion resistance and are normally overcoated with protective films in order to improve their reliability. Tin oxide has been used for overcoating metallic films in magnetic recording media [216]. Such overcoated metallic films have low static friction and good lifetimes.

Transparent conducting oxide coatings have been extensively used as transparent electrodes in various display devices, e.g. liquid crystal displays (LCD), electroluminescent (EL) devices, image sensors based on amorphous silicon, light emitting diodes (LED), etc. [217-219].

In addition to these main applications, transparent conducting films are now being used in a variety of other applications, such as, the production of heating layers for protecting vehicle windscreens from freezing and misting over [220], optical waveguide based electro-optic modulators [221], the photocathode in photoelectrochemical cells [222] and antistatic surface layers on temperature control coatings in orbiting satellites [223].

Thin film electroluminescent devices require a top and bottom electrode, one of which must be transparent. The most common transparent electrodes used are SnO_2, In_2O_3, In_2O_3:Sn, ZnO and ZnO: (Al, In, Ga) etc. Transparent layers should have high transmittance and high conductivity.

This chapter describes the preparation and properties of the transparent conductive oxide films used in this study.

7.2 Preparation and properties of transparent conductive aluminum-doped zinc oxide thin films deposited by sol-gel process

7.2.1 Introduction

Numerous electrically conductive oxides have been discovered and extensively investigated. Of these, indium tin oxide (ITO) and ZnO are well known for their transparency when made into thin films and are expected to find wide use as transparent electrodes for many devices, such as electrochromic displays (ECDs), liquid crystal displays (LCDs) and solar cells [224]. The performances of these devices are greatly dependent on the properties of the electrodes; thus it is very important to improve the manufacturing process and the properties of the transparent electrodes. ZnO thin films with suitable dopants are also used as photoconductors in electrography [225], varistors in ceramic technology [226], and sensor elements in sensing combustible gases [227]. They also exhibit piezoelectric properties, which are used in various pressure transducers and acousto-optic devices, surface and bulk acoustic wave devices [228,229].

Thin films based on oxides of Zn, Cd, In, Sn and mixtures of these, can combine transmittance of luminous radiation with infrared reflectance and electrical conductance. Among these, ZnO-based films have the following advantages:

(i) they consist of cheap and abundant elements, which may be contrasted with the more expensive In-containing films;

(ii) they are non-toxic, whereas Cd-containing films have potential health hazards;

(iii) they are readily produced by the sol-gel process, which is currently preferred for large-scale architectural coatings;

(iv) they allow tailoring of the ultraviolet absorption, which is possible because the fundamental band gap of ZnO (~3.3 eV) lies just at the end of the luminous spectrum [25]; and

(v) they show stability in hydrogen plasmas, which is of prime importance in amorphous and microcrystalline silicon related fields, whereas tin oxide and indium oxide reduce to metallic forms when exposed to a hydrogen plasma [230].

Transparent conducting zinc oxide thin films have been prepared by a variety of techniques, such as r.f. magnetron sputtering [231], reactive magnetron sputtering [232], chemical vapor deposition [233,234], ion-beam evaporation [235], electron-beam evaporation [236], spray pyrolysis [237,238], laser ablation [239] and more recently by sol-gel process [240-242]. Amongst the different techniques available, the sol-gel method seems to be the most attractive. This is due to ease of coating on the desired shape and area, easy control of the doping level, solution concentration and homogeneity without using expensive and complicated equipment when compared to other methods.

In general, the metal alkoxides are used as raw materials for the sol-gel process. But the preparation of a solution is tedious and the reagents of the metal alkoxide are very expensive. Therefore, many thin films have been prepared using metal salts as raw materials [240]. In this study, we have attempted to obtain a suitable solution from simple salts such as acetates, which are more convenient to use and less costly. This chapter reports the preparation of transparent conductive aluminum doped zinc oxide thin film by the sol-gel process and the optimization of the resistivity of the film by controlling the annealing temperature and dopant concentration in the solution.

7.2.2 Experimental Procedure

Zinc acetate ($Zn(CH_3CO_2)_2.2H_2O$) and aluminum nitrate ($Al(NO_3)_3.9H_2O$) were mixed together and dissolved in ethanol. The solution was refluxed at 80^0C for 3 hours to get a clear solution. Substrates were dipped into the solution and withdrawn at a rate of 0.5 cm/sec. The coated substrates were heated at 260^0C for 10 minutes in air after each dipping. By repeating the above procedure, aluminum doped zinc oxide films of different thickness were obtained. The flowchart that shows the procedure used for preparing aluminum doped zinc oxide is given in Fig. 7.1.

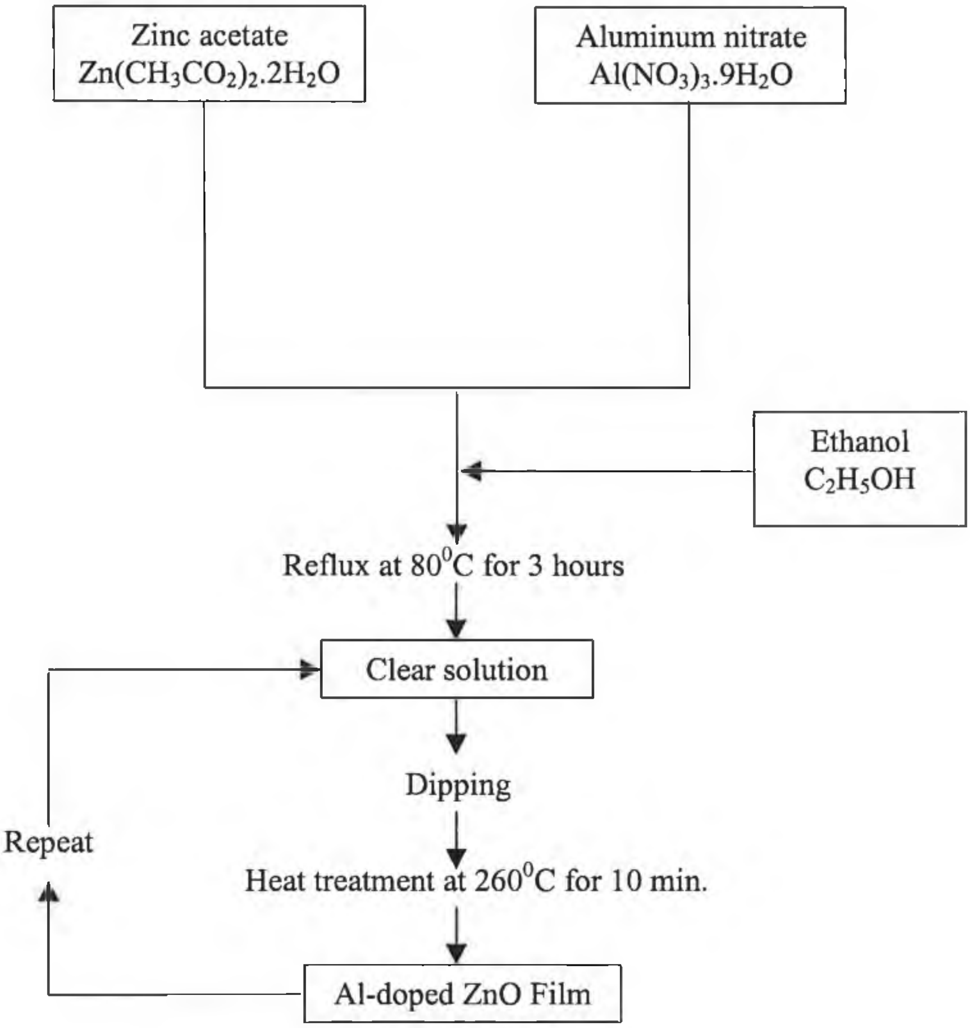

Figure 7.1 Preparation procedure of ZnO:Al thin film by sol-gel process.

7.2.3 Results and discussion

7.2.3.1 Electrical Properties

Fig. 7.2 shows the resistivity of aluminum doped zinc oxide thin films with aluminum dopant concentrations in the solution annealed at 500^0C in air, oxygen and nitrogen. It was found that their resistivity is strongly dependent on the Al doping concentration. The resistivity of the film decreased with increasing Al content up to 0.8 at.% and thereafter the resistivity started to increase with increased doping in all cases. The resistivity of 0.8 at.% Al content ZnO films showed the minimum value of $1.5\text{x}10^{-4}$ Ω-cm in air, $1.8\text{x}10^{-4}$ Ω-cm in oxygen and $1.3\text{x}10^{-4}$ Ω-cm in nitrogen. Resistivities were measured for different positions on the sample and the average value of the resistivity was taken. For different values of the resistivity for the same sample, the measurement error was calculated to be ± 2.5 %.

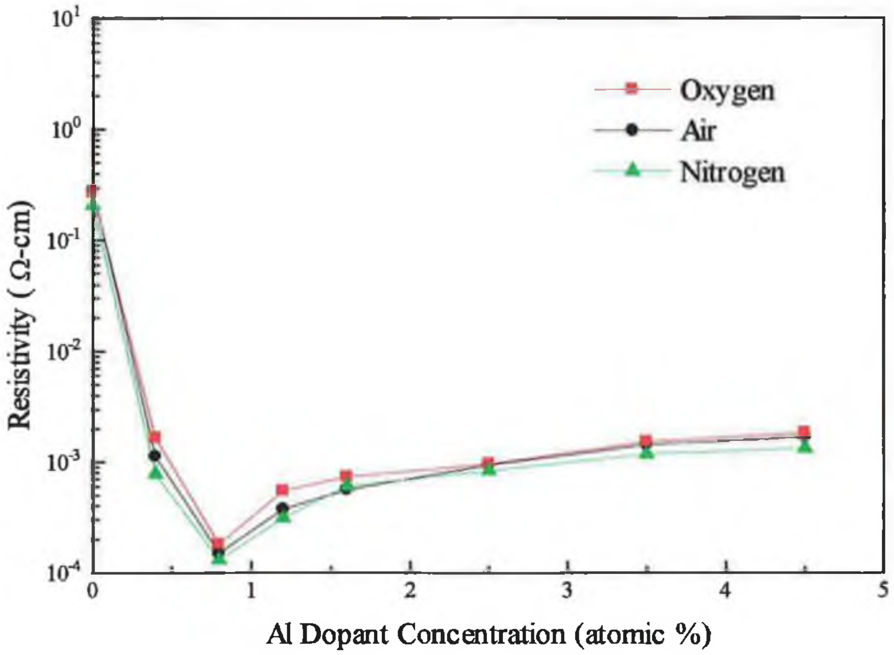

Figure 7.2 Resistivity of the ZnO:Al thin films as a function of aluminum dopant concentration in the solution annealed at 500^0C in air, oxygen and nitrogen.

Fig. 7.3, 7.4 and 7.5 show the variation of hall mobility (μ) and carrier concentration (n) with Al doping concentration annealed at 500^0C in presence of air, oxygen and nitrogen respectively. The carrier concentration of the film was found to increase with Al doping concentration below 0.8%, above this, a tendency towards saturation was observed which was also found by other authors [243]. Such behaviour was expected as a result of substitutional doping of Al^{3+} at the Zn^{2+} site creating one extra free carrier in the process. As the doping level is increased, more dopant atoms occupy lattice sites of zinc atoms resulting in more charge carriers. High aluminum concentration in the film does not always increase the free electron concentration since the aluminum atoms must replace zinc atoms inside the crystallites to contribute conduction electrons. However, after a certain level of doping, the extra aluminum atoms might not occupy the correct places inside the zinc oxide crystallites because of the limited solubility of aluminum inside ZnO. The ionic radius of aluminum is smaller than that of zinc and therefore excess aluminum may occupy interstitial positions [244] leading to distortion of the crystal structure. Hence, the dopant atoms become ineffective as donors as the higher levels of Al incorporation lead to interstitial incorporation of Al in the form of Al_2O_3 [244] giving rise to the greater electron scattering. This explains the initial rise followed by the saturation of carrier concentration with the dopant level.

Fig.7.3, 7.4 and 7.5 show that mobility increases initially and after certain dopant concentration it decreases. The mobility behaviour of such a polycrystalline extrinsic semiconductor is governed mainly by ionized impurity scattering and grain boundary scattering [245]. The resultant mobility is given by the well-known Mattheissen's rule

$$\frac{1}{\mu} = \frac{1}{\mu_{gb}} + \frac{1}{\mu_{is}} \qquad (7.1)$$

where μ = resultant mobility,

μ_{gb} = mobility due to grain boundary scattering,

μ_{is} = mobility due to ionized impurity scattering.

The initial increase in mobility with doping concentration seen in fig. 7.3, 7.4 and 7.5 may be due to an improvement in the grain growth (grains of larger size) and textured growth of the films. Improvement in grain size results in a reduction of grain boundary scattering, while improvement in textured growth results in less resistance to the electron flow. Increasing the dopant concentration after a certain doping level results in the decrease in carrier mobility due to the segregation of Al dopant atoms at the grain boundaries in the form of Al_2O_3, which will increase the grain boundary barrier. High doping concentration increases the ionized impurity scattering from the substitutional donors and also scattering from the interstitials, which may also be the reason of decrease in mobility. Thus, the doping concentration reaches a maximum when the substitutional doping of the zinc oxide by aluminum is at a maximum whereas the mobility will continue to fall as the scattering by the ionized impurities, the defects in the crystal and the grain boundaries increases with higher aluminum concentration.

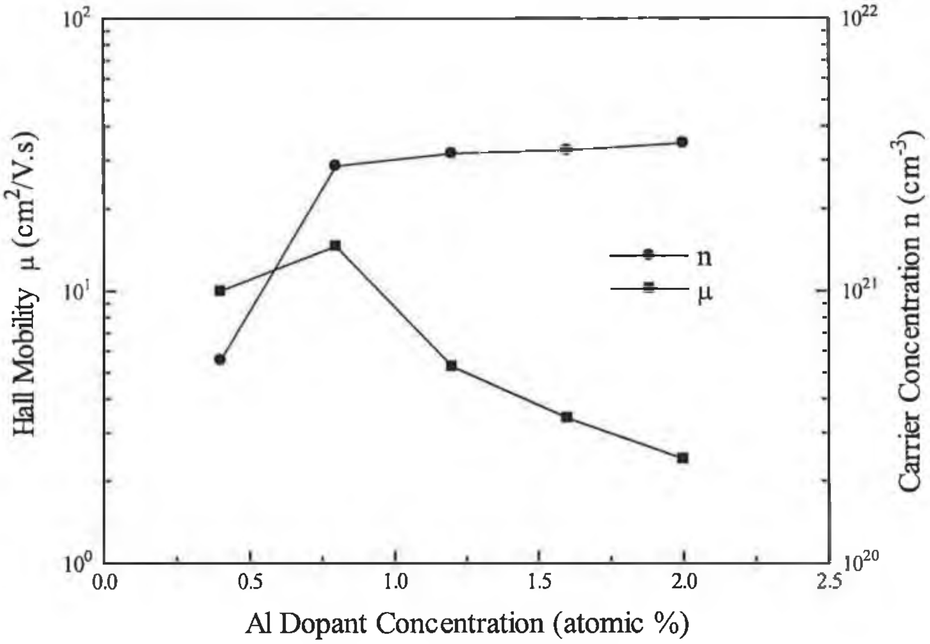

Figure 7.3 Variation of hall mobility (μ) and carrier concentration (n) with Al doping concentration annealed at 500^0C in presence of air.

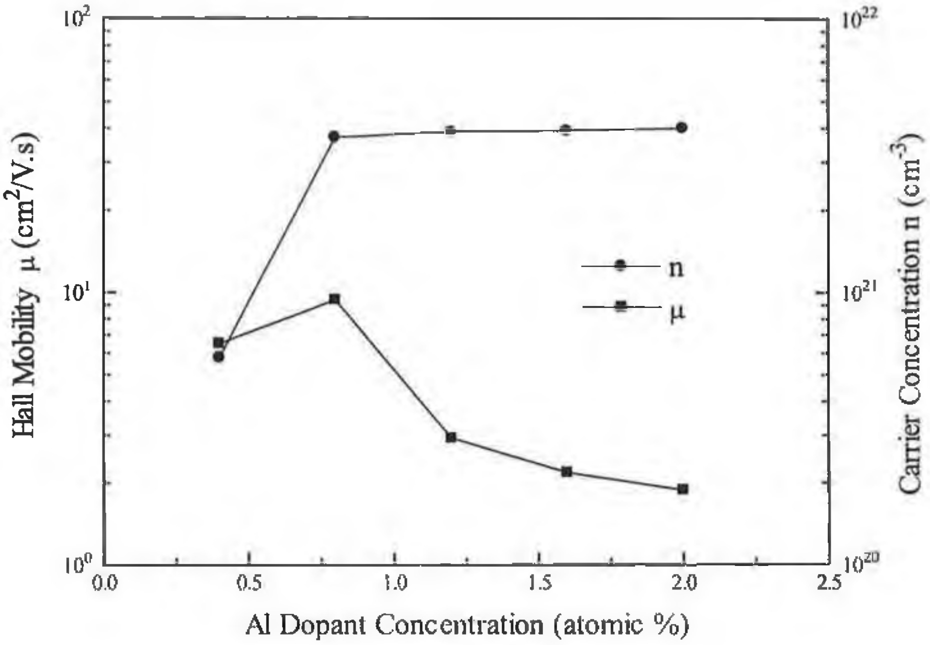

Figure 7.4 Variation of hall mobility (μ) and carrier concentration (n) with Al doping concentration annealed at 500^0C in presence of oxygen.

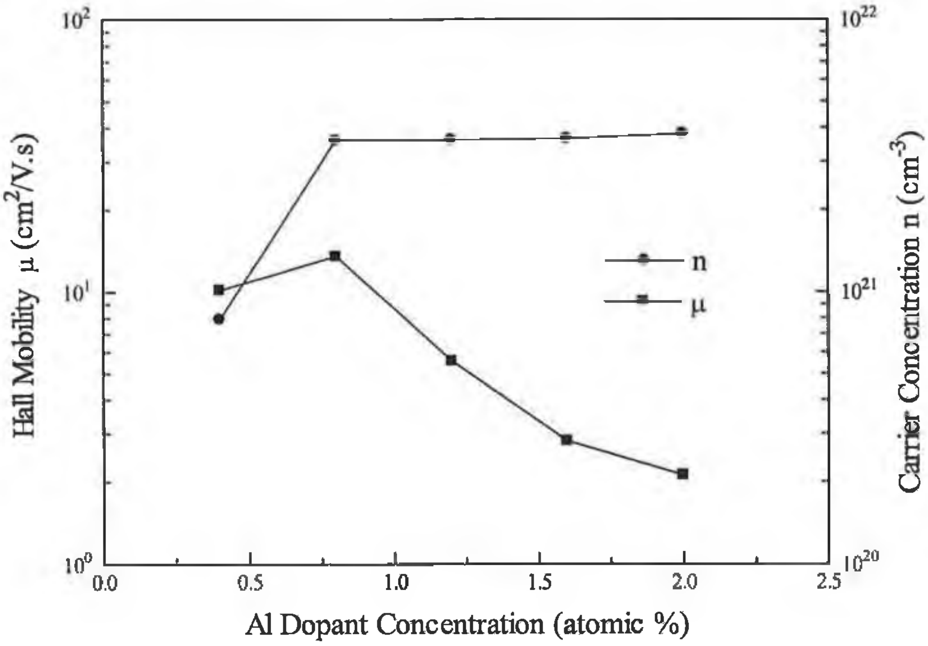

Figure 7.5 Variation of hall mobility (μ) and carrier concentration (n) with Al doping concentration annealed at 500^0C in presence of nitrogen.

Fig. 7.6 shows the resistivity of 0.8 at.% Al doped ZnO films as a function of annealing temperature annealed in air, oxygen and nitrogen. Samples were annealed for 1 hour at each temperature. The resistivity decreased significantly with annealing temperature up to 500^{0}C and then it started increasing. The minimum value of resistivity obtained after annealing at 500^{0}C was 1.5x10^{-4} Ω-cm in air, 1.8x10^{-4} Ω-cm in oxygen and 1.3x10^{-4} Ω-cm in nitrogen. Electrical conduction of ZnO:Al film is caused by electrons from oxygen-deficient defects due to Al substituted for Zn. The difference in resistivity between the three atmospheres was caused by the difference in carrier concentration and mobility [258,259] as shown in fig. 7.7, 7.8 and 7.9.

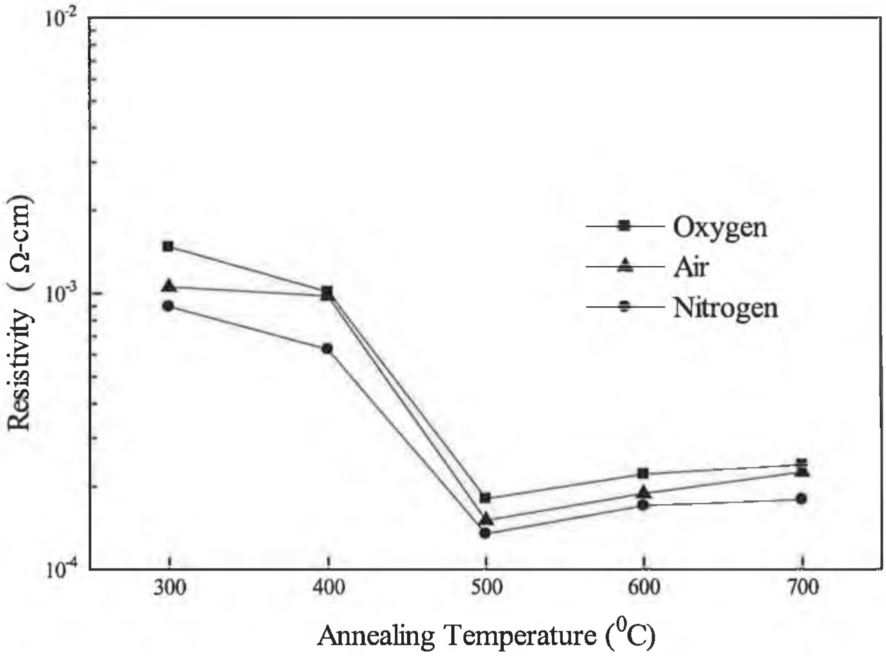

Figure 7.6 Resistivity of 0.8 at.% Al doped ZnO thin films as a function of annealing temperature in air, oxygen and nitrogen.

Fig. 7.7, 7.8 and 7.9 show the variation of hall mobility (μ) and carrier concentration (n) with annealing temperature for 0.8 at.% Al doped ZnO films annealed in air, oxygen and nitrogen respectively. The resistivity ρ is proportional to the reciprocal of the product of carrier concentration n and mobility μ. Fig. 7.7, 7.8 and 7.9 show that the carrier concentration increases with annealing temperature owing to saturation. One of the causes of the decrease in resistivity due to annealing up to 500⁰C is thought to be an increase in carrier concentration resulting from a liberation of electrons from the adsorbed oxygen on the surface of ZnO:Al crystallites.

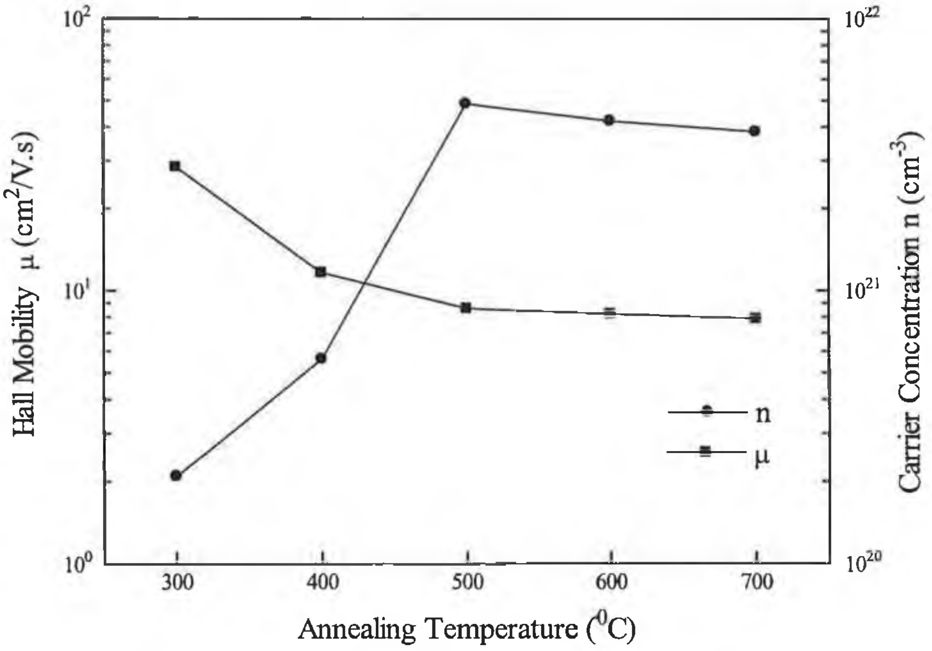

Figure 7.7 Variation of hall mobility (μ) and carrier concentration (n) as a function of annealing temperature in air for ZnO:Al film with Al/Zn 0.8 at.%.

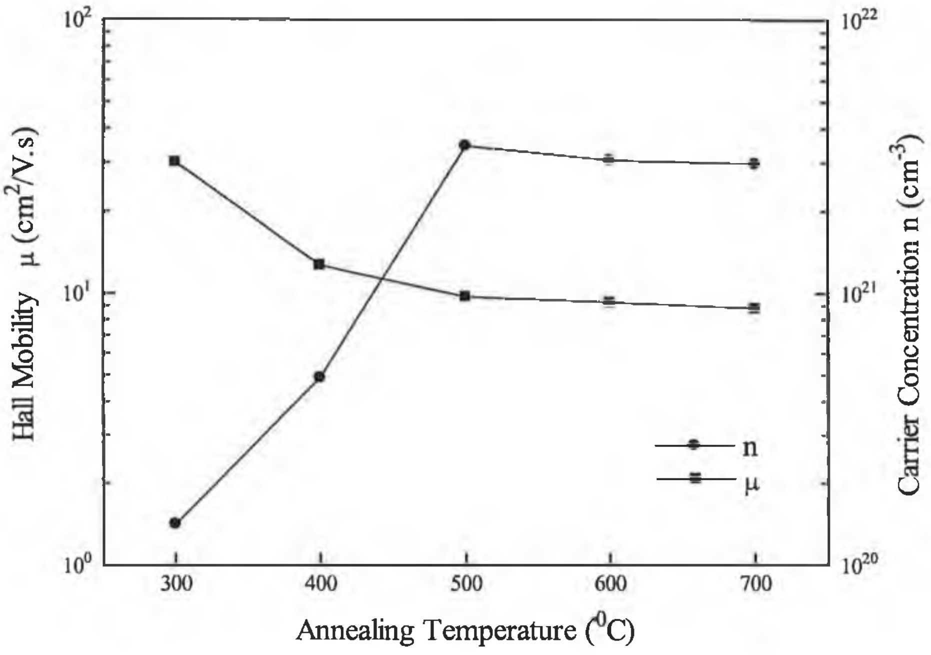

Figure 7.8 Variation of hall mobility (μ) and carrier concentration (n) as a function of annealing temperature in oxygen for ZnO:Al film with Al/Zn 0.8 at.%.

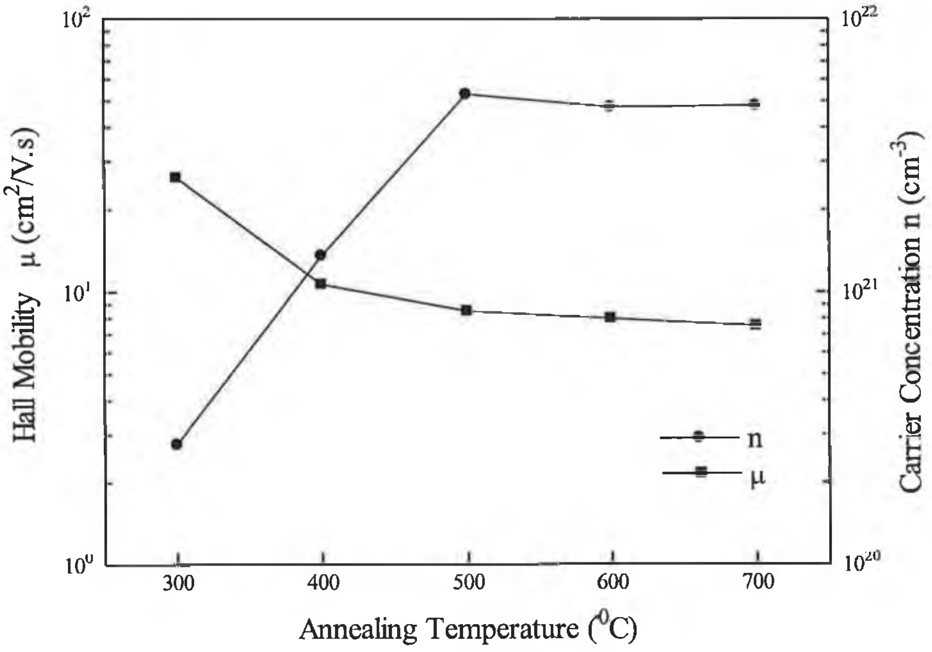

Figure 7.9 Variation of hall mobility (μ) and carrier concentration (n) as a function of annealing temperature in nitrogen for ZnO:Al film with Al/Zn 0.8 at.%.

The chemisorption of oxygen and the location of Al atoms which are not on zinc sites result in a low carrier concentration before heat treatment in atmosphere. In general, an increase in conduction electrons is attributable to an increase in donors. Therefore, it is reasonable to suppose that, by an interaction of zinc atoms diffused through grain boundaries with ZnO:Al surfaces, interstitial zinc atoms and/or oxygen vacancies acting as donors were formed. However, an increase in donors leads to an increase in scattering centers, resulting in a decrease in the mobility. The chemisorption of acceptor oxygen on the ZnO:Al surface, in the pores of the film and between grain boundaries forms an electronic depletion layer which acts as a surface potential barrier and causes the decrease in mobility [246]. Therefore, we consider that the decrease in resistivity during annealing up to 500^0C results in a change of carrier concentration and mobility from the movement of Al atoms to Zn lattice sites and the desorption of oxygen from the ZnO:Al surface, pores and grain boundaries. According to the scattering mechanism of transparent conducting films, suggested by Zhang et al. [247], for the investigated films, ionized impurity scattering seems to be dominant in the low temperature range. In the high temperature range, grain boundary scattering becomes the dominant scattering mechanism. So the increase in resistivity after 500^0C may be related to the increase of grain boundary scattering for the free electrons and hence the decrease of the carrier mobility [248]. The minimum value of resistivity of $1.3\text{x}10^{-4}$ Ω-cm which has been obtained at 0.8 at.% aluminum concentration annealed at 500^0C in nitrogen by the sol-gel process, is better than those obtained by other conventional methods. Table 7.1 shows the resistivity of ZnO:Al films produced by different techniques.

Table 7.1: Resistivity of ZnO:Al films

Deposition technique	Resistivity(Ω-cm)
Sol-gel (this work)	$1.3\text{x}10^{-4}$
Laser ablation [239]	$9\text{x}10^{-4}$
Spray pyrolysis [237]	$2\text{x}10^{-3}$
Magnetron sputtering [249]	$1.84\text{x}10^{-3}$
Thermal evaporation [250]	$2\text{x}10^{-3}$

7.2.3.2 Roughness

The average roughness (R_a) values were measured for ZnO:Al thin films annealed at different temperature in presence of air, oxygen and nitrogen. Fig. 7.10 shows the variation of R_a with annealing temperature. Roughness of the substrate was measured to be 0.01 μm and for the as-deposited film 0.03 μm. The minimum resolution of the instrument is 0.01 μm. So we could not measure the roughness beyond this value. Roughness decreases with temperature and a small change in R_a was observed with varying the temperature due to the crystallization effect.

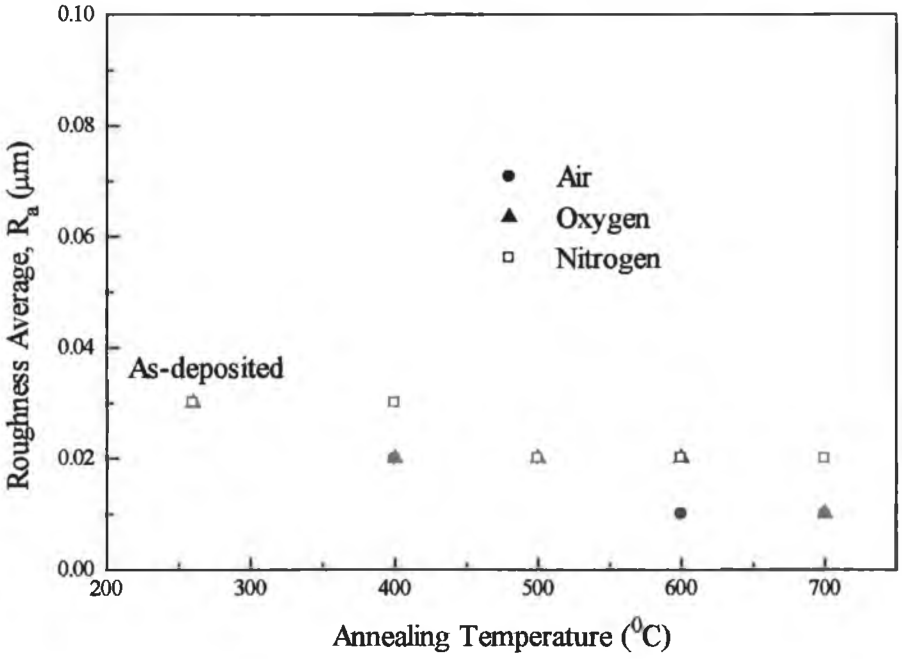

Figure 7.10 Variation of Roughness as a function of annealing temperature annealed in air, oxygen and nitrogen for ZnO:Al film with Al/Zn 0.8 at.%.

7.2.3.3 Structural Properties

7.2.3.3.1 X-ray Diffraction Spectroscopy

Fig. 7.11, 7.12 and 7.13 show the X-ray diffraction spectra for ZnO:Al films with Al/Zn 0.8 at.% annealed at different temperatures in the presence of air, oxygen and nitrogen respectively. From the figures, it is seen that as-deposited ZnO:Al films are amorphous. After annealing in atmosphere at higher temperature, the films showed evidence of conversion from an amorphous state to polycrystalline state with a hexagonal structure, which is in very good agreement with the Joint Committee on Powder Diffraction Standards (JCPDS) database (Card No. 36-1451). All the spectra show that the intensity of the peaks increased with the annealing temperatures annealed in air, oxygen and nitrogen. From this behaviour, we can conclude that the crystallinity of ZnO:Al films is improved with the increase of annealing temperature in all cases and also the crystallinity of the films is temperature rather than atmosphere dependent. The spectra show well-defined diffraction peaks showing good crystallinity. In random orientation the (002)/(101) peak ratio is 0.44 whereas it is 1.25 for the samples annealed at 700^0C in the presence of air, oxygen and nitrogen (See Appendix A). Therefore, the films show a preferred orientation with the c-axis perpendicular to the substrate.

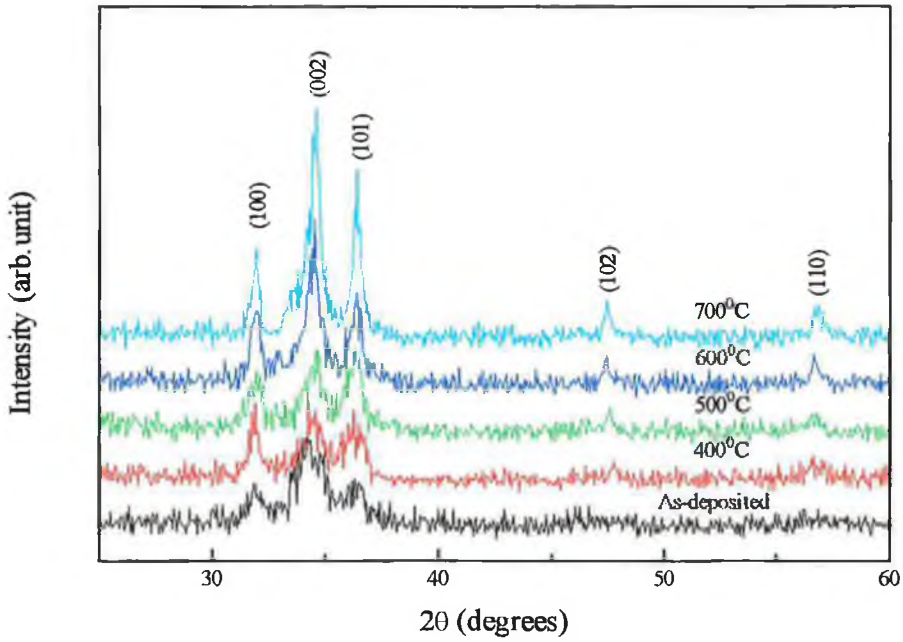

Figure 7.11 XRD spectra for ZnO:Al film with Al/Zn 0.8 at.% annealed at different temperatures in presence of air.

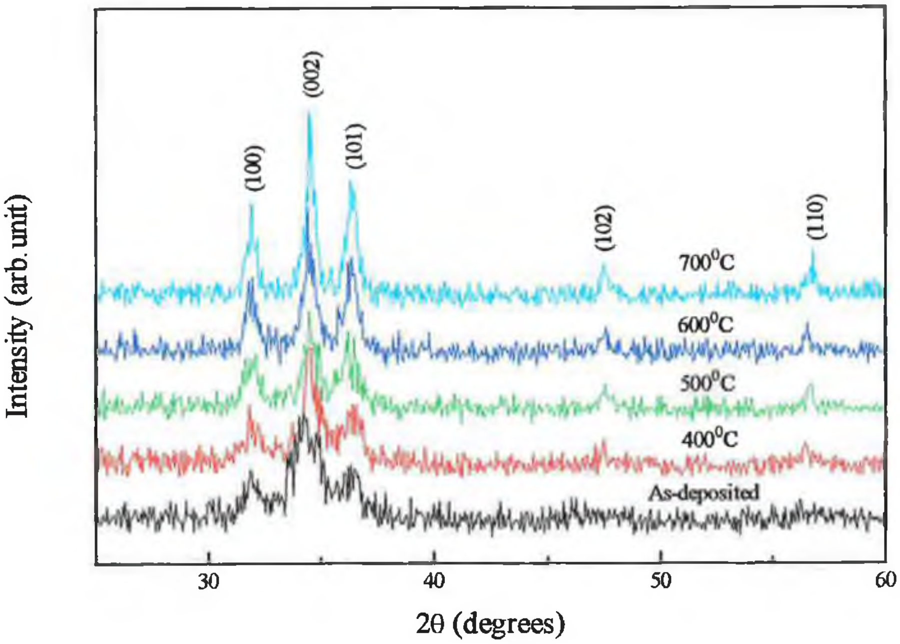

Figure 7.12 XRD spectra for ZnO:Al film with Al/Zn 0.8 at.% annealed at different temperatures in presence of oxygen.

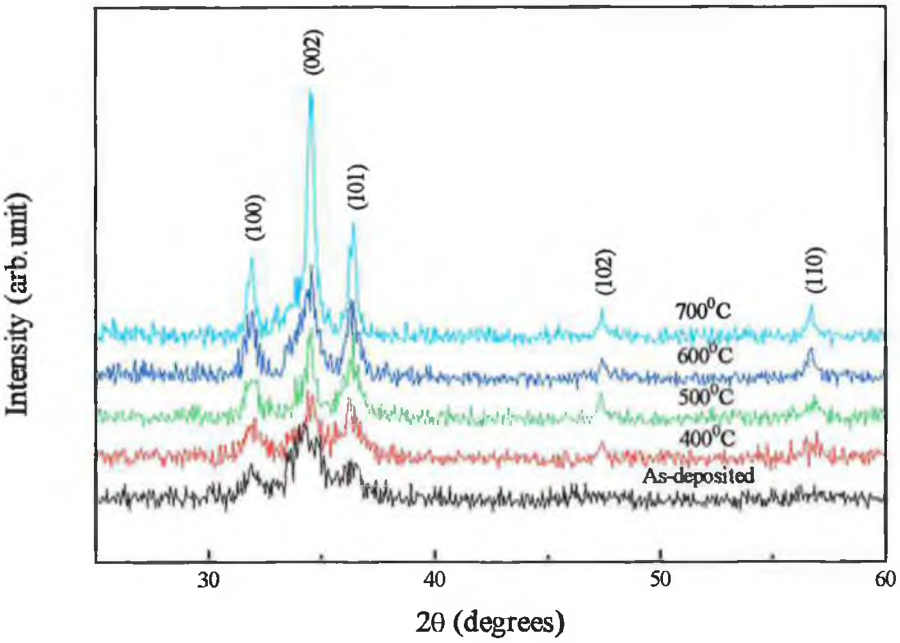

Figure 7.13 XRD spectra for ZnO:Al film with Al/Zn 0.8 at.% annealed at different temperatures in presence of nitrogen.

7.2.3.3.2 Raman Spectroscopy

Fig. 7.14, 7.15 and 7.16 show the typical Raman spectra of ZnO:Al films excited with 325 nm He-Cd laser radiation annealed at different temperatures in air, oxygen and nitrogen respectively. All the spectra show the longitudinal optical (LO) E_1 mode at 572 cm^{-1} and second order vibration at 1140 cm^{-1}. The broad features between 1050 and 1200 cm^{-1} are assigned to the two-phonon modes (2 LO) characteristic of this II-IV semiconductor [251]. From the fig. 7.14, 7.15 and 7.16, it is seen that the intensity of the band decreases upon annealing. This can be interpreted as an indication of changes in oxygen deficiency [252] and interstitial Zn concentration [253]. Upon annealing in different atmosphere, excess zinc in the film becomes oxidized, the impurity states disappear and consequently the magnitude of resonance Raman enhancement of the E_1 (LO) mode decreases. Upon annealing at higher temperature, peaks are horizontally shifted to higher wavenumber. This is due to the better crystallization of the films as there is less lattice disorder and the lattice parameter becomes smaller.

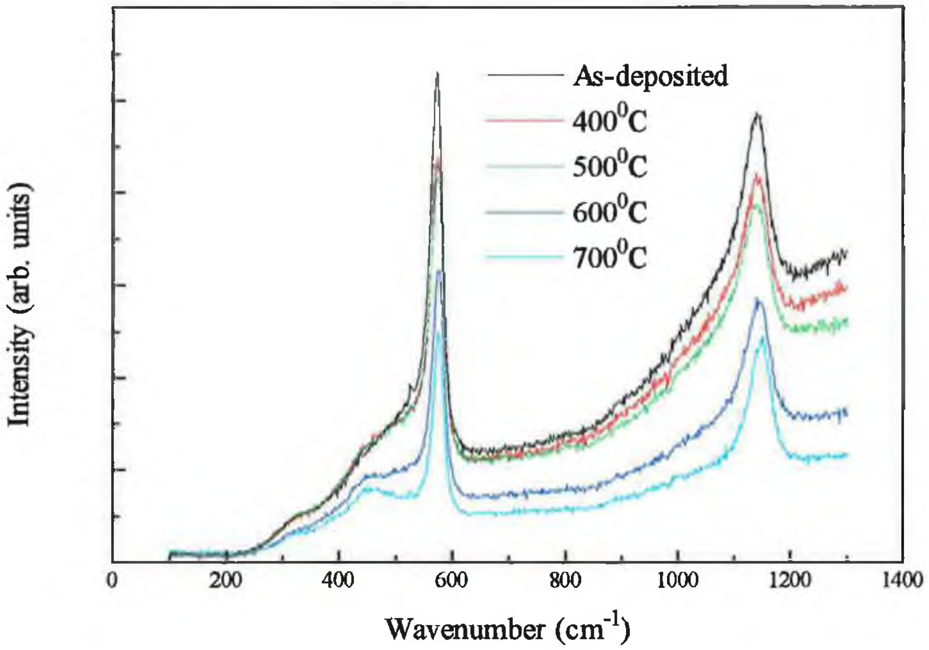

Figure 7.14 Raman spectra for ZnO:Al films with Al/Zn 0.8 at.% annealed in air for different temperatures.

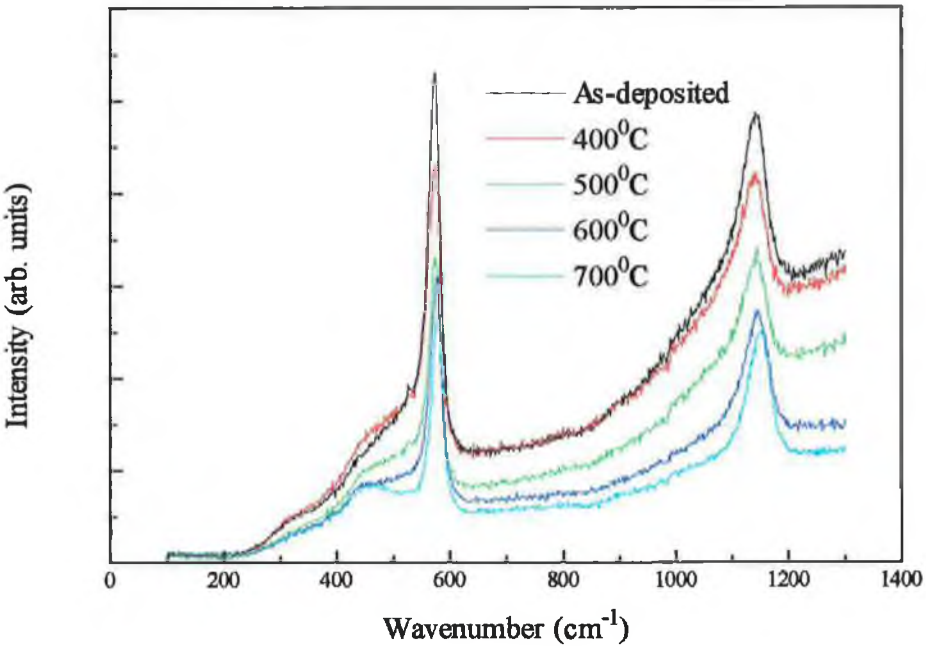

Figure 7.15 Raman spectra for ZnO:Al films with Al/Zn 0.8 at.% annealed in oxygen for different temperatures.

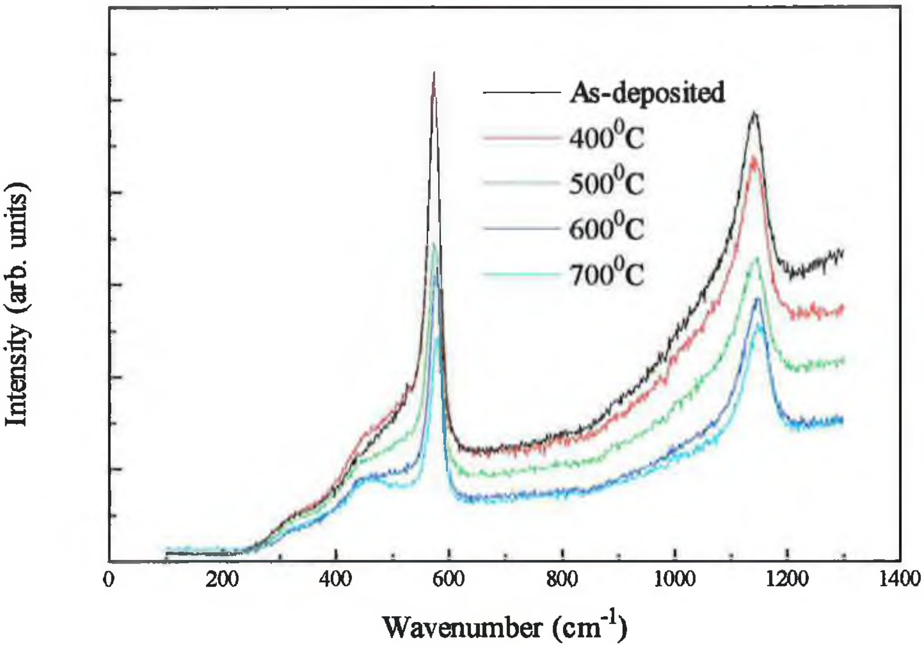

Figure 7.16 Raman spectra for ZnO:Al films with Al/Zn 0.8 at.% annealed in nitrogen for different temperatures.

7.2.3.4 Optical Properties

Fig. 7.17, 7.18 and 7.19 show the optical transmission spectra for ZnO:Al films with Al/Zn 0.8 at.% with a thickness of 300 nm annealed at different temperatures in presence of air, oxygen and nitrogen respectively. The films have an optical transparency up to 88%. The oscillations on the spectrum are due to the film thickness and the consequent interference in the layer. The optical transmission of ZnO:Al films in the visible region improves with annealing at higher temperature showing maximum transmittance of 86.2% for as-deposited films and 88%, 87.92% and 87.88% when annealed at 700^{0}C in air, oxygen and nitrogen respectively. From the transmission spectra of ZnO:Al films in different atmospheres, we can see that the atmosphere has no significant effect on the optical transmission of the films.

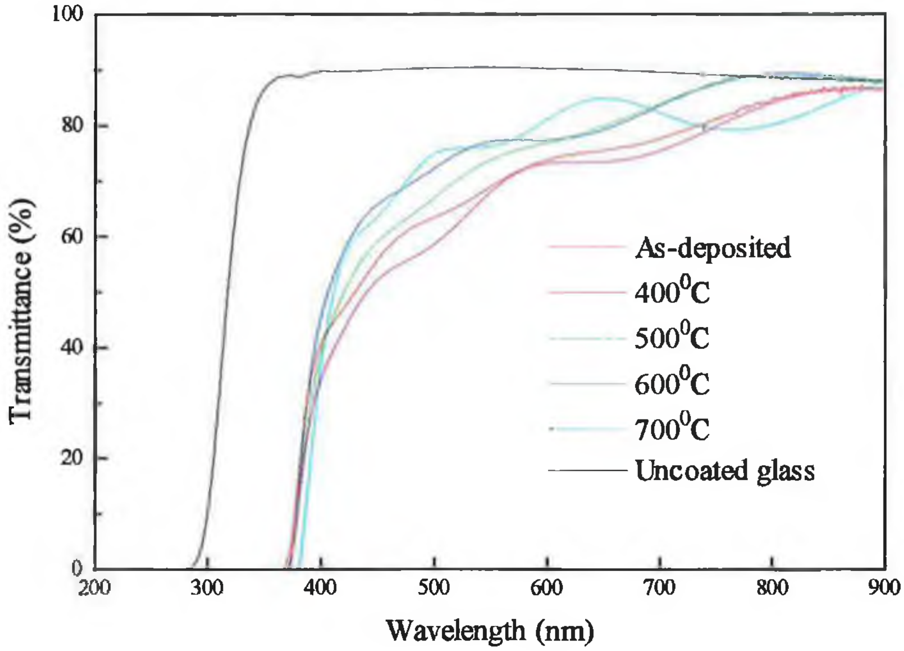

Figure 7.17 Optical transmission spectra for ZnO:Al films with Al/Zn 0.8 at.% with a thickness of 300 nm annealed at different temperatures in presence of air.

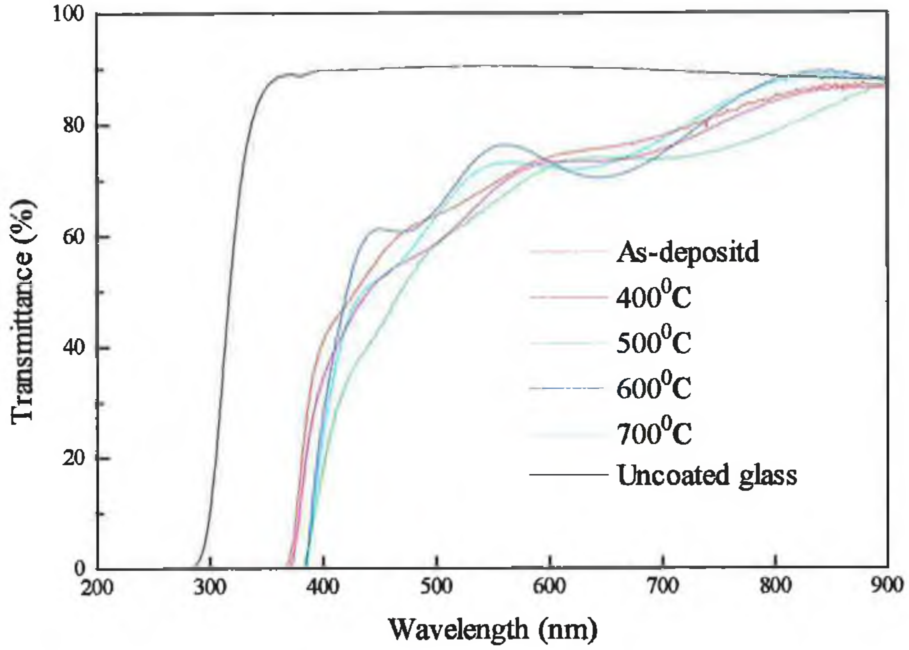

Figure 7.18 Optical transmission spectra for ZnO:Al films with Al/Zn 0.8 at.% with a thickness of 300 nm annealed at different temperatures in presence of oxygen.

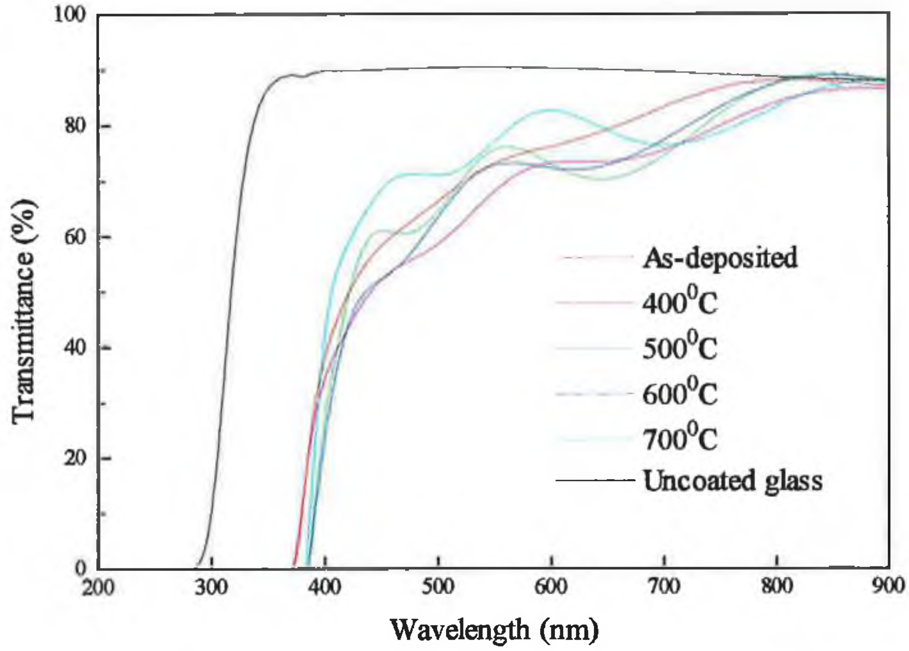

Figure 7.19 Optical transmission spectra for ZnO:Al films with Al/Zn 0.8 at.% with a thickness of 300 nm annealed at different temperatures in presence of nitrogen.

From the transmission spectra in the UV region, the absorption coefficient, α can be calculated from the expression [254]

$$\alpha = \frac{1}{t}\ln\left(\frac{1}{T}\right) \qquad (7.2)$$

where, T is the ratio of transmission and t is the film thickness. The absorption coefficient for the as-deposited ZnO:Al film with 0.8 at. % Al with a thickness of 300 nm is $4.95\text{x}10^3$ cm^{-1} at a wavelength of 900 nm. The absorption coefficients for the ZnO:Al film with 0.8 at. % Al are $4.26\text{x}10^3$, $4.29\text{x}10^3$ and $4.31\text{x}10^3\text{cm}^{-1}$ annealed at 700^0C in air, oxygen and nitrogen respectively. We can see that the absorption coefficients decrease with the annealing temperatures in different atmospheres.

7.2.4 Conclusions

Highly conductive and transparent films of aluminum doped zinc oxide have been prepared by the sol-gel process. The resistivity, hall mobility and carrier concentration of the films were measured for different Al concentrations in the solution and also annealed at different temperatures in the presence of air, oxygen and nitrogen. The resistivity of the films containing 0.8 at.% Al has a minimum value of $1.5\text{x}10^{-4}$ Ω-cm, $1.8\text{x}10^{-4}$ Ω-cm and $1.3\text{x}10^{-4}$ Ω-cm when annealed at 500^0C in air, oxygen and nitrogen respectively.

The films have an optical transparency up to 88% at 900 nm for a thickness of 300 nm. The transparency of the films increases with the annealing temperature but the atmosphere does not have any significant effect on the transmission of the films.

The annealed films are polycrystalline with a hexagonal structure. The spectra show well defined diffraction peaks indicating good crystallinity and a preferred orientation with the c-axis perpendicular to the substrate. The crystallinity of ZnO:Al films is improved with the increase of annealing temperature. The crystallinity of the films has no effect of atmosphere.

ZnO:Al films prepared by this sol-gel process have properties of transparency and resistivity which are comparable to or better than those prepared by other methods and are thus eminently suitable for application as a low cost transparent electrode in thin film electroluminescent devices.

7.3 Preparation and properties of transparent conductive ITO thin films deposited by sol-gel process

7.3.1 Introduction

Indium tin oxide commonly referred to as ITO is an n-type semiconductor with a band gap between 3.5 and 4.3 eV and a maximum possible charge carrier concentration of the order of 10^{21} cm^{-3} [255-257]. Consequently ITO is transparent to visible and near-infrared light and has a low electrical resistivity. ITO films have high luminous transmittance, high infrared reflectance, good electrical conductivity, excellent substrate adherence, hardness and chemical inertness and hence, have been widely and intensively studied for many years [257-261]. Because of these properties, ITO films are extensively used as coating electrodes in optoelectronic devices [262], electroluminescent devices [263], photovoltaic cells [264-266], electrochromic devices [262], liquid crystal displays [262,267], sensors [268], storage-type cathode ray tubes [262], biological devices [269], flat panel display devices [270,271] and heat reflecting mirrors [272].

The optical and electrical properties of ITO films are found to be sensitive to preparation conditions. Transparent conductive ITO thin films have been prepared by a variety of methods, such as reactive electron beam evaporation [273], DC magnetron sputtering [274-276], evaporation [277], reactive thermal deposition [278], spray pyrolysis [266,279], laser ablation [280] and more recently by the sol-gel process [259,281-283]. Amongst the different techniques available, the sol-gel method seems to be the most attractive one due to ease of coating on the desired shape and area, easy control of the doping level, solution concentration and homogeneity without using expensive and complicated equipment when compared with other methods. In general, this sol-gel process also uses metal alkoxides as raw materials, but it is very difficult to obtain indium and tin alkoxides because of preparation problems, unavailability or expensive cost. Thus as for the ZnO films, we have prepared ITO thin films from the sol-gel process using inorganic metal salts as raw materials with appropriate organic solvents.

This chapter reports the properties of ITO films prepared by the sol-gel process from non-alkoxide compounds and inorganic salts. The resistivity of the ITO films has been measured as a function of tin dopant concentration and annealing temperature in different atmospheres and the structure and composition of the films has been investigated.

7.3.2 Experimental procedure

Anhydrous indium trichloride ($InCl_3$) was dissolved in acetylacetone and the solution was refluxed at 60^0C for 3 hours. Anhydrous tin (IV) chloride ($SnCl_4$) was dissolved in ethanol and this solution was mixed with the refluxed solution at room temperature. Fig. 7.20 shows the preparation procedure of ITO thin film by the sol-gel process. Substrates were dipped in the starting solution and withdrawn at a rate of 0.2 cm s^{-1}. The coated substrates were heated at 260^0C for 10 min. after each dipping. The thickness of the film was approximately 40 nm for each dipping. By repeating the above procedure, indium tin oxide films of different thickness were obtained.

7.3.3 Results and discussion

7.3.3.1 Electrical Properties

Fig. 7.21 shows the resistivity of ITO thin films with tin dopant concentrations in the solution annealed at 500^0C in air, oxygen and nitrogen for one hour. It was found that the resistivity of ITO films is strongly dependent on the tin doping concentration. The resistivity of the film decreased with increasing Sn content up to 10 wt. % and the resistivity increased for greater Sn content. The resistivity of 10 wt. % Sn content ITO films showed a minimum value of $8.5x10^{-4}$ Ω-cm in air, $9.8x10^{-4}$ Ω-cm in oxygen and $8.0x10^{-4}$ Ω-cm in nitrogen. Resistivities are measured on different positions on the sample and the average value is taken. From the measurements of different positions, measurement error was calculated to be ± 2.5 %. Fig. 7.22, 7.23 and 7.24 show the variation of hall mobility (μ) and carrier concentration (n) with Sn doping concentration annealed at 500^0C in presence of air, oxygen and nitrogen respectively. These figures show that the carrier concentration of the films increases and the hall mobility decreases with higher Sn content.

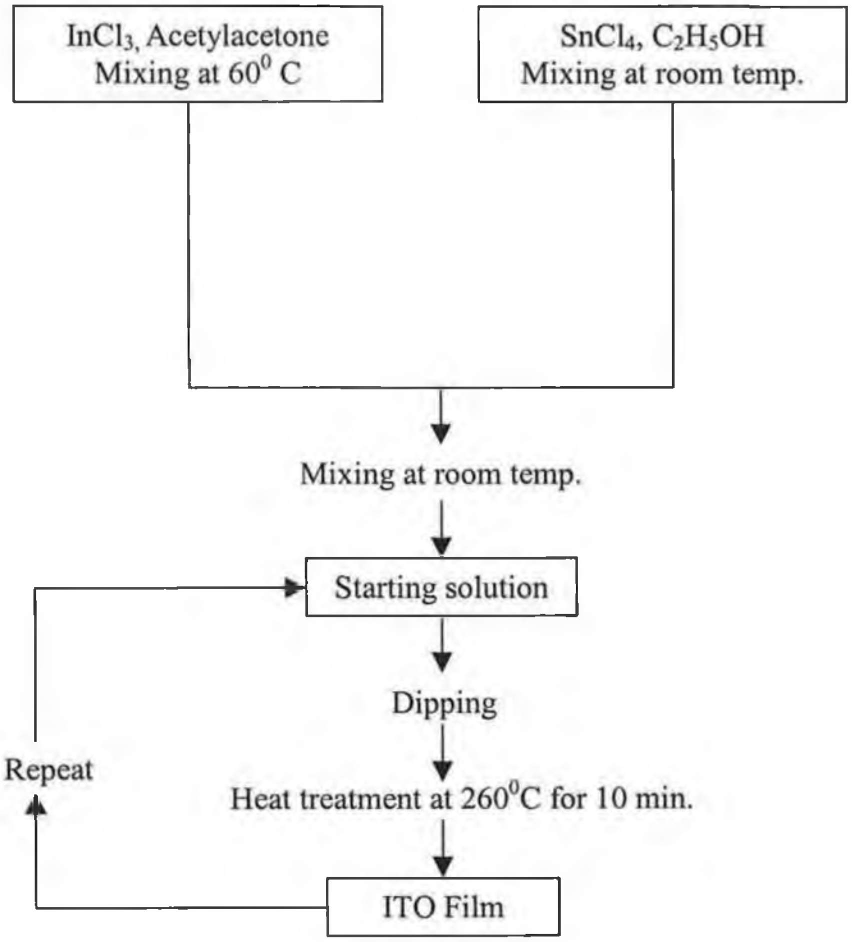

Figure 7.20 Preparation procedure of ITO thin film by sol-gel process.

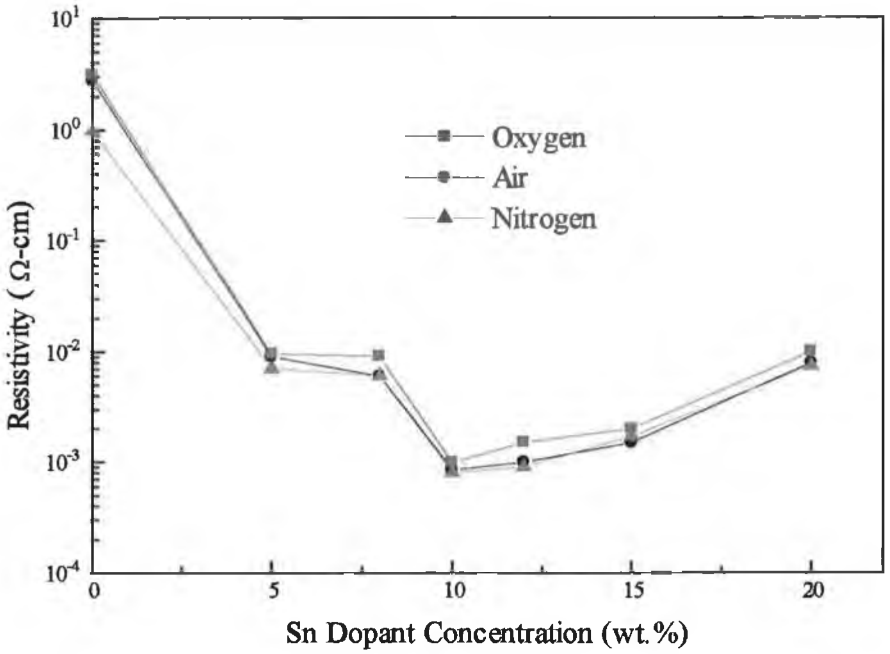

Figure 7.21 Resistivity of the ITO thin films as a function of tin dopant concentration in the solution annealed at 500^{0}C in air, oxygen and nitrogen.

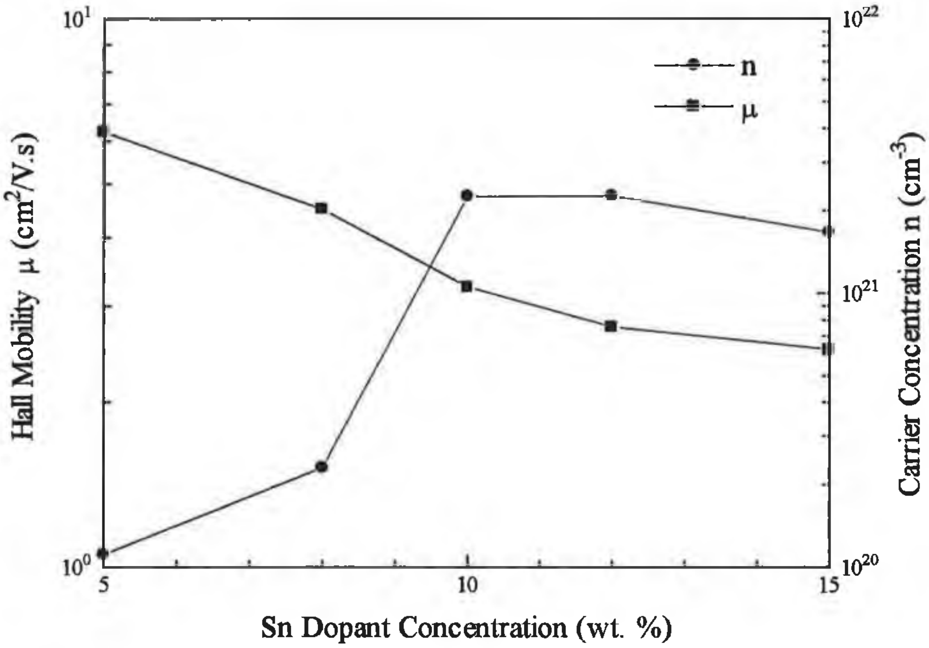

Figure 7.22 Variation of hall mobility (μ) and carrier concentration (n) with Sn doping concentration annealed at 500^{0}C in presence of air.

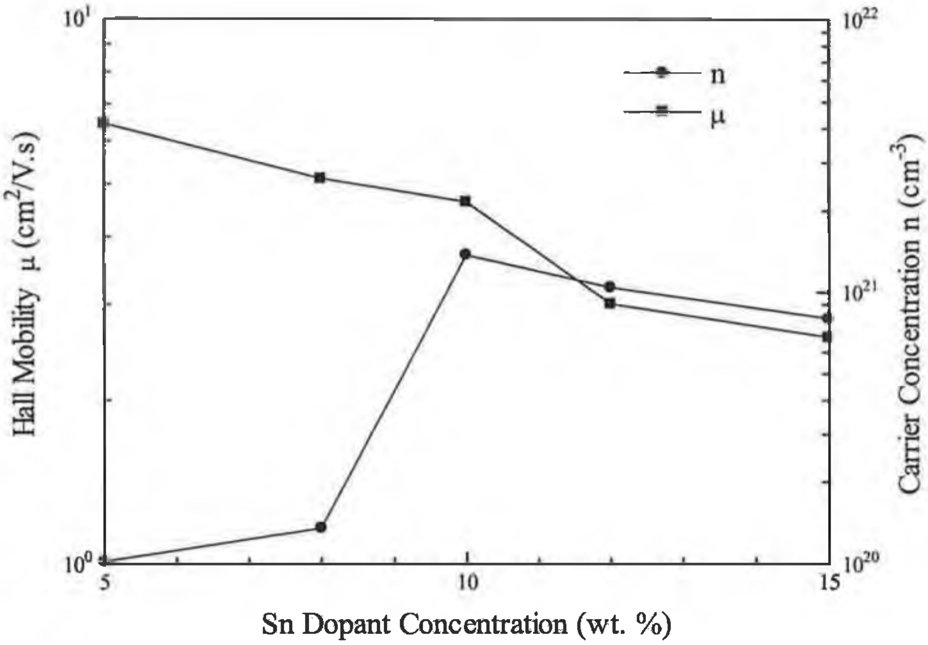

Figure 7.23 Variation of hall mobility (μ) and carrier concentration (n) with Sn doping concentration annealed at 500^{0}C in presence of oxygen.

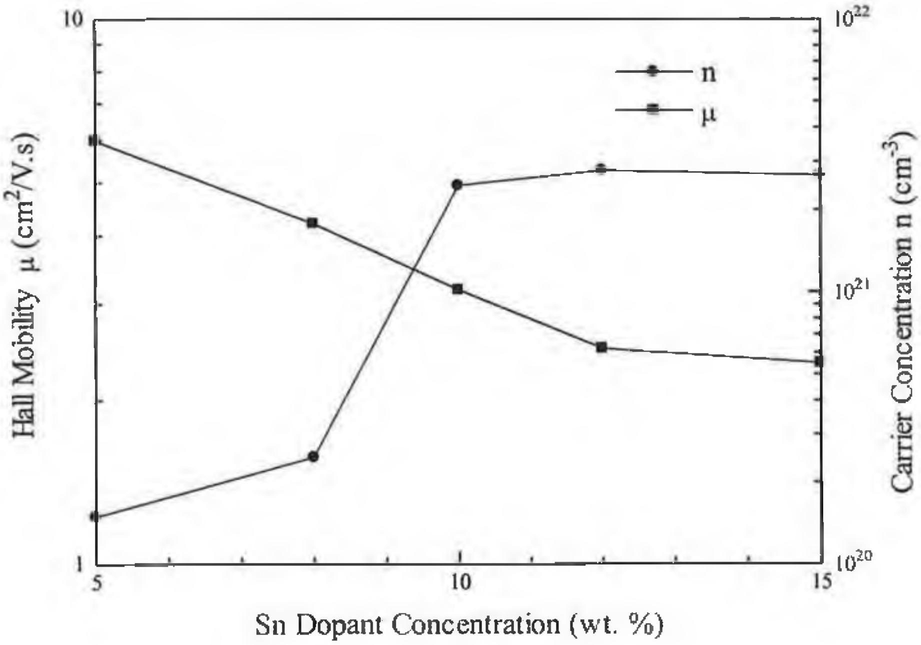

Figure 7.24 Variation of hall mobility (μ) and carrier concentration (n) with Sn doping concentration annealed at 500^{0}C in presence of nitrogen.

This behaviour where an initial reduction in resistivity with increasing Sn content followed by increasing resistivity at higher Sn concentrations is well known from the measurements of ITO films prepared by other methods [284,285]. With increasing Sn content, not all the Sn atoms can be substituted to In atom sites. Sn atoms which can not be substituted to indium sites do not behave as effective donors. A small amount of Sn(IV) is changed to Sn(II) which act as acceptors. Kostlin et al. [285] reported that Sn ions are very close to each other when the concentration of Sn ions is very high. When this occurs, one of the neighbouring Sn(IV) ion has the tendency to change into Sn(II). Sn(IV) ions are associated with Sn(II) ions by an electrostatic force. This association forms a kind of defect complex. The average electrical charge of the complex is +3. The associated Sn ions that have the average charge +3 may not contribute to the electrical conduction. The mobility of the thin films annealed in air, oxygen and nitrogen is very low. The reason for the low mobility was considered to be due to the defects in the In_2O_3 crystal structure doped with Sn and the higher resistivity at higher Sn content was considered to be due to the very small crystals in the thin films [258]. The small crystal grains have many grain boundaries which may behave as barriers against the electron moving inside thin film. It was considered that these factors caused high resistivities at higher Sn content in ITO thin films [258,259].

Fig. 7.25 shows the variation of resistivity of films with 10 wt. % Sn doping as a function of annealing temperature in air, oxygen and nitrogen. The samples were annealed for 1 hour at each temperature. Up to 500^0C there was a large reduction in resistivity. This reduction coincides with the improvement in film crystallinity, which is shown later in the X-ray diffraction measurements. The increase in resistivity at higher temperatures is in contrast to the results reported by Nishio et al. [258] which showed no increase in resistivity at higher annealing temperature. The reason for the increase seen here may be due to outdiffusion of oxygen from the films at higher temperatures since it has been shown that the resistivity reduction is greater when annealing is carried out in atmospheres with a higher oxygen concentration [286] suggesting that oxygen vacancies play an important role. The minimum value of resistivity obtained after annealing at 500^0C was $8.5x10^{-4}$ Ω-cm in air, 9.8x10^{-4} Ω-cm in oxygen and 8.0x10^{-4} Ω-cm in nitrogen. It is well known that electrical conduction of ITO film is caused by electrons from oxygen-deficient defects due to Sn substituted for In [286]. The difference in resistivity between the three atmospheres was caused by the difference in carrier concentration and mobility as well as shown in fig. 7.26, 7.27 and 7.28.

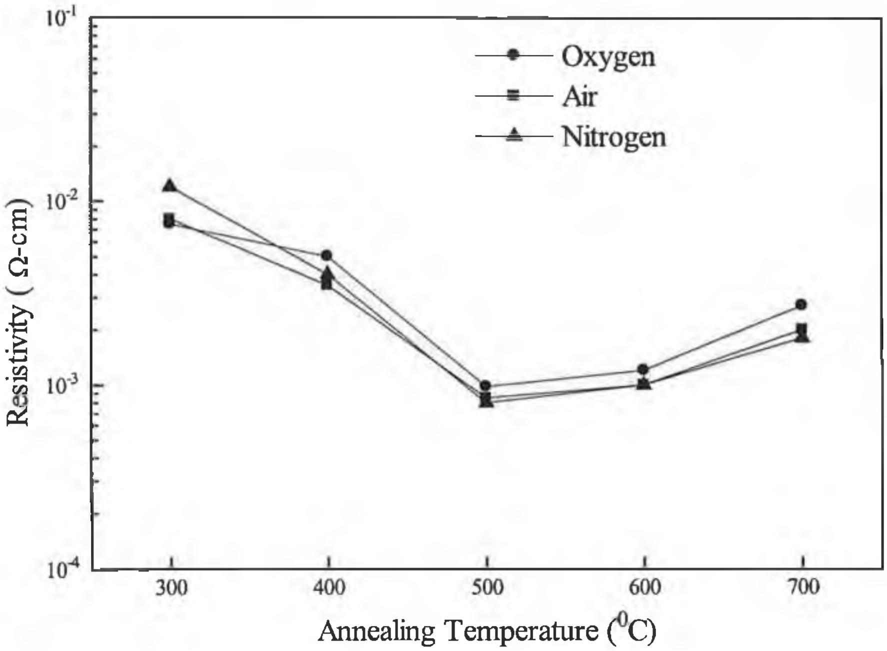

Figure 7.25 Resistivity of 10 wt.% Sn-doped ITO films as a function of annealing temperature in air, oxygen and nitrogen.

Fig. 7.26, 7.27 and 7.28 show the variation of hall mobility (μ) and carrier concentration (n) with annealing temperature for 10 wt.% Sn-doped ITO films annealed in air, oxygen and nitrogen respectively. These figures show that the carrier concentration increases and the Hall mobility decreases with annealing temperature. The increase in carrier concentration with annealing temperature could be related to the tin that could not enter the indium sites and was replaced with indium. The increase in carrier concentration may also be due to the increase in the number of oxygen vacancies with the high temperature annealing. The decrease in mobility with high temperature annealing may be due to the increased grain boundary scattering

[287]. The minimum value of resistivity of 8.0×10^{-4} Ω-cm which has been obtained for 10 wt.% Sn-doped ITO films annealed at 500^0C in nitrogen by the sol-gel process, which is comparable to those obtained by other conventional methods. Table 7.2 shows the resistivity of ITO films produced by different techniques.

Table 7.2: Resistivity of ITO films

Deposition technique	Resistivity(Ω-cm)
Sol-gel (this work)	8.0×10^{-4}
Magnetron sputtering [288]	3.74×10^{-4}
Thermal evaporation [289]	9.1×10^{-4}
Chemical Vapor Deposition [290]	2.83×10^{-3}
Reactive evaporation [291]	3.6×10^{-2}

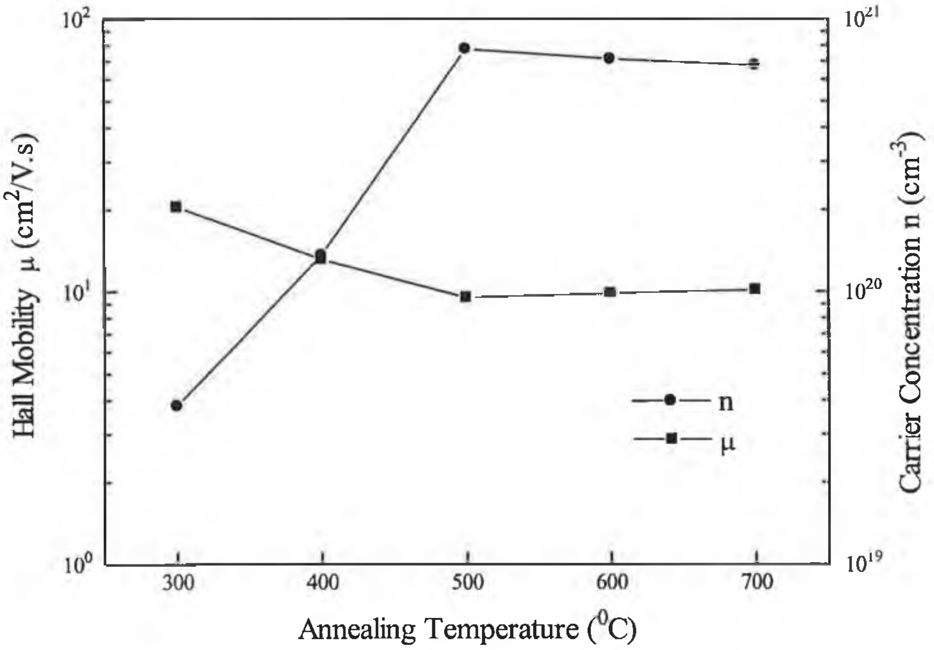

Figure 7.26 Variation of hall mobility (μ) and carrier concentration (n) as a function of annealing temperature in air for 10 wt.% Sn-doped ITO films.

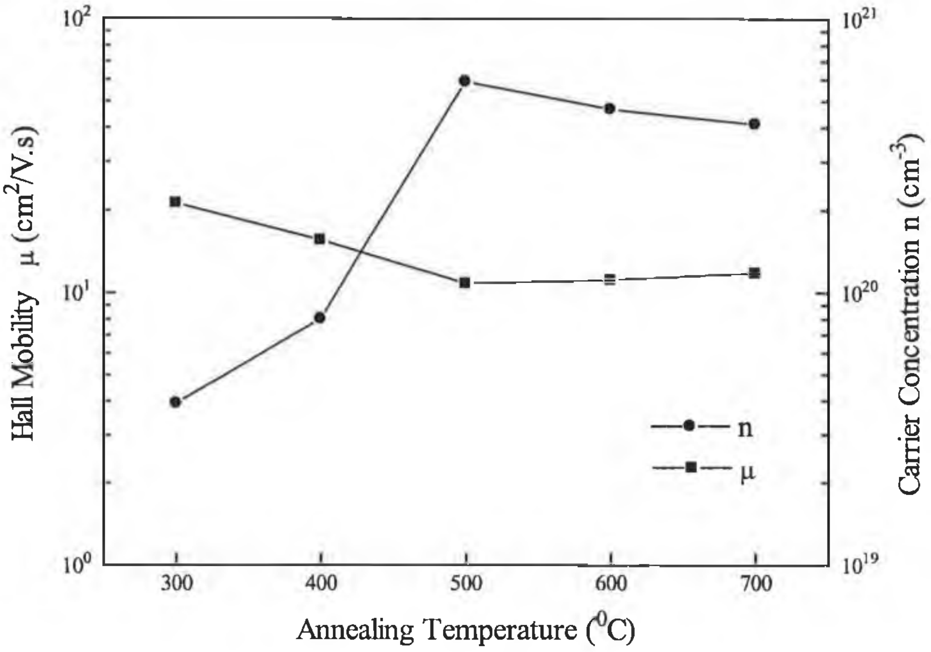

Figure 7.27 Variation of hall mobility (μ) and carrier concentration (n) as a function of annealing temperature in oxygen for 10 wt.% Sn-doped ITO films.

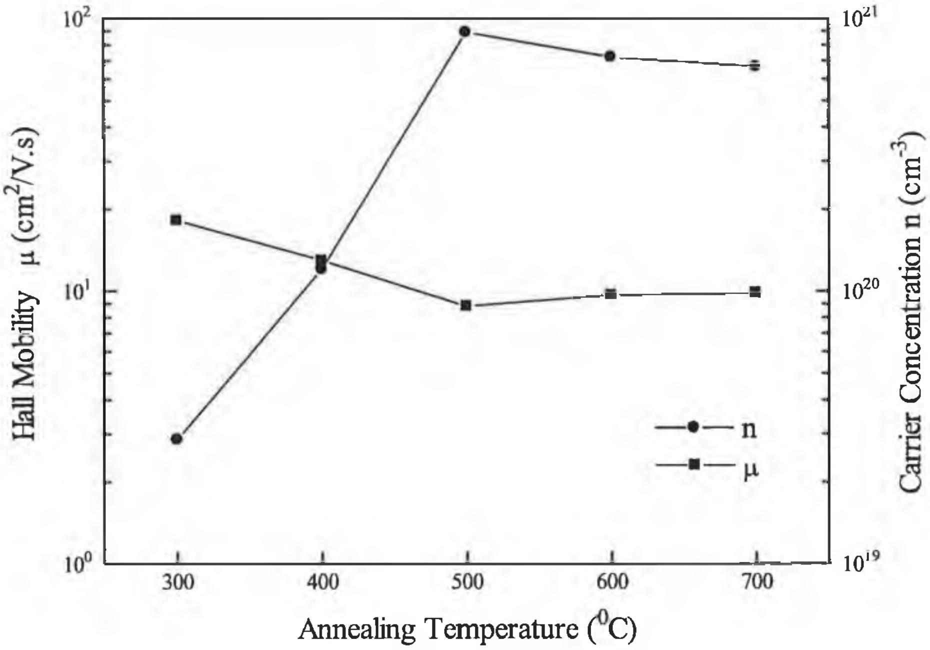

Figure 7.28 Variation of hall mobility (μ) and carrier concentration (n) as a function of annealing temperature in nitrogen for 10 wt.% Sn-doped ITO films.

7.3.3.2 Roughness

The average roughness (R_a) values were measured for 10 wt.% Sn-doped ITO films annealed at different temperature in presence of air, oxygen and nitrogen. Fig. 7.29 shows the variation of R_a with annealing temperature. Roughness of the substrate was measured to be 0.01 µm and for the as-deposited film was 0.08 µm. The minimum resolution of the instrument is 0.01 µm. This is the limitation of this instrument. So we could not measure the roughness beyond this minimum range. Roughness decreases with varying the temperature due to the crystallization effect.

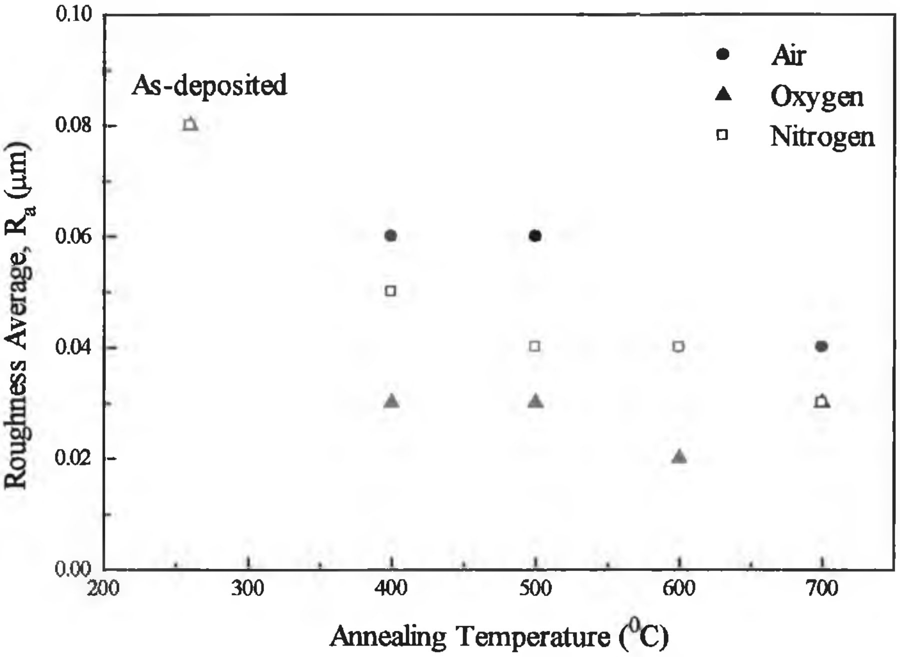

Figure 7.29 Variation of Roughness as a function of annealing temperature annealed in air, oxygen and nitrogen for 10 wt.% Sn-doped ITO films.

7.3.3.3 Structural Properties

7.3.3.3.1 X-ray Diffraction Spectroscopy

Fig. 7.30, 7.31 and 7.32 show the XRD spectra for 10 wt.% Sn-doped ITO films prepared from anhydrous indium trichloride by the sol-gel process annealed at different temperatures in presence of air, oxygen and nitrogen respectively. All the spectra show that as-deposited films are amorphous. After annealing in atmosphere at 400^0C and higher temperatures, the films showed evidence of conversion from an amorphous state to a polycrystalline state. As is seen, the position of the peaks agree well with the polycrystalline cubic bixbyite In_2O_3 structure with no preferred orientation (See Appendix A), which are in very good agreement with the Joint Committee on Powder Diffraction Standards (JCPDS) data base (Card No. 44-1087). No phases corresponding to tin or to other tin compounds were detected suggesting that the Sn was in solution in the In_2O_3. From all the XRD spectra, it is seen that the height of the main peak increases with increasing the annealing temperatures. Thus we can conclude that the crystallinity of ITO films is improved with an increase of annealing temperature in all atmospheres. Again, the XRD spectra of the ITO films annealed in air, oxygen and nitrogen show that the crystallinity of the films depends on the annealing temperatures rather than the atmosphere.

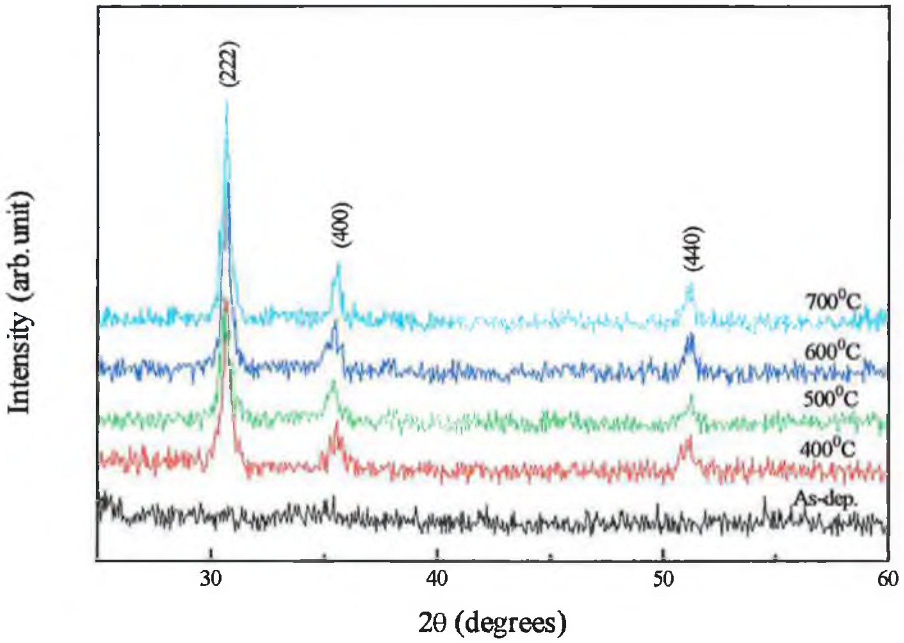

Figure 7.30 XRD spectra for 10 wt.% Sn-doped ITO films annealed at different temperatures in presence of air.

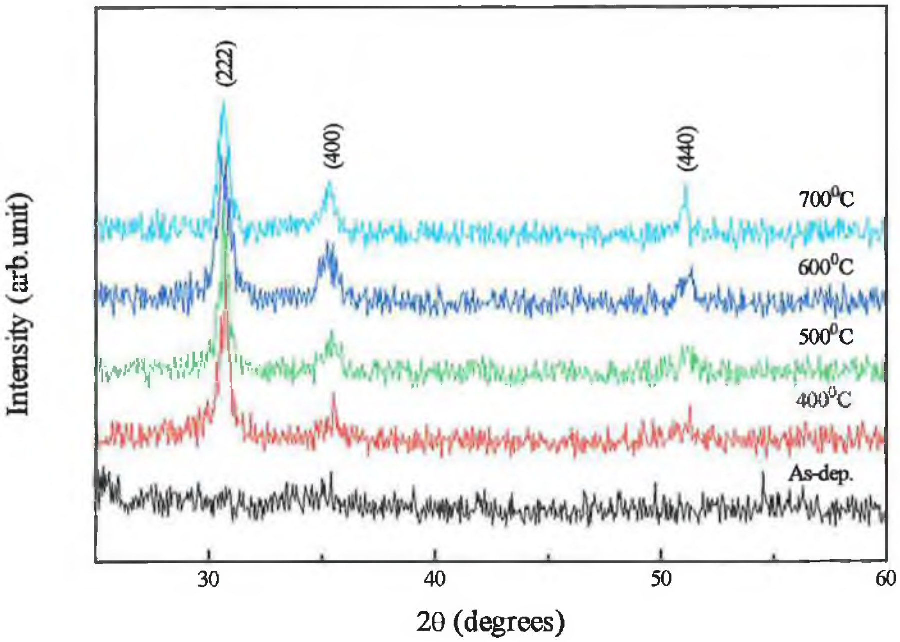

Figure 7.31 XRD spectra for 10 wt.% Sn-doped ITO films annealed at different temperatures in presence of oxygen.

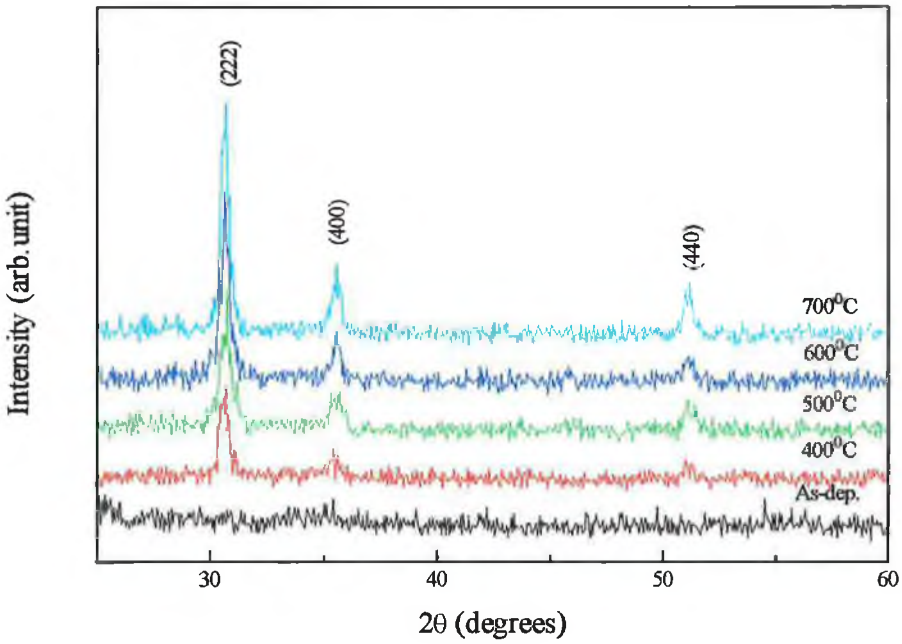

Figure 7.32 XRD spectra for 10 wt.% Sn-doped ITO films annealed at different temperatures in presence of nitrogen.

7.3.3.3.2 X-ray Photoelectron Spectroscopy

A X-ray photoelectron spectroscopy (XPS) spectrum of the as-deposited indium tin oxide thin films with 10% tin content deposited on a silicon wafer is shown in fig. 7.33. Photoelectron peaks for In, Sn, O and C were recorded for the ITO film in the binding energy range of 0 to 1100 eV. The binding energy of the O 1s photoelectron peak is at 534 eV. A C 1s peak at a binding energy of 284 eV is also observed on the surface of the film. The presence of this peak is related to surface pollution which corresponds to the fact that the samples were exposed to air before the XPS measurements.

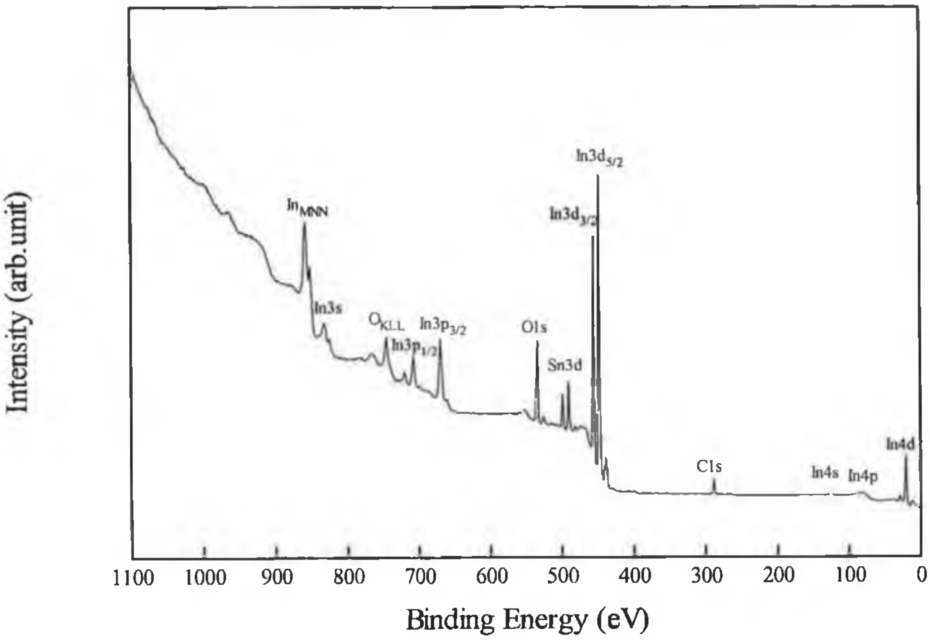

Figure 7.33 XPS wide scan spectra of the as-deposited 10 wt.% Sn-doped ITO thin film deposited on silicon.

The XPS spectra for the O 1s peak and the In 3d and Sn 3d doublets are shown in fig. 7.34, fig. 7.35 and fig. 7.36 respectively. These show evidence of only one binding state for In and Sn since there is no sign of broadening or splitting of the peaks. Fig. 7.34, fig. 7.35 and fig. 7.36 indicate that oxygen is bonded to the indium and tin and that ITO is formed [292,293]. The binding energy of In $3d_{5/2}$ at 445.1 eV measured from ITO film shown in fig. 7.35 can be attributed to the In^{3+} bonding state from In_2O_3 which corresponds to the previous studies [294,295]. The binding energy of Sn $3d_{5/2}$ is at 487.1 eV (fig. 7.36) and corresponds to the Sn^{4+} bonding state from SnO_2 [294,296].

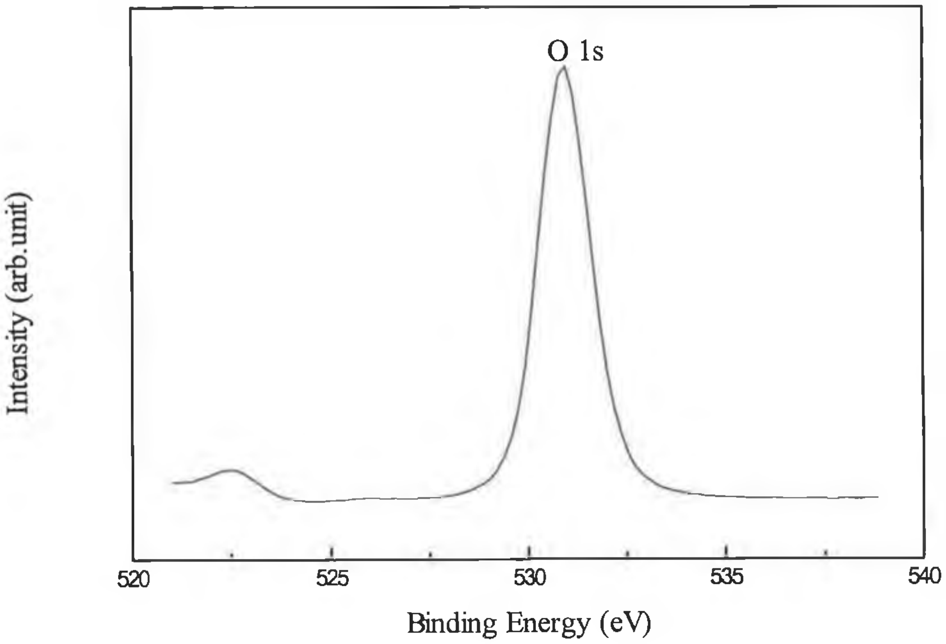

Figure 7.34 XPS narrow scan spectra of O 1s peak from ITO film.

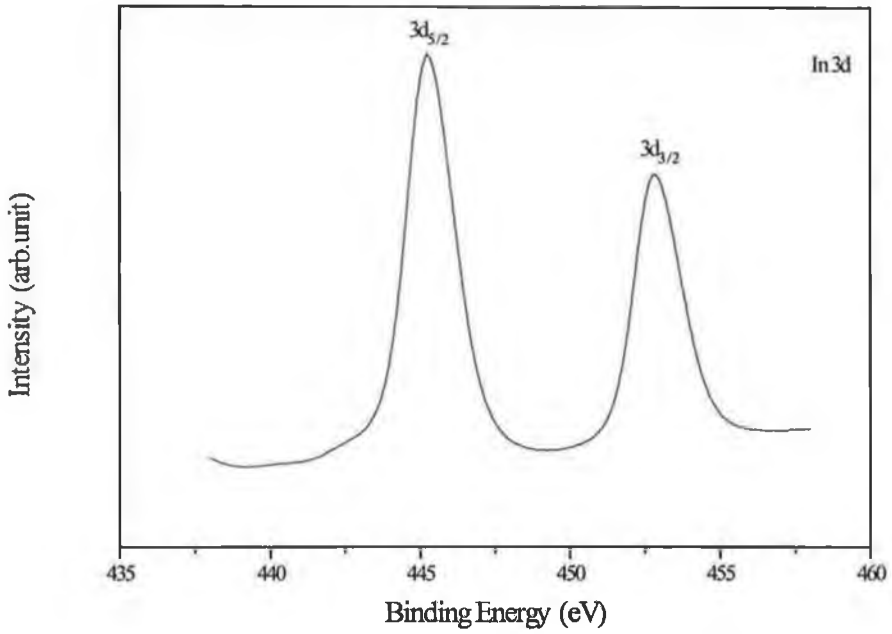

Figure 7.35 XPS narrow scan spectra of In 3d doublet from ITO film.

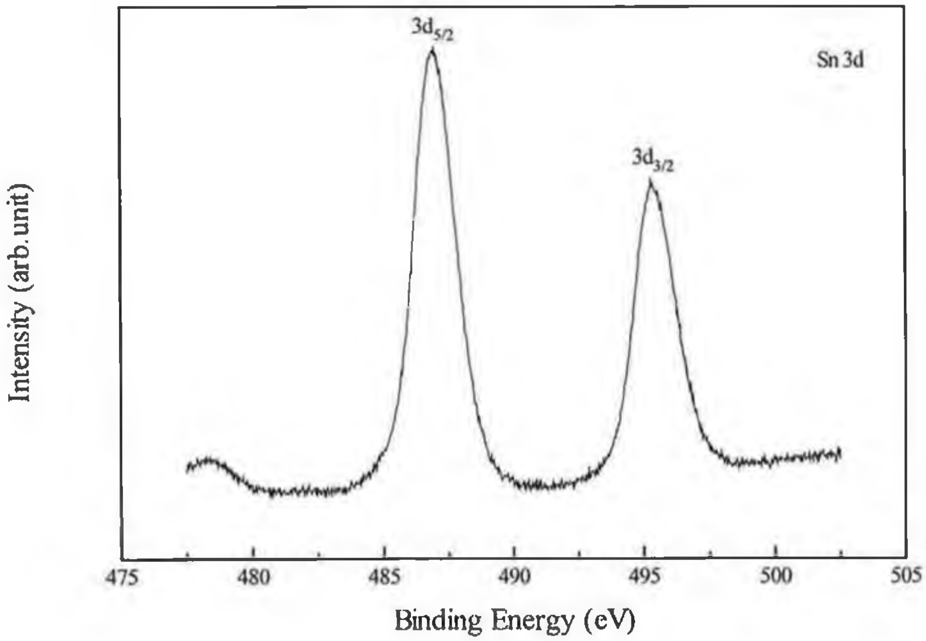

Figure 7.36 XPS narrow scan spectra of Sn 3d doublet from ITO film.

7.3.3.4 Optical Properties

Information concerning optical transmittance is important in evaluating the optical performance of conducting oxide films. A high transparency for the ITO thin film in the visible region is required in applications with transparent electrodes for optoelectronic devices. Fig. 7.37, 7.38 and 7.39 show the optical transmission spectra for 10 wt.% Sn-doped ITO films with a thickness of 250 nm annealed at different temperatures in the presence of air, oxygen and nitrogen. The optical transmission of ITO films in the visible region improved with increasing annealing temperature showing maximum transmittance at 900 nm of 78% for as-deposited film and 88.69%, 87.24% and 87.21% when annealed at 700^0C in air, oxygen and nitrogen respectively. The UV absorption edge is located at approximately 300 nm. The optical transmission of ITO film increases from 78% to 89% at 900 nm in all cases, which is sufficiently high for use as a transparent electrode in thin film electroluminescent devices [289,297]. From the transmission spectra of ITO films in different atmospheres, we can see that the atmosphere has no significant effect on the optical transmission of the films.

High temperature annealing leads to films with a steeper optical absorption curve, which indicates a better crystallinity of the films and lower defect density near the band edge. The increase in optical transmittance with temperature can be attributed to the increase of structural homogeneity and crystallinity [257].

From the transmission spectra in the UV region, the absorption coefficient, α can be calculated using equation 7.2. The absorption coefficient for the as-deposited 10 wt.% Sn-doped ITO films with a thickness of 250 nm is $9.94 \mathrm{x} 10^3$ cm^{-1} at a wavelength of 900 nm. The absorption coefficients for 10 wt.% Sn-doped ITO films with a thickness of 250 nm are $5.46 \mathrm{x} 10^3$, $4.80 \mathrm{x} 10^3$ and $5.47 \mathrm{x} 10^3 \mathrm{cm}^{-1}$ at a wavelength of 900 nm annealed at 700^0C in air, oxygen and nitrogen respectively. We can see that the absorption coefficients decrease with the annealing temperatures in different atmospheres.

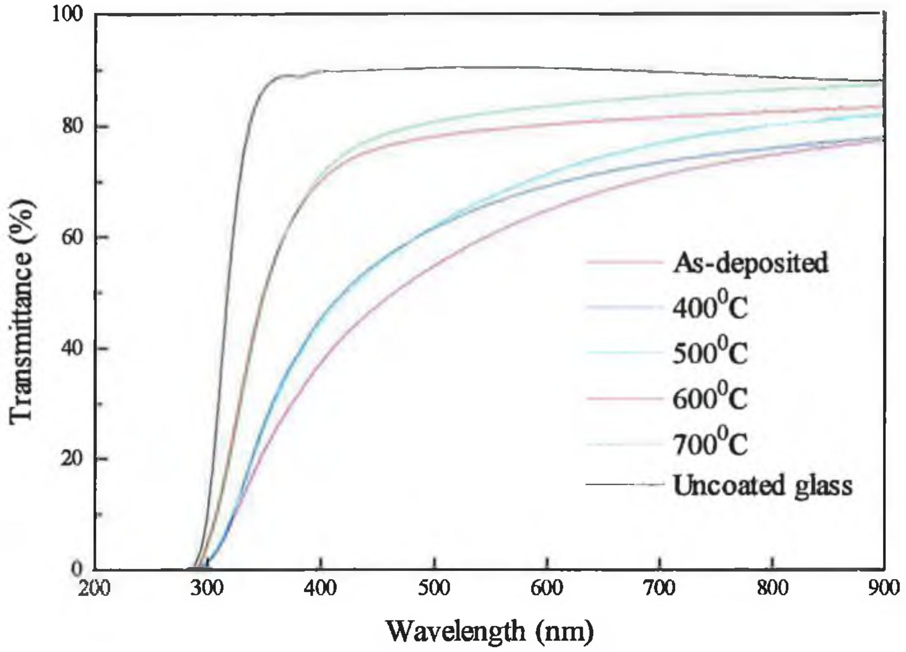

Figure 7.37 Optical transmission spectra for 10 wt.% Sn-doped ITO films with a thickness of 250 nm annealed at different temperatures in presence of air.

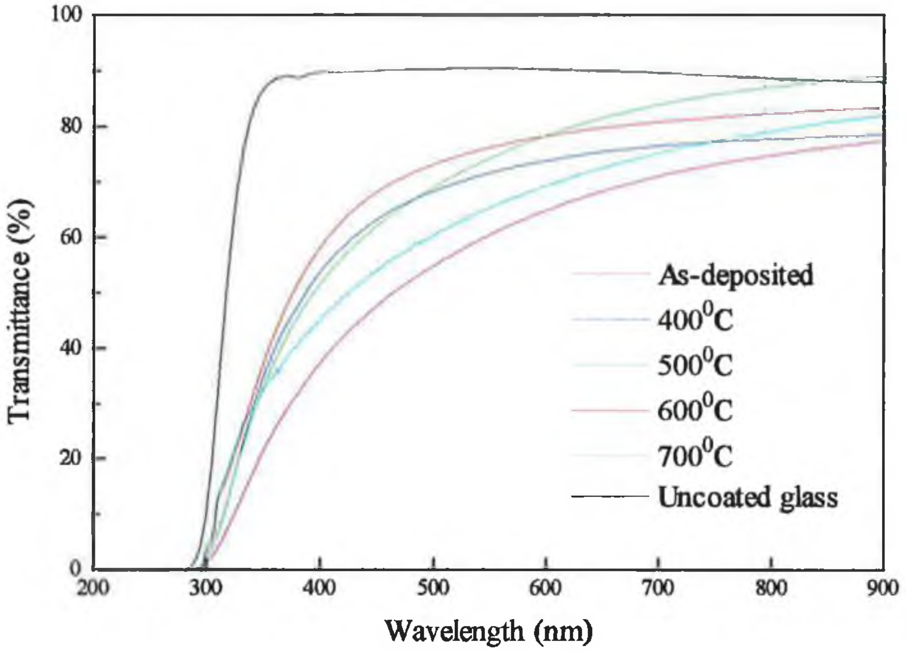

Figure 7.38 Optical transmission spectra for 10 wt.% Sn-doped ITO films with a thickness of 250 nm annealed at different temperatures in presence of oxygen.

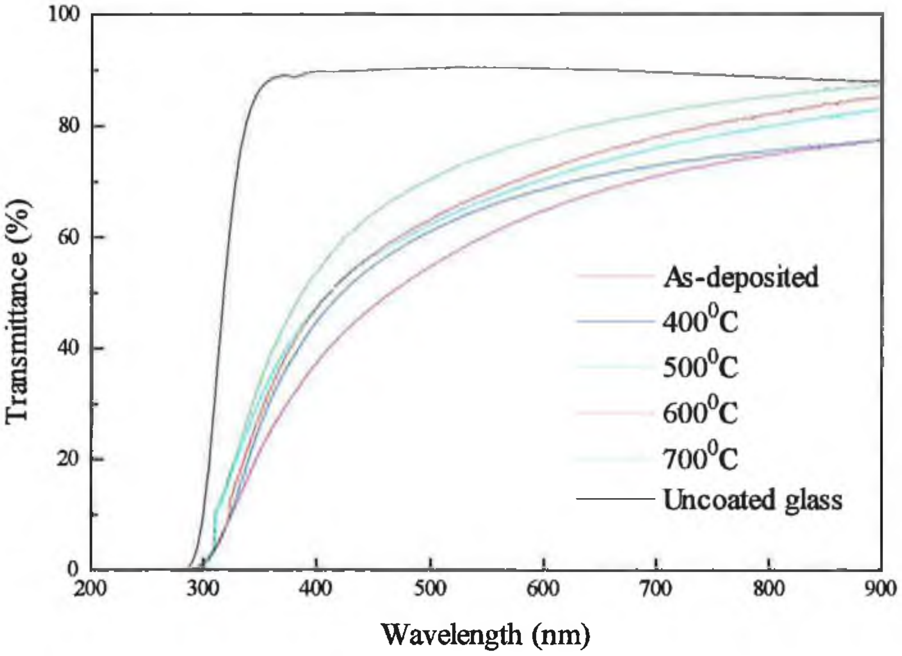

Figure 7.39 Optical transmission spectra for 10 wt.% Sn-doped ITO films with a thickness of 250 nm annealed at different temperatures in presence of nitrogen.

7.3.4 Conclusions

ITO films have been prepared by the sol-gel process using low cost, non-alkoxide compounds. The resistivity, hall mobility and carrier concentration of the films were measured for different Sn concentration in the solution and also annealed at different temperatures in the presence of air, oxygen and nitrogen. The resistivity of the films containing 10% Sn has a minimum value of 8.5×10^{-4} Ω-cm, 9.8×10^{-4} Ω-cm and 8.0×10^{-4} Ω-cm when annealed at 500^0C in air, oxygen and nitrogen respectively.

The films have an optical transparency up to 89% at 900 nm. The atmosphere has no significant effect on the optical transmission of the films.

The films are polycrystalline indium oxide with a cubic bixbyite structure with no preferred orientation. There is no evidence of Sn compound (SnO, SnO_2, etc.) in the XRD spectrum showing that a solution of Sn in In_2O_3 is formed. The crystallinity of the films is not impacted by exposure to different atmospheres (air, O_2 and N_2).

XPS analysis has shown that the oxygen atoms are bonded to In atoms and Sn atoms indicating the formation of ITO compound.

ITO films prepared by this sol-gel process have properties of transparency and resistivity which are comparable to those prepared by other methods and have the potential for application to large panels at low cost.

Chapter 8

COMBINED EFFECT OF INSULATING AND TRANSPARENT CONDUCTING LAYERS USED IN THIN FILM ELECTROLUMINESCENT DEVICES

8.1 Introduction

Generally thin film electroluminescent devices consist of an insulating layer, transparent conducting layer and an active layer, called the phosphor layer. There are two device structures used in practical thin film electroluminescent displays: (a) a conventional device structures and (b) an inverted device structures.

Fig. 8.1 shows the fundamental device structure of a conventional thin film electroluminescent device consisting of metal electrode/ insulating layer/ phosphor layer/ insulating layer/ transparent electrode/ glass substrate. Generally the device consists of a triple layer structure, namely, an active layer sandwiched between two insulating layers. Because of this sandwich structure, undesirable leakage current flowing through the device is prevented. Consequently, the device can keep a sufficiently high electric field for EL operation across the active layer without breakdown. In the conventional TFEL device, there is a transparent electrode on top the of substrate and a metal electrode on top of the upper insulator.

Fig. 8.2 shows the structure of an inverted thin film electroluminescent device consisting of transparent electrode/ insulating layer/ phosphor layer/ insulating layer/ metal electrode/ glass substrate. In the inverted TFEL device, the metal electrode is on top of the substrate and the transparent electrode is on top of the upper insulator.

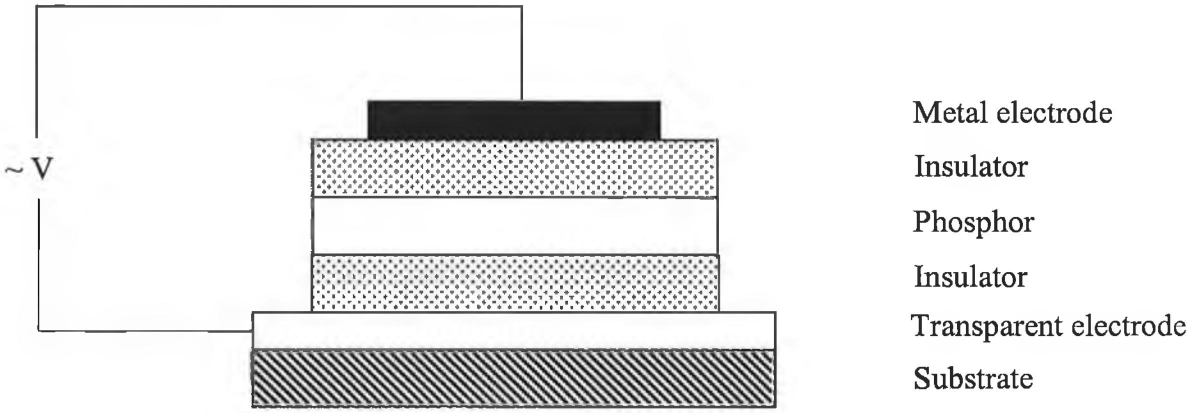

Figure 8.1 Fundamental structure of a conventional thin film electroluminescent device.

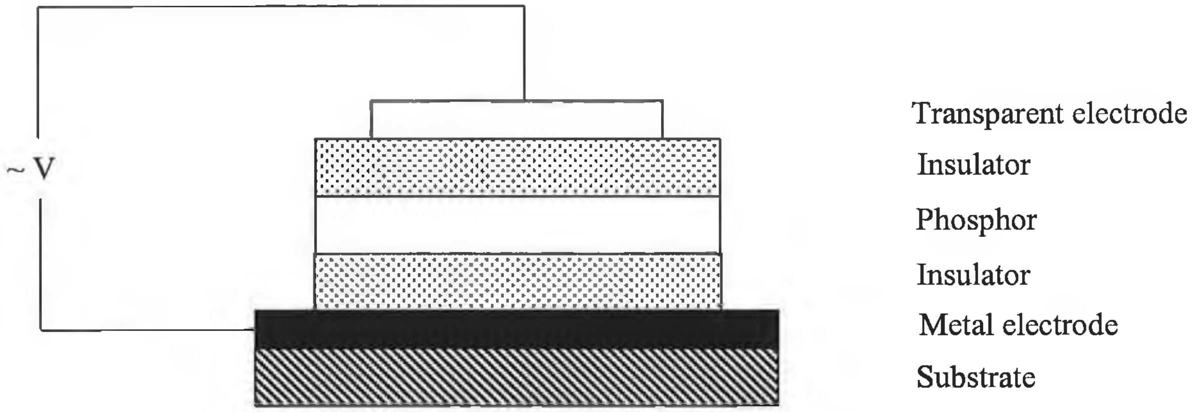

Figure 8.2 Fundamental structure of an inverted thin film electroluminescent device.

The electrical, optical and structural properties of insulating layers and transparent electrodes prepared by sol-gel process are discussed in chapter 6 and chapter 7 respectively. In an inverted thin film electroluminescent device, the transparent electrode is used on top of the upper insulator. The individual characteristics of insulating and transparent conducting films studied in chapter 6 and 7 are found to be suitable for use in thin film electroluminescent devices. But if the transparent conducting films are deposited on top of insulating films, their properties may be changed. The combined characteristics of transparent electrodes deposited on top of the insulating layer are studied and discussed in this chapter.

8.2 Characterization of Transparent Conductive ZnO:Al Thin Films Deposited on Titanium Dioxide Film and Tantalum Oxide Film by Sol-gel Process

8.2.1 Introduction

Transparent conducting oxide coatings have been extensively used as transparent electrodes in electroluminescent display devices. The electrode material for display devices must be conducting and optically transparent. Zinc oxide based coatings have recently received much attention as transparent electrodes because they have advantages over the more commonly used indium and tin-based oxide films. Indium oxide and tin oxide films are usually more expensive than zinc oxide films. Pure zinc oxide films, although transparent, are usually highly resistive. Non-stoichiometric and doped zinc oxide films have high conductivities. For practical applications, therefore, doped ZnO films are more suitable.

Aluminum doped zinc oxide thin films have been prepared on glass substrates by the sol-gel process and their electrical resistivity has been measured. The resistivity of 0.8 at.% Al content ZnO films showed the minimum value of $1.3\text{x}10^{-4}$ Ω-cm annealed at 500^0C in nitrogen. Now ZnO:Al thin films have been deposited on titanium dioxide and tantalum oxide coated substrates and the performance of the transparent conducing ZnO:Al films on top of these insulating films was investigated for their use in thin film electroluminescent devices.

8.2.2 Results and Discussion

Fig. 8.3 shows the resistivity of aluminum doped zinc oxide thin films with aluminum dopant concentrations in the solution annealed at 500^0C in nitrogen deposited on titanium dioxide thin film. The resistivity of the film decreased with increasing Al content up to 0.8 at.%. The resistivity of 0.8 at.% Al content ZnO films showed a minimum value of $2.5\text{x}10^{-3}$ Ω-cm and thereafter the resistivity started to increase with increased doping similar to the behaviour shown for ZnO:Al thin films deposited on glass.

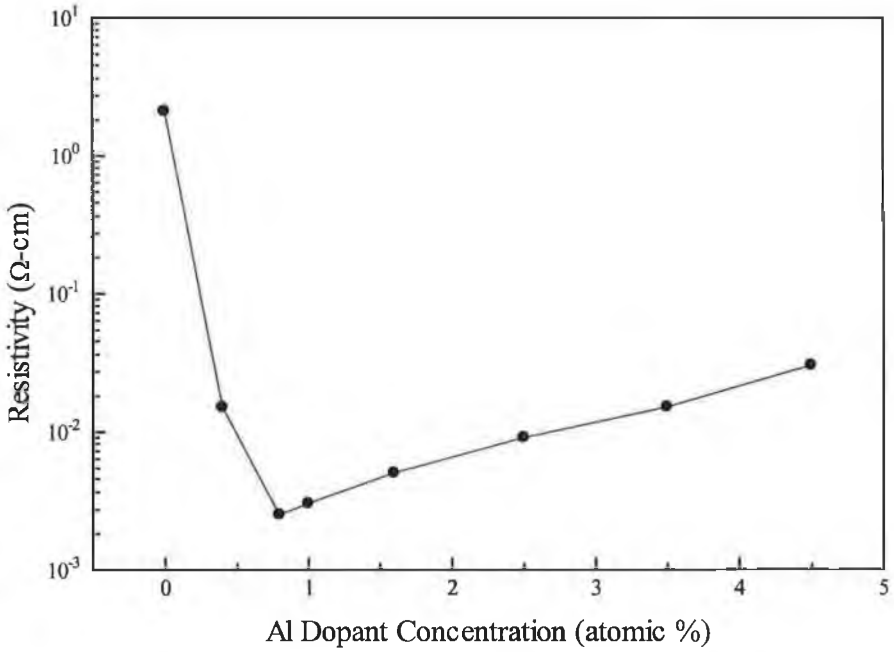

Figure 8.3 Resistivity of the ZnO:Al thin films as a function of aluminum dopant concentration in the solution deposited on titanium dioxide thin film annealed at 500^0C in nitrogen.

Fig. 8.4 shows the resistivity of 0.8 at.% Al doped ZnO films as a function of annealing temperature in nitrogen deposited on titanium dioxide thin film. Samples were annealed for 1 hour at each temperature. The resistivity decreased significantly with annealing temperature up to 500^{0}C in nitrogen and then it started increasing similar to the behaviour shown for ZnO:Al thin films deposited on glass. The minimum value of resistivity of 2.5x10^{-3} Ω-cm was obtained after annealing at 500^{0}C in nitrogen which is higher than the resistivity of 1.3x10^{-4} Ω-cm obtained for ZnO:Al thin films on glass.

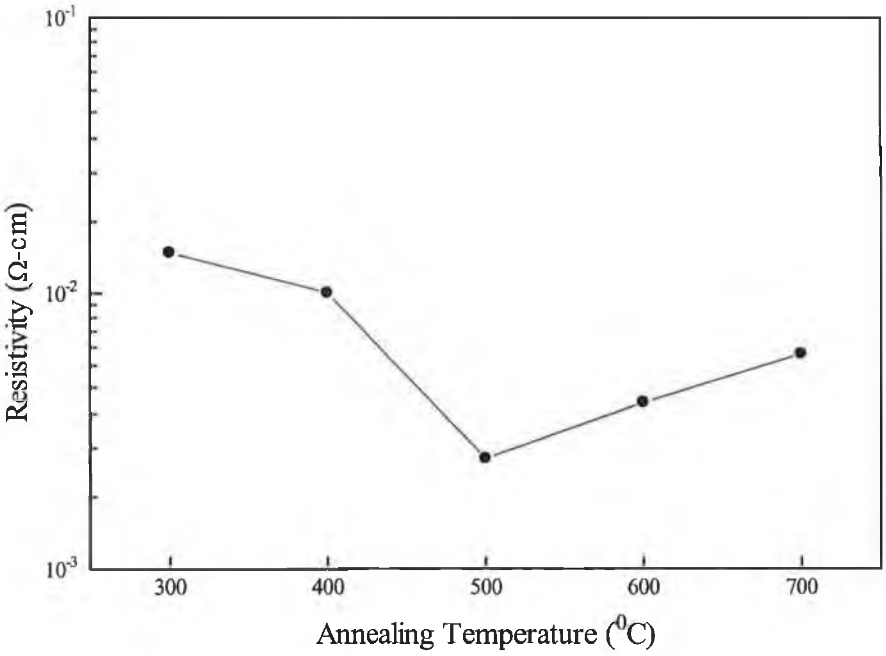

Figure 8.4 Resistivity of 0.8 at.% Al doped ZnO thin films as a function of annealing temperature in nitrogen deposited on titanium dioxide thin film.

Fig. 8.5 shows the resistivity of aluminum doped zinc oxide thin films with aluminum dopant concentrations in the solution annealed at 500^{0}C in nitrogen deposited on tantalum oxide thin film. The resistivity of the film decreased with increasing Al content up to 0.8 at.%. The resistivity of 0.8 at.% Al content ZnO films showed the minimum value of 9.6x10^{-4} Ω-cm and thereafter the resistivity started to increase with increased doping similar to the behaviour shown for ZnO:Al thin films deposited on glass.

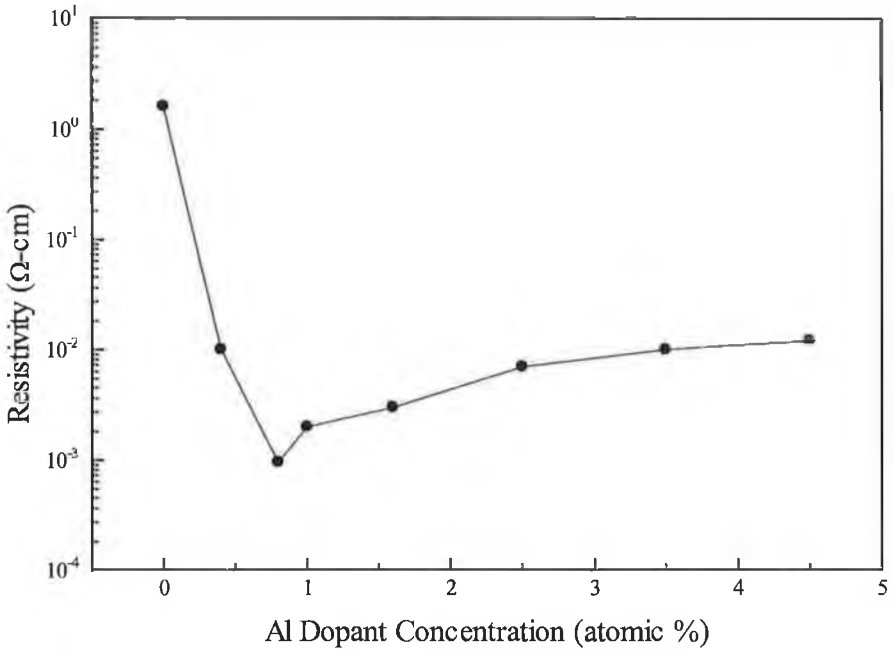

Figure 8.5 Resistivity of the ZnO:Al thin films as a function of aluminum dopant concentration in the solution deposited on tantalum oxide thin film annealed at 500^0C in nitrogen.

Fig. 8.6 shows the resistivity of 0.8 at.% Al doped ZnO films as a function of annealing temperature in nitrogen deposited on tantalum oxide thin film. Samples were annealed for 1 hour at each temperature. The resistivity decreased significantly with annealing temperature up to 500^0C in nitrogen and then it started increasing similar to the behaviour shown for ZnO:Al thin films deposited on glass. The minimum value of resistivity of $9.6x10^{-4}$ Ω-cm was obtained after annealing at 500^0C in nitrogen for ZnO:Al films deposited on top of tantalum oxide films.

The resistivity curves of ZnO:Al thin films deposited on titanium dioxide and tantalum oxide film show the same general behaviour as when deposited on glass, but higher resistivity. One possible reason might be interdiffusion between insulating and conducting layers. Aluminum could diffuse into the insulating layer or titanium or tantalum could diffuse into the conducting layer. In order to test this, transparent conducting films of various thickness were deposited on top of titanium dioxide and tantalum oxide films and the conductivity of the ZnO:Al films were measured to see how the conductance changes with film thickness. Fig. 8.7 shows the variation of conductance of ZnO:Al film as a function of thickness deposited on glass and deposited on titanium dioxide and tantalum oxide film on glass annealed at 500^{0}C in nitrogen.

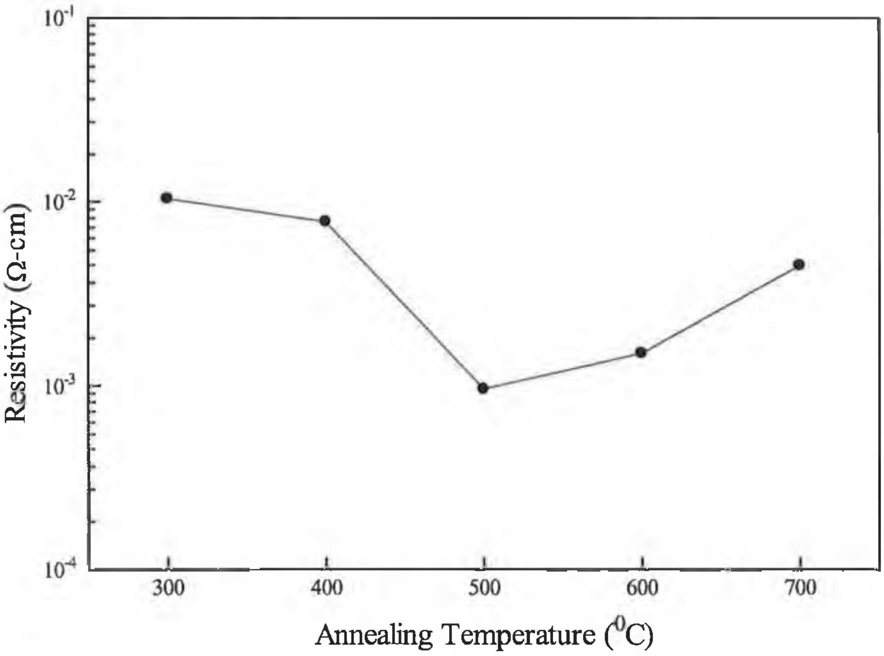

Figure 8.6 Resistivity of 0.8 at.% Al doped ZnO thin films as a function of annealing temperature in nitrogen deposited on tantalum oxide thin film.

Fig. 8.7 shows that the conductance of ZnO:Al thin films deposited on glass and tantalum oxide increases linearly with the increase of thickness showing that there is no interdiffusion between the conducting and insulating layers. But the conductance of ZnO:Al thin films deposited on titanium dioxide film on glass is very small up to the thickness of 300 nm and then it increases with a similar slope to the others. This means that there is a approximately 300 nm zone whose conductivity is affected by the substrate, e.g. by outdiffusion of titanium from the titanium dioxide insulating layer and there is no effect of the titanium after 300 nm thickness of ZnO:Al.

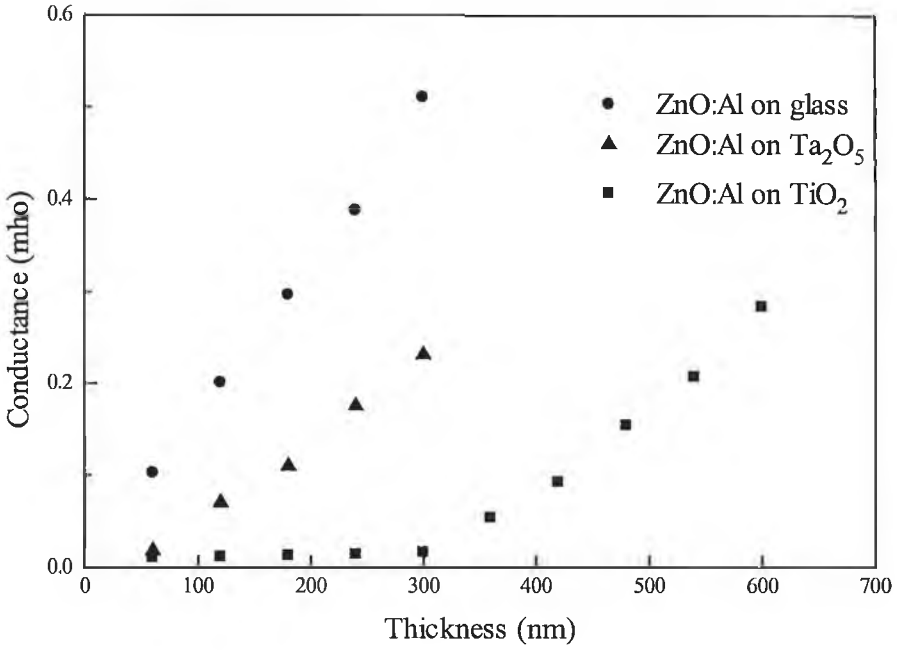

Figure 8.7 Conductance of ZnO:Al thin films as a function of thickness deposited on glass and on titanium dioxide and tantalum oxide film on glass annealed at 500^0C in nitrogen.

8.3 Characterization of Transparent Conductive ITO Thin Films Deposited on Titanium Dioxide Film and Tantalum Oxide Film by Sol-gel Process

8.3.1 Introduction

Transparent conductive indium tin oxide thin films can also be used as transparent electrode on top of the insulating layer in an inverted thin film electroluminescent device. Indium tin oxide thin films have been prepared on glass substrate by the sol-gel process and their electrical resistivity has been measured. The resistivity of 10 wt.% Sn content ITO films showed the minimum value of $8.0\text{x}10^{-4}$ Ω-cm annealed at 500^0C in nitrogen. Now ITO thin films have been deposited on titanium dioxide and tantalum oxide coated substrates and the performance of the ITO conductor on top of these insulating films was investigated for their use in thin film electroluminescent devices.

8.3.2 Results and Discussion

Fig. 8.8 shows the resistivity of ITO thin films with tin dopant concentrations in the solution annealed at 500^{0}C in nitrogen for one hour deposited on titanium dioxide film on glass. It was found that the resistivity of ITO films is strongly dependent on the tin doping concentration. The resistivity of the film decreased with increasing Sn content up to 10 wt. %. The resistivity of 10 wt. % Sn content ITO films showed a minimum value of approximately 9.5x10^{-4} Ω-cm and the resistivity increased for greater Sn content.

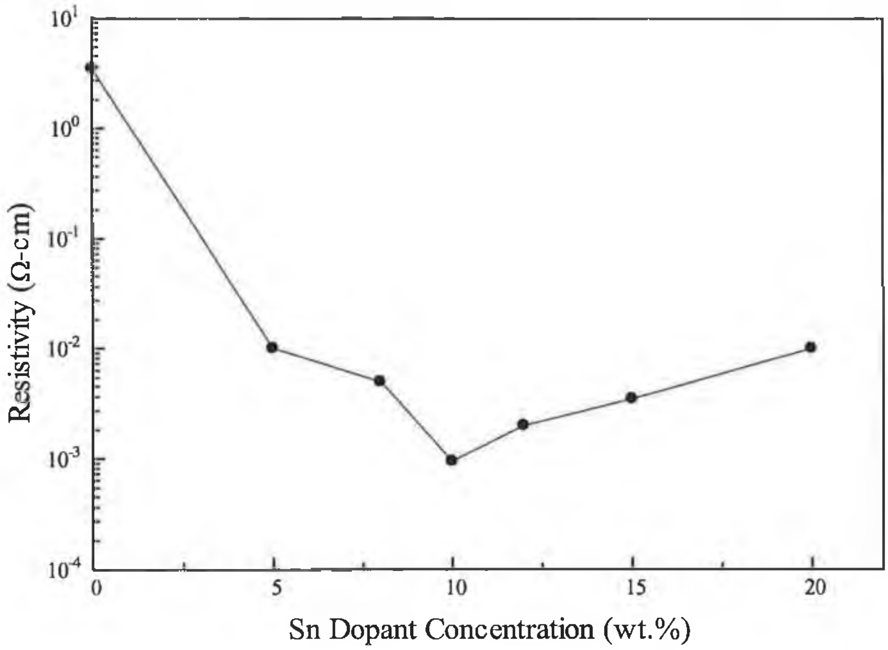

Figure 8.8 Resistivity of the ITO thin films as a function of tin dopant concentration in the solution deposited on titanium dioxide thin film annealed in nitrogen.

Fig. 8.9 shows the variation of resistivity of films with 10 wt. % Sn doping as a function of annealing temperature in nitrogen deposited on titanium dioxide thin film on glass. Samples were annealed for 1 hour at each temperature. Up to 500^{0}C there was a large reduction in resistivity and after that it started to increase. The resistivity of the films was measured by depositing them on top of a titanium dioxide layer by a sol-gel process. This combination of an ITO transparent conductor and a high permittivity TiO_2 insulator is an important constituent of a thin film electroluminescent display. The minimum value of resistivity of 9.5x10^{-4} Ω-cm was obtained after annealing at 500^{0}C in nitrogen.

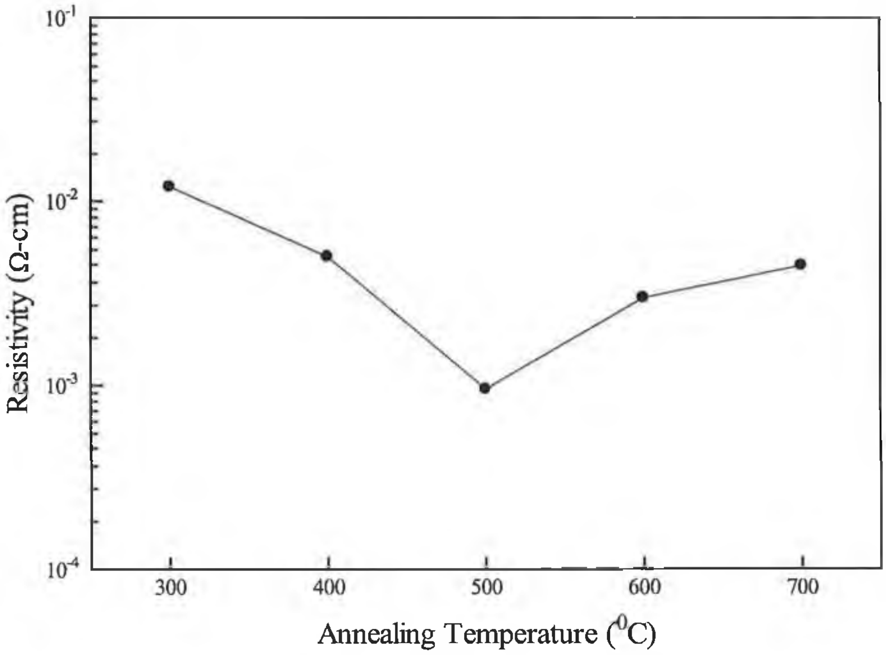

Figure 8.9 Resistivity of the ITO thin films as a function of annealing temperature in nitrogen deposited on titanium dioxide thin film.

Fig. 8.10 shows the resistivity of ITO thin films with tin dopant concentrations in the solution annealed at 500^{0}C in nitrogen for one hour deposited on tantalum oxide film on glass. It was found that the resistivity of ITO films is strongly dependent on the tin doping concentration. The resistivity of the film decreased with increasing Sn content up to 10 wt. %. The resistivity of 10 wt. % Sn content ITO films showed a minimum value of approximately 9.0x10^{-4} Ω-cm and the resistivity increased for greater Sn content.

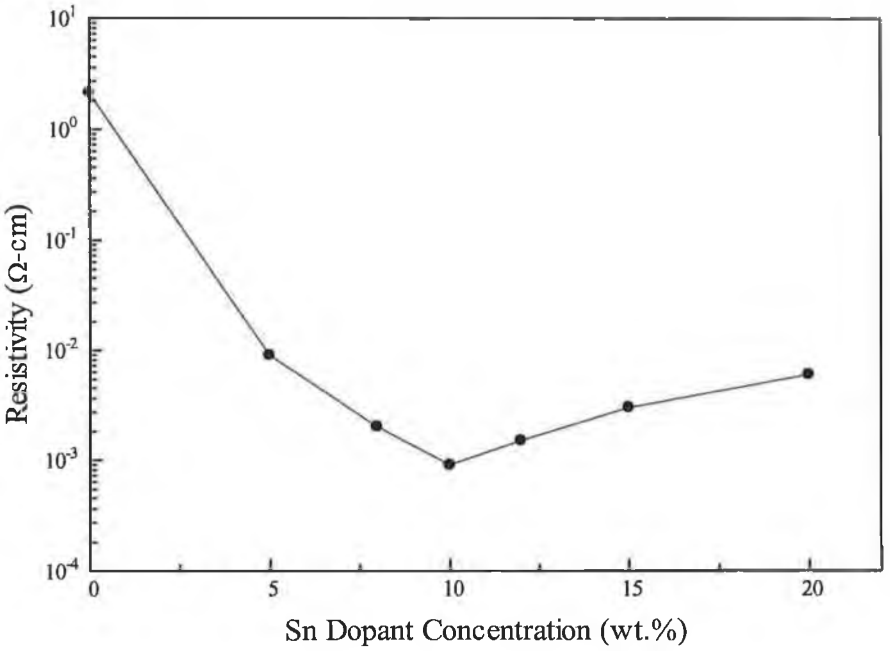

Figure 8.10 Resistivity of the ITO thin films as a function of tin dopant concentration in the solution deposited on tantalum oxide thin film annealed in nitrogen.

Fig. 8.11 shows the variation of resistivity of films with 10 wt. % Sn doping as a function of annealing temperature in nitrogen deposited on tantalum oxide thin film on glass. Samples were annealed for 1 hour at each temperature. Up to 500^0C there was a large reduction in resistivity and after that it started to increase. The resistivity of the films was measured by depositing them on top of a tantalum oxide layer by a sol-gel process. The minimum value of resistivity of $9.0x10^{-4}$ Ω-cm was obtained after annealing at 500^0C in nitrogen .

In this case also, the resistivity curves of ITO thin films deposited on titanium dioxide and tantalum oxide film show the same general behaviour as deposited on glass, but higher resistivity. One possible reason for this higher resistivity might be interdiffusion between insulator and conductor. Indium or tin could diffuse into the insulating layer or titanium or tantalum could diffuse into the conducting layer. In order to check this interdiffusion, transparent conducting ITO films of various thickness were deposited on top of titanium dioxide and tantalum oxide films and the conductivity of the ITO films were measured to see how the conductance changes with film thickness. Fig. 8.12 shows the variation of conductance of ITO film as a function of thickness deposited on glass and deposited on titanium dioxide and tantalum oxide film on glass annealed at 500^0C in nitrogen. This figure shows that the conductance of ITO thin films increases linearly with the increase of thickness in all the cases. But the ITO thin films deposited on titanium dioxide and tantalum oxide film on glass show lower conductance than that when deposited on glass. This shows that depositing the ITO on to TiO_2 and Ta_2O_5 has a small but significant effect on the conductance, probably due to some interdiffusion. If the conductance line for ITO film deposited on top of titanium dioxide is extrapolated, we see that it intersects the x-axis approximately at 40 nm. From this, we can conclude that there is an affect of interdiffusion between the interface up to the thickness of 40 nm of ITO film on top of titanium dioxide and after that there is no affect of interdiffusion between the conducting and insulating layers.

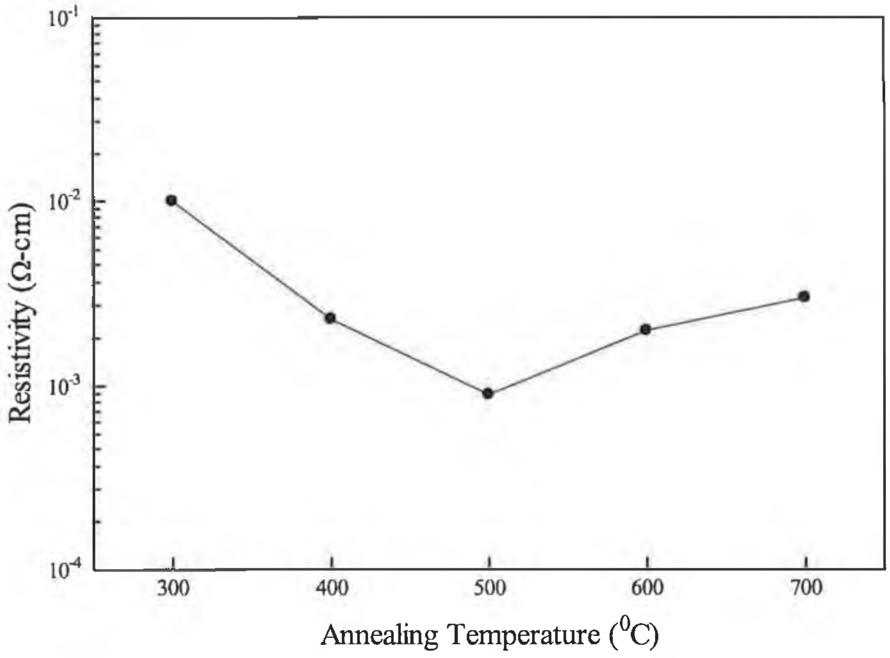

Figure 8.11 Resistivity of the ITO thin films as a function of annealing temperature in nitrogen deposited on tantalum oxide thin film.

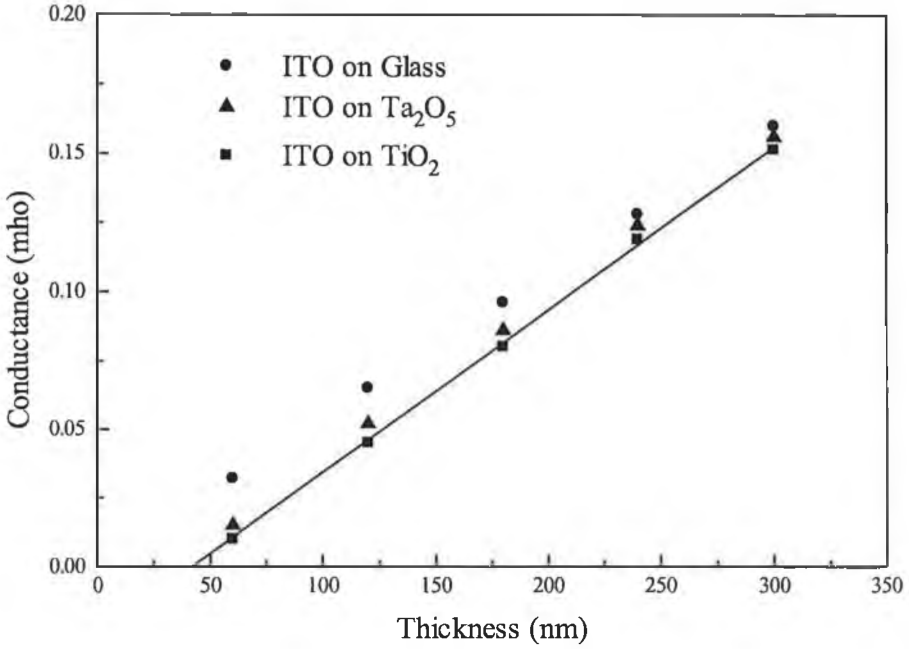

Figure 8.12 Conductance of ITO thin films as a function of thickness deposited on glass and deposited on titanium dioxide and tantalum oxide film on glass annealed at 500^0C in nitrogen.

8.4 Conclusions

The resistivity of ZnO:Al thin films containing 0.8 at.% Al deposited on glass has a minimum value of $1.3\text{x}10^{-4}$ Ω-cm when annealed at 500^0C in nitrogen. The resistivity of ZnO:Al thin films deposited on titanium dioxide and tantalum oxide film on glass have a minimum value of $2.5\text{x}10^{-3}$ Ω-cm and $9.6\text{x}10^{-4}$ Ω-cm respectively annealed at 500^0C. So ZnO:Al thin films deposited on tantalum oxide film on glass have lower resistivity as that on glass but ZnO:Al thin films deposited on titanium dioxide film on glass have a higher resistivity than that of deposited on glass. This increase in resistivity on titanium dioxide film is due to the diffusion of titanium into the zinc oxide layer. The graph of conductance versus thickness (fig. 8.7) shows that titanium is diffused up to the thickness of 300 nm of ZnO:Al layer where there is no affect of titanium into the ZnO:Al layer after 300 nm. So it is clear that this combination of transparent conductive ZnO:Al and titanium dioxide insulating layer is not suitable for thin film electroluminescent devices whereas ZnO:Al on top of Ta_2O_5 can be used for thin film electroluminescent devices.

Indium tin oxide thin films were deposited on titanium dioxide and tantalum oxide film on glass for thin film electroluminescent devices. The resistivity of ITO thin films containing 10 wt.% Sn deposited on glass has a minimum value of 8.0×10^{-4} Ω-cm annealed at 500^0C. The resistivity of ITO films deposited on titanium dioxide and tantalum oxide film has a minimum value of 9.5×10^{-4} Ω-cm and 9.0×10^{-4} Ω-cm respectively annealed at 500^0C which are higher than that deposited on glass. Conductance versus thickness graph (fig. 8.12) for ITO thin films shows that there is a very small diffusion of titanium and tantalum into the indium oxide layer. There is an affected zone of up to approximately 40 nm when ITO is deposited on TiO_2 or Ta_2O_5 due to out diffusion of Ti or Ta into the ITO film. Therefore, this combination of transparent conductive ITO thin films and titanium dioxide or tantalum oxide insulating layer can be used for thin film electroluminescent devices.

Chapter 9

CONCLUSIONS AND RECOMMENDATIONS

This chapter describes the conclusions that can be drawn from different experimental measurements and investigations carried out for the high permittivity insulators, transparent conductors and the combination of transparent conducting films deposited on top of insulating films by the sol-gel process. Recommendations for future work that can be carried out are also described in this chapter.

9.1 Conclusions of the Work

The high permittivity insulators and transparent conductors have been prepared by the sol-gel process and their electrical, optical and structural properties are described in this work. The results described in this thesis have shown that the sol-gel technique is suitable for producing insulating and transparent conducting layers for fabricating an electroluminescent display. Thin films prepared by this sol-gel process are very uniform and cheaper compared to other conventional thin film deposition process.

Insulating films of titanium dioxide and tantalum oxide have been prepared by the sol-gel process and their structural, electrical and optical properties have been investigated after annealing at different temperatures in the presence of air, oxygen and nitrogen.

The electrical properties of the as-deposited and annealed TiO_2 thin films were characterised by C-V and I-V measurements. The I-V measurement shows that the leakage current density of the films decreases upon annealing at higher temperatures where this reduction in leakage current density is due to the reduction of the concentration of impurities such as carbon and the reduction of oxygen vacancies in TiO_2 films. The leakage current for the as-deposited film is approximately 5.0×10^{-5} A/cm^2 at 1 MV/cm and it decreases to 6.0×10^{-6} A/cm^2 upon annealing at 700^0C in different atmosphere. The leakage current densities for the 700^{0}C annealed films are 6.6x10^{-6} A/cm^2, 6.0x10^{-6} A/cm^2 and 6.8x10^{-6} A/cm^2 annealed in the presence of air, oxygen and nitrogen respectively. Electric breakdown was observed at a field strength of 2.7 MV/cm. The dielectric constant of the TiO_2 film was calculated from the maximum capacitance of the Al/TiO_2/Si structure under the accumulation condition and it was found to be approximately 26 for the as-deposited film. The dielectric constant of the films increased upon annealing at higher temperature and it varies from 75 to 82 upon annealing at 700^{0}C in different atmosphere, which is higher than those prepared by other methods.

Current-voltage (I-V) and dielectric characteristics of Ta_2O_5 films exhibited a strong annealing temperature dependency. The leakage current density for the as-deposited film was 1.0x10^{-5} A/cm^2, whereas a leakage current density as low as 8.0x10^{-7} A/cm^2 at an electric field of 1 MV/cm can be achieved annealing at 700^{0}C in the presence of oxygen. The leakage current densities for annealed tantalum oxide films for an applied field of 1 MV/cm are 1.5x10^{-6} A/cm^2, 8.0x10^{-7} A/cm^2 and 1.2x10^{-6} A/cm^2 for the films annealed at 700^{0}C in air, oxygen and nitrogen respectively. The electric breakdown voltage was observed at 3.5 MV/cm. The dielectric constant of the as-deposited Ta_2O_5 film is estimated to be about 20 and varies from 37 to 50 depending on annealing temperature in different atmospheres.

Transparent conductive aluminum-doped zinc oxide and indium tin oxide thin films have been prepared by a sol-gel process. All the films are annealed at different temperatures in the presence of air, oxygen and nitrogen and their structural, electrical and optical properties have been investigated.

The resistivity of the ZnO:Al films containing 0.8 at.% Al has a minimum value of 1.5x10^{-4} Ω-cm, 1.8x10^{-4} Ω-cm and 1.3x10^{-4} Ω-cm when annealed at 500^{0}C in air, oxygen and nitrogen respectively. These resistivities of ZnO:Al films prepared by this sol-gel process are lower than those prepared by other conventional methods as shown in table 7.1. The films have an optical transparency up to 88% at 900 nm for a thickness of 300 nm. Annealed films are polycrystalline with a hexagonal structure.

The crystallinity of ZnO:Al films is improved with the increase of annealing temperature.

The resistivity of the ITO films containing 10 wt.% Sn has a minimum value of 8.5×10^{-4} Ω-cm, 9.8×10^{-4} Ω-cm and 8.0×10^{-4} Ω-cm when annealed at 500^0C in air, oxygen and nitrogen, respectively. The resistivity of these ITO thin films prepared by this sol-gel process is also lower than those prepared by other processes as shown in table 7.2. The films have an optical transparency up to 89% at 900 nm. The films are polycrystalline indium oxide with a cubic bixbyite structure with no preferred orientation.

Aluminum doped zinc oxide thin films have been deposited on titanium dioxide and tantalum oxide films on glass by a sol-gel process. The resistivity of ZnO:Al thin films containing 0.8 at.% Al deposited on glass has a minimum value of 1.3×10^{-4} Ω-cm when annealed at 500^0C in nitrogen. The resistivity of ZnO:Al thin films deposited on titanium dioxide and tantalum oxide film on glass has a minimum value of 2.5×10^{-3} Ω-cm and 9.6×10^{-4} Ω-cm, respectively, when annealed at 500^0C in nitrogen. The ZnO:Al thin films deposited on a tantalum oxide film on glass have lower resistivity as that on glass but ZnO:Al thin films deposited on titanium dioxide film on glass have a higher resistivity than those deposited on glass. This increase in resistivity on titanium dioxide film is due to the diffusion of titanium into the zinc oxide layer. The effective region of the ZnO:Al film decreases due to the diffusion of titanium into the zinc oxide layer and subsequently increases the resistivity of ZnO:Al film. The conductance versus thickness curve for ZnO:Al films deposited on titanium dioxide film shown in chapter 8 shows that there is an approximately 300 nm zone whose conductivity is affected by the substrate, e.g. by outdiffusion of titanium from the titanium dioxide insulating layer and there is no effect of the titanium after 300 nm thickness of ZnO:Al.

Indium tin oxide thin films were deposited on titanium dioxide and tantalum oxide film on glass for thin film electroluminescent devices. The resistivity of ITO thin films containing 10 wt.% Sn deposited on glass has a minimum value of 8.0×10^{-4} Ω-cm annealed at 500^0C in nitrogen. The resistivity of ITO films deposited on titanium dioxide and tantalum oxide film has a minimum value of $9.5\text{x}10^{-4}$ Ω-cm and $9.0\text{x}10^{-4}$ Ω-cm, respectively, when annealed at 500^0C in nitrogen which are very low as deposited on glass. This combination of transparent conductive ITO thin films and titanium dioxide or tantalum oxide insulating layer can be used for thin film electroluminescent devices.

From all the experimental results, we see that the bonding structures, crystallinity and optical transmission of the films do not depend on the annealing atmosphere. They only change with the annealing temperatures. The resistivity of the transparent conductive films depends on both the atmospheres and annealing temperatures. We found the minimum value of resistivities for the transparent conductive films occurs for an anneal at 500^0C in the presence of nitrogen. From the combined characteristics of the transparent conductive films deposited on insulating films, we can see that the ITO films deposited on tantalum oxide film have the lowest resistivity when annealed at 500^0C in nitrogen. Thus we can conclude that the combination of transparent conductive ITO films deposited on tantalum oxide film is the best combination for thin film electroluminescent devices.

9.2 Future Work

Thin film electroluminescent devices consist of an insulating layer, a transparent conducting layer and a phosphor layer. The phosphor layer is sandwiched between two insulating layers. In conventional thin film electroluminescent devices, there is a transparent electrode on top of the substrate and a metal electrode on top of the upper insulator. In the inverted thin film electroluminescent devices, the metal electrode is on top of the substrate and the transparent electrode is on top of the upper insulator. The preparation and structural, electrical and optical properties of insulating and transparent conducting layers and their combined characteristics have been studied in this thesis. In a conventional thin film electroluminescent device, the bottom insulator is deposited on top of the transparent electrode. So the combined characteristics of insulating films deposited on top of the transparent conducting film can also be studied. The preparation and properties of the phosphor layer can be studied as an extension of this work. Then all these layers can be deposited on top of each other as shown in fig. 8.1 and fig. 8.2 and the overall performance of thin film electroluminescent devices can be studied.

Transparent conducting aluminum-doped zinc oxide was deposited on top of titanium dioxide film and we tried to get EL emission using manganese doped zinc sulfide phosphor layer. Light emission was obtained but it was not stable. There may be some interdiffusion between the titanium dioxide and aluminum-doped zinc oxide layer. A very thin layer of silicon dioxide may be used on top of titanium dioxide film or any other insulating film can be used instead of titanium dioxide film to make this EL emission stable.

Improvement and alternative use of insulating and transparent conducting layers could improve the performance of thin film electroluminescent devices. To avoid any interdiffusion between the insulating and transparent conducting layers, a very thin layer of insulating silicon dioxide (SiO_2) can be deposited on top of titanium dioxide and tantalum oxide films.

A list of different insulating materials with their properties is shown in table 2.1. Among these insulating materials, the preparation and properties of TiO_2 and Ta_2O_5 thin films have been studied in this work. There are other insulating materials with high dielectric constants, such as, Y_2O_3, $BaTiO_3$, $PbTiO_3$, $SrTiO_3$ and $Sr(Zr,Ti)O_3$. These materials could also be prepared by the sol-gel process and their properties could be studied for use as insulating layers in thin film electrolumunescent devices. Generally, dielectric thin films with high dielectric constants have propagating breakdown mode. Coupled with other dielectric thin films, insulating layers with the propagating breakdown mode can be converted into the self-healing type.

Among the various transparent conducting materials, ZnO:Al and ITO have been studied in this work. In or Ga doped ZnO films or $CdSnO_3$ films could also be studied for use as transparent conducting layers in thin film electroluminescent devices.

It may not be possible to prepare all of the layers of this device by the sol-gel process to produce a good thin film electroluminescent device. A combination of different deposition technologies can be used to prepare the different layers, which may produce a better thin film electrolumunescent device.

REFERENCES

[1] P. D. Rack, A. Naman, P. H. Holloway, S. -S. Sun, R.T. Tuenge, MRS Bulletin 21 (1996) 49.

[2] C. N. King, Journal of the Society of Information Display 1 (1996) 1.

[3] H. Guden, R. W. Pohl, Z.F. Physik 2 (1929) 192.

[4] G. Destriau, Journal de Chem. Phys. et Physico-Chemie Boil. 33 (1936) 620.

[5] L. E. Tannas, Flat Panel Displays and CRTs, van Nostrand Reinhold Co., New York, 1985.

[6] J. A. Castellano, Handbook of Display Technology, Hartcourt Brace Jovanovich, New York, 1992, pp. 8.

[7] A. Vecht, Journal of Applied Physics 1 (1968) 134.

[8] E. J. Soxman, R.D. Ketchpel, JANAIR, Electroluminescence Thin Film Research Report, 1972.

[9] T. Inoguchi, M. Takeda, Y. Kakihara and M. Yoshida, SID Digest (1974) 86.

[10] M. J. Russ and D. I. Kennedy, Journal of the Electrochemical Society (1967) 1066.

[11] J. A. Castellano, Handbook of Display Technology, Hartcourt Brace Jovanovich, New York, 1992, pp. 9.

[12] R. E. Coovert, C. N. King and R. T. Tuenge, SID Digest (1982) 128.

[13] W. A. Barrow, R. C. Coovert, E. Dickey, C. N. King, C. Laakso, S. -S. Sun and R.T. Tuenge, SID Digest (1993) 76 1.

[14] Y. A. Ono, Electroluminescent Displays, in H.L. Ong (Ed.), Series on Information Display, World Scientific, Singapore, 1995, Vol. 1, pp. 61.

[15] R. Khormaei, S. Thayer, K. Ping, C. King, G. Dolney, A. Ipri, F.-L. Hsueh, R. Stewart, T. Keyser, G. Becker, D. Kagey, M. Spitzer, SID Digest (1994) 137.

[16] P. Bailey, D. Carkner, X. Wu. SID Digest (1995) 484.

[17] P. M. Alt, SID Digest (1984) 79.

[18] J. D. Davidson, J.F. Wager, I. Khormaei, C. N. King and R. Williams, IEEE Transactions of Electron Devices ED-39 (1992) 1122.

[19] A. A. Douglas and J.F. Wager, SID Digest (1992) 356.

[20] S. Kobayashi, J.F. Wager, A. Abu-Dayah, EL 92 (1992) 234.

[21] K. Miyashita, M. Shibata, Digest of Japan Display (1993) 100.

[22] C. N. King, SID Lecture Notes, 1988.

[23] E. Bringuier, Journal of Applied Physics 70 (1991) 4505.

[24] E. Bringuier, Journal of Applied Physics 67 (1990) 7040.

[25] K. L. Chopra, S. Major, D.K. Pandya, Thin Solid Films 102 (1983) 1.

[26] P. M. Alt, Proc. SID 25 (1984) 123.

[27] W. E. Howard, IEEE Trans. Electron Devices ED-24 (1977) 903 and Proc. SID 18 (1977) 119.

[28] S. K. Tiku and G. C. Smith, IEEE Trans. Electron Devices ED-31 (1984) 105.

[29] W. E. Howard, IEEE Transactions on Electronic Devices 24 (1977) 903.

[30] Y. A. Ono, Electroluminescent Displays, in H.L. Ong (Ed.), Series on Information Display. World Scientific, Singapore, 1995, Vol. 1, pp. 65.

[31] Y. Fujita, J. Kuwata, M. Nishikawa, T. Tohda, T. Matsuoka, A. Abe and T. Nitta, Japan Display'83 (1983) 76 and Proc. SID 25 (1984) 177.

[32] A. Mikami, K. Terada, K. Okibayashi, K. Tanaka, M. Yoshida and S. Nakajima, J. Appl. Phys., 72 (1992) 773.

[33] C. N. King, 1985 SID Seminar Lecture Notes Vol. 1, S-4.1 (1985) 4.1/1.

[34] Y. A. Ono, Electrolumineseent Displays, in H.L. Ong (Ed.), Series on

Information Display, World Scientific, Singapore, 1995, Vol. 1, pp. 148.

[35] L. I. Maissel and R. Glang, editors, Handbook of Thin Film Technology, McGraw-Hill, New York, (1970).

[36] J. L. Vossen and W. Kern, editors, Thin Film Process, Academic Press, New York (1978).

[37] R. F. Bunshah, editor, Deposition Technologies for Films and Coatings: Developments and Applications, Noyes Publications, Park Ridge, New Jersey (1982).

[38] S. K. Ghandhi, VLSI Fabrication Principles, John Wiley & Sons, New York (1983).

[39] H. Dislich and E. Hussmann, Thin Solid Films, 77 (1981) 129.

[40] K. L. Chopra and I. Kaur, Thin Film Device Applications, Plenum Press, New York (1983).

[41] D. A. Glocker and S. I. Shah, Handbook of Thin Film Process Technology, Institute of Physics publishing, Bristol and philadelphia (1995).

[42] K. Wasa and S. Hayakawa, Handbook of Sputter Deposition Technology: Principles, Technology and Application, Noyes Publications, New Jersey (1992).

[43] J. K. Robertson and C. W. Clapp, Nature 132 (1933) 479.

[44] G. S. Anderson, W. N. Mayer and G. K. Wehner, J. Appl. Phys., 33 (1962) 2291.

[45] P. D. Davidse and L.I. Maissel, J. Appl. Phys., 37 (1966) 754.

[46] F. M. Penning, U. S. Patent 2, 146, 025 (Feb. 1935).

[47] W. D. Gill and E. Kay, Rev. Sci. Instrum., 36 (1965) 277.

[48] E. Kay, U. S. Patent 309, 159 (Sept. 1963), assigned to IBM Corp.

[49] S. Hayakawa and K. Wasa, J. Phys. Soc. Jpn., 20 (1965) 1692.

[50] K. Wasa and S. Hayakawa, J. Phys. Soc. Jpn., 20 (1965) 1219.

[51] K. Wasa and S. Hayakawa, IEEE Trans. Parts Materials Packaging, PMP-3: 71 (1967).

[52] K. Wasa and S. Hayakawa, Rev. Sci. Instrum., 40 (1969) 693.

[53] K. Wasa and S. Hayakawa, Thin Solid Films, 52 (1978) 31.

[54] K. Wasa and S. Hayakawa, Jpn. Patent 642, 012 (1967), assigned to Matsushita Electric Ind. Corp.

[55] P. J. Clarke, U. S. Patent 3, 616, 450 (Oct. 1971).

[56] J. S. Chapin, Res./Dev., 25 (1974) 37.

[57] V. Hoffman, Solid State Technol., 57 (Dec. 1976).

[58] R. Phol and P. Pringsheim, Verh. DTSCH. Phys. Ges., 14 (1912) 546.

[59] G. Bauer, Ann. Phys. Lpz., 19 (1934) 434.

[60] J. Strong, J. Opt. Soc. Am., 26 (1936) 73.

[61] C. Cartwright and A. Truner, Multilayer films of high reflecting power Phys. Rev., 55 (1939) 1128A.

[62] Eastman Kodak Co., private communication.

[63] 1951 British patent 754 210.

[64] 1969 US patent 3230 110.

[65] D. M. Mattox, Fundamentals of ion plating, 10 (1973) 47.

[66] E. Hantzche, IEE Trans. Plasma Sci., 18 (1990) 883.

[67] K. H. Muller, J. Appl. Phys., 59 (1986) 2803.

[68] N. Uetake, T. Asano and K. Suzuki, Rev. Sci. Instrum., 62(1991) 1942.

[69] P. C. Zalm, 1989 Quantitative sputtering Handbook of Ion Beam Technology ed J. J. Cuomo, S. M. Rossnagel and H. R. Kaufman (New Jersey:Noyes) pp 78-111.

[70] R. F. Bunshah, IEEE Trans. Plasma Sci., 18 (1990) 846.

[71] I. H. Khan, in Handbook of Thin Film Technology, (L. Maissel and R. Glang,

eds.) 10-1, McGraw Hill, New York (1970).

[72] C. J. Brinker and G. W. Scherer, Sol-Gel Science (Boston, Mass: Academic Press) (1990).

[73] J. J. Ebelmen, Ann., 57 (1846) 331.

[74] W. Geffcken and E. Berger, German Patent 736 411 (May 1939).

[75] H. Schroeder, Phys. Thin Films, 5 (1969) 87.

[76] T. Graham, J. Chem. Soc., 17 (1864) 318.

[77] C. B. Hurd, Chem. Rev., 22 (1938) 403.

[78] S. S. Kistler, J. Phys. Chem., 36 (1932) 52.

[79] R. H. Ewell and H. Insley, J. Res. NBS, 15 (1935) 173.

[80] R. M. Barrer and L. Hinds, Nature, 166 (1950) 562.

[81] R. Roy, J. Am. Ceram. Soc., 39[4] (1956) 145.

[82] R. Roy, J. Am. Ceram. Soc., 52[6] (1969) 344

[83] R. M. Dell, in Reactivity of solids, eds. J. S. Anderson, M. W. Roberts, and F. S. Stone (Chapman and Hall, N. Y., 1972), 553.

[84] J. L. Woodhead, Silicates Ind., 37 (1972) 191.

[85] L. Levene and I. M. Thomas, U. S. patent 3,640,093 (February 8, 1972).

[86] H. Dislich, Angewandt Chemie, 10[6] (1971) 363.

[87] E. Wainer, German Patent 1,249,832 (April 11, 1968).

[88] H. G. Sowman, U. S. Patent 3,795,524 (March 5, 1974).

[89] S. Horikuri, K. Tsuji, Y. Abe, A. Fukui and E. Ichiki, Japanese Patent 49-108325 (October 15, 1974).

[90] B. E. Yoldas, J. Mater. Sci., 10 (1975) 1856.

[91] B. E. Yoldas, J. Mater. Sci., 12 (1977) 1203.

[92] M. Yamane, A. Shinji and T. Sakaino, J. Mater. Sci., 13 (1978) 865.

[93] A. J. Vega and G. W. Scherer, J. Non-Cryst. Solids, 111 [2,3] (1989) 153.

[94] T. W. Zerda, I. Artaki and J. J. Jonas, J. Non-Cryst. Solids, 81 (1986) 365.

[95] G. Orcel, L. L. Hench, I. Artaki, J. Jonas and T. W. Zerda, J. Non-Cryst. Solids, 105 (1988) 223.

[96] R. W. Hopper and D. R. Uhlmann, Mater. Sci. and Eng., 15 (1974) 137.

[97] J. Frenkel, J. Phys. (Moscow), 9[5] (1945) 385.

[98] L. E. Scriven in better Ceramics Through Chemistry III eds. C. J. Brinker, D. E. Clarke and D. R. Ulrich (Mat. Res. Soc., Pittsburg, Pa., 1988), pp. 717-729.

[99] R. P. Spiers, C. V. Subaraman and W. L. Wilkinson, Chem. Eng. Sci., 29 (1974) 389.

[100] L. D. Landau and B. G. Levich, Acta Physiochim, U. R. S. S., 17 (1942) 42.

[101] D. E. Bornside, C. W. Macosko and L. E. Scriven, J. Imaging Tech., 13 (1987) 122.

[102] B. Higgins, Phys. Fluids, 29 (1986) 3522.

[103] A. G. Emslie, F. T. Bonner and L. G. Peck, J. Appl. Phys., 29 (1958) 858.

[104] D. E. Clark, W. J. Dalzell and D. C. Folz, Ceram. Eng. Sci. Proc., 9 (1988) 1111.

[105] L. Foss, M. S. Thesis, Massachusetts Institute of Technology, Cambridge, Mass. (1982).

[106] S. Storz, J. Colloid and Int. Sci., 65 (1978) 118.

[107] B. Derjaguin, Ya. I. Rabinovich, A. I. Storozhilova and G. I. Shcherbing, J. Colloid Interface Sci., 57 (1976) 451.

[108] W. J. Dalzell and D. E. Clark, Cer. Eng. And Sci. Proc., 7 (1986) 1014.

[109] T. J. Garino, Ph.D. Thesis, Massachusetts Institute of Technology, Cambridge, Mass. (1986).

[110] T. J. Garino and H. K. Bowen, J. Am. Ceram. Soc., 70 (1987) 315.

[111] T. J. Garino and H. K. Bowen, J. Am. Ceram. Soc., 70 (1987) 311.

[112] L. G. Bunville in Modern Methods of Particle Size Analysis, ed. H. G. Barth (Wiley, New York, 1984), p. 6.

[113] M. Lottiaux, C. Boulesteix, G. Nihoul et al., Thin Solid Films, 170 (1989) 107.

[114] J. D. Mackenize, L. L. Hench and D. R. Ulrich in Ultrastructure Processing of Glasses, Ceramics and Composites, eds. (Wiley, New York, 1984), p. 15.

[115] W. H. Steel, Interferometry, 2nd. Edition, Cambridge University Press, (1983).

[116] E. Passaglia, R. R. Stromberg and J. Kruger (eds.), "Ellipsometry in the Measurement of Surface and Thin Films," NBS Misc. Publ. 256, Government Printing Office, Washington, D. C., 1964.

[117] H.G. Tompkins, A Users Guide to Ellipsometry, Academic Press Inc., San Diego, (1993).

[118] K. Riedling, Ellipsometry for Industrial Application, Springer-Verlag Wien, New York, (1988).

[119] L. B. Valdes, "Measurement of minority carrier lifetime in germanium," Proc. I.R.E., 40 Nov. (1952) 1429.

[120] F. Wenner, Bulletin of the Bureau of Standards, 12(1915) 469.

[121] L. B. Valdes, "Resistivity measurements on germanium for transistors", Proc. I.R.E., 42 Feb. (1954) 420.

[122] L. B. Valdes, "Effect of electrode spacing on the equivalent base resistance of point-contact transistors" Proc. I.R.E., vol. 40, Nov (1952) 1429.

[123] L. J. Van der Pauw, Philips Research Reports, 13, 1 (1958) 1-9.

[124] D. C. Look, "Electrical characterization of GaAs materials and devices", Wiley, NY (1989) 12-20.

[125] H. Weider, "Laboratory notes on electrical and galvanomagnetic measurements", Elsevier, Amsterdam (1979) 7-9.

[126] E. H. Hall, "On a new action of the magnet on electric currents", Amer. J.

Math, 2 (1879) 287-292.

[127] "Surface texture (surface roughness, waviness and lay)", American Society of Mechanical Engineers, 1996. (ASME B46.1-1995), New York, NY.

[128] D. Lin-Vien, N. B. Colthup, W. G. Fateley and J. G. Grasselli, "The Handbook of Infrared and Raman Characteristic Frequencies of Organic Molecules", Academic Press, Inc., New York, 1991.

[129] N. B. Colthup, L. H. Daly and S. E. Wiberly, Introduction to Infrared and Raman Spectroscopy, Academic Press, inc., San Diego, 1990

[130] K. Nakamoto, Infrared and Raman Spectra of Inorganic and Coordination Compounds, 4th edn., John Wiley & Sons, New York, 1986.

[131] J. P. Glusker and K. N. Trueblood, Crystal Structure Analysis, 2nd Edition, Oxford University Press, 1985.

[132] W. L. Bragg, The Crystalline State, Vol. I: A General Survey, George Bell, London, 1933.

[133] E. Rutherford, Phil. Mag., 28 (1914) 305.

[134] J. C. Vickerman, editor, Surface Analysis-The Principal Techniques, John Wiley & Sons, New York (1997).

[135] H. H. Perkampus, UV-VIS Spectroscopy and Its Application, Springer-Verlag Berlin Heidelberg,New York, 1992.

[136] W. Tang, Electroluminescent Displays by Sol-Gel Process, Ph.D. Thesis, Dublin City University, Dublin, Ireland, 1994.

[137] T. Inoguchi and S. Mito, Electroluminescence, Topics in Applied Physics 17, eds. J. I. Pankove (Springer, New York, 1982), pp. 197.

[138] C. N. King, Society for Information Display (1985), Seminar Lecture Notes 4.1.

[139] A. R. Bally, K. Prasad, R. Sanjines, P. E. Schmid, F. Levy, J. Benoit, C. Barthou and P. Benalloul, Mat. Res. Soc. Symp. Proc., Vol. 424 (1997) 471.

[140] Y. Fujita, J. Kuwata, M. Nishikawa, T. Tohda, T. Matsuoka, A. Abe and T.

Nitta, Japan Disply, 76 (1983).

[141] H. Schroder, G. Haas and R. E. Thun (eds.), Physics of Thin Films, Academic, New York, (1969) 87.

[142] H. K. Pulker, Thin Film Science and Technology, Coatings on Glass, Elsevier, Amsterdam, 6 (1984).

[143] B. E. Yoldas and T. W. O'Keefe, Appl. Opt. 18 (1979) 3133.

[144] B. E. Yoldas, Appl. Opt. 21 (1982) 2960.

[145] T. Fuyuki and H. Matsunami, Jpn. J. Appl. Phys., 25 (1986) 1288.

[146] P. A. Bertrand and P. D. Fleischauer, Thin Solid Films, 103 (1983) 167.

[147] T. Yoko, K. Kamiya, A. Yuasa, K. Tanaka and S. Sakka, J. Non-cryst. Solids, 100 (1988) 483.

[148] S. Doeuff, M. Henry and C. Sanchez, MRS Symp. Proc., 73 (1986) 653.

[149] J. Livage, MRS Symp. Proc., 73 (1986) 717.

[150] N. Nabavi, S. Doeuff, C. Sanchez and J. Livage, Mater. Sci. Eng. B, 3 (1989) 203.

[151] J. G. Mavroides, D. I. Tchernev, J. A. Kafalas and D. F. Koleser, Mat.Res. Bull., 10 (1975) 1023.

[152] M. R. Kozlowski, P. S. Tyler, W. H. Smyrl and R. T. Atanasoski, J. Electrochem. Soc., 136 (1989) 442.

[153] S. Schiller, G. Beister and W. Sieber, Thin Solid Films, 83 (1981) 239.

[154] M. H. Suhail, G. Mohan Rao and S. Mohan, J. Appl. Phys., 71 (1992) 1421.

[155] B. Bellan, J. Non-cryst. Solids, 55 (1983) 405.

[156] G. W. Rice, J. Am.Ceram. Soc., 70 (1987) C-117.

[157] S. Zhang, Y. F. Zhu and D. E. Brodie, Thin Solid Films, 213 (1992) 265.

[158] K. S. Yeung and Y. W. Lam, Thin Solid Films, 109 (1983) 169.

[159] J. P. Lu, J. Wang and R. Raj, Thin Solid Films, 204 (1991) L13.

[160] L. M. Williams and D. W. Hess, J. Vac. Sci. Technol. A, 1 (1983) 1810.

[161] M. J. Alam and D. C. Cameron, "Optical and electrical properties of titanium dioxide thin films deposited by the sol-gel process", Proceedings of the international Conference on Advances in Materials and Processing Technologies (AMPT'99), Vol. II, pp. 1185-1193, Dublin City University, August, 1999.

[162] K. A. Vorotilov, E. V. Orlova and V. I. Petrovsky, Thin Solid Films, 207 (1992) 180.

[163] V. J. Nagpal, R. M. Davis and S. B. Desu, J. Mater. Res., 10 (1995) 3068.

[164] I. Manzini, G. Antonioli, P. P. Lottici, G. Gnappi and A. Montenero, Physica B, 208 & 209 (1995) 607.

[165] H. Shin, M. R. De Guire and A. H. Heuer, J. of Appl. Phys., 83 (1998) 3311.

[166] S. M. Sze, Physics of Semiconductor Devices, John Wiley & Sons, New York, 1981.

[167] H. Shinriki and M. Nakata, IEEE Trans. Electron Devices, 38 (1991) 455.

[168] S. Kamiyama, H. Suzuki and H. Watanable, J. Electrochem. Soc., 141 (1994) 1246.

[169] W. G. Lee, S. I. Woo, J. C. Kim, S. H. Choi and K. H. Oh, Thin Solid Films 237 (1994) 105.

[170] H. Kimura, J. Mizuki, S. Kamiyama and H. Suzuki, Appl. Phys. Lett., 66 (1995) 2209.

[171] C. J. Kang, J. S. Chun and W. J. Lee, Thin Solid Films, 189 (1990) 61.

[172] J. Patsher and S. Veprek, Plasma Chem. Plasma Process., 12 (1990) 129.

[173] M. L. Calzada and L. Del Olmo, J. Non-Cryst. Solids, 121 (1992) 413.

[174] T. Kamada, M. Kitagawa, M. Shibuya and T. Hirao, Jpn. J. Appl. Phys., 30 (1991) 3594.

[175] A. Turkovic, M. Ivanda, A. Drasner, V. Vranesa and M. Persin, Thin Solid

Films, 198 (1991) 199.

[176] T. Ohsaka, F. Isumu and Y. Fujiki, J. Raman Spectrosc., 7 (1978) 321.

[177] Y. Kagami, T. Yamauchi, Y. Osada, I. Yoshizaura, J. Appl. Phys., 68 (1990) 610.

[178] K. Bange, C. R. Ottermann, O. Anderson, U. Jeschkowski, Thin Solid Films, 197 (1991) 279.

[179] F. Rubio, J. Denis, J. M. Albella and J. M. Martinez-Duart, Thin Solid Films, 90 (1982) 405.

[180] Y. –K. Tu, C. –C. Lin, W. –S. Wang and S. –L. Huang, Proc. SPIE, 836 (1987) 40.

[181] K. Kukli, J. Ihanus, M. Ritala and M. Leskela, J. Electrchem. Soc., 144 (1997) 1.

[182] M. A. Mohammed and D. V. Morgan, Phys. Status Solidi (a), 115 (1989) 213.

[183] T. Saito, Y. Ushio, M. Yamada and T. Niwa, Solid State Ion., 40/41 (1990) 499.

[184] N. Ozer, Y. X. He and C. H. Lambert, Proc. SPIE, 2255 (1994) 456.

[185] C. Hashimoto, H. Oikawa and N. Honma, IEEE Trans. Electron Devices, 36 (1989) 14.

[186] W. C. Herrmann, Jr., J. Vac. Sci. Technol., 18 (1981) 1303.

[187] D. W. Graham and D. P. Stinton, J. Am. Ceram. Soc., 77 (1994) 2298.

[188] R. Chapman and F. Monaldo, J. Am. Ocean. Tech., 12 (1995) 190.

[189] S. Tanimoto, M. Matsui, K. Kamisako, K. Kuroiwa and T. Tarui, J. Electrochem. Soc., 139 (1990) 320.

[190] W. R. Hitchens, W. C. Krusell and D. M. Dobkin, Mater. Res. Soc. Symp. Proc., 284 (1993) 499.

[191] H. S. Moon, J. S. Lee, S. W. Kan, J. W. Park, J. H. Lee, S. K. Yang and H. H. Park, J. Mater. Sci., 29 (1994) 1545.

[192] F. C. Chiu, J. J. Wang, J. Y. Lee and S. C. Wu, J. Appl. Phys., 81 (1997) 6911.

[193] H. Demiryont, J. R. Sites and K. Geib, Appl. Opt., 24 (1985) 490.

[194] M. Cevro and M. Carter, Opt. Eng., 34 (1995) 596.

[195] W. M. Paulson, F. S. Hickernell and R. L. Davis, J. Vac. Sci. Technol., 16 (1979) 307.

[196] S. Schiller, U. Heisig, K. Steinfelder and J. Strumpfel, Thin Solid Films, 63 (1979) 363.

[197] H. O. Sankur and W. Gunning, Appl. Opt., 28 (1989) 341.

[198] G. A. Al-Jumaily and S. M. Edlou, Thin Solid Films, 209 (1992) 223.

[199] J. Y. Zhang, L. J. Bie, V. Dusastre and I. W. Boyd, Thin Solid Films, 318 (1998) 252.

[200] P. G. Clem, N. L. Jeon, R. G. Nuzzo and D. A. Payne, J. Am. Ceram. Soc., 80 (1997) 2821.

[201] M. J. Duggan, T. Saito and T. Niva, Solid State Ionics, 62 (1993) 15.

[202] T. Aoyama, S. Saida, Y. Okayama, M. Fujisaki, K. Imai and T. J. Arikado, J. Electrochem. Soc., 143 (1996) 977.

[203] K. Badeker, Ann. Phys. (Leipzig) 22 (1907) 749.

[204] C. M. Lampert, Sol. Energy Mater., 6 (1981) 1.

[205] G. Frank, E. Kauer and H. Kostlin, Thin Solid Films, 77 (1981) 107.

[206] C. G. Granqvist, Thin Solid Films, 93/94 (1990) 730.

[207] N. Croitoru and E. Bannett, Thin Solid Films, 82 (1981) 235.

[208] R. Singh, M. A. Green and K. Rajkanan, Solar Cells, 3 (1981) 95.

[209] J. B. Dubow and D. E. Burk, Appl. Phys. Lett., 29 (1976) 494.

[210] M. S. Tomar, Thin Solid Films, 164 (1988) 295.

[211] T. Oyaby, Y. Ohta and T. Kurobe, Sens. Actuators, 9 (1986) 301.

[212] G. Martinelli and M. C. Carotta, Sens. Actuators B, 7 (1992) 717.

[213] S. M. Budd, Thin Solid Films, 77 (1981) 13.

[214] N. Jackson and J. Ford, Thin Solid Films, 77 (1981) 23.

[215] F. J. Trojer, Thin Solid Films, 77 (1981) 3.

[216] V. J. Novotny and A. S. Kao, IEEE Trans. Mag., 26 (1990) 2449.

[217] R. Latz, K. Michael and M. Scherer, Jpn. J. Appl. Phys., 30 (1991) L149.

[218] N. Kuck, K. Leiberman, A. Lewis and A. Vecht, Appl. Phys. Lett., 61 (1992) 139.

[219] Y. Chubachi and K. Aoyama, Jpn. J. Appl. Phys., 30 (1991) 1442.

[220] H. Yoshida, H. Furubayashi, Y. Inque and T. Tonomura, J. Vac. Soc. Japan, 19 (1976) 13.

[221] R. T. Chen and D. Robinson, Appl. Phys. Lett., 60 (1992) 1541.

[222] H. T. Tien and J. Higgins, J. Electrochem. Soc., 127 (1980) 1475.

[223] G. Hass, J. B. Heaney and A. R. Toft, Appl. Opt., 18 (1979) 1488.

[224] Y. Sawada, Mater. Forum, 6 (1986) 15.

[225] R. M. Schaffert, Electrography, The Focal Press, London, 1971, p. 237.

[226] G. Hohenberger and G. Tomandl, J. Mater. Res., 7 (1992) 546.

[227] S. P. S. Arya, A. D'Amico and E. Verona, Thin Solid Films, 157 (1988) 169.

[228] M. H. Francombe and S. V. Krishnaswamy, J. Vac. Sci. Technol., A8 (1990) 1382.

[229] M. S. Wu, A. Azuma, T. Shiosaki and A. Kawabata, IEEE Trans. Ultrasonics, Ferroelectrics, Freq. Control, 36 (1989) 442.

[230] S. Major, S. Kumar, M. Bhatnagar and K. L. Chopra, Appl. Phys. Lett., 49 (1986) 394.

[231] T. Minami, H. Nanto and S. Takata, Jpn. J. Appl. Phys., 23 (1984) L280.

[232] Z. C. Jin, I. Hamberg and C. G. Granqvist, J. Appl. Phys., 64 (1988) 5117.

[233] O. F. Khan and P. O'Brien, Thin Solid Films, 173 (1989) 95.

[234] T. Maruyama and A. Nakai, Jpn. J. Appl. Phys., 28 (1989) L346.

[235] D. H. Zhang and E. D. Brodie, Thin Solid Films, 238 (1994) 95.

[236] A. Kuroyanagi, Jpn. J. Appl. Phys., 28 (1989) L219.

[237] A. F. Aktaruzzaman, G. L. Sharma and L. K. Malhotra, Thin Solid Films, 198 (1991) 67.

[238] S. Major, A. Banerjee and K. L. Chopra, Thin Solid Films, 108 (1983) 333.

[239] Z. Y. Ning, S. H. Cheng, S. B. Ge, Y. Chao, Z. Q. Gang, Y. X. Zhang and Z. G. Liu, Thin Solid Films, 307 (1997) 50.

[240] M. J. Alam and D. C. Cameron, J. Vac. Sci. Technol. A 19(4) (2001) 1642.

[241] T. Isago, S. Sonobe, T. Ohkawa and H. Sunayama, J. Ceram. Soc. Jpn., 104 (1996) 1052.

[242] Y. Ohya, H. Saiki and Y. Takahashi, J. Mater. Sci., 29 (1994) 4099.

[243] D. Goyal, P. Solanki, B. Marathe, M. Takwale and V. Bhide Jpn. J. Appl. Phys., 31 (1992) 361.

[244] D. Cossement and J. M. Streydio, J. Cryst. Growth, 72 (1985) 57.

[245] H. Haitjema, J. J. Elich and C. J. Hoogendoorn, Sol. Energy Mater., 18 (1989) 283.

[246] P. Ponasewicz, R. Littbarski and M. Grunze, in E. Kaldis (ed.), Current Topics in Materials Science, Vol. 7, North-Holland, Amsterdam, 1981.

[247] D. H. Zhang and H. L. Ma, Appl. Phys. A 62 (1996) 4.

[248] I. Hamberg, G. C. Granqvist, K. F. Berggren, B. E. Sernelius and L. Enstron, Phys. Rev. B, 30 (1984) 3240.

[249] T. L. Yang, D. H. Zhang, J. Ma, H. L. Ma and Y. Chen, Thin Solid Films, 326 (1998) 60.

[250] J. Ma, F. Ji, D. H. Zhang, H. L. Ma and S. Y. Li, Thin Solid Films, 357 (1999) 98.

[251] C. A. Arguello, D. L. Rousseau and S. P. S. Porto, Phys. Rev., 1813 (1969)

1351.

[252] J. M. Liu, C. K. Ong and L. C. Lim, Ferroelectrics, 231 (1999) 223.

[253] S. K. Sharma and G. J. Exarhos, Solid State Phenomena, 55 (1997) 32.

[254] G. E. McGuire, G. K. K. Schweitzer and T. A. Carlson, Inorg. Chem., 12 (1973) 2451.

[255] O. H. L. Weijitens, P. A. C. Van loon, Thin Sold Films, 196 (1991) 1.

[256] T. Nagatoma, Y. Martua, O. Omao, Thin Solid Films, 192 (1990) 17.

[257] I. Hambergend, C. G. Granquist, J. Appl. Phys., 60 (1986) R123.

[258] K. Nishio, T. Sei, T. Tsuchiya, J. Mat. Sci., 31 (1996) 1761.

[259] Y. Djaoued, V. H. Phong, S. Badilescu, P. V. Ashrit, F. E. Girouard, V. V. Truong, Thin Solid Films, 293 (1997) 108.

[260] T. Furusaki, K. Kodaira, High Performance Ceramic Films and Coatings, 1 (1991) 241.

[261] D. M. Mattox, Thin Solid films, 204 (1991) 25.

[262] J. I. Pankove, Display Devices, Topics in Applied Physics, Vol. 40, Springer-Verlag,Berlin, 1980.

[263] L. J. Meng, C. H. Li, G. Z. Zhong, J. Lumin. 39 (1987) 11.

[264] J. R. Bellingham, A. P. Mackenzie, W. A. Philips, Appl. Phys. Lett., 58 (1991) 2506.

[265] A. Valentini, F. Quaranta, M. Penza, F. R. Rizzi, J. Appl. Phys., 73 (1993) 1143.

[266] C. H. Lee, C. S. Huang, Mater. Sci. Eng. (Solid State Mater Adv. Technol.) B22 (1994) 223.

[267] K. Osaza, T. Ye, Y. Aoyagi, Thin Solid Films, 246 (1994) 58.

[268] B. J. Luff, J. S. Wilkinson, G. Perrone, Appl. Opt., 36 (1997) 7066.

[269] L. Tamisier, A. Carani, Electrochim. Acta, 32 (1987) 1365.

[270] J. E. Costellamo, Handbook of Display Technology, Academic Press, New York, 1992.

[271] S. Ishibashi, Y. Higuchi. Y. Ota, K. Nakamuva, J. Vac. Sci. Technol., 18 (1990) 1399.

[272] K. L. Copra, S. R. Das, Thin film solar cell, Plenum Press, New York, 1983, p. 321.

[273] I. A. Rauf, J. Appl. Phys., 79 (1996) 4057.

[274] Y. Shigesato, D. C. Paine, Thin Solid Films, 238 (1994) 44.

[275] T. Suzuki, J. Mater. Sci. Lett., 7 (1988) 79.

[276] S. Bhagwat, R. P. Howson, Surface and Coatings Technology, 111 (1999) 163.

[277] George, C. S. Menon, Indian J. Pure Appl. Phys., 33 (1995) 700.

[278] P. Thilakan, S. Kalainathan, J. Kumar, P. Ramssamy, J. Electron. Mater., 24 (1995) 719.

[279] M. Rami, E. Benamar, C. Messaoudi, D. Sayah, A. Ennaoui, European Journal of Solid State and Inorganic Chemistry 35 (1998) 211.

[280] C. Cali, M. Mosca, G. Taragia, Solid State Electron., 42 (1998) 877.

[281] M. J. Alam and D. C. Cameron, Thin Solid Films, 377-378 (2000) 455.

[282] M. Toki, M. Aizawa, J. Sol-Gel Science Technol., 8 (1997) 717.

[283] T. F. Stoica, T. A. Stoica, V. Vanca, E. Lakatos, M. Zaharescu, Thin Solid Films, 348 (1999) 273.

[284] D. B. Fraser and H. D. Cook, J. Electrochem. Soc., 119 (1972) 1368.

[285] H. Kostlin, R. Jost and W. Lems, Phys. Status Solidi A 29 (1975) 87.

[286] S. S. Kim, S. Y. Choi, C. G. Park and H. W. Jin, Thin Solid Films, 347 (1999) 155.

[287] E. Shanti, A. Banerjee, V. Dutta and K. L. Chopra, J. Appl. Phys. 53 (1982) 1615.

[288] L. J. Meng and M. P. D. Santos, Thin Solid Films, 322 (1998) 56.

[289] A. Salehi, Thin Solid Films, 324 (1998) 214.

[290] T. Maruyama and T. Kitamure, Jpn. J. Appl. Phys., 28 (1989) L1096.

[291] M. Penza, S. Cozzi, M. A. Tagliente, L. Mirenghi, C. Martucci and A. Quirini, Thin Solid Films 349 (1999) 71.

[292] J. C. C. Fan and J. B. Goodenough, J. Appl. Phys., 48 (1977) 3524.

[293] Jill Chastain (Ed.), Handbook of X-ray Photoelectron Spectroscopy, Perkin-Elmer Corp, Minnesota, 1992.

[294] A. W. C. Lin, N. R. Armstrong and T. Kuwana, Anal. Chem., 49 (1977) 1228.

[295] G. E. McGuire, G. K. K. Schweitzer and T. A. Carlson, Inorg. Chem., 12 (1973) 2451.

[296] W. E. Morgan and J. R. Van Wazer, J. Phys. Chem., 77 (1973) 96.

[297] S. Ray, R. Banerjee, N. Basu, A. K. Batabyal and A. K. Barua, J. Appl. Phys., 54 (6) (1983) 3497.

Appendix A

X-Ray Diffraction Data Table For Titanium Dioxide (Card No. 21-1272)

2θ	Intensity	h k l
25.281	100	1 0 1
36.947	10	1 0 3
37.801	20	0 0 4
38.576	10	1 1 2
48.050	35	2 0 0
53.891	20	1 0 5
55.062	20	2 1 1

X-Ray Diffraction Data Table For Tantalum Oxide (Card No. 25-0922)

2θ	Intensity	h k l
22.901	85	0 0 1
28.290	100	1 1 0
36.664	75	1 1 1
46.685	25	0 0 2
49.727	17	0 2 0
50.703	18	0 2 2
55.475	35	0 2 1

X-Ray Diffraction Data Table For Zinc Oxide (Card No. 36-1451)

2θ	Intensity	h k l
31.770	57	1 0 0
34.422	44	0 0 2
36.253	100	1 0 1
47.539	23	1 0 2
56.603	32	1 1 0

X-Ray Diffraction Data Table For Indium Tin Oxide (Card No. 44-1087)

2θ	Intensity	h k l
35.451	28	4 0 0
37.688	3	4 1 1
39.809	1	4 2 0
41.841	< 1	3 3 2
43.797	< 1	4 2 2
45.684	3	4 3 1
49.288	2	5 2 1
51.019	35	4 4 0
52.708	1	4 3 3
54.360	< 1	6 0 0
55.975	2	6 1 1
57.565	1	6 2 0
59.127	1	5 4 1

Appendix B

Publications on This Work

1. M. J. Alam, D. C. Cameron, "Characterization of transparent conductive ITO thin films deposited on titanium dioxide film by sol-gel process", Surface and Coatings Technology, 142-144 (2001) 776-780.

2. M. J. Alam, D. C. Cameron, "Preparation and properties of transparent conductive aluminum-doped zinc oxide thin films by sol-gel process", Journal of Vacuum Science and Technology A, 19(4), Part II, pp. 1642-1646, July/August 2001.

3. M. J. Alam, D. C. Cameron, "Electrical, Optical and Structural Properties of Sol-gel Deposited Tantalum Oxide Thin Films", Accepted for presentation at the AVS 48th International Symposium in San Francisco, California, October 28-November 2, 2001.

4. M. J. Alam, D. C. Cameron, "Investigation of annealing effects on sol-gel deposited indium tin oxide thin films in different atmospheres", Accepted for presentation at the International Conference On Metallurgical Coatings And Thin Films (ICMCTF) in San Diego, California, April 22-26, 2002.

5. M. J. Alam, D. C. Cameron, "Optical and Electrical properties of transparent conductive ITO thin films deposited by sol-gel process", Thin Solid Films, 377-378 (2000) 455.

6. M. J. Alam, D. C. Cameron, "Optical and Electrical properties of titanium dioxide thin films deposited by the sol-gel process", Proceedings of the International

Conference on advances in Materials and Processing technologies (AMPT'99), Vol. II, pp. 1185-1193, Dublin City University, August, 1999.

7. M. J. Alam, D. C. Cameron, "Preparation and Characterization of TiO_2 thin films by Sol-gel Method", submitted to the Journal of Sol-gel Science and Technology.

8. M. J. Alam, D. C. Cameron, "Effect of annealing in different temperatures on electrical, optical and structural properties of sol-gel deposited tantalum oxide thin film", in preparation for submission to Thin Solid Films.